Biomimetic hydrogels for in situ bone tissue engineering.

Nature-inspired crosslinking methods as a tool to tune scaffold physical properties.

Author: Aitor Sánchez Ferrero

Director: Dra. Elisabeth Engel López

PhD program in Biomedical Engineering

Department of Materials Science and Metallurgical Engineering (CMEM)

Technical Superior School of Industrial Engineering of Barcelona (ETSEIB)

Technical University of Catalonia (UPC)

Barcelona, November 2015

This dissertation is submitted to the Technical University of Catalonia in fulfillment of the requirements for the degree of Doctor in Biomedical Engineering.

ABSTRACT

The global incidence of bone fractures, and subsequently that of non-healing ones, is expected to rise in the coming decades, mostly due to an increased risk of age-related conditions. Currently, the biomaterials field is moving towards the design of scaffolds mimicking the cell microenvironment to guide stem cells differentiation and recapitulate the development of target tissues. Biomimicry is a wide concept and several approaches have been adopted to produce cell-instructive scaffolds. Herein, we have explored the use of citric acid and lysyl oxidase, both of them related to bone nanostructure and mechanical performance, to develop scaffolds resembling the extracellular matrix of developing bone.

First, elastin-like recombinamers (ELRs) hydrogels were achieved through a one-step chemical crosslinking reaction with citric acid, a molecule currently considered to be essential for the proper performance of bone tissue. By systematically studying the crosslinking reaction and its contribution to hydrogel properties, we were able to control the architecture and stiffness of citric acid-crosslinked hydrogels while preserving the integrity of adhesion sequences in ELRs. Interestingly, the use of citric acid conferred so-produced hydrogels the ability to nucleate calcium phosphate.

Mechanically-tailored citric acid-crosslinked hydrogels were shown to be able to support the growth of human mesenchymal stem cells and to lead to seemingly biocompatible degradation products. Despite in vitro differentiation studies weren't conclusive as to their osteogenic potential, both mechanically-tailored and non-tailored citric acid-crosslinked hydrogels were shown to integrate into bone and to be partially degraded upon implantation in critical size defects in mouse calvaria. Even though cell invasion in mechanically-tailored scaffolds was seemingly lower than in non-tailored counterparts, both types of matrices allowed the formation of bone tissue, by intramembranous ossification, to a similar extent by the end of the study. At the time points selected for the in vivo study, both tailored and non-tailored hydrogels were found to be osteoconductive; osteoinduction was not observed in any of the cases. Mechanically-tailored hydrogels not being seemingly superior to control matrices at selected time points could to be due to (i) a high surface polymer density hindering cell invasion and thus delaying osteoinduction, or

to (ii) a non-osteoinductive combination of properties (chemical + physical) despite hydrogels possessing theoretically osteoinductive stiffness. These results point out that scaffolds must be seen as a whole given the high complexity of the in vivo cell niche, whose signals act synergistically to define cell behavior. Thus, more complex designs are required if recapitulation of bone development is to be targeted.

Additionally, recombinant lysyl oxidase (LOX) from human aorta was successfully produced in *Escherichia coli* to high purity. Despite achieving LOX with copper cofactor amounts and activity higher than those found in the literature, overall activity was low and the insolubilization of ELRs was not achieved, suggesting that novel expression and purification systems not compromising enzymatic activity are required if LOX is to be used to produce scaffolds.

ACKNOWLEDGEMENTS

Ha arribat el moment que sovint vaig pensar que mai no arribaria. Aquest ha sigut un camí llarg i ple de reptes, durant el qual he aprés moltíssim i he trobat grans persones que m'han ajudat a aixecar el cap i tirar endavant. En primer lloc, vull donar les gràcies a la Dra. Engel (a.k.a. la jefa) per donar-me l'oportunitat d'haver entrat al grup, per haver valorat i confiat en les idees que anaven sorgint, per haver arriscat a desmarcar-nos dels projectes pre-establerts, per haver confiat en mi quan ni jo era capaç de fer-ho, per haver-me escoltat quan ho necessitava, per tenir sempre una bona paraula i un somriure a la recàmera,… La veritat és que estic molt orgullós d'haver treballat amb tu; tant és així que sempre he pressumit de jefa. T'he dit moltes vegades que algun dia et faria un club de fans; ara veus que no t'ho deia de forma gratuïta, jaja.

Vull aprofitar també per agrair al professor Planell també per haver-me donat l'oportunitat de formar part del seu grup i per haver-me també ajudat a créixer com a investigador. Potser en el seu moment em costava veure la part constructiva de les critiques però, ara, amb perspectiva, veig que m'han servit per millorar a nivell professional.

I'd like to thank Karlo for giving me the opportunity to visit your lab. Being at CSUB was a great experience both on a personal and professional levels; I'm happy I learned so much in such a short period of time. Thanks for your help with the experiments and for that wonderful welcome BBQ. Thanks also to Tola for being so nice and helpful, I laughed so much with you; you and frozen yoghourt made life in the lab much easier. Thanks also to the Smiths, Maddie and Megan, which were so nice, funny and helpful; whenever I go back to the States, I'd love to share an onion in bloom with you, guys. Tola, Maddie, Megan you three are brilliant and beautiful people; I have no doubt you'll be really successful!

Special thanks go to John G., Lolo and Renée. You made living in Bakersfield such an amazing and great experience. You were like a family, always looking after me and helping me. Thanks for the crazy (remember the meteor shower night?) and funny

experiences we shared, for your friendship and for your patience with me trying to communicate. You guys are one of a kind! P.S. Carmen Electra.

Thanks also to Mark! We shared some great moments and I'll always be thankful for you helping me moving to San Diego. You, Ángela and I made such a great team!

Gracias también a mi Onjolota por ser como es y por haber sido un importante apoyo durante todo este viaje. Tu optimismo y energía están siempre patentes y resulta tremendamente fácil contagiarse de ellos. Me alegro mucho de haber podido compartir contigo la experiencia de vivir en San Diego y parte de nuestro *road trip*. Fue un placer volver a compartir vivienda y experiencias contigo, aunque esta vez no hiciéramos guerras de pinzas, cojines o zapatillas. Team Doña Rosita representin'!

Gracias también a todo el grupo ahora conocido como "Biomaterials for regenerative therapies" y acogidos. A Nadège, Xavi, Riccardo, Arlyng, Tiziano, Ana y Ale, y a Astrid por tantos buenos momentos en cenas, comidas, meriendas en la panadería colombiana,... La verdad es que recuerdo con mucho cariño nuestras reuniones. También a Zaida que, aunque la veíamos poco por el PCB, también compartimos buenos momentos con ella. Gracias también a Miguel y Óscar por llevar siempre el buen humor a cuestas, por amenizar reuniones y demás eventos, por echarme un cable cuando he tenido dudas existenciales de química y por los consejos que me habéis ido dando, especialmente en este último tramo de la tesis. También a Sole por tu buena disposición a echar una mano, por tus consejos, por las risas que nos hemos echado y por la paciencia que has tenido antes de y durante las histologías. También a las nuevas generaciones, Irene, Joan y Claudia por los buenos momentos en el laboratorio. También a Belén, cuya ayuda ha sido importante durante toda la tesis, pero especialmente en las últimas semanas. Ha sido un placer trabajar con todos vosotros.

Una menció especial per tu, Gerard, ja que sense la teva ajuda amb l'in vitro (i l'energia aportada per les sobrassades de Mallorca) potser encara estaria fent experiments. Sempre he dit que, tot i que al principi estava una mica cagat perque no sabia què em trobaria, vaig tenir molta sort de tenir-te com a estudiant; la motivació i dedicació (recordem aquells dilluns començant a les 6:30 del matí) que vas demostrar durant els mesos que vas estar al

lab no tenen “parangón”. Però afortunadament no tot va ser feina, també vam riure molt fent el person amb la Cris i la Irene (a.k.a las rubias) entre experiment i experiment, o ensenyant-li a la gent com es juga al *beer pong*. No tinc cap mena de dubte que el futur et depara coses molt bones! Un plaer haver-lo conegut, jove.

Gracias también a Olaia por enseñarme a coser, a hacer las cirugías, por la gran ayuda durante las laaargas sesiones de implantaciones y por la paciencia demostrada las innumerables veces que me surgían dudas. També a la Núria per haver-nos fet un cop de mà en els moments crítics després de la “gran evasión”.

Gracias a Elena por su paciencia y ayuda con el SP5. De esta tesis han salido imágenes muy chulas, y parte de la “culpa” es tuya (y de los benditos *lambda scans*). Ha sido un placer haber compartido charlas y risas con una microscopista y una aikidōka de tu talla.

French monster (a.k.a mademoiselle), MarT (a.k.a mà de foca) i Ms. Toumanidou (a.k.a Dra. P), especial menció per vosaltres. M’heu ensenyat que l’amistat i la feina són compatibles. Gràcies per haver-me escoltat i haver-me donat ànims en les diferents fases d’aquesta tesi i… òbviament, pels grans moments que hem compartir i per haver-me fet riure tant.

Gracias también a mis padres por TODO. Por vuestro apoyo, vuestros consejos, por haberme enseñado que nada es imposible si se tienen ganas y por haber vivido este doctorado también con ilusión y curiosidad, especialmente en lo que respecta a los resultados “de las cabezas”. Esto ha sido posible también gracias a vosotros, por vuestros esfuerzos para que tuviera una buena educación y formación.

Gracias también a Cris (a.k.a. Mari Carmen, jaja). Has sido un gran apoyo desde hace ya unos cuantos años y sabes que a día de hoy no estaría escribiendo estos agradecimientos si no hubiera sido por ti. Tienes mi eterna gratitud y amistad, aunque tu gato me odie.

Gràcies també a tu, Albert, pel teu suport incondicional, per la paciència que has tingut i l’empatia que m’has demostrat durant aquests anys. Em sento molt afortunat d’haver compartit aquesta experiència amb tu.

Per acabar, gràcies a tots els amics i familiars que no han rebut agraïments específics però que han estat al meu costat durant aquests anys.

TABLE OF CONTENTS

LIST OF FIGURES

LIST OF TABLES

ABBREVIATIONS

ACP: Amorphous calcium phosphate

AdvDMEM: Advanced Dulbecco's Modified Eagle's Medium

ALP: Alkaline phosphatase

Amax: Maximum absorbance

BCA: Bicinchoninic acid

BMD: Bone mineral density

BMPs: Bone morphogenetic proteins

BMU: Basic multicellular unit

BRC: Bone remodeling compartment

BS^3: Bis(sulfosuccinimidyl) suberate

BSA: Bovine serum albumin

CMCI: N-Cyclohexyl-N′-(2-morpholinoethyl)carbodiimide metho-p-toluene-sulfonate

CPCs: Calcium phosphate cements

CFU-Fs: Colony-forming unit fibroblasts

DAPI: 4',6-diamino-2-phenylindole dihydrochloride

DCP: Dicumyl peroxide

DPBS: Dulbecco's phosphate-buffered Saline

ECM: Extracellular matrix

EDC: N-(3-Dimethylaminopropyl)-N'-ethylcarbodiimide

DAPI: 4′,6-Diamidino-2-phenylindole dihydrochloride

DPBS: Dulbecco's phosphate-buffered saline

DSG: Disuccinimidyl glutarate

DSS: Disuccinimidyl suberate

EDS: Energy Dispersive X-Ray Spectroscopy

ELISA: Enzyme-linked immunosorbent assay

ELPs: Elastin-like polymers

ELRs: Elastin-like recombinamers

ESCs: Embryonic stem cells

Et_2O: diethyl ether

FBS: Fetal bovine serum

FGF: Fibroblast growth factors

FESEM: Field Emission Scanning Electron Microscopy

GEPBPs: Genetically-engineered protein-based polymers

H&E: Hematoxylin and eosin

HA: Hydroxyapatite

HDI: Hexamethylene diisocyanate

hMSCs: Human mesenchymal stem cells

HRP: Horseradish peroxidase

HSCs: Hematopoietic stem cells

IGFs: Insulin-like growth factors

IKVAV: Ile-Lys-Val-Ala-Val pentapeptide

iPSCs: Induced pluripotent stem cells

IPTG: Isopropyl β-D-1-thiogalactopyranoside

ISCT: International society for cellular therapy

ITT: Inverse transition temperature

LB: Luria broth

LOX: Lysyl oxidase

LOX02: Urea-soluble lysyl oxidase

LOX09: Water-soluble lysyl oxidase

LOXL: Lysyl oxidase-like protein

LTQ: Lysyltyrosylquinone

MAPCs: Multipotent adult progenitor cells

MASCs: Multipotent adult stem cells

MES: 2-(N-Morpholino)ethanesulfonic acid

MIAMI: Marrow-isolated adult multilineage inducible (cells)

M-PER: Mammalian protein extraction reagent

MSCs: Mesenchymal stem cells

mTLL: Mammalian Tolloid-like

MWCO: Molecular weight cut-off

NaCT: Sodium-coupled citrate transporter

NCPs: Non-collagenous proteins

NHS: N-hydroxysuccinimide

OCN: Osteocalcin

OPG: Osteoprotegerin

OPN: Osteopontin

PBS: Phosphate-buffered aaline

PDMS: polydimethylsiloxane

PET: Polyethylene therephthalate

pI: Isoelectric point

pNPP: p-Nytrophenyl phosphate

PQQ: Pyrroloquinoline quinone

PSCs: Perivascular stem cells

PTH: Parathyroid hormone

PV/TV: Polymer volume fraction; percentage polymer-occupied volume

RANK: Receptor activator of necrosis factor kappa B

RANKL: Receptor activator of necrosis factor kappa B ligand

REDV: Arg-Glu-Asp-Val tetrapeptide

RGD: Arg-Gly-Asp tripeptide

RGD-C: Citric acid cross-linked HRGD6 hydrogels

RGD-G: Glutaraldehyde-crosslinked HRGD6 hydrogels

rMSCs: Rat mesenchymal stem cells

RT: Room temperature

SBF: Simulated Body Fluids

SCID: Severe combined immunodeficiency

SDS-PAGE: Sodium dodecyl sulfate-polyacrylamide gel electrophoresis

SEM: Scanning Electron Microscopy

S.O.C.: Super optimal broth with catabolite repression

TB: Terrific broth

TCPS: Tissue Culture Polystyrene

TGF-β: Transforming growth factor β

THF: Tetrahydrofuran

THPC: Tetrakis(hydroxymethyl) phosphonium chloride

THPP: β-[tris(hydroxymethyl)phosphino]propionic acid

TNBS: 2,4,6,-trinitrobenzenesulfonic acid

TSAT: Tris-succinimidyl aminotriacetate

µCT: Micro-computed tomography

USSCs: Unrestricted somatic stem cells

VEGFs: Vascular endothelial growth factors

Vmax: Maximum velocity

VOI: Volume of interest

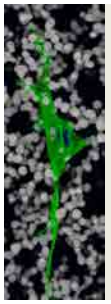

Chapter 1

1. **INTRODUCTION**

1.1 BONE: AN OVERVIEW

1.1.1 The skeletal system

The skeletal system, the framework of vertebrates, consists of 206 bones orchestrated to shape our body and protect our valuable, delicate internal organs. Bones have been long known for being the primary source of hematopoietic cells and a reservoir of salts to maintain systemic mineral homeostasis. Furthermore, recent discoveries have shown that bones act also as a source of endocrine hormones regulating metabolic homeostasis [1], pointing out that the skeletal system is an essential complex and multifunctional player in assuring systemic wellbeing.

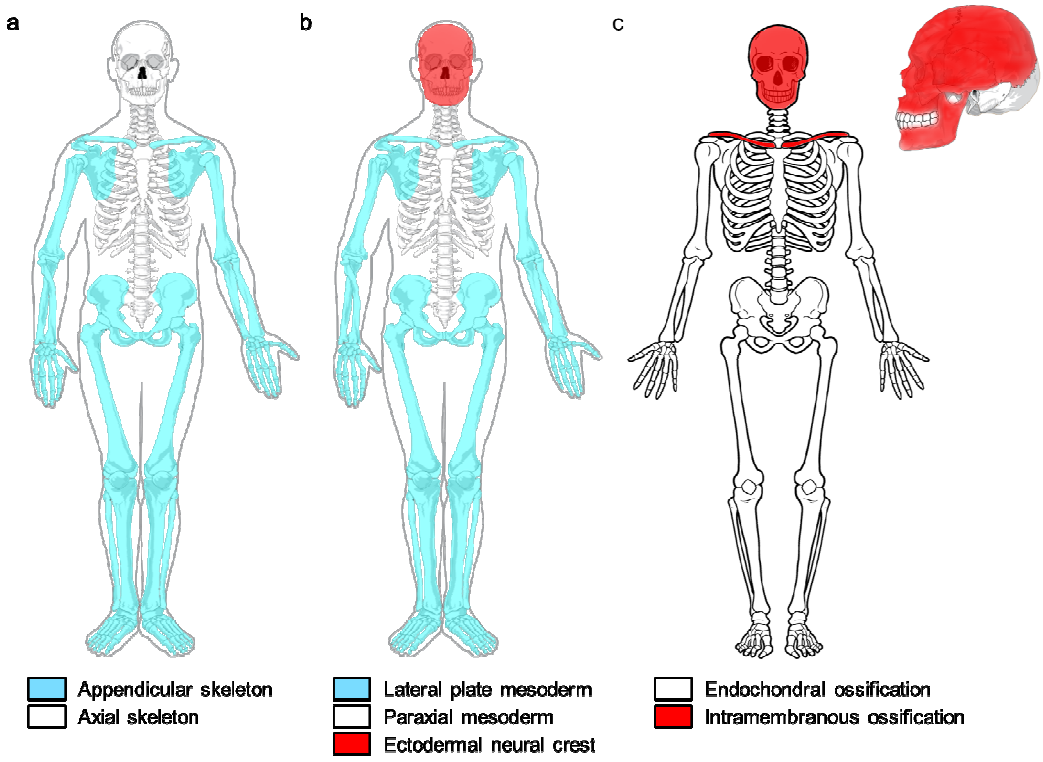

Figure 1. Classification of bones. Bones can be classified on the basis of their a) function, b) developmental origin, and c) mode of osteogenesis.

The 206 human bones can be classified on the basis of their function, ontogenic origin, mode of osteogenesis and shape. From a functional point of view, the skeleton can be

divided into i) the axial part (skull and trunk), which supports and protects organs in the ventral and dorsal cavities and provides surface for muscle attachment and, ii) the appendicular part (upper and lower limbs), which allows movement (Figure 1a). From a developmental point of view, bones come from three different embryonic origins: the paraxial mesoderm (axial skeleton except for craniofacial bones), the lateral plate mesoderm (appendicular skeleton) and the ectodermal neural crest (craniofacial bones) [2] (Figure 1b). From a mode-of-osteogenesis point of view, bones can be divided into those formed by intramembranous ossification (i.e. direct bone formation; facial bones, mandibles, flat bones of the skull and clavicles) and those arising by endochondral ossification (i.e. bone formation through a transient cartilage template) [3] (Figure 1c). Finally, under a shape criterion, bones can be classified into those being i) long (length>width; e.g. femur), ii) short (length≈width; e.g. carpal bones), iii) flat (plate-like; e.g. calvaria) and iv) irregular (shape not fitting none of the above; e.g. vertebrae) [3].

1.1.2 Bone composition

Bone is made up of cells, nerves, blood vessels and matrix, with the latter representing ca. the 90% of the total weight of the tissue. Bone matrix is a composite material comprising both organic (ca. 20% in weight) and inorganic (ca. 65% in weight) fractions that contribute to its exceptional mechanical behavior [4].

The organic matrix provides flexibility, thus making the tissue able to withstand tension. It is composed of collagens (90% of the organic matrix), mainly type I, although small amounts of other types are also present. The additional 10% is due to non-collagenous proteins, proteoglycans (i.e. highly glycosylated proteins), glycoproteins, citric acid, and growth factors to a lesser extent [4–6]. The organic matrix represents the trails that guide the deposition of the inorganic matrix, responsible for bone's resistance to compression. The inorganic matrix, commonly known as mineral phase, is also an ion reservoir for mineral homeostasis, containing approximately the 99% of the calcium, the 85% of the phosphorous, and the 40-60% of the sodium and magnesium in the human body [4].

1.1.3 Bone hierarchy: from macro to nano

1.1.3.1 Bone macrostructure

Prior to going through bone's hierarchical organization, let's briefly review the anatomy of a long bone. A long bone such as the femur can be divided into 3 anatomical parts: diaphysis (shaft), metaphysis and epiphysis (Figure 2a). The diaphysis, the shaft of a long bone is a sheath that protects the medullary cavity filled with fat (yellow bone marrow). Bone extends proximally and distally and eventually flattens and expands (metaphyses) to both ends (epiphyses).

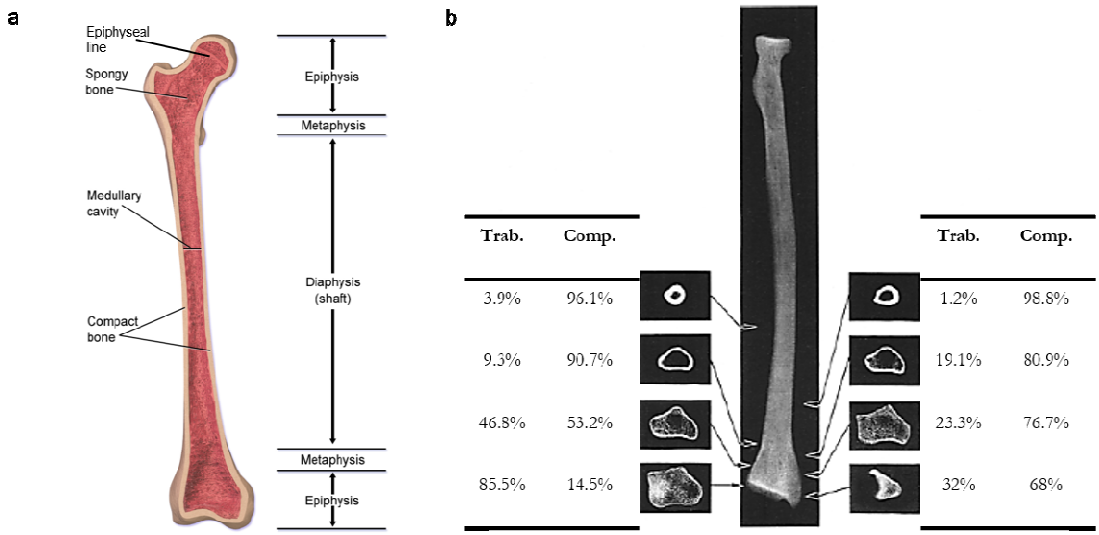

Figure 2. Anatomy of long bones. a) Structure of the femur as a model for long bones with detailed anatomical sites and parts; from [7]. b) Radiographic image of a human radius showing the distribution of the volumetric percentages of compact and trabecular bones in sections from different anatomical sites; adapted from [8].

All the human bones contain two distinctly arranged forms of bony tissue: trabecular (cancellous or spongy) and compact (or cortical). Trabecular bone, a mesh of rod and plate-like struts found in the inside of bones, is a low-density tissue with 50-90% of its volume being pores [4] which accommodate blood vessels and the marrow, the primary post-natal site of hematopoiesis. In contrast, compact bone is a dense tissue with ca. 10% porosity found in the outer shell of bones that represents ca. the 80% of bony tissue, thus actively contributing to the load-bearing role of the skeleton [9]. In one particular bone, the proportion of trabecular and compact tissues varies among anatomical sites. While the diaphysis contains a thick layer of cortical bone and little amount of cancellous tissue, the

compact-to-trabecular ratio decreases distally and proximally (Figure 2b), with the metaphyses and diaphyses containing most of the cancellous bone and being filled with hematopoietic cells (red bone marrow). The proportion of both types of bone varies not only among bones and anatomical sites [8,10], but also among patients with different gender [11] or age [8]. Despite these particular differences, the organization of cortical and trabecular bony tissues at the microscale is a common trait to all bones.

1.1.3.2 Bone microstructure

The basic structural unit of mature cortical bone (i.e. lamellar bone) is the osteon, a cylindrical system consisting of concentric plate-like portions of bone matrix (concentric lamellae) with a central canal (Haversian canal) that contains blood vessels and nerves (Figure 3a). Lamellae consist of densely packed oriented collagen fibers surrounding matrix-free spaces (lacunae) containing embedded osteocytes (See section 1.1.4.1) with branched and elongated cell processes extending radially along canaliculi. These cell processes connect osteocytes to Haversian canals, the primary source of nutrients for osteocytes [4], but also to each other and to osteoprogenitors located in bone surfaces (lacuno-canalicular network) [12]. Osteocyte-to-osteocyte connections run even through adjacent concentric lamellae, whose collagen fibers display displaced orientation, an organization often considered to resemble that of plywood. Osteons are delimited by cement lines (5-μm thick mineralized boundaries [9]) and are often separated one from each other by remnants of old osteons, the so-called interstitial lamellae, and confined between circumferential lamellae, which demarcate the inner (inner circumferential lamellae) and outer (outer circumferential lamellae) perimeters of cortical bone.

Outwardly, compact bone is covered by articular cartilage (hyaline cartilage) in those regions where the bone articulates with another one (Figure 3b), and wrapped in periosteum elsewhere. The periosteum comprises an inner layer containing osteoprogenitors and a fibrous outer layer, both of them containing collagen fibers running parallel to bone surface except in those regions where ligaments and tendons attach to bone, where fibers extend to compact bone (perforating or Sharpey's fibers) [3]. The periosteum also contains blood vessels that penetrate bone and branch to nourish osteons and connect them through the so-called Volkmann's (or perforating) canals, which run transversally to the longitudinal axis of osteons. This vascular system ensures no cell is

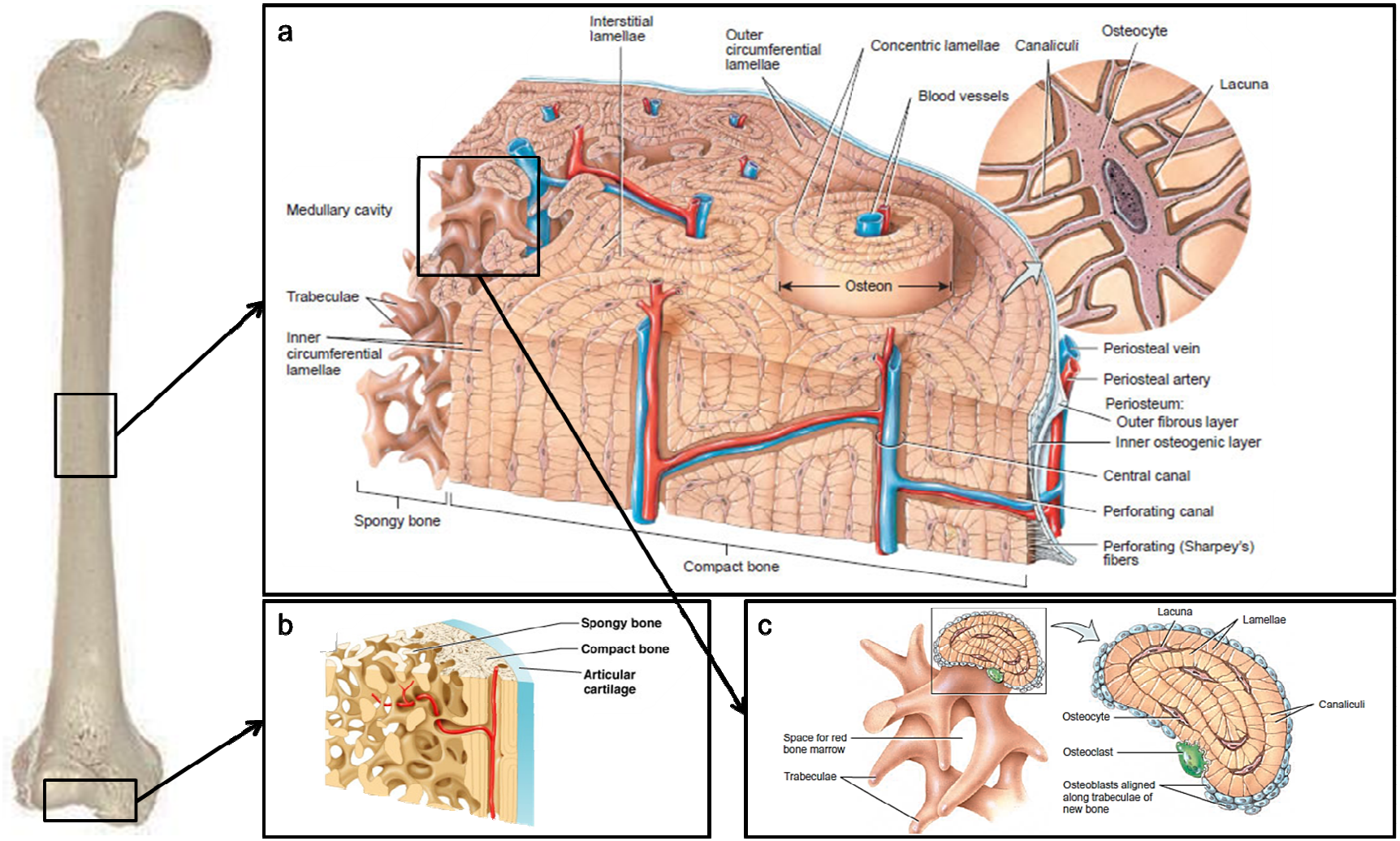

Figure 3. Microscopic anatomy of compact and trabecular bone. a) Detailed anatomy of a section from a long bone diaphysis; from [552]. b) Simplified anatomy of a diaphysis showing the particular outermost envelope in articulations; from [553]. c) Microstructure of trabecular bone; from [552].

more than 300 μm away from a blood vessel [4].

Internally, compact bone is surrounded by the endosteum (it thus covers Haversian and Volkmann's canals [3]), which is often one cell layer thick and comprises osteoprogenitors and bone-lining cells (See section 1.1.4.1). The endosteum also covers cancellous bone, whose structural unit is the hemiosteon (or bone packet), a crescent-shaped structure that results from the partial resorption of osteons, but lacking the central canal (Figure 3c). The high porosity of trabecular bone provides a high surface area for bone to be in contact with blood vessels [9], an important fact for mineral homeostasis.

1.1.3.3 Bone nanostructure

Collagen fibers making up osteons and hemiosteons mainly comprise organized oriented collagen fibrils with interspersed mineral crystals (Figure 4a), although mineralization-related molecules such as non-collagenous proteins [13] and citric acid [6] may be present to a lesser extent. The basic unit of collagen in bone is heterotrimeric tropocollagen (or collagen molecule), the assemblage of two type I collagen α1 chains and one α2 chain in the form of a triple helix about 300 nm long and 1.5 nm thick [5] (Figure 4b). Collagen molecules arrange laterally and longitudinally in a staggered manner [14], with longitudinally neighboring molecules shifted by ca. 40 nm (gap region) [15]. This shift gives microfibrils, which comprise 5 tropocollagen units with quasi-hexagonal arrangement [16], their particular pattern when stained with metal ions: alternating dark (overlap regions) and light (gap regions) bands, which together make up the 67 nm so-called D period. Microfibrils have been suggested to interdigitate to give rise to fibrils [17], which would possess transverse channels (gap channels) deriving from the alignment of gap zones in neighboring microfibrils [18]; fibrils (ca. 0.5-mm diameter) further pack to make up fibers of ca. 5-mm diameter [19]. The detailed collagen hierarchy has been mainly derived from studies using turkey tendon which, although probably possessing a nanostructure slightly differing from that of bone, is studied as a model for the biomineralization of type I collagen in mineralizing tissues.

The mineral fraction in bone is accepted to be made of carbonated hydroxyapatite (commonly termed hydroxyapatite; HA) crystals [4]. These crystals possess a plate-shaped

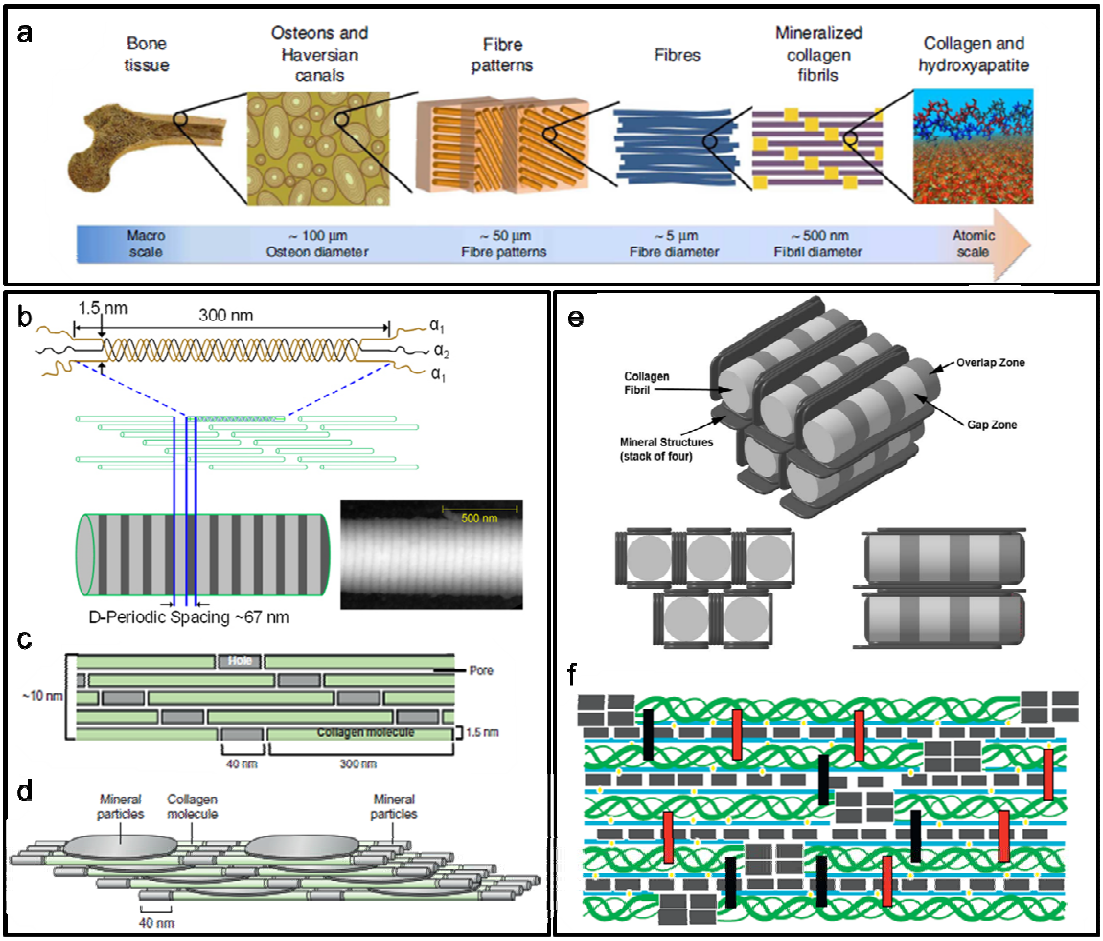

Figure 4. Nanostructure of bone tissue. a) Hierarchical bone organization, from the macro to the nanoscale; from [20]. b) Hierarchical structure of type I collagen fibrils depicting the staggered arrangement of tropocollagen to give rise to its characteristic D period; from [5]. c-e) Detailed schemes of staggered collagen molecules with hydroxyapatite plate-like crystals filling gap regions and intermolecular spaces; c-d from [5]; e from [21]. f) Scheme of bonds stabilizing the bone nanocomposite. Collagen molecules (green helices) are linked to each other through lysyl oxidase-catalyzed crosslinks (black and red bars). Water (blue lines) is located in between crystals and collagen molecules, which bind to each other through salt bridges and hydrogen bonds (yellow dots); from [5].

morphology and are about 5 nm thick, 30 nm wide and 50 nm long, although they can eventually grow up to few hundreds of nanometers in length [21]. Hydroxyapatite crystals have been found to run parallel to collagen, with their long crystallographic axis (or c-axis) extending along the longitudinal axis of collagen molecules. Hydroxyapatite is considered to nucleate and grow within collagen fibers with the gap region (and subsequently, gap channels) being the primary site of mineral deposition (Figure 4c)

although it seems to occur also in the overlap region as well as in the intermolecular and extrafibrillar spaces [20] (Figure 4 d and e).

Type I collagen has been long considered to be inert during biomineralization but, despite the underlying mechanism is yet to be resolved, some evidences have pointed out that collagen would play an important role in its own mineralization. The study of the amino acid sequence and 3D spatial arrangement of the collagen triple helix has led to finding regions with accumulation of either positively or negatively-charged residues (or the mixture of both) in the gap region that could accommodate Ca^{2+} and PO_4^{3-} ions and thus serve as nucleation points. These charged regions are known to possess structural flexibility, which would allow for nucleation and crystal growth to occur [22]. Thus, factors affecting collagen chemistry and/or structure, such as genetic abnormalities [23] and enzymatic [24] and non-enzymatic crosslinking [5], are likely to alter mineralization and subsequently the mechanical properties of the tissue.

Collagen fibers result from the dense packing of its hierarchical constituents. Although the processes ruling their mineralization remain unsolved, studies are slowly shedding light on how this may actually take place. Initially, calcium phosphate with unclear origin would precipitate in the form of amorphous calcium phosphate (ACP), which would then penetrate the collagen structure and transform into hydroxyapatite. The infiltration of ACP into collagen seems, at least partially, to be driven by the coordinated action of non-collagenous proteins (NCPs) such as dentin phosphophorin, dentin matrix protein 1 and fetuin, which would mediate the surface and intrafibrillar deposition of ACP [13]. Despite the mechanisms underlying ACP maturation into HA remain elusive, recent evidences point out that it could be controlled and terminated by citric acid [6] in concert with NCPs [25] to achieve a mechanically optimum crystal size [26]. The collagen-HA nanocomposite is further mechanically optimized by lysyl oxidase-catalyzed crosslinking [24] and mineral-organic matrix salt bridges and hydrogen bonds [20] (Figure 4f), laying the groundwork for an exquisitely optimized tissue.

1.1.4 Cell types in bone

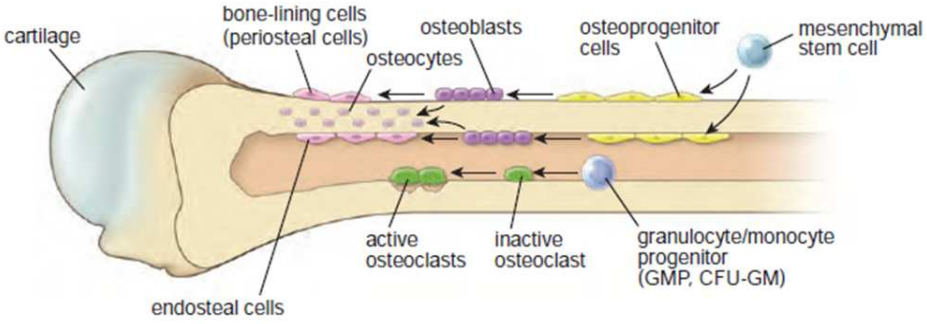

Figure 5. Cell types in bone. Cells in bone arise from two types of stem cells, which determines their fate as bone-forming (MSCs-derived lineage) or bone-resorbing (HSCs-derived lineage) cells. Cells are depicted with a differentiation degree increasing from right to left; from [3].

Bone is accepted to contain five main cell types from two different lineages (Figure 5). On one hand, osteoprogenitors, osteoblasts, osteocytes and bone-lining cells belong to the osteoblastic lineage [4] and represent particular differentiation stages from common precursors, mesenchymal stem cells (MSCs; section 1.1.5). On the other hand, osteoclasts belong to the hematopoetic lineage [4], deriving from hematopoietic stem cells (HSCs). Interestingly, the osteoblastic and hematopoietic lineages are related to bone formation and resorption, respectively, two processes spatially and temporally related and potentially cross-regulated (See section 1.1.8). Below, a brief description of bone cells is provided; specific cellular activities will be presented in detail in section 1.1.8.

1.1.4.1 Osteoblastic lineage: towards bone formation

The most primitive of the abovementioned cell types are osteoprogenitors. Osteoprogenitors arise from the osteogenic commitment of MSCs and are resting cells that reside in the internal and external surfaces in bone (i.e. periosteum and endosteum, including those regions surrounding Haversian and Volkmann's canals) [3]. When stimulated, osteoprogenitors differentiate towards pre-osteoblasts, proliferative cells that start expressing genes responsible for extracellular matrix production [27]. Pre-osteoblasts further differentiate to become osteoblasts (they can probably also arise from pericytes [28]), which are commonly found lining bone surfaces [4]. Osteoblasts actively synthetize and deposit osteoid (i.e. unmineralized bone matrix) and probably induce and control its mineralization by secreting calcium phosphate vesicles, the so-called matrix vesicles [29],

non-collagenous proteins [30,31] and citric acid [32]. At the end of the matrix deposition and mineralization stage, most osteoblasts undergo apoptosis [33] and those having survived can turn into osteocytes or bone-lining cells (also known as resting osteoblasts).

Bone-lining cells are located on the surface of quiescent bone, covering a ca. 2 μm-thick osteoid layer on top of the mineralized matrix [34]. These cells are thought to help create an isolated space for resorption to occur [35], to play a role in regulating the mineral influx and efflux between bone and the extracellular fluid, and to redifferentiate to secreting osteoblasts upon proper stimulation [36].

Osteocytes are terminally differentiated osteoblasts entombed in the bone matrix and the most abundant cell type in bone, representing up to the 90% of cells in the tissue [4]. They are accepted to act as mechanosensors, translating mechanical disturbances in the tissue after loading into biochemical changes signaling the need for bone formation or resorption [37,38]. Additionally, they seem to play a role (i) in the release of calcium during lactation, having the apparent ability to mobilize (i.e. osteocytic osteolysis) and replace mineral in the perilacunar and canalicular spaces [39] and (ii) in regulating the function of the rest of bone cell types [40].

1.1.4.2 Hematopoietic lineage: towards bone resorption

Osteoclasts are multinucleated cells that arise from the fusion of 3-12 circulating or marrow-derived mononuclear osteoclast progenitors [34]. Although osteoclasts have been long known as the specialized bone-resorbing cells contributing to bone's capacity to be remodeled in response to mechanical loading, their active role seems to be above and beyond degrading the tissue. Evidences point out that osteoclasts might regulate the proliferation and differentiation of osteoprogenitors and thus the coupling of bone resorption and formation, contribute to HSCs mobilization, and play a role in regulating the activity of CD8+ T lymphocytes, responsible for the destruction of tumor cells [41], and collectively suggest that osteoclasts are potential regulators of the bone microenvironment.

1.1.5 Mesenchymal stem cells

Stem cells are unspecialized entities with the capacity of self-renewal for long periods of time and able to give rise to a given number of tissue-specific cell types, which defines their potency (i.e. degree of commitment). On the basis of their potency, stem cells can be classified, from more to less committed, into uni, oligo, multi, pluri and totipotent, with multi and pluripotent stem cells being the center of stem cells research due to their potential in the treatment of human conditions, defects or injuries. Pluripotent stem cells are those able to differentiate into cell types from any of the three germ layers (e.g. embryonic stem cells; ESCs), while multipotent stem cells are able to turn into a limited number of cell types, often exclusively from one germ layer. Although much research focused on ESCs and iPSCs (induced pluripotent stem cells) has been and is actually being carried out, their clinical application is still hindered by their known tendency to induce the formation of teratomas and teratocarcinomas in vivo [42,43]. In contrast, multipotent stem cells are already being included in clinical setups. Examples of multipotent stem cells currently used in the clinics are HSCs, used to treat leukemia, and MSCs, included in clinical trials targeting the repair of a variety of tissues [44].

MSCs are adherent spindle-shaped cells first termed colony-forming unit fibroblasts (CFU-Fs) given their capacity to generate clonogenic colonies [45]. These cells are known to be “capable of bone formation” [45] and of undergoing adipogenic and chrondrogenic differentiation in vitro [46]. This feature has long characterized them so much so that the International Society for Cellular Therapy (ISCT) stablished the trilineage differentiation capacity, along with adherence to plastic and the expression of given surface antigens, as a minimum criterion for a cell to be considered a MSC [47]. The term “Mesenchymal stem cells” was coined given their capacity to give rise to connective tissues [48], which arise from the mesoderm-derived embryonic tissue mesenchyme. However, studies published in the last decade have shown MSCs to be able to differentiate into cell types such as astrocytes, neurons and oligodendrocytes [49,50], hepatocytes [51], cardiomyocytes [52] and insulin-producing cells [53]. In other words, MSCs’ differentiation potential seems to be beyond the endoderm, extending to all three germ layers. Whether this phenomenon is due to MSCs being (i) pluripotent, (ii) a heterogenic population regarding differentiation potential and /or (iii) able to transdifferentiate [54] is still a riddle.

Although MSCs have been classically considered to arise from the endoderm (and thus, they would reside in endoderm-derived tissues), experimental evidences suggest they may derive from multiple developmental origins [55]. These cells were first isolated from bone marrow [45], lately reported from adipose tissue [56] and a myriad of fetal [57] and post-natal tissues [58,59], and now considered to reside in all the adult tissues [58]. However, differences regarding proliferation, differentiation potential, proteome and the expression of surface markers have been noticed when comparing MSCs isolated from different tissues [44,55,58]. This may well mean that the tissue of origin imprints some specific features such as a preferential cell fate [60,61] or that different populations exist in single preparations from a specific source [62–64]. The latter seems more likely given the recent description of MAPCs (Multipotent adult progenitor cells) [65,66], MIAMI (Marrow-isolated adult multilineage inducible) cells [67], USSCs (Unrestricted somatic stem cells) [68] and MASCs (Multipotent adult stem cells) [69] (sub)populations in MSCs preparations. These (sub)populations (i) may be a result of the surface markers criterion imposed by the ISCT being not restrictive enough to generate pure MSCs preparations or (ii) may be artifacts [70] derived from culture-induced genetic and epigenetic alterations [61]. How these (sub)populations are related to MSCs is still a mystery, and so it is the anatomical location of the latter. In this respect, evidences on their widespread distribution in adult tissues have led to suggesting that a ubiquitous source of MSCs would exist. Pericytes (or mural cells), perivascular cells that wrap microvessels and capillaries, have been suggested to be primitive precursors for MSCs. These cells have been shown to possess clonogenic potential and to express cell markers characteristic to MSCs in vitro and to generate bone, cartilage and adipose tissue phenotypes both in vitro and in vivo [28,55,58,59]. Recent evidences, though, point out that pericytes wouldn't be the only precursor for MSCs, which may also derive from adventitial cells (i.e. cells found in the tunica adventitia, the outermost layer of larger vessels). Adventitial cells have been isolated from several tissues and found to be clonogenic, to differentiate into osteoblasts, adipocytes and chondrocytes in vitro, and to express MSCs markers in vivo [71]. Together, recent advances on the biology of pericytes and adventitial cells, collectively termed PSCs (Perivascular stem cells), have led to suggesting the perivascular space as the in vivo MSC niche and the source of "multipotent" cells for local tissue repair [55].

MSCs are known to support the hematopoietic niche [72], to mobilize to sites of inflammation after injury [73] after the local release of chemokines [74], and to secrete trophic factors (cytokines and growth factors) that exert a vast number of paracrine effects [75–77]. Thanks to their microenvironment-induced secretory behavior, MSCs are capable of promoting immunomodulation [78,79], the protection of injured tissues from autoimmunity [80], and the recruitment of vascular cells [75] and progenitors [81] to the site of injury, among others. Together with the capacity to differentiate into several cell types, these functionalities point MSCs as a central population contributing both directly and indirectly to creating a regenerative microenvironment to achieve tissue repair. The use of MSCs in clinical trials has gained momentum lately thanks to their pro-regenerative profile and demonstrated therapeutic safety [82], which have led them to being included in studies targeting a wide spectrum of conditions [44,83,84].

1.1.6 Bone formation

As introduced in section 1.1.1, bones are formed by two modes of osteogenesis: intramembranous and endochondral. Although many details about intramembranous ossification are yet to be deciphered, it is known that it consists in the direct formation of bone. In this mode of osteogenesis, MSCs would aggregate in the form of preosteogenic condensations that would grow and would be invaded by blood vessels. The vascular invasion would lead to a proper microenvironment for ossification in the condensation core (i.e. ossification center), where cells would undergo osteogenic differentiation, secrete osteoid and get embedded in the matrix, thus reaching terminal differentiation (i.e. becoming osteocytes). The local secretion of osteoid would lead to the emergence of bone spicules (i.e. local aggregates of osteoid). Further mesenchymal cells would differentiate into osteoprogenitors that would secrete more osteoid, leading to the enlargement and occasional fusion of spicules (and thus to the emergence of trabeculae) by appositional growth [3,85], giving rise to trabecular bone. Intramembranous ossification not only takes place during embryonic development, but also during fracture repair.

In contrast, endochondral ossification is more complex and well described, involving the formation of bone from a temporal cartilaginous framework. It starts with the emergence

of prechondrogenic mesenchymal condensations at the site of skeletogenesis. Cells in the core of condensations proliferate and differentiate in an avascular microenvironment and start depositing cartilage matrix rich in type II collagen, giving rise to the cartilaginous anlage, a hyaline cartilage model that serves as a template for ossification (Figure 6a). Hyaline cartilage is covered by the perichondrium, a sheath of connective tissue and a source of osteo and chondroprogenitors [86], with the latter widening the anlage by deposition of further matrix (i.e. appositional growth) [3]. Additionally, chondrocytes in the inside of the anlage (i.e. interstitial growth) proliferate in a perichondrium-controlled fashion. When the anlage achieves a critical size, chondrocytes in the shaft stop proliferating, undergo hypertrophy, degrade the type II collagen-rich matrix, secrete matrix rich in type X collagen and trigger its mineralization (Figure 6b) [3,86]. Concurrently, cells near the ends of the anlage keep proliferating, thus enlarging it longitudinally; perichondrial cells close to hypertrophic chondrocytes undergo osteogenic differentiation giving rise to the intramembranous formation of a cortical sheath, the periosteum, around the diaphyseal region of the developing bone. Mineralized matrix deprives hypertrophic chondrocytes of nutrients and they start dying, leaving cavities in the matrix. Blood vessels then penetrate the developing bone through the periosteum, stablishing the primary ossification center, reaching the cavities and allowing osteoclasts to reach the hypertrophy region, where they erode the mineralized cartilage. Osteoblasts arrive at the erosion place and start depositing osteoid onto remnants of mineralized cartilage and trabeculae are formed (Figure 6c) [87]. As the primary ossification center expands distally and proximally, a primitive medullary cavity is created (deposited trabecular bone is partially resorbed), extending to both metaphyseal regions (Figure 6d).

Cartilage keeps growing in the epiphyseal ends and blood vessels eventually penetrate the developing epiphyses, leading to the development of the secondary ossification centers, in which the cartilage-bone transition proceeds as previously stated, except for trabecular bone, which in this case is not resorbed (Figure 6e). At this point, cartilage has not been totally replaced by bone; two cartilaginous regions remain: i) the articular cartilage at the very end of epiphyses, meant to reduce friction in articulations, and ii) the growth (or epiphyseal) plate, a template for the post-natal longitudinal growth of bone located between the primary and secondary ossification centers (Figure 6f).

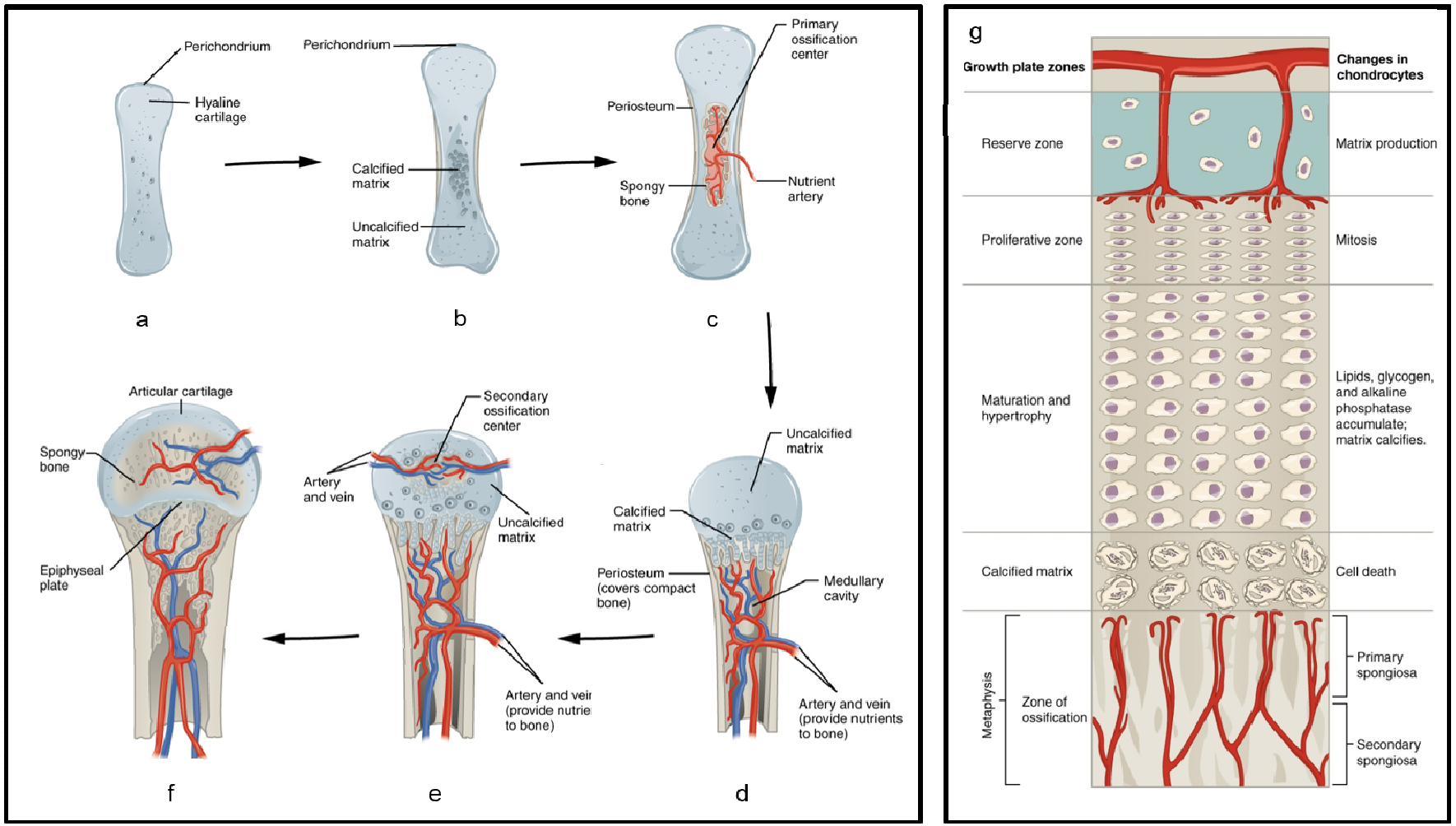

Figure 6. Endochondral ossification of a long bone. a-f) Detail on the stages of the cartilaginous anlage-to-bone transition. g) Scheme of depicting the different functional regions making up the epiphyseal growth plate. Adapted from [88].

The growth plate recapitulates the events taking place during the development of ossification centers and can be divided into five different functional zones (Figure 6g). The most proximal is the reserve zone, a region characterized by the presence of quiescent chondrocytes. The former is followed by the proliferative zone, where chondrocytes in column-like arrangements actively proliferate and secrete matrix. Distal to the proliferative zone, the maturation and hypertrophy zone contains enlarged and metabolically active chondrocytes that secrete matrix and start mineralizing it. The next region is the zone of calcified cartilage, where chondrocytes undergo apoptosis due to nutrient deprivation. In the most distal end of the growth plate (i.e. the zone of ossification), invasion of blood vessels, osteoclastic resorption and bone deposition occur [3,88]. The growth plate remains active until skeletal maturity is achieved, when the production of new cartilage ceases and the diaphyseal and epiphyseal medullary cavities converge; the only remnant of the growth plate is then a bony layer known as epiphyseal line [3]. At this point, the only cartilage remaining in bones is articular cartilage.

Regardless of the mode of ossification, the tissue is initially laid down in the form of immature (or woven) bone, which makes up the embryonic skeleton and those regions undergoing fracture repair [4]. Woven bone, characterized by a haphazard collagen distribution, irregular mineralization and high cellularity [4], is rapidly deposited and mineralized. Due to the random distribution of its collagen fibers, it is considered to possess poor mechanical properties [89], which denotes it is a temporal tissue (otherwise, the skeleton couldn’t fulfill its structural function). Indeed, woven bone is replaced with mature (or lamellar) bone - which is slowly laid down and more organized, and contains a lower number of osteocytes per unit volume [4] (more details on the structure of mature cortical and trabecular bone can be found in section 1.1.3.2) - in a process known as bone remodeling (see section 1.1.8). The speed at which lamellar bone is laid down is so low that a temporal tissue is required for the bone growth rate to be consistent with the growth rate of the animal/individual; woven bone is thus slowly converted to lamellar bone to finally meet the mechanical requirements of the tissue [89].

1.1.7 Bone modeling: growth and mechanical adaption

Bone is a highly dynamic tissue that senses and adapts to the mechanical requirements of the organism. The mechanism by which this adaptation takes place is called bone modeling [90] and it always occurs on preexisting bone on the periosteal, endocortical and trabecular surfaces; it is generally meant to increase bone mass and to shape bones (i.e. changing their geometry) mainly during childhood, although it may occur during adulthood [91]. Modeling may involve bone formation mediated by osteoblasts (formation modeling) and/or osteoclasts-driven resorption (resorption modeling). However, although formation and resorption may occur synchronously and in a coordinated manner to shape the tissue, these two processes are not coupled, meaning they take place on different surfaces.

Modeling is triggered by mechanical strain; if the strain is high, formation modeling occurs in order for the tissue to withstand the mechanical solicitations; if the strain is low, resorption modeling takes place to remove "excess" bone. Regardless of the type of modeling, it contributes to three processes: radial growth, longitudinal growth and bone drift.

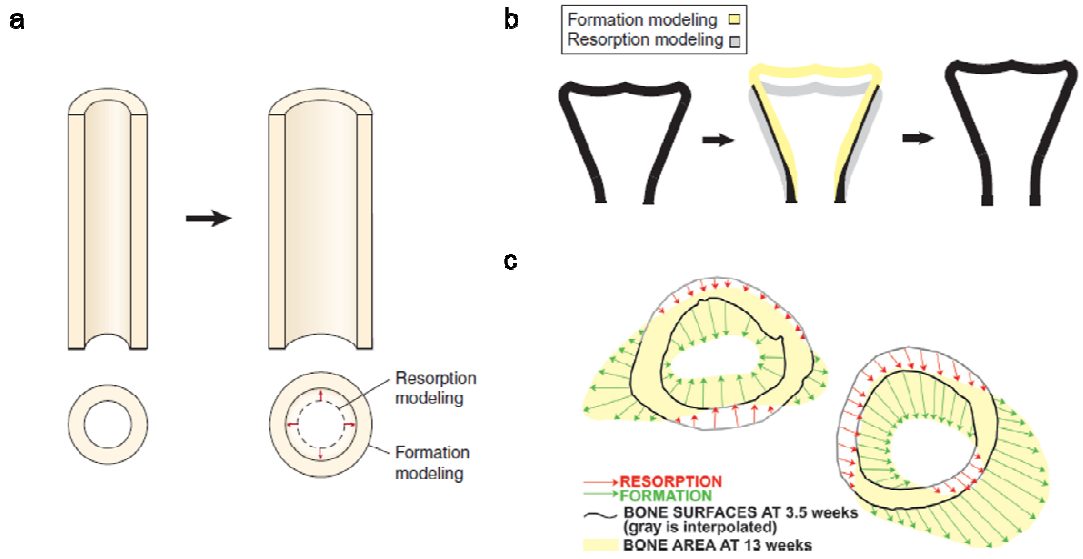

Figure 7. Effects of modeling on bone structure. Examples depicting the contribution of formation and resorption modeling to a) the diaphyseal radial growth and b) the metaphyseal longitudinal growth of model long bones; c) illustrates bone drift due to modeling in murine ulna (left) and radius (right) of a growing mouse. Adapted from [91].

Radial growth consists in the coordination of formation and resorption to increase the diaphyseal diameter of long bones while keeping cortex thickness constant (resorption occurs in the endocortical surface, while formation takes place in the periosteal region; Figure 7a); it is gender and age specific [91]. During endochondral ossification, formation and resorption occur in the metaphyses to preserve the shape of bones during longitudinal growth; in this case, bone is resorbed in the periosteum, while new bone is deposited into the endocortical surface (Figure 7b). Bone drift is the process by which trabecular struts are moved and the distance cortex-central axis at a diaphyseal level is modified. In the latter case, depicted in Figure 7c, resorption occurs in two periosteal or endocortical surfaces, while formation takes place in one endocortical and one periosteal surfaces.

1.1.8 Bone remodeling: mineral homeostasis and renewal

Bone remodeling is the process by which bone is locally resorbed and reformed in a coupled manner to maintain the systemic mineral balance and to preserve the mechanical integrity of the tissue [37,91]. Remodeling associated with mineral homeostasis is thought to be nontargeted (i.e. non site-specific) since it can take place in any skeletal site as long as it doesn't mechanically compromise the tissue. In contrast, remodeling related to the preservation of mechanical integrity is considered to be targeted (i.e. site-specific) given it is aimed to repair bone defects [92] such as microcracks.

While modeling mostly takes place during growth, remodeling is a continuous process in which bone resorption and formation result from the temporally and spatially-coupled activity of osteoclasts and osteoblasts. In both cases, cellular events leading to bone resorption and/or formation are assumed to be regulated by osteocytes, considered to act as mechanosensors [37]. Briefly, mechanical loads are thought to induce movement of the insterstitial fluid in the lacuno-canalicular network, which produces shear stress on the membrane of osteocytes [93]. Osteocytes, then, would produce signals for the activation/inhibition of osteoclasts and osteoblasts [94–96], thus being important regulators of bone's adaption to mechanical overuse or disuse through modeling.

Osteocyte death is accepted to trigger targeted remodeling to repair microcracks derived from repeated mechanical loading (i.e. fatigue). Microcracks would disrupt the lacuno-

canalicular network, thus depriving some osteocytes from nutrients and leading to cell death [37]. Osteocyte death is thought to induce bone resorption [97] by either the apoptosis-related release of pro-resorption signals or by the absence of osteoclast-inhibiting signals produced under normal conditions; these signals (or the lack thereof), in concert with osteoclasts-inhibiting signals from healthy osteocytes, would lead to targeted remodeling events to occur only at damaged regions [98].

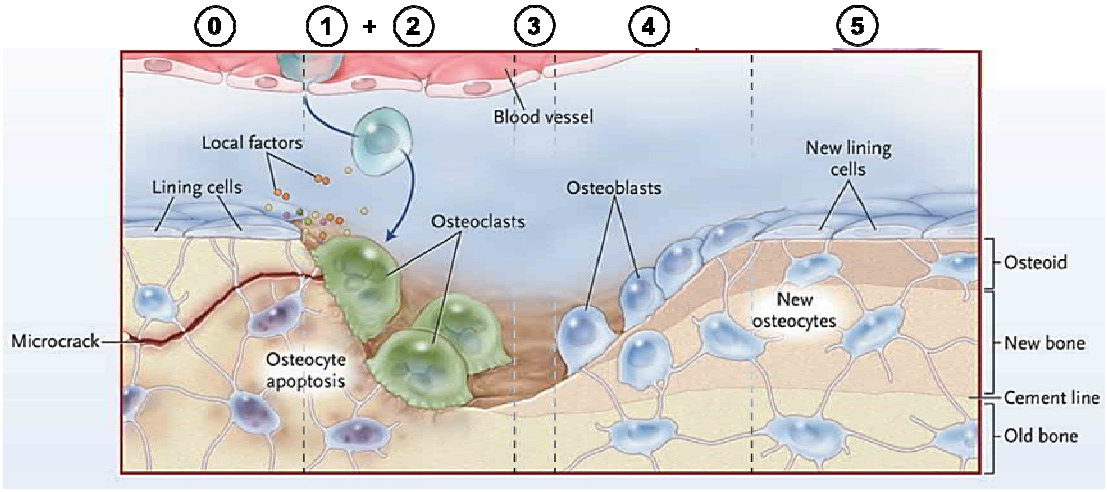

Figure 8. The bone remodeling cycle. Osteoblasts, osteoclasts and bone lining cells team up to renew bone in a spatially and temporally coupled manner. Adapted from [100].

In bone remodeling, the cellular actions leading to coupled bone resorption and formation are conducted by the so-called basic multicellular unit (BMU), a cellular team comprising osteoclasts, osteoblasts and bone lining cells. The events occurring during bone remodeling make up the remodeling cycle (Figure 8), a sequential process in which cellular actions are tightly regulated (differences can be found in the bibliography as to the number of stages of the cycle; herein, the number of stages has been maximized to easily identify the main cellular events). When damage is produced, the need for remodeling is signaled through yet unclear mechanisms and bone lining cells degrade the outward unmineralized matrix layer in the tissue, exposing the mineralized matrix [99] (Figure 8, stage 0). The bone lining cells monolayer then detaches partially from the surface creating an isolated space for remodeling known as the bone remodeling compartment (BRC) [35]. The presence of blood vessels close to the BRC allows the arrival of mononuclear cells [101], which fuse together to make up mature osteoclasts (Activation phase; Figure 8,stage

1). Osteoclasts then adhere to bone surface and become polarized, exposing the tissue to a highly specialized set of membrane domains for bone resorption (Resorption phase; Figure 8, stage 2). Briefly, osteoclasts anchor to bone by means of peripheral actin rings (sealing zone) to create an isolated space for resorption [102]. Within this space, the apical membrane is known as the ruffled border, which contains a sophisticated machinery for the release of HCl and lysosomal enzymes such as cathepsin K, and for the uptake of matrix degradation products. HCl is used to lower the pH and induce the dissolution of HA; cathepsin K then degrades the organic fraction of the matrix along with metalloproteinases [102]. Osteoclasts move forward and degrade a few hundreds of microns. Behind the osteoclasts front, a subset of bone lining cells smooth the surface and deposit a thin layer of osteoid that once mineralized is known as cement line [9,91] (Reversal phase; Figure 8, stage 3). Finally, osteoblasts secrete new osteoid (Formation phase; Figure 8, stage 4) to fill the cavity excavated by osteoclasts (Howship's lacuna) and terminally become either osteocytes or bone lining cells. When remodeling has finished, bone enters a quiescent state (Figure 8, stage 5) in which newly deposited osteoid mineralizes with time.

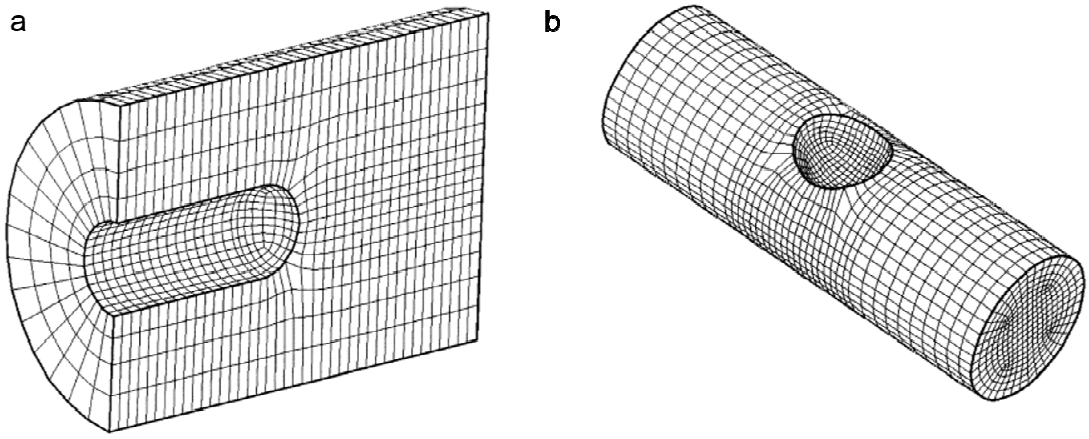

Figure 9. Span of the osteoclastic activity in a remodeling cycle. Finite element models displaying the Howship's lacunae created by osteoclasts in a) cortical, and b) cancellous bone. Adapted from [90].

Despite the cellular events in cortical and trabecular remodeling are essentially the same, differences exist as to the geometry of the remodeled bone portion (Figure 9). In cortical bone, osteoclasts dig a tunnel about 2 mm long and 200 µm wide [103], and are followed

by osteoblasts depositing osteoid in centripetal layers (lamellae) and finally leaving a central void space (Haversian canal) [9], giving rise to an osteon. In cancellous bone, osteoclasts dig a trench across the trabecular surface about 200 µm long [104] and 60 µm deep [90]. Generally, the remodeling cycle can take up to 6 months [100], with the remodeling rate being affected by factors such as gender, age and physical activity [91]. Remodeling is regulated systemically by hormones such as parathyroid hormone (PTH), and locally by the osteoblasts-osteoclasts crosstalk through the OPG/RANKL/RANK (Osteoprotegerin/ receptor activator of necrosis factor kappa B ligand/ receptor activator of necrosis factor kappa B) axis [103].

1.1.9 Bone healing: structural and functional re-establishment

As previously stated, the major function of our bony framework is to shape our body and to protect our internal organs. Such an important role requires a robust mechanical performance to allow movement and to resist the many types of mechanical loads bones are subjected to on a daily basis. The strength of bone tissue is mainly due (i) to its biocomposite nature, which allows a homogenous distribution of the load to minimize the concentration of stresses on the brittle mineral phase [26], and (ii) to its structure. At the nanoscale, factors such as (i) the staggered arrangement of collagen fibrils, (ii) the degree of mineralization, and (iii) the large aspect ratio and distribution of mineral platelets have been seemingly optimized to make the tissue able to withstand high loads before failing by fracture [26,105,106]. At the microscale, the osteonal lamellae arrangement and the density and orientation of trabeculae clearly influence the mechanical properties of cortical [107–110] and trabecular bone [111], respectively. At the macroscale, the overall mechanical properties of the tissue are related to the total amount (mass and size) of bone as well as to its geometry [112]. Despite this hierarchical optimization, bones are susceptible to overloads and to the coalescence of microfractures, two of the most common causes of bone fracture along with osteoporosis, an age-related condition involving decreased bone density and propensity to recurrent fractures [113]. Whatever the cause underlying fractures, bone healing (or fracture repair) normally takes place through the so-called indirect (or secondary) fracture healing [114], a multistep process

involving inflammation, soft callus formation, hard callus formation, and remodeling (Figure 10). It proceeds as follows.

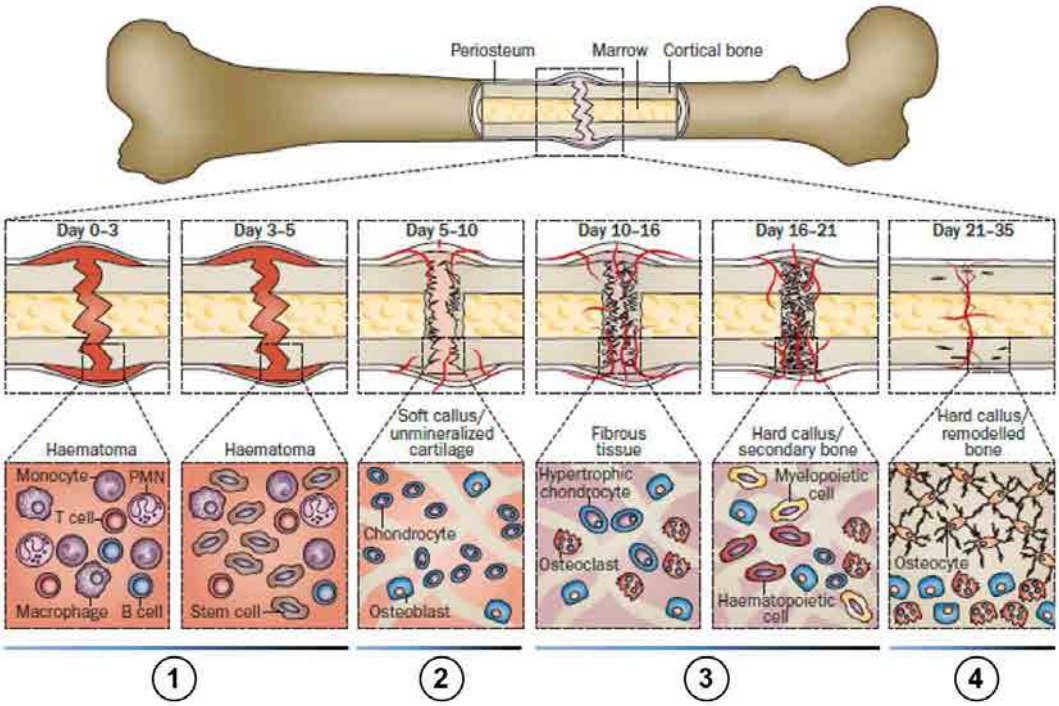

Figure 10. Time course of indirect bone healing. After injury, a hematoma is created at the fracture site, which becomes a strongly pro-inflammatory environment that induces the recruitment of MSCs (stage 1). MSCs then differentiate into chondrocytes, which create a fibrocartilage callus in concert with fibroblasts (stage 2). The soft callus undergoes endochondral ossification to create bone (stage 3), which is ultimately remodeled (stage 4). Adapted from [120].

Shortly upon damage, a hematoma is formed due to the extravasation of blood from disrupted vessels. This hematoma arises in between and around fracture ends and contains inflammatory cells that release proinflammatory factors to induce the recruitment of MSCs [115], to prevent infection [116] and to promote angiogenesis (i.e. the formation of vessels from pre-existing ones) [117,118]. Additionally, macrophages and phagocytic cells remove necrotic tissue [119,120] to clear fracture ends. Platelet-derived factors induce the recruitment and chondrogenic differentiation of MSCs from the bone marrow, the periosteum and surrounding soft tissues as well as the proliferation of fibroblasts and endothelial cells [121] (Figure 10, stage 1). Fibroblasts and chondrocytes then give rise to a soft callus (or fibrocartilage), an initial fracture-stabilizing structure developed under the regulation of periosteum-secreted factors [122]. Concomitantly, the ends of the disrupted

subperiosteal bone are bridged by periosteal progenitors-mediated intramembranous ossification [123], further stabilizing the fracture (Figure 10, stage 2). Additionally, blood vessels invade the soft callus, which undergoes endochondral ossification (Figure 10, stage 3); during this process, the soft callus is gradually revascularized and substituted by mineralized matrix, thus becoming the so called hard (or bony) callus [119]. Ultimately, bone remodeling takes place to turn woven bone into mature, lamellar bone (Figure 10, stage 4). By the end of this process, bone has been structurally and functionally restored. Herein described events correspond to the process commonly taking place after an injury; restoration proceeds through direct healing in those rare cases in which the fracture is stably fixed and the gap between fracture ends is negligible (more details can be found in [114]).

1.1.10 Failed fracture repair: delayed unions and non unions

Fracture repair is affected by a myriad of systemic factors such as age, nutritional status, diseases, use of pharmacological drugs, smoking and alcohol abuse [124] and local factors such as fixation-related intrafragmentary motions and the length of the fracture gap [125,126]. Both systemic and local factors can result in impaired healing either in the form of delayed unions or even non unions of bone ends, with local factors being especially important for the clinical management of fractures. It has been proven that the use of fixation methods allowing micromotions is beneficial for secondary bone healing to occur [127], but their effect is minimized in the case of large gaps [126]. Gap size has been demonstrated to be a critical factor that can lead to incomplete and delayed healing, or to the lack thereof [126] when it exceeds a threshold length above which bone can't spontaneously heal (i.e. critical-sized defects).

It is estimated that the 5-10% of fractures undergo delayed or non unions [128]. The latter have received much attention in the last decades and much effort is being made to find an effective and safe treatment to help the body regenerate large defects. Critical-sized defects have been classically treated by bone grafting (i.e. bone transplantation), either using bone from the same patient (i.e. autograft) or from another individual belonging to the same species (i.e. allograft). Autografts are the ideal option since the patient receives

its own tissue, which is highly osteoinductive and osteoconductive because of the presence of bone cells, bone matrix and signaling molecules [129]. However, the use of autografts requires multiple surgical procedures to harvest and subsequently implant the tissue, the available quantity of which may be insufficient in the case of large defects [130]. Allografts, normally from cadavers, overcome the limitations imposed by autografts, but may be a vehicle for disease transmission [130].

The number of people aged 60 or over is expected to dramatically increase globally by 2050 [131]. In this context, the prevalence of osteoporosis is estimated to rise by 23% in the European Union (EU), which translates to an increment of 28% in the number of annual fractures in the region by 2025 [132]. These prospects, together with the high risk of recurrent fractures [113], foresee a globally increased need for bone grafts in the coming decades, urging scientists to develop approaches overcoming the limitations of autografts and allografts.

1.2 BIOMATERIALS AND TISSUE ENGINEERING

1.2.1 Biomaterials: from substitution to regeneration

The history of biomaterials started in the late 1940s, when the ophthalmologist Harold Ridley noticed that fragments of cockpit canopies in the eyes of pilots were well tolerated by the body. After performing some "biocompatibility" assays with the material the canopies were made of, poly(methyl methacrylate), he used it to produce intraocular lenses to replace cataractous lenses in the early 50s [133]. More or less concomitantly, Dr. Arthur Voorhees successfully implanted tubes made of Vinyon (polyvinyl chloride fibers) cloth to bridge dog aortas without signs of foreign body reaction [134]. These are examples of early biomaterials (known as first-generation biomaterials), where materials not specifically meant to be used in humans/animals were used to produce implants. By then, biomaterials were meant to functionally replace a tissue without eliciting toxicity to the host tissue (i.e. being bioinert) [135].

The second generation of biomaterials was born in the 1980s. This generation, still aiming substitution, introduced two important concepts: bioactivity and biodegradability. The field moved from using materials eliciting a minimal host response to materials intended to induce specific responses once implanted (i.e. bioactivity). Early bioactive materials were bioglasses and ceramics, mainly HA, shown able to create a strong bond with host bone (i.e. osseointegration), thus providing structural and mechanical stabilization [136]. The field moved also towards the use of temporal implants that would be resorbed after their intended mission was completed, so only host tissue could be found at the site of implantation by the end of the process. Biodegradable polymers allowed the development of resorbable sutures made of polylactic and polyglycolic acids [135] and of temporal carriers for drug delivery such as polylactic acid systems for the release of contraceptives [137].

Third-generation biomaterials appeared with the new millennium aiming to induce highly specific cellular behaviors at the molecular level [138]. Biocompatibility, bioactivity and biodegradability are inherent to third-generation biomaterials, which should ideally be

injectable to minimize the pain related to implantation. They are mainly used to achieve tissue regeneration and to deliver cells and/or drugs.

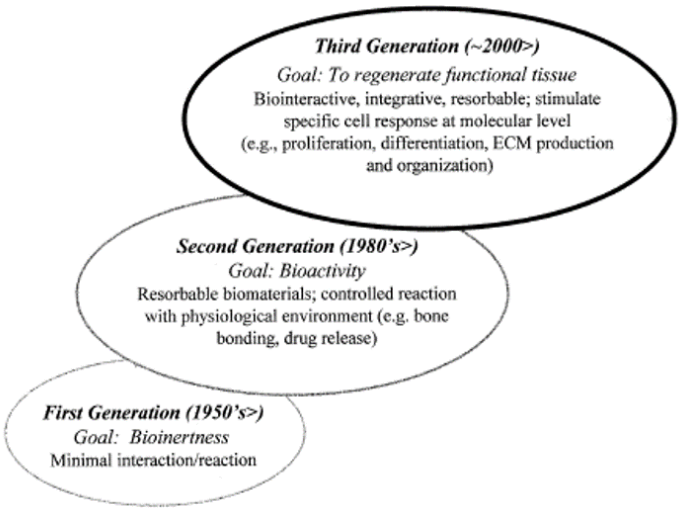

Figure 11. The evolution of biomaterials. Scheme depicts the three generations of biomaterials with their corresponding goal and main properties.

By now, it is obvious the field has rapidly evolved and become more and more ambitious in the last decades (Figure 11). Biomaterials, first defined as "non-viable materials used in a medical device, intended to interact with biological systems" [139] are now described as "substances that have been engineered to take a form which, alone or as a part of a complex system, are used to direct, by control of interactions with components of living systems, the course of any therapeutic or diagnostic procedure, in human or veterinary medicine" [140]. With the purpose of achieving tissue regeneration, a current-generation biomaterial could be more specifically defined as a substance for the therapeutic reconstruction of the human body that selectively stimulates cell responses through chemical and physical signals (adapted from [140]). In the case of bone, biomaterials for tissue regeneration should stimulate MSCs to undergo osteogenic differentiation (i.e. osteoinduction) and be a platform (scaffold) for cell growth and bone development (i.e. osteoconduction) [141]. With this purpose, materials can be selectively engineered and processed to achieve scaffolds with desired structure, surface chemistry and mechanical properties to induce and guide the regenerative process.

1.2.2 Tissue engineering

The evolution of biomaterials gave birth to tissue engineering, “an interdisciplinary field that applies the principles of engineering and the life sciences towards the development of biological substitutes that restore, maintain, or improve tissue function” [142]. Two types of tissue engineering strategies are currently being explored: those administering ex vivo-expanded cells and those using or stimulating cell homing, the endogenous machinery for the recruitment of cells to the site of injury (i.e. in situ tissue engineering). Regardless of the type of strategy, bone tissue engineering involves the use of cells (mainly MSCs), growth factors, scaffolds and their combinations.

MSCs can be used alone or in combination with scaffolds. Cell transplantation, whatsoever the cell source, requires an ex vivo expansion step, increasing costs, delaying interventions and potentially inducing phenotypic alterations such as reduced migration and engraftment potential, proliferation, differentiation potential and trophic (secretory) activity [143–149]. When used alone, MSCs are usually infused intravenously, resulting in potentially reduced viability upon injection [150] and low percentage of cells reaching target tissues [151,152], which can be bypassed by seeding or encapsulating them on scaffolds. Although pre-seeded/encapsulating constructs can improve cell engrafting to the target tissue and be a source of signals to recruit stem cells and progenitors to the defect site, problems related to ex vivo expansion remain unsolved.

A first alternative to cell transplantation is the use of bone growth factors, molecules that interact with membrane-bound receptors to elicit the activation of signaling cascades important to bone development and repair. Growth factors, which have attracted much interest lately, are commonly used in combination with scaffolds or microparticles, either encapsulated/loaded or grafted [153]. Several bone growth factors such as bone morphogenetic proteins (BMPs) [154–157], transforming growth factors β (TGF-β) [155,156,158], insulin-like growth factors (IGFs) [159] and fibroblast growth factors (FGFs) [160] have proved useful to induce osteogenesis in vitro and/or in vivo. Among them, BMPs are the most popular since the U.S. Food and Drug Administration (FDA) approved the use of recombinant human BMP-2 (INFUSE, Medtronic) and BMP-7 (OP-1, Stryker) in 2004. Although many studies have demonstrated the potential of BMPs,

especially that of BMP-2, in bone tissue engineering, heterotopic ossification has been described in patients treated with BMP-7 [161] and BMP-2 [162], with the latter being associated to several serious side effects when used in patients suffering from spinal fusion [163]. In the wake of these events, BMP-2, long considered to be a gold standard for osteoinduction, in now under investigation, raising concern about the use of growth factors in bone tissue engineering.

A second and more interesting alternative to cell therapy for bone tissue engineering is the use of scaffolds, commonly based on calcium phosphate cements (CPCs) and polymers. The former group, CPCs, emerged in the early 80s and has been thoroughly investigated ever since, becoming a promising family of biomaterials for bone regeneration. Several CPCs-based bone fillers are on the market [164], although their use is restricted to fractures in non load-bearing skeletal sites because of their poor mechanical performance [164–166]. CPCs are biocompatible and osteoconductive, can be injectable [167,168], and display composition and structure-dependent bioresorption and osteoinduction [169–171].

During the last decade, a new desired property has been added to those assumed for a third-generation biomaterial scaffold, biomimicry, which literally consists on the imitation of life or nature [172]. In the field of tissue engineering, it specifically consists on the imitation of the cellular microenvironment to finely drive cell behavior to recapitulate tissue development and ultimately achieve tissue regeneration. In the case of bone tissue engineering, biomimicry is the tool to develop osteoinductive constructs taking the extracellular matrix, the natural cellular scaffold, as a reference. The field is now moving towards the development of ECM-mimicking polymeric scaffolds with osteoinductive potential superior to that of CPCs. Biomimetic biomaterials represent the 4th generation of biomaterials [173].

1.2.3 The extracellular matrix: an archetype for scaffold design

The extracellular matrix (ECM) has been classically defined as the tissue- and developmental stage-specific [174,175] nanofibrillar scaffold physically supporting cells. This natural scaffold is dynamically remodeled during development [176] and tissue adaptation [177–179] as well as in response to disease and injury [180], leading to features

such as composition and stiffness changing over time and space [181–183]. The ECM properties and cell behavior are reciprocally regulated: ECM's composition, structure and stiffness depend upon cell-mediated synthesis and remodeling and, in turn, the matrix regulates cell processes such as adhesion, migration, proliferation and differentiation [176,184]. Thus, the ECM, once considered to be an inert scaffold, is now seen as a key player on tissue development and repair (and subsequently on tissue engineering) in light of its many functions in the cell niche (i.e. cell microenviroment) (Figure 12).

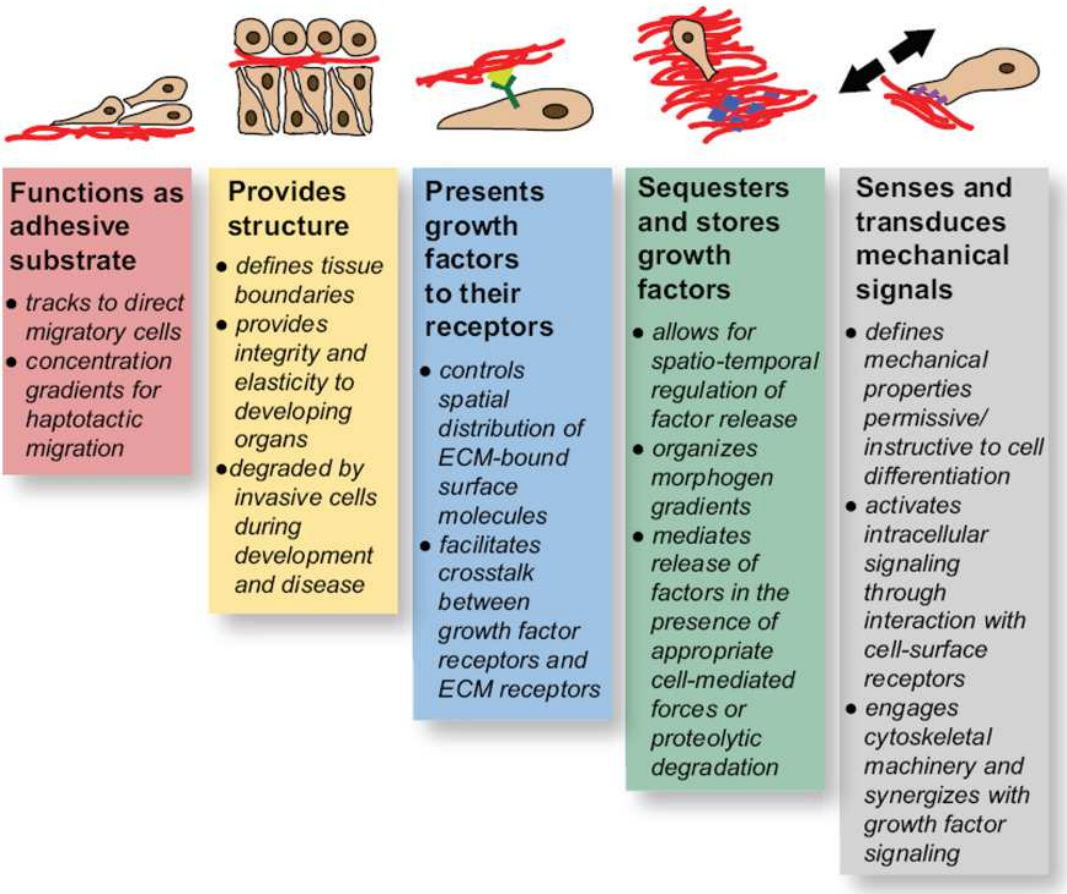

Figure 12. Functions of the extracellular matrix. From [185].

The ECM composition is tissue-specific but, in general terms, the matrix is a complex mesh of structural fibrillar proteins such as collagen, elastin and fibronectin, anchored molecules such as growth factors, proteoglycans, and water [184,186]. Fibrillar proteins and proteoglycans allow cell adhesion and growth by being both a physical support and a source of sequences for cell adhesion [187] such as the (i) universal cell adhesion Arg-

Gly-Asp (RGD) tripeptide from glycoproteins such as fibronectin [188], vitronectin [189] and collagen I [190], (ii) the endothelial cells-specific Arg-Glu-Asp-Val (REDV) tetrapeptide from fibronectin [191], and (iii) the Ile-Lys-Val-Ala-Val (IKVAV) pentapeptide from laminin for neuron adhesion [192]. ECM constituents serve also as a source of signaling molecules after proteolytic processing [193–197] and as molecule presenters to facilitate the access of growth factors to their cellular receptors [185,197,198]. The charged nature of glycoproteins and proteoglycans in the ECM allows the binding and storage of growth factors such as BMPs, FGFs and vascular endothelial growth factors (VEGFs), which can be maturated [199], presented and/or released to create a growth factors gradient/patterning for a spatio-temporal control of cell behavior [180,185,200]. Charges in ECM components also attract counter-ions, inducing an osmotic pressure and the subsequent swelling of the matrix [201], which acts like a sponge. The nature and chemical state of ECM constituents thus determine its water content which, together with the physical properties of the components, defines the mechanical properties of the matrix as well as the integrity and mechanical performance of the tissue [186,202–204]. Last but not least, ECM molecules transmit tissue-applied loads to cells, thus mechanically connecting cells to their microenvironment [204].

1.2.3.1 ECM-cell crosstalk

The ECM and the intracellular space are mainly linked through integrins, a family of heterodimeric (α and β subunits) transmembrane receptors that mediate cell-cell adhesions as well as cell-to-ECM (inside-out) and ECM-to-cell (outside-in) signaling [205]. The cell-ECM connection is possible thanks to the association of integrins with adapter proteins that link them to the cytoskeleton and to other signaling-related proteins such as growth factor receptors [206]. Upon binding to the ECM, integrins are clustered and their intracellular domains bind adapter proteins such as vinculin, tallin and paxillin, which induces actin polymerization, giving rise to actin filaments [206,207]. Actin filaments organize into stress fibers and further integrin clustering is induced, strengthening the cell-ECM binding and leading to the emergence of local protein complexes known as focal contacts (or focal adhesions) [208]. Focal contacts mechanically connect the ECM and the intracellular space (i.e. mechanosensing), and activate complex signaling cascades extending to the nucleus that regulate a myriad of cellular processes [206].

Several α and β subunits have been described and they can assemble into up to 24 different combinations, each of which shows specific binding and signaling features [206,209]. The coordination of specific integrins, soluble molecules and growth factor receptors triggers signaling cascades leading to changes at a gene expression level, thus allowing the integration of signals coming from the cell microenvironment to regulate cell behavior [206,210,211]. Interestingly, outside-in signals induce cellular responses that, in turn, produce changes in the ECM (inside-out signals) that can be felt by cells that will respond accordingly. This integrin-mediated feedback mechanism [212,213] permits the existence of a highly dynamic microenvironment for cells to be able to respond rapidly to tissue requirements.

1.2.3.2 Lessons from the ECM

Multiple integrins can bind to a given ligand and, at the same time, multiple ligands can be recognized by a single integrin [205]. This redundancy is somehow striking given the outstanding optimization of the cell machinery. In this sense, authors have shown that the binding of different integrins to one particular ligand leads to different signals being transmitted [214] and have suggested that integrin specificity could be somehow cell-type specific [205]. Thus, a relatively narrow spectrum of integrins would allow for a wide range of specific signaling outcomes.

It is well known that the composition of the ECM, by eliciting the binding of specific integrins, regulates cell morphology [215], migration [216,217], proliferation [197,218], differentiation [216,219,220] and survival [214,215,221,222] upon adhesion. Interestingly, adhesion through integrins is itself a checkpoint for adherent cells survival [223] as detachment leads to adherence-dependent apoptosis (i.e. anoikis) [224]. This is a mechanism to maintain homeostasis, preventing survival of detached cells that could adhere to inappropriate locations [206]; resistance to anoikis is assumed to be the reason why cancer cells can metastasize [225].

The effect of the structural and mechanical properties of the ECM has been extrapolated from studies based on the use of non-natural substrates, which have revealed that physical properties of the substrate affect cell adhesion, morphology, migration, proliferation and differentiation [226–230]. And collectively, studies have shown that substrate structural,

chemical and mechanical properties condition integrin distribution [231–233], clustering [231–236] and specific binding [219,235–237] and, as previously stated, the signals being transduced [238] and thus the cellular outcome. It is seemingly reasonable, then, to design tailored scaffolds with characteristics mimicking those of target tissue's natural ECM.

1.2.3.3 In situ bone tissue engineering: integrating lessons from the ECM

As stated in section 1.2.2, two main bone tissue engineering strategies involving the use of scaffolds are currently being explored: (i) the implantation of cells, either encapsulated or seeded, and (ii) the stimulation or exploitation of cell homing (i.e. in situ bone tissue engineering; Figure 13). Those strategies involving the implantation of cells and scaffolds or the stimulation of cell homing, commonly achieved by combining scaffolds and growth factors, won't be further discussed given the limitations related to ex vivo cell expansion and to the use of growth factors. We'll focus on the use of scaffolds meant to achieve bone regeneration by taking advantage of the natural cell homing signaling pathways. In short, this strategy consists on implanting scaffolds shortly after injury (ideally, by injection; Figure 13a) so MSCs being homed to the site of injury find a platform to adhere to (Figure 13b). After adhesion, MSCs should be able to grow, and to differentiate in a scaffold-controlled manner to rebuild the tissue (Figure 13c). For this control to be possible, scaffolds must be tailored to possess features inducing MSCs to undergo osteogenic differentiation (besides, of course, promoting MSCs adhesion).

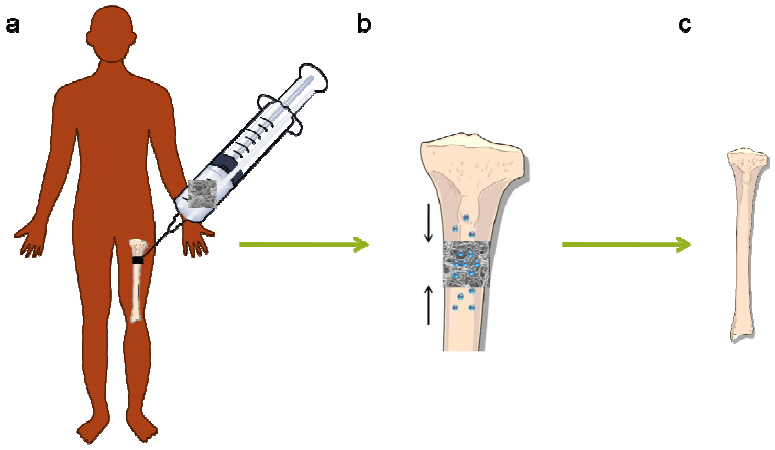

Figure 13. Schematic representation of in situ bone tissue engineering. a) After implantation, ideally by injection, b) progenitors homing to the insult site would colonize the scaffold, which

would instruct them to c) regenerate bone. During the process, the scaffold should be degraded by growing cells to achieve a scaffold-free native tissue.

Separately, matrix structure [239–241], stiffness [242] and surface chemistry [237,243] have been proven useful to induce osteogenic differentiation of MSCs, and parameters such as ligand nature [219], density [244] and presentation [230] have been shown to influence the behavior of cells belonging to the osteoblastic lineage. Although studies have pointed out that tailored stiffness or topography of scaffolds would be sufficient to regulate stem cells fate [239,242], the debate about using scaffolds relying on a single parameter, mainly stiffness, acting as a master force driving differentiation is now open [245]. Combinatorial studies [246–248] have reported contradictory results as to the stiffness value at which stem cell differentiation is induced, suggesting that the results published by Engler and co-workers [242], and by extension those by Oh and coworkers [239], would be valid in the set of conditions used in their experiments and need to be taken as proofs of concept. Thus, the design of scaffolds for in situ bone tissue engineering is moving towards more complex setups accounting for the contribution of multiple matrix properties in order to achieve a superior level of biomimicry.

1.2.3.4 Hydrogels: lessons learnt

Scaffolds mimicking the ECM can be basically classified as either electrospun mats or hydrogels. Electrospinning has become very popular in the last decade since it allows the creation of mats of fibers with diameters close to that of ECM structural proteins. Electrospun mats can be tailored to possess surface chemistry permissive for cellular processes either by using specific polymers or by functionalization [249–256]. However, electrospinning commonly leads to scaffolds with low pore size [257], hindering cellular colonization, and affecting proliferation and matrix deposition [258]. Pore size and interconnectivity are also important for vascularization [259–261] and thus for the nutrition of cells growing within the scaffold.

The abovementioned limitations may be overcome by using hydrogels, three-dimensional polymeric networks that can absorb large quantities of water thanks to their interconnected microscopic pores [262]. Their open network structure allows for gas (O_2 and CO_2) exchange and determines the diffusion of solutes (e.g. nutrients, metabolic wastes and soluble signaling molecules) [263] and swelling [264,265], and thus their mechanical

properties and degradability. Hydrogel network properties can be tailored by crosslinking, a chemical, physical or enzymatic reaction leading to the creation of bonds linking different polymer chains (interchain crosslinking) or regions (intrachain crosslinking). Thus, crosslinking allows tuning hydrogel architecture, mechanical properties and degradability [266–268], which evidences the tailorable nature of hydrogel physical properties. Hydrogels can be prepared from a myriad of natural polymers [269–275] as well as from synthetic polymers [276–282], further evidencing hydrogels are highly versatile platforms that allow the tailoring of multiple parameters to achieve implants with properties resembling those of the ECM.

1.3 ELASTIN-LIKE POLYMERS

1.3.1 Genetically-engineered protein-based polymers

When designing hydrogels for a given application, selecting the polymer to be used is the first step to take. On one hand, synthetic polymers are commercially available and stable in a wide range of conditions, and allow the fabrication of hydrogels with tuned mechanical properties and chemical modifications, but they may show reduced biocompatibility and biodegradability [283]. In contrast, natural polymers are biodegradable, possess a chemistry allowing chemical modifications and interactions with cellular receptors, and both themselves and their degradation byproducts are biocompatible [283,284] (Table 1). On the other hand, natural polymers may display batch-dependent features, may elicit immunogenic responses and be a vehicle for disease transmission, and may lose their properties during processing (E.g. protein denaturation) [283–285]. These limitations, especially critical in the case of ECM structural proteins obtained from animal sources, can be overcome by using their engineered counterparts.

Advantages	Drawbacks
Biocompatibility	Limited commercial availability
Inherent biodegradability	Batch-to-batch differences
Biocompatible degradation byproducts	Potential immunogenicity
Sequences for cellular receptors	Possible loss of biological properties
Functional groups usable for modifications	Risk of disease transmission

Table 1. General features of natural polymers.

In the last years, the concept of protein engineering has gained momentum in the biomaterials field. The synthesis of engineered proteins was initially carried out by chemical synthesis [286] but has gradually moved into recombinant synthesis by using genetically modified biological bioreactors, mainly *Escherichia coli*. By this latter methodology, the amino acid sequence and polypeptide (from now on, polymer) length can be easily modified by changing the nucleotide sequence and the length of the codifying DNA sequence, allowing for a precise design of the polymer and its properties [287]. This strategy allows producing polymers with monodisperse molecular weight of

up to hundreds of kDa, a constantly increasing limit [288,289]. Interestingly, the molecular tailoring of DNA sequences allows the cost-effective production of polymers with increased molecular complexity and functionalities not displayed in natural polymers [288] at high yields [290]. Engineered polymers designed and produced by recombinant DNA technology are known as genetically-engineered protein-based polymers (GEPBPs), including polymers based on natural proteins suchs as resilin [291], elastin [288,292,293], and *Nephila clavipes* spider silk [294,295].

1.3.2 Elastin-like polymers: main properties

Among GEPBPs, elastin-like polymers (ELPs) stand out as a powerful tool given their versatility and interesting properties. These polymers are based on the sequence of mammalian elastin [296], a protein from the ECM conferring elasticity to tissues like skin, large blood vessels and muscles, and to organs such as the lungs [297,298]. Elastin includes crosslinking (rich in alanine and lysine) and hydrophobic (rich in proline, glycine and hydrophobic amino acids such as valine and alanine) regions [299]. The latter seem to be a common trait to elastomeric proteins [292] and to play an essential role in determining their physical properties [300]. Hydrophobic regions such as PGGV, PGVGV, PGVGVA and GGLGV have been found repeated along the sequence of mammalian elastin, and the protein in different animal species displays differences as to the predominant hydrophobic region [299] and the number of repetitions. As an example, the VPGVG pentapeptide is repeated three, eleven and fifteen times in human, bovine and chicken elastin, respectively [301]. Assuming the contribution of hydrophobic regions to elastin physical properties, these regions are the basic building blocks of ELPs. Two main types of ELPs have been developed: (i) those developed by Tamburro and coworkers (building block: XxGGYyG, where Xx and Yy correspond to hydrophobic residues) [292], and (ii) those developed by Urry and coworkers (building block: VPGXG, where X is known as visiting residue, a position that can be occupied by any amino acid except proline [302]).

VPGXG-based ELPs have been extensively studied and used in the form of poly(VPGVG), considered to be a model ELP. This model polymer was subjected to

several biological in vitro and in vivo tests and it was shown to be biocompatible [303], a feature assumed to be a common trait for all VPGXG-based ELPs, given that the organism would be unable to distinguish them from native elastin [287]. The model polymer was also found to be inherently anti-fouling [296], so ELPs meant to be included in tissue engineering strategies need to be designed to include cell adhesion sequences such as RGD [304] and REDV [305,306]. Further bioactivity can be achieved by the inclusion of sequences such as (i) the SN15 fragment of human salivary statherin [307] or (ii) the VGVAPG hexapeptide, a natural target sequence for elastase [306] that can act as a chemoattractant for monocytes, fibroblasts, keratinocytes and vascular smooth muscle cells upon enzymatic processing [195]. Although ELPs would be degradable by generic proteases, sequences like VGVAPG can be included to adjust their biodegradability to that required for a given application, which gives an idea of the great versatility of these polymers.

ELPs are not only biocompatible, biodegradable and potentially multifunctional polymers but also smart, self-aggregating and thus segregating from the aqueous phase (i.e. coacervation) in response to external stimuli. This feature seems to be common to elastomeric proteins with hydrophobic domains [299]. Self-aggregation has been described for elastin, the hydrophobic domains of which would organize leading to the formation of filamentous coacervates made up by fibrous structures of about 5 nm [308] in response to temperature increases; this phenomenon has been also described for VPGXG-based ELPs [309].

1.3.3 ELPs: the inverse transition phenomenon

Proteins are known for undergoing a transition from an ordered to a disordered state (denaturation) in response to increases in temperature. Both elastin and ELPs undergo the inverse process (disorder to order; Figure 14), which led to coining the term “inverse transition temperature” (ITT) for ELPs [309].

In a solution below the ITT, the polymer chains remain disordered in the form of random coils, with water surrounding the hydrophobic domains of the polymer [309]. When temperature is raised, the non-polar solvation layer is broken [310] and the polypeptide

chains undergo hydrophobic folding, with each PVGXG pentamer leading to a type II β turn. This leads to polypeptide chains folding in the form of β spirals that hydrophobically aggregate to make up nanometric particles that segregate from the solution [309]. This aggregation would involve weak bonds such as van der Waals forces and hydrogen bonds that allow the creation of 3D structures [287] and the reversibility of the process when temperature is decreased below the ITT [296]. Interestingly, a single PVGVG pentamer is enough for the phase transition to occur [311], thus stablishing a sequence-functionality relation that explains this striking property of elastin and ELPs. It is noteworthy to mention that the self-aggregation process is affected by a myriad of parameters which should be considered when using ELPs as raw materials for the creation of scaffolds or drug delivery systems (Table 2).

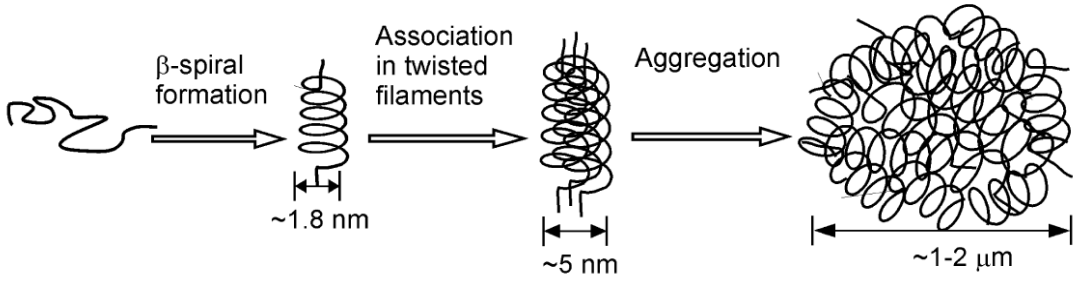

Figure 14. Proposed mechanism for the coacervation of ELPs. From [287].

Up to date, ELPs have been used in many applications, such as (i) drug delivery [313,315–320], (ii) development of cell harvesting systems [321], (iii) improvement of the efficiency of recombinant protein purification [322], (iv) prevention of postoperative adhesions [323,324], (v) soft tissue augmentation for correcting urinary incontinence [325], and (vi) bone [326–328], (vii) cartilage [329–331], (viii) vascular [332,333], (ix) nervous system [334] and (x) ocular surface regeneration [335].

1.3.4 ELPs: crosslinking

As previously mentioned, ELPs are able to coacervate in response to increases in temperature, with the coacervation process being reversible and affected by many external parameters that can compromise the stability of ELPs-based scaffolds. In order to produce

hydrogels stable over a wide range of conditions, ELPs have been crosslinked by means of a myriad of methods (Table 3), being chemical crosslinking the most commonly used.

Parameter	Reference
Mean polarity	[309,312]
Molecular weigth	[306,312,313]
Sequence composition	[314]
Amino acid in the visiting residue position	[313]
Working concentration	[311,313]
Amino acid distribution along the sequence	[312]
Salt type and concentration, and presence of organic solvents	[296,311]
Solution pH	[306,309]
Pressure	[311]

Table 2. Parameters affecting the inverse aggregation phenomenon.

Modern (i.e. recombinant) ELPs are generally designed to be enriched in lysine residues as a source of primary amines (ε-NH_2) to be used for crosslinking purposes (an additional trait inherited from elastin [336]) and are thus commonly crosslinked by using lysine-to-lysine chemical methods. Among the chemical species used in lysine-to-lysine chemical crosslinking, glutaraldehyde stands out as a highly reactive compound that gets incorporated into the nascent polymeric network. Although this compound is widely used [337], concern has been raised about its use to produce hydrogels for tissue engineering, which may be inherently cytotoxic due to the exposure of highly reactive pendant groups [338] or to glutaraldehyde depolymerization during the degradation of the scaffold [339]. Another lysine-to-lysine integrative crosslinker is genipin, a natural molecule with increasing interest in the biomaterials field that can lead to cytotoxicity upon scaffold degradation [340].

In order to avoid cytotoxicity related to the release of toxic crosslinking products during scaffold degradation, non-integrative methods such as enzymatic crosslinking have been developed. ELPs have already been crosslinked with bacterial transglutaminase, which despite not being a lys-to-lys method, is an approach to how the ECM in bone is crosslinked; however, it is still far from producing the particular crosslinks responsible for bone ECM mechanical properties (see section 1.5.1). Another example of non-toxic

crosslinking method is catalyst-free click-chemistry, which consists on reticulation mediated by highly specific modular reactions that yield non-toxic crosslinking products [341,342]. Despite click chemistry is an interesting approach, it requires the time-consuming chemical modification of polymers to introduce the reactive groups of interest [342]. This, along with crosslinking, can be achieved by using water-soluble carbodiimide, which induces the formation of cytocompatible crosslinks and can be easily removed from the so-produced scaffolds.

Method	Crosslinker	Reference
Physical	Coacervation	[325,330]
	Gamma irradiation	[303,343,344]
Chemical	Glutaraldehyde	[292,300,305,306,345]
	β-[tris(hydroxymethyl)phosphino]propionic acid (THPP)	[331,346,347]
	Dicumyl peroxide (DCP)	[344]
	Hexamethylene diisocyanate (HDI)	[348,349]
	N-Cyclohexyl-N′-(2-morpholinoethyl)carbodiimide metho-p-toluenesulfonate (CMCI)	[286,350]
	N-(3-Dimethylaminopropyl)-N′-ethylcarbodiimide (EDC)	[344]
	Disuccinimidyl glutarate (DSG)	[292]
	Bis(sulfosuccinimidyl) suberate (BS^3)	[351–353]
	Disuccinimidyl suberate (DSS)	[351]
	Tris-succinimidyl aminotriacetate (TSAT)	[354]
	Pyrroloquinoline quinone (PQQ)	[293,355]
	Genipin	[326,355]
	Tetrakis(hydroxymethyl) phosphonium chloride (THPC)	[356]
	Catalyst-free click chemistry	[342]
Enzymatic	Microbial transglutaminase	[329,333,357]

Table 3. Methods proven useful to crosslink ELPs.

1.3.4.1 Water-soluble carbodiimide

EDC, a water-soluble zero-length crosslinker belonging to the family of carbodiimides, is a widely used reagent to crosslink proteins; it catalyzes the formation of amide (peptide) bonds by inducing the condensation of carboxyl groups (-COOH) with primary amines ($-NH_2$) [358]. Interestingly, both EDC and its main byproduct are water-soluble, and

peptide bonds can be degraded by generic proteases, which suggests that EDC is useful to produce biodegradable hydrogels with minimally compromised biocompatibility.

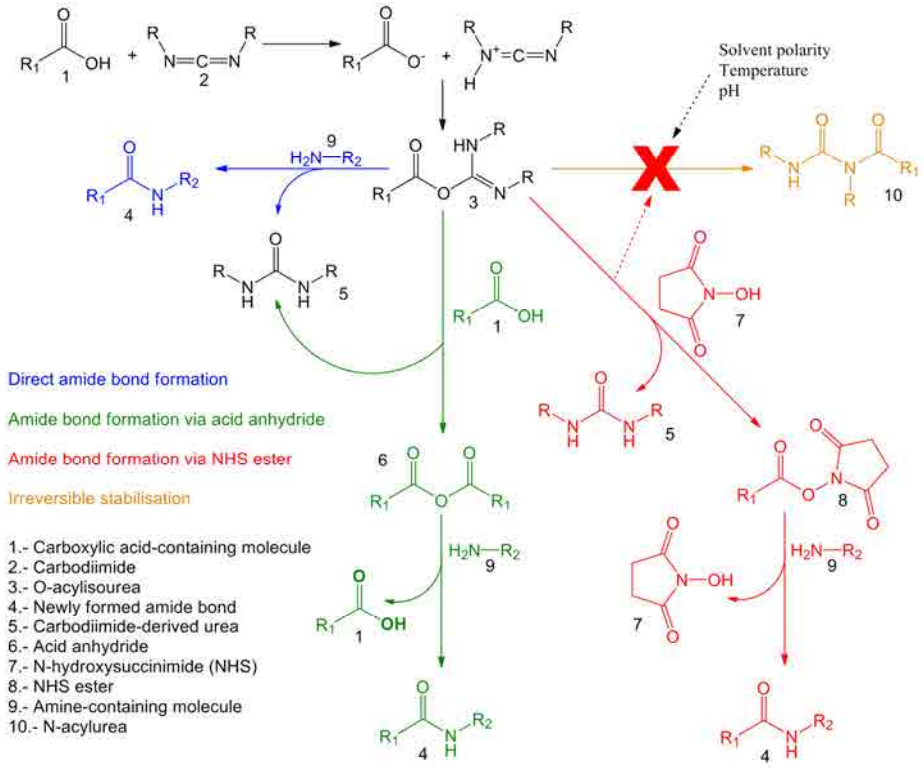

Figure 15. Reaction mechanism of EDC-mediated activation of –COOH groups. The **f**ormation of amide bonds can occur through direct (blue route) and indirect mechanisms (green route). The reaction can evolve to the formation of non-desired unreactive species (orange route), which can be avoided by adjusting some reaction parameters or by producing NHS esters (red route).

The reactions involved in the EDC-catalyzed formation of peptide bonds, along with side reactions, are depicted in Figure 15. EDC reacts with carboxyl groups (i.e. activation) to give rise to O-acylisourea, an intermediate specie that can suffer nucleophilic attack by an $–NH_2$ group to produce a peptide bond (blue route). O-acylisourea can also (i) lead to the formation of acid anhydride, an unstable specie that can react with primary amines and produce peptide bonds (green route), or (ii) irreversibly stabilize into N-acylurea, a non-reactive specie (orange route).The latter can be avoided by performing the reaction in solvents with low dielectric constant at low temperatures [359] or using N-hydroxysuccinimide (NHS), which reacts with O-acylisourea to form a more stable intermediate to react with primary amines [360]. Parameters such as solvent polarity

[361], presence of water [362,363] and pH [358,364] are important for the stability of EDC and O-acylisourea [358,362] and may determine the main route through which the reaction evolves; others like the EDC:NHS molar ratio [360,365], EDC:COOH and COOH:NH_2 molar ratios [365] and reaction time [358,362,365] mainly influence the yield of the reaction. The outcome of the EDC-mediated activation of –COOH groups depends on many reaction parameters, so optimization is required in order to achieve and control crosslinking. Interestingly, EDC can be used not only to catalyze crosslinking, but also to engraft –COOH or –NH_2-terminated molecules to provide polymers with new functionalities.

As previously noted, ELPs are generally designed to display –NH_2 groups for crosslinking. It is noteworthy to mention that they are also commonly short on –COOH groups [366] so EDC-mediated crosslinking would hardly take place unless carboxyl group-donor molecules are used. In these conditions, a donor molecule would act as a bridge connecting polypeptide chains, thus getting physically integrated into the network. Examples of donor molecules are nitriloacetic, suberic and glutaric acids, which have been already used in the form of commercially available NHS esters (TSAT, BS3, DSS and DSG; Table 3) to crosslink ELPs. Suberic and glutaric acids possess two –COOH groups, both of them required to condense with primary amines for crosslinking to occur. Polycarboxylic acids (i.e. they contain >2 –COOH groups) such as nitriloacetic acid are more versatile molecules, allowing to achieve higher degrees of crosslinking and thus to tune hydrogel features such as mechanical properties and degradability [267,367]. Additionally, under controlled conditions, polycarboxylic acids can partially react to both crosslink the polymer and to introduce carboxylates on surface, which may help driving cell differentiation [237,243] or inducing scaffold mineralization [368,369]. Thus, polycarboxylic acids activated with carbodiimides can be potentially used both to achieve crosslinking and to provide the network with new functionalities.

1.4 CITRIC ACID

1.4.1 Citric acid in bone

Citric acid is a central molecule in Krebs cycle, a set of enzymatic mitochondrial reactions coupling nutrients degradation with energy production. As such, this tricarboxylic acid is distributed along the body but it seems to be particularly abundant in bone. Authors have reported citric acid to represent the 1.42% of ground ox and sheep bones [370], 1% of dog bones [370], 0.5-1% of wet weight in dog, beef and rabbit bones [371] and the 5.5% of the organic fraction in bone from several animal species [6], quantities much higher than those found in any other tissue. It's for this reason that bone is considered to be the main citric acid deposit in the body, containing up to the 70% and 80% of the total citric acid in adult mice [370] and humans [372], respectively. Citric acid accumulation in bone seems not to be accidental, as illustrated by its synthetic enzymatic activities being overexpressed compared to that responsible for its degradation [373,374]. Collectively, these studies from the 30s, 40s, 50s and 60s evidenced that citric acid, recently suggested to be produced by osteoblasts [32], plays a role in bone mineralization, although by then this role was unknown.

1.4.2 Citric acid and biomineralization

In 2010, Hu, Rawal and Schmidt-Rohr [6] published a study focused on the relation between citric acid and hydroxyapatite. After removing endogenous citrate, the authors exposed cow, chicken and fish bone to solutions containing radiolabelled citric acid and found the tricarboxylic acid closely bound to mineral phase, covering 1/6 of its surface (Figure 16a) and representing the 0,42% of the mineral phase weight. These authors concluded that citrate, with a spacing of its carboxylate groups matching that of calcium ions along the c-axis in HA crystals, would bind to the mineral phase of bone and prevent the binding of further calcium phosphate, thus stopping its growth.

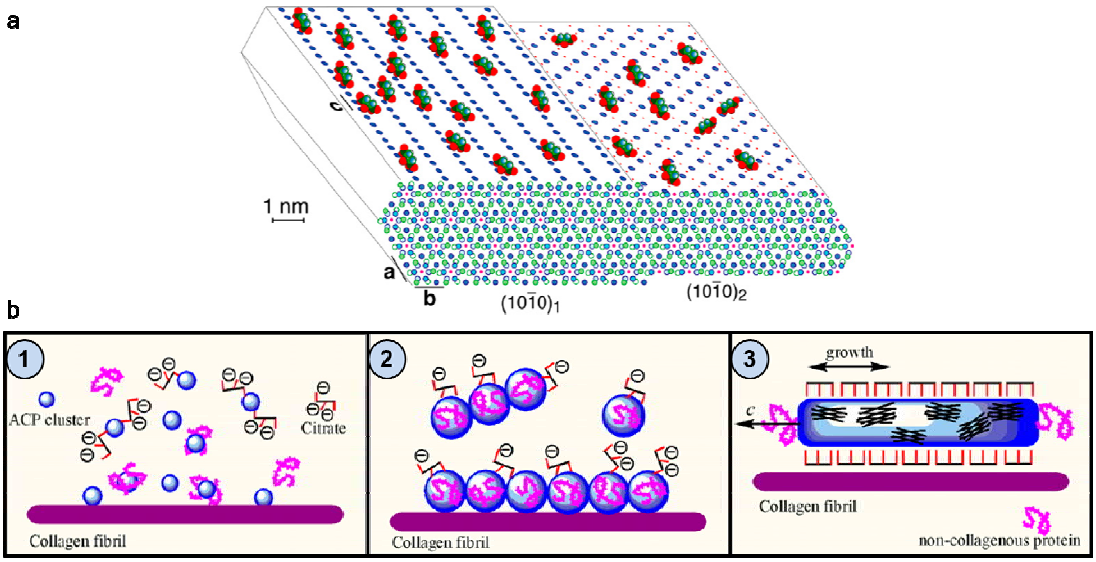

Figure 16. Models of the citrate-HA interaction. a) Diagram of citrate (with oxygen from carboxylates depicted in red) bound to two HA surfaces (with calcium ions depicted in dark blue). Calcium ions in the $(1010)_1$ surface are spaced by c/2=0.34 nm, which matches the distance spacing the central and terminal carboxylates of citrate; in the $(1010)_2$ surface, calcium ions are spaced by c=0.688 nm, which matches the distance between the terminal carboxylates of citrate. Blue-filled circles: calcium atoms; green: phosphorus atoms; pink dots: OH^- ions; red circles: carboxylates in citric acid. From [6]. b) Diagram depicting the model for biomineralization proposed by Xie and Nancollas. According to this model, citrate and non-collagenous proteins would collaborate to drive the directional growth of HA crystals. Adapted from [25].

Some authors have reported charge anisotropy along the facets of the HA crystals [375–377], so citrate binding and thus the introduced charges, wouldn't be homogeneous along the crystalline surface. Through electrostatic repulsion, this would result in the conditioned aggregation of crystals, which would undergo oriented growth, mainly in their longitudinal axis [378]. In a recent model for bone mineralization (Figure 16b), Xie and Nancollas [25] proposed that crystal growth would be dependent on the distance between contiguous calcium ions, so crystal thickening would be stopped when this distance matches that spacing the carboxylates of citrate. In the model of Hu, Rawal and Schmidt-Rohr, bound citrate would be almost parallel to the HA surface, thus exposing methylene groups ($-CH_2$) to make the surface less hydrophilic and thus more compatible with hydrophobic residues from collagen [6] in the osteoid. Finally, the growth of HA crystals along their long axis would be controlled and stopped by NCPs in order for the crystals to achieve an optimum size [25,26], thus conferring fracture strength and tolerance to flaws on the crystals, and a proper stiffness on the composite material that is bone. Interestingly,

the role of citric acid in biomineralization seems to extend beyond bone, as suggested by studies showing a coordination of citrate and NCPs to control the shape and size of calcium oxalate monohydrate crystals, the main component of kidney stones [379,380]. Collectively, these evidences point out citrate as an important global regulator of in vivo biomineralization.

1.4.3 Citric acid and in vitro calcium phosphate nucleation

In the 40s, calcium, phosphate and citrate were found able to form complexes when at proper concentrations in alkaline conditions [381,382], a phenomenon that is likely to underlie the binding of citrate to HA crystals to stop their growth and that points out that citrate might act as calcium phosphate-nucleating molecule.

Using surfaces functionalized with several functional groups, Tanahashi and Matsuda demonstrated that negatively charged surfaces are good substrates for HA nucleation. Although phosphates showed an obviously favored nucleation capacity, carboxylates were found able to nucleate HA almost at the same rate as phosphates after an induction period [383], suggesting citrate could act as a nucleating molecule. This was demonstrated by Rhee and Tanaka after exposing bovine collagen matrices to 1.5x simulated body fluids (SBF). HA was found only when 1.5x SBF was supplemented with citric acid [384] and the process was found to be dependent on the Ca^{2+}-to-citrate molar ratio on the supplemented solution [385]. Interestingly, HA precipitated in the presence of citrate was found to display X-ray diffraction peaks broader than those from normal HA, which would be due to citrate inducing the formation of crystals with either low crystallinity or low size. Although both phenomena have been described when preparing CPCs in the presence of citric acid [386–388], citrate has been reported to be especially effective on reducing crystal size down to the nanoscale [389–392]. Together with Rhee and Tanaka's work, these studies suggest that citric acid is useful to both induce HA nucleation and to stop crystal growth.

1.4.4 Citric acid in the biomaterials field

Citric acid is a molecule with an increasing interest in the biomaterials field, where it has been basically used (i) as a raw material for the development of biodegradable polymers, (ii) an additive in the preparation of scaffolds, and (iii) a crosslinking agent.

In the early 2000s, Yang and co-workers developed poly(diol citrate) [393], a biodegradable polyester elastomer based on citric acid and already used in the development of vascular implants [394–398], fixation devices for bone fractures [399], composites for bone regeneration [400–402] and gene delivery systems [403]. These elastomers have been doped with urethane bonds [404], and modified with amino acids [405], maleic acid [406] and sebacic acid [407], thus increasing the number of potential applications of these polymers. More recently, glycerol and citric acid-based biodegradable polyesters for drug delivery have been developed [408].

Citric acid, as an additive, has been used as a porogen in combination with carbonate salts in the development of porous scaffolds based on poly(L-lactic acid) [409], glycolic acid and lactic acid [410], poly(propylene fumarate) [411], ELPs [348] and CPCs [412]. In the case of CPCs, citrate has been also used to achieve scaffolds with improved injectability [413,414], compression strength [413,414], and biocompatibility and osteoconduction. [390,391].

Citrate has also been used as a crosslinker, given that it is a natural and biocompatible molecule possessing three carboxyl groups feasible to be used in reticulation reactions. However, carboxyl groups lack reactivity, so crosslinking with citric acid needs to be induced. First, the formation of peptide bonds by the condensation of –COOH from citric acid and primary amines from prolamines and collagen [415–417] has been achieved by applying high temperatures (usually, in the 125-150ºC range), conditions clearly detrimental if natural proteins or GEPBPs are to be crosslinked. A second and more gentle strategy is based on the use of NHS esters of citric acid upon chemical activation with carbodiimides. NHS-esterified citric acid has been produced by chemical synthesis, a time-consuming option involving the use of organic solvents, and employed to produce hydrogels [418,419] to be used as tissue adhesives [420], vascular stents [421,422] or scaffolds for vascular tissue engineering [423]. Interestingly, the in vivo role suggested for citrate in biomineralization has not yet been considered when using it for reticulation

purposes. This points out that citric acid can be used as a novel bioactive crosslinker providing lysine-displaying polymers with calcium phosphate nucleation potential.

1.5 LYSYL OXIDASE

1.5.1 Lysyl oxidase: an overview

Lysyl oxidase (or LOX; EC 1.4.3.13) is a copper-dependent amine oxidase responsible for the in vivo crosslinking of elastin and type I collagen. This protein, first described in embryonic chick bone, catalyzes the specific oxidative deamination of ε-NH_2 (Figure 17) from lysine present in collagen and elastin [424], as well as from hydroxylysine in collagen [425].

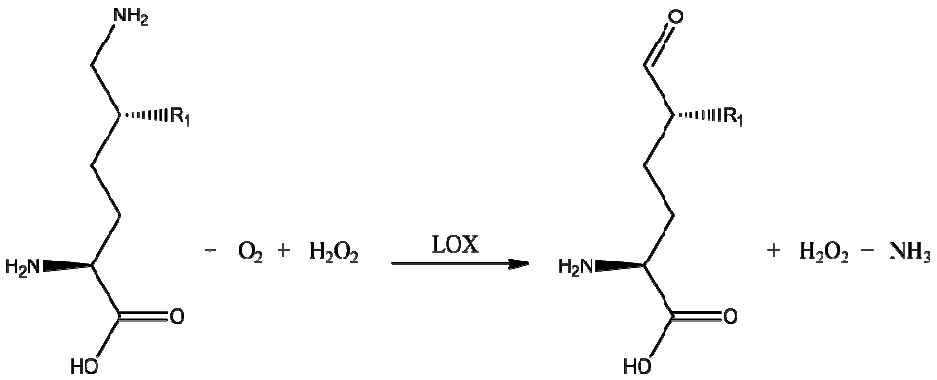

Figure 17. LOX-catalyzed oxidative deamination of lysine and hydroxylysine residues. R_1: H in lysine; R_1:OH in hydroxylysine.

LOX belongs to the lysyl oxidases family, together with lysyl oxidase-like (LOXL) proteins 1-4. All the members of the family show a highly conserved C-terminus (it suggests LOXL proteins would also possess enzymatic activity [426,427]; Figure 18) and divergence in the N-terminus, which is thought to be related to LOX/L-to-protein interactions, as evidenced by studies showing that the N-terminal of LOX and LOXL mediate substrate recognition [428].

Increasing evidences point out that LOX and LOXL proteins possess a spatially and temporally-regulated expression and oxidize specific substrates. Lysyl oxidases have been shown to possess tissue-specific expression patterns [426,429–433] which, together with their temporally-regulated expression, may have an effect on their functions, as evidenced by studies pointing out that these enzymes can possess a tumor suppressor role and can

also be involved in cancer progression, vascularization and metastasis [434,435]. Although the substrate specificity of LOXL proteins is still unclear, studies focused on the spatial expression of lysyl oxidases are shedding light on their putative substrates. For example, LOX and LOXL have been shown to co-localize with type I and III collagens, respectively [436], and LOX-2 co-localizes with type IV collagen in several tissues [426], which suggests that lysyl oxidases would have preferential substrates. However, a given protein can be oxidized by different lysyl oxidases, as in the case of elastin, which can be processed both by LOX and LOXL, with LOX showing a higher oxidative activity for elastin [426] and assumed to be the main member of the family crosslinking this protein.

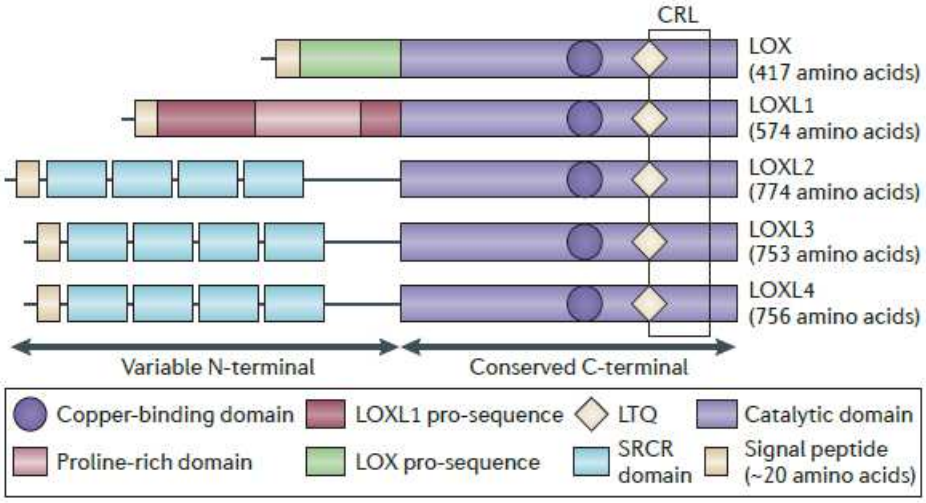

Figure 18. Schematic representation of domains within LOX and LOXL proteins. From [434].

Human LOX is synthetized in the form of a 47 kDa preproenzyme that, after undergoing removal of the signal peptide and N-glycosilation, is secreted in the form of a 50 kDa proenzyme [437] (Figure 19). Once in the extracellular space, the proenzyme undergoes proteolysis carried out by C-proteinases [438–440], mainly BMP-1 and mTLL-1 (mammalian Tolloid-like 1) [440], leading to the 32 kDa non-glycosilated, active version of the enzyme [438,441] and to a 18 kDa N-glycosilated pro-peptide. Interestingly, the propeptide has been shown to mediate substrate recognition [442], to inhibit osteoblast proliferation [443] and to be a tumor suppressor [442,444–447] and it is a candidate oligopeptide to be used in the treatment of cancer.

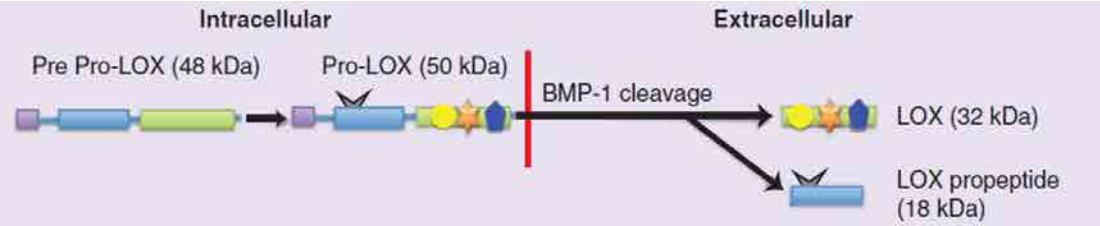

Figure 19. Synthesis of active human LOX. Adapted from [434].

For LOX to be active, it requires the presence of two cofactors: Cu^{2+} and lysyl-tyrosylquinone (LTQ). During the proenzyme stage, a Cu^{2+} atom is incorporated into the active site by complexation with histidine residues [448–451]. The incorporation of the metallic atom induces a self-catalytic reaction leading to the formation of a covalent bond linking a tyrosine residue with the side chain of a lysine residue, thus leading to the formation of LTQ [452].

The LTQ cofactor gets reversibly modified during oxidative deamination, which follows a ping-pong mechanism. During the first half of the reaction, an ε-NH_2 from a lysine or hydroxylysine residue binds to the active site through LTQ, it becomes oxidized and it is then released while the LTQ is now in an "aminated" (reduced) state; in the second half of the reaction, the enzyme is reconstituted to its initial (oxidized) state [336,453]. The modified residue possesses now an aldehyde group and it is known as allysine or hydroxyallysine depending on whether the oxidized residue was lysine or hydroxylysine, respectively. The modified residue can then react with another modified residue (aldol condensation) or with an unmodified residue to form a Schiff base, which can undergo Amadori rearrangement leading to a ketoimine. Divalent crosslinks further react with single residues to form pyrroles and pyridinolines mature trivalent crosslinks in collagen, or tetravalent desmosine and isodesmosine in elastin; both divalent and more complex crosslinks coexist both in collagen [24] (Figure 20a) and elastin [454] (Figure 20b).

Crosslinking of fibrillar collagens is essential for their structural role [455] and, interestingly, collagen in tough tissues displays great content in trifunctional crosslinks [455], suggesting a mechanical role for multivalent crosslinks also assumed for desmosines in elastin. Thus, LOX-catalyzed crosslinking is likely to be essential in determining the mechanical performance of elastic tissues such as blood vessels.

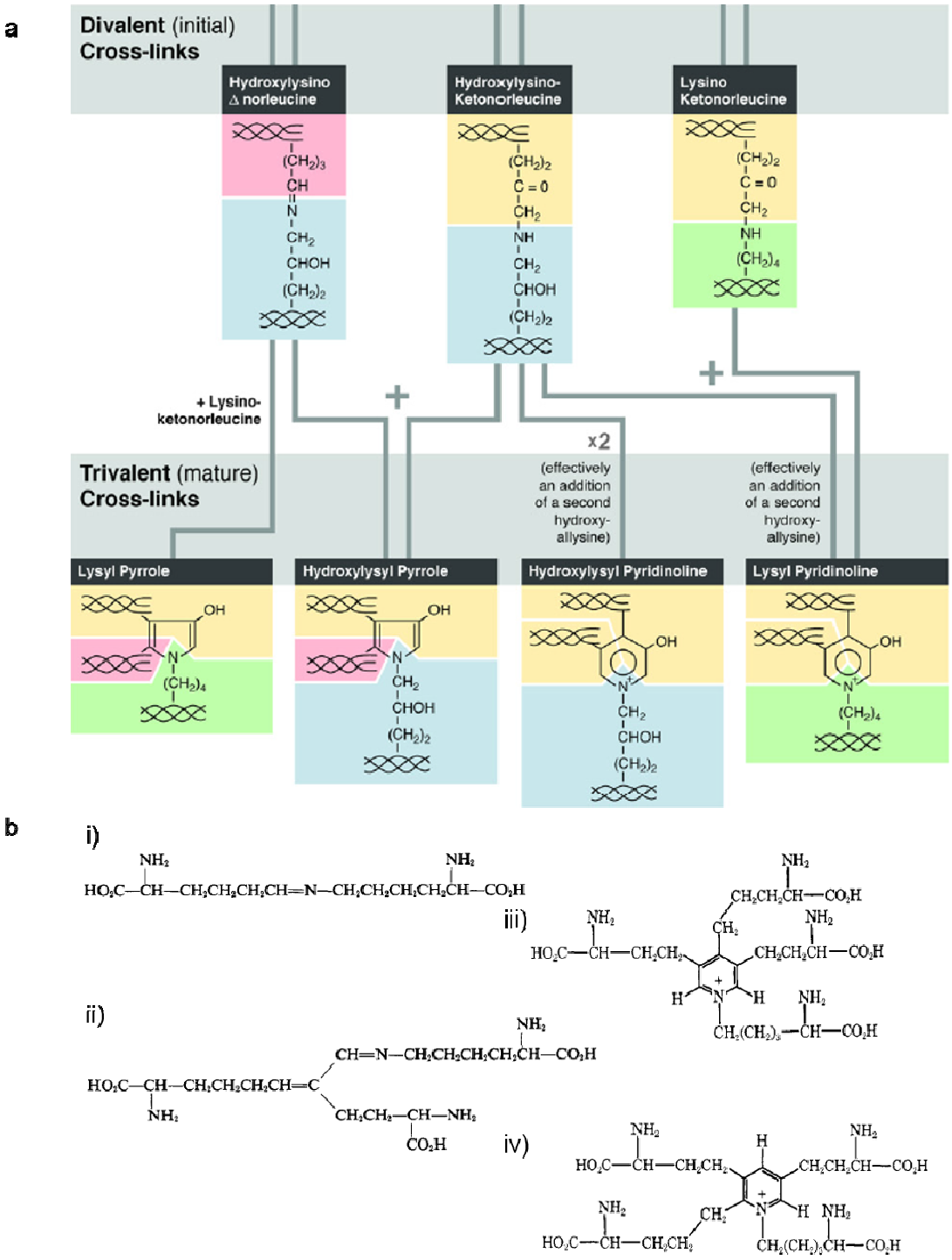

Figure 20. LOX-catalyzed crosslinks in collagen and elastin. a) Divalent and mature crosslinks found in collagen; adapted from [455]. c) Main crosslinking products found in elastin; i) lisinonorleucine, ii) merodesmosine (precursor for desmosines [456]), iii) demosine, and iv) isodesmosine; Adapted from [457].

1.5.2 Factors affecting LOX activity

During decades, scientists have been intrigued as to the capacity of LOX to crosslink both elastin and collagen despite sequences contiguous to lysine residues are quite different in both proteins [458]. Early studies on the specificity of the enzyme showed it is active against short aliphatic diamines, but its activity seemed to be limited in these conditions, given that short compounds would end up inactivating the enzyme [459], especially when two lysine residues are close to each other [460,461]. In the case of elastin, positively-charged residues close to lysine residues would permit a proper interaction between the substrate and the active site (it would be acidic, just like the protein itself [458]) for oxidative deamination to take place. Globally, the net charge of the substrate would have also an effect on LOX activity, showed to be boosted when the substrate to crosslink has an isoelectric point (pI) higher than 8 [458]. However, the most important parameter seems to be the side chain volume of those amino acids flanking lysine residues: the more voluminous the side chain, the lower the oxidation rate [458,461]. This is consistent with the fact that lysine residues in tropoelastin are commonly located in domains rich in alanine (i.e. crosslinking domains) [462], the amino acid with the second shortest side chain. Interestingly, this parameter not only affects reaction kinetics, but it has also an effect on the type of crosslink generated during the reaction. Residues with voluminous side chain are commonly found contiguous to –KAAK- domains, which would prevent the oxidation of the closest lysine; -KAAAK- domains are generally flanked by alanine residues so lysines can be effectively oxidized [454] (Figure 21). Additionally, the three-dimensional configuration of the substrate plays a role in determining the type of crosslink generated. For example, desmosine and isodesmosine are formed exclusively when the protein is in a coiled state so –KAAK- and –KAAAK- sequences are close to each other. Elastin also contains –KP- domains, where lysine is spaced by one or more proline residues [463], which are not involved in the formation of tetravalent crosslinks. To sum up, LOX activity is affected by the length, sequence, charge and spatial configuration of the substrate.

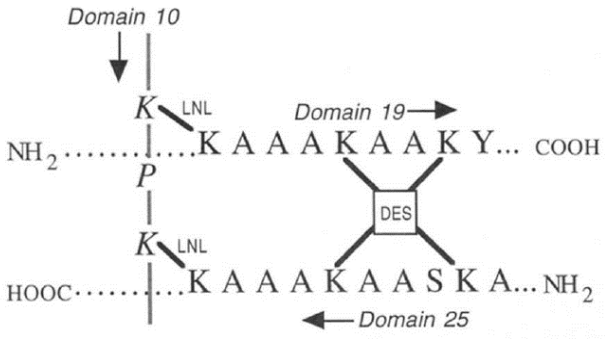

Figure 21. Crosslinks occurring in domains 10, 19 and 25 in coiled tropoelastin. From [454].

1.5.3 LOX and ELPs

Using collagen [425] and tropoelastin [464], scientist have demonstrated that these proteins are crosslinked with maximum efficiency when aggregated in the form of fibrillary collagen and coacervated elastin. In the case of tropoelastin, coacervation would be required for a proper alignment of molecules [465]. Kagan and co-workers investigated the specificity of the enzyme for ELPs poly(X-Pro-Gly-Gly), poly(Val-Pro-Gly-X-Gly) and poly(Ala-Pro-Gly-X-Gly-Val), where X is valine or lysine, and the valine-to-lysine ratio is 4:1 [466]. When incubating the polypeptides with purified LOX, they detected the formation of allysyl residues in all cases, but crosslinks were just found in the case of the pentapeptide-based polymer, which was thought to be due to differences regarding their capacity to coacervate. When repeating the experiment with the poly(VPGXG) polymer at 55ºC, they found an increased formation of allysyl and crosslinking products. This would be due to a displaced equilibrium favoring the coacervated form of the polymer and thus the intra- and interchain interactions. Additionally, the authors of the study concluded that the pentapeptide most of modern ELPs are based on would possess a proper hydrophobicity to allow enzyme-polymer interactions and crosslinking to take place. LOX-catalyzed crosslinking is thus an interesting strategy to design highly biomimetic hydrogels having (VPGXG)-based ELPs as raw materials.

ELPs-based polymeric matrices for tissue engineering have already been produced by enzymatic crosslinking [329,333,357]. However, these approaches are based on the use of transglutaminase, which catalyzes the formation of covalent bonds between lysine and glutamine residues in type II [467,468], type III B [469], and type V and IX [470]

collagens and for which no activity against elastin has been demonstrated in vivo. Up to date, just two studies have reported the successful use of LOX to insolubilize (i) ELPs when studying the specificity of the enzyme [466] and (ii) polymers based on adhesive proteins of mussel foot to study the adhesion mechanisms of these animals [461]. In the vascular tissue engineering field, vascular smooth muscle cells have been supplemented with hyaluronic acid and Cu^{2+} [471,472] or bovine LOX [473] in order to successfully increase the cellular deposition of insoluble elastin. To our knowledge, LOX has not yet been used to produce scaffolds for tissue engineering and is a novel method to produce scaffolds highly resembling the extracellular matrix of selected tissues.

Up to date, LOX has been mainly obtained and purified from animal sources such as bovine aorta [458–461,466,473–479], human placenta [480], mussel foot [461], bovine articular cartilage [475], bone from chick embryo [424], cartilage from chick embryo [481], piglet skin [482] and aorta from chick embryo [475]. Despite the protocols to obtain active LOX from animal tissues are quite established, especially using bovine aorta as a source, the purification process is complex and time-consuming and, additionally quantity and activity-related batch-to-batch issues are inherent. Given that the active form of the enzyme doesn't possess any post-translational modification (N-glycosilation is lost during proteolysis of the proenzyme), it is feasible to produce it in good yields using *Escherichia coli* as a bioreactor [483–485]. This would allow the in vitro use of the enzyme to produce nature-inspired scaffolds for tissue engineering.

1.6 CHALLENGES IN BONE TISSUE ENGINEERING

Global aging and the increased incidence of age-related pathologies are expected to lead to a rise in the number of fractures in the coming decades [131,132]. With allo and autografts being a gold standard, yet a limiting factor for the treatment of non-healing fractures [130], synthetic scaffolds making the most of the natural regenerative cascades and helping the body reconstruct the damaged tissue hold great promise. Fourth-generation (i.e. biomimetic) biomaterials aim to recapitulate the cellular events taking place during development by specifically stimulating stem and progenitor cells. With this purpose, the ECM is taken as a reference for the design and development of hydrogels for bone tissue engineering, which are now aimed to provide MSCs with complex combinations of signals to drive their differentiation towards osteogenic phenotypes.

In the last decades, much effort has been made to develop polymers with nature-inspired chemical motifs to create synthetic matrices. More recently, authors have demonstrated that physical cues such as stiffness and topography from the extracellular matrix also affect cell behavior [239,242]. However, scaffolds focusing on single signals, either chemical or physical, fail to reproduce the complex microenvironment surrounding cells, whose behavior depends on the integration of multiple specific signals. Despite scaffolds with such a complexity level are far from being available, great efforts are being made to develop matrices with increasing complexity and with a greater control of their particular parameters.

Early combinatorial studies have shown that cell behavior strongly depends on the synergistic effect of matrix parameters [246–248], evidencing that an exquisite scaffold design is required to induce the formation of native tissue. While much work has been done to achieve polymers with tailored chemistry, either by chemical/recombinant synthesis [306,307,486] or by functionalization [247], tailoring physical properties of hydrogels is still challenging.

Two of the most studied physical cell-instructing features are stiffness and structure. Stiffness has been successfully modified by adjusting the amount of crosslinker used to

prepare scaffolds [246,247]; structure is commonly tailored by means of techniques such as electrospinning or lithography, or by using chemical additives such as porogens. However, electrospinning and lithography usually suffer porosity [257] and thickness limitations [487], respectively, thus leading to scaffolds with tailored topography (2.5D) rather than tailored bulk structure (3D). The use of porogens is effective at creating matrices with open pores to allow cell colonization (and thus the formation of tissues in 3D) [348], but fail to provide cells with specific structural features. New strategies to tailor scaffold architecture are then required in order to produce hydrogels with increased complexity able to finely control cell behavior.

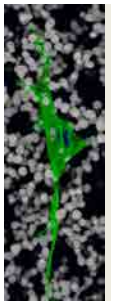

Aims

2.1 RATIONALE AND SPECIFIC AIMS OF THE THESIS

2.1.1 Rationale

In this thesis, we explore the usefulness of crosslinking as a tool to produce hydrogels with chemical and physical signals to induce the osteogenic differentiation of MSCs. With this purpose, two nature-inspired crosslinking methods have been considered for the production of cell-free scaffolds for in situ bone tissue engineering.

2.1.2 Specific aims

1. Selecting biologically-relevant molecules feasible to be used to crosslink elastin-like polymers into cyto and biocompatible scaffolds.

2. Developing and characterizing citric acid-crosslinked hydrogels with tailored physical properties.

3. Characterizing the in vitro and in vivo biological performance of citric acid-crosslinked hydrogels.

4. Producing, purifying and characterizing recombinant human lysyl oxidase for the production of hydrogels for tissue engineering.

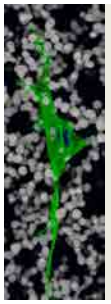

Chapter 2

2. FABRICATION OF TAILORED SCAFFOLDS FOR BONE TISSUE ENGINEERING

CHAPTER 2

PREFACE

This chapter represents the systematic study that allowed the design of citric acid-crosslinked hydrogels with cell-instructive features. After optimizing the generic chemical crosslinking reaction, the effect of specific reaction parameters on hydrogels properties was systematically assessed. Understanding and controlling the crosslinking reaction allowed the production of tailored structurally and mechanically-tailored hydrogels displaying functional groups for scaffold mineralization and peptide sequences available for cell adhesion.

3.1 MATERIALS AND METHODS

3.1.1 Elastin-like recombinamers (ELRs)

ELRs were provided by BIOFORGE group. Three different ELRs were used, all of them being based on the repetition of the VPGXG peptapeptide (Figure 22). HRGD6 polymer contains the RGD tripeptide and lysine residues for cell adhesion and crosslinking, respectively [304]; REDV polypeptide contains REDV for the adhesion of vascular cells, lysines for crosslinking and VGVAPG, the target sequence for elastase [306]; IK24 ELR contains crosslinking residues [488].

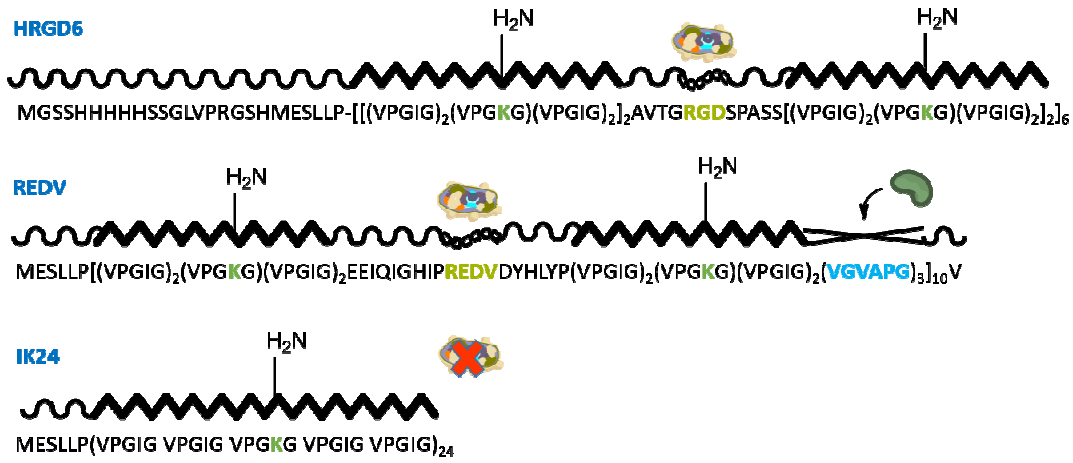

Figure 22. Schematic representation of HRGD6, REDV and IK24 ELRs. Light green: cell adhesion sequences; light blue: target sequence for elastase; green: crosslinking residues.

3.1.2 Glutaraldehyde-crosslinked hydrogels

3.1.2.1 Sample preparation

40 mg/ml HRGD6-glutaraldehyde (from now on, HRGD6-glut) hydrogels were prepared at a 1:3 lysine:aldehyde group ratio. The polymer was dissolved in ultrapure water overnight at 4ºC and mixed with 5% glutaraldehyde in ultrapure water at a 1:1 volume ratio. Reaction mixes were vortexed thoroughly, dispensed on 6-mm polydimethylsiloxane (PDMS; Sylgard 184 Elastomer kit, Dow Corning) molds and let to react for 7:30 at 4ºC. Then, unreacted aldehydes were reduced by incubating hydrogels on ice for 2 h with 1%

$NaBH_4$ in phosphate-buffered saline (PBS), and washed several times with PBS. 54 mg/ml HRGD6 samples (RGD-G) were prepared as abovementioned, reduced on ice with 5% $NaBH_4$ in PBS for 2 hours, and thoroughly washed with PBS.

3.1.2.2 Autofluorescence: selection of candidate chemical treatments

HRGD6-glut hydrogels were prepared as previously stated (but not reduced with $NaBH_4$) and assessed for nonspecific fluorescence. Samples for the reduction of autofluorescence were also prepared as abovementioned and subjected to six candidate chemical treatments (Table 4).

Treatment	Function	Reference
$NaBH_4$	Reduction of aldehydes and Schiff bases	[489,490]
NH_4Cl	Blockage of aldehydes	[491]
Glycine	Blockage of aldehydes	[489]
Schiff's reagent + $NaBH_4$	Blockage of aldehydes+quenching of fluorescence	[492]
Trypan blue	Quenching of fluorescence	[493]
Toluidine blue	Quenching of fluorescence	[494]

Table 4. Treatments used to reduce autofluorescence.

Toluidine blue (TolB), trypan blue (TryB), NH_4Cl and glycine treatments consisted on incubating samples with 0.1% TolB in PBS, 0.4% TryB (Sigma) or 50 mM NH_4Cl in PBS, respectively, for 3h at RT. After incubation, samples were washed several times with PBS. $NaBH_4$ treatment consisted on incubating hydrogels with 0.1% $NaBH_4$ in PBS for 2 h on ice. Samples were then washed several times with PBS. Schiff's reagent + $NaBH_4$ treatment consisted on incubating hydrogels with Schiff's reagent (Sigma) for 3h at RT. Samples were then washed for 5 minutes 3 times with sulfurous water (5 ml 10% $Na_2S_2O_5$ in ultrapure water + 5 ml HCl + 100 ml ultrapure water for a final volume of 110 ml) and subjected to $NaBH_4$ treatment as previously stated. Control (untreated) samples were crosslinked and washed several times with PBS.

To qualitatively assess the effect of chemical treatments, treated and untreated samples were visualized under an Eclipse TE200 inverted microscope (Nikon, Japan) and MetaMorph Microscopy Automation & Image Analysis Software (Molecular Devices, version 5.0r1). A 4x objective, a gain of 2 and a binning of 1x1 were used; images in blue,

green and red channels were acquired with 150 ms, 100 ms and 50 ms exposure, respectively. To assess the emission spectra of treated and untreated samples, hydrogels were placed on glass slides and visualized under a Leica TCS SP5 confocal microscope (Leica, Germany) and LAS-AF software (Leica; version 2.4.1 build 6384) in xyλ mode. Hydrogels were excited with different laser lines and emission was recorded with wavelength increases of 7 nm, a pinhole of 53.1 µm (1 airy unit) and a constant gain. Excitation and emission wavelengths are summarized in Table 5.

Excitation wavelength	Emission wavelength
405 nm	415-695 nm
458 nm	465-699 nm
488 nm	495-792 nm
514 nm	520-789 nm
561 nm	570-797 nm
633 nm	640-797 nm

Table 5. Summary of excitation and emission wavelengths used to study the effect of chemical treatments on hydrogel autofluorescence.

3.1.2.3 Optimization of candidate chemical treatments to reduce autofluorescence

HRGD6-glut hydrogels were prepared as previously stated in 16-well Lab-Tek glass chamber slides (Nunc) and tested for the effect of toluidine blue and trypan blue treatments before cell seeding (post-treatment seeding) and after cell staining (pre-treatment seeding). In both cases, samples were incubated with either toluidine blue or trypan blue for 3 hours at RT; pre-seeding treatment samples were washed until no apparent dye release was noticed; post-treatment seeding samples were washed to remove excess dye limiting light exposure in order to avoid the bleaching of specific fluorescence. Rat MSCs (rMSCs) were cultured in 75 cm^2 flasks at 37°C in a 5% CO_2 atmosphere. Cell expansion was carried out in complete medium: AdvDMEM (Gibco) supplemented with 15% FBS (Gibco), 2 mM L-glutamine (Gibco), 100 U/ml Penicillin and 100 µg/ml Streptomycin (Gibco). Cells were detached at a confluence of about 80% with Tryp-LE Express (Gibco) and the number of viable cells was determined after staining with Trypan blue. $2.5 \cdot 10^3$ viable cells were seeded on each sample and kept in culture for 24 hours. Samples were then treated with fixative solution (3% paraformaldehyde and 40 mM sucrose in PBS) for 10 minutes at 4°C, washed three times with cold 0.15% glycine in

PBS (PBS-gly), permeabilized with 0.1% Triton X-100 (Sigma-Aldrich) for 5 minutes and stained with 4 μg/ml 4′,6-Diamidino-2-phenylindole dihydrochloride (DAPI; Sigma) for 2 minutes for nuclei observation. Samples were visualized under an Eclipse TE200 inverted microscope by using MetaMorph software.

3.1.3 Citric acid-crosslinked hydrogels

3.1.3.1 Reaction setup

3.1.3.1.1 *Reaction optimization*

As previously mentioned, the dielectric constant (ε) of the solvent can affect the route through which the carbodiimide-catalyzed reaction evolves. Thus, the suitability of using different solvents was assessed by testing the solubility of citric acid (11.8 mM), IK24 ELR (80 mg/ml), NHS (76.95 mM) and EDC (192.38 mM) in N-hexane (Panreac), diethyl ether (Aldrich), tetrahydrofuran (Sigma), 96% ethanol (Panreac), 8:2 ethanol:water, and 2-(N-Morpholino)ethanesulfonic acid (MES, Sigma) buffer.

To test the effect of the pH of reaction mixes on crosslinking occurrence, different samples were prepared. IK24 polymer was dissolved in 0.109 M MES buffer containing citric acid; EDC and NHS were independently dissolved in MES buffer. Citric acid-IK24, EDC and NHS solutions were mixed at 1:1:1 volume ratio (polymer concentration: 26.7 mg/ml) at a constant 2:2:1 EDC:NHS:COOH molar ratio and 1:1.06, 1:3.25, 1:5.44 and 1:9.3 NH_2:COOH molar ratios to produce 1:1, 1:3, 1:5 and 1:10 samples, respectively. Reaction mixes with adjusted and non-adjusted pH were incubated at 37ºC for 2 h and assessed for gelation occurrence. Additionally, samples 1:1 were prepared at a 2:-:1 EDC:NHS:COOH molar ratio (NHS was substituted by MES buffer) to assess whether EDC alone could lead to crosslinking. The pH of all reaction mixes was measured by properly mixing all reagents except IK24 polymer, assumed not to contribute to the pH of the solution.

To test the effect of polymer concentration on hydrogel consistency, IK24 hydrogels were prepared at EDC:COOH 1.88:1 and COOH:NH_2 1:1 molar ratios in MES buffer. 26.7 mg/ml samples were prepared by mixing citrate-polymer, EDC, and MES solutions at a 1:1:1 volume ratio; 40 mg/ml samples were prepared by mixing citrate-polymer and EDC

solutions at a 1:1 volume ratio. pH was adjusted to ca. 6 and reaction mixes were incubated at 37ºC for 2 hours.

In order to check whether the crosslinking method developed with IK24 could be applied to HRGD6 polymer, 40 mg/ml IK24 and HRGD6 hydrogels at EDC:COOH 3.33:1 and COOH:NH_2 1:1 molar ratios were prepared. Polymers were independently dissolved in citrate-containing MES buffer at 4ºC and mixed with EDC solutions. pH was adjusted to ca. 6 and reaction mixes were incubated at 37ºC for 2 hours.

The pH evolution of selected samples was monitored to make sure that reaction mixes are properly buffered to keep a crosslinking-permissive pH during the reaction. HRGD6 polymer, citric acid and EDC were mixed in a microtube to achieve reaction mixes with a 40 mg/ml polymer concentration, and EDC:COOH 9.3:1 and COOH:NH_2 3.25:1 molar ratios in MES buffer. pH was adjusted to ≈ 6 and the microtube tube was partially immersed in a jacketed water bath at 37ºC. pH was monitored using a Crison 50 28 microelectrode and a Crison GLP 22+ pHmeter (Crison, Spain).

To check whether REDV, an ELR containing a high number of acidic residues, is feasible to be crosslinked by means of herein developed reaction, REDV was assessed for crosslinking in the absence of citric acid. Thus, REDV was dissolved in MES buffer and mixed with EDC solutions to achieve reactions mixes with 1:1, 2:1 and 3:1 EDC:COOH molar ratio and a 2.48:1 COOH:NH_2 molar ratio at a 40 mg/ml polymer concentration and pH ≈ 6.

3.1.3.1.2 *Effect of acid/base temperature*

To test the effect of the temperature of the acid/base used to adjust pH on the kinetic variability of crosslinking, HRGD6 polymer, citric acid and EDC were mixed to achieve reaction mixes with a 40 mg/ml polymer concentration, and EDC:COOH 9.3:1 and COOH:NH_2 3.25:1 molar ratios in MES buffer. pH was adjusted to ≈ 6 with HCl either at 4ºC or RT and reaction mixes were poured into 96-well plates at RT. Absorbance evolution was recorded at 37°C and λ=750 nm for 62.5 minutes using an Infinite M200 Pro multimode reader and i-control software (Tecan, Switzerland), and collected data were treated with Origin (OriginLab, version 8.0724). Four kinetic parameters were analyzed:

(i) latency time (i.e. the time lapse between the beginning of the incubation and the initial increase in turbidity), (ii) reaction length (i.e. the time lapse between the onset of variations in turbidity and the time by which dAbs/dt returns to basal levels), (iii) maximum velocity (Vmax, max dAbs/dt), and (iv) maximum absorbance (Amax). Latency time, reaction length and Vmax were obtaining by using the Spectroscopy Peak Analyzer tool in Origin after performing mathematical derivation of the absorbance data.

3.1.3.1.3 *Effect of substrate temperature*

To test the effect of the temperature of the substrate on the kinetic variability of crosslinking, reaction mixes with a 40 mg/ml polymer concentration, and EDC:COOH 9.3:1 and COOH:NH_2 3.25:1 molar ratios in MES buffer were prepared. pH was adjusted to ≈ 6 and reaction mixes were poured into 96-well plates at either 4ºC, RT or 37ºC. The absorbance evolution was recorded and kinetic parameters were obtained as previously stated.

3.1.3.1.4 *Autofluorescence of citric acid-crosslinked hydrogels*

40 mg/ml HRGD6 hydrogels were prepared at EDC:COOH 1.88:1, COOH:NH_2 2.16:1.06 molar ratios (pH ≈ 6) and washed with PBS to remove excess reagents. Autofluorescence was visually assessed under an Eclipse TE200 inverted microscope using MetaMorph software and emission spectra were acquired using a Leica TCS SP5 confocal microscope as previously stated.

To test the effect of trypan blue on reducing the autofluorescence of citric acid-crosslinked hydrogels, samples were prepared as abovementioned and incubated with 0.4% trypan blue for 3 h at RT. Hydrogels were thoroughly washed until no apparent dye release was noticed, sterilized with 70% ethanol under UV irradiation for 1 hour and washed several times with PBS. $5 \cdot 10^3$ rMSCs were seeded on samples, which were kept in culture for 24 hours. Cells were fixed and permeabilized as previously stated and stained with Acti-Stain 488 phalloidin (Cytoskeleton) in the conditions suggested by the manufacturer, and with 4 μg/ml DAPI for 2 minutes. Hydrogels were then mounted with Mowiol 40-88 (Sigma-Aldrich), sealed with nailpolish and observed by confocal microscopy with a stepsize of 670 nm and a pinhole of 1 airy unit.

3.1.3.2 Effect of molar ratios on hydrogels properties

3.1.3.2.1 *Sample preparation*

HRGD6 polymer was crosslinked with citric acid through an EDC-catalyzed reaction in 0.109 M MES buffer. Seven different hydrogels, each one characterized by a particular combination of EDC:COOH and COOH:NH_2 molar ratios, were prepared (Table 6). Setups were encoded in the form EXCY, where EX denotes the molar excess (X) of EDC with respect to –COOH groups and CY denotes the molar excess (Y) of -COOH with respect to -NH_2 groups. In all cases, HRGD6 polymer was dissolved overnight at 4ºC in MES buffer containing citric acid monohydrate; similarly, EDC was dissolved overnight at 4ºC in MES buffer. Polymer-citrate and EDC solutions were mixed at a 1:1 volume ratio (polymer concentration: 40 mg/ml) and pH was adjusted to ≈ 6 by adding cold NaOH or HCl. Crosslinking reactions were carried out at 37°C for 1 h on substrates at RT and stopped by incubation with 0.1 M Na_2HPO_4 at room temperature for 3 hours. Samples were then washed by performing 5 swelling/shrinking incubation cycles in ultrapure water at 4°C (swelling)/37°C (shrinking) to allow excess EDC and reaction by-products to be released.

Code	EDC:COOH	COOH:NH_2
E2C1	1.88:1	1.06:1
E3C1	2.82:1	1.06:1
E5C1	4.7:1	1.06:1
E9C1	9.3:1	1.06:1
E9C2	9.3:1	2.16:1
E9C3	9.3:1	3.25:1
E9C5	9.3:1	5.44:1

Table 6. Summary of the conditions used to prepare citric acid-crosslinked hydrogels.

3.1.3.2.2 *Gelification and kinetics*

Reaction mixes for all seven different hydrogels were prepared as abovementioned and poured into 96-well plates. Absorbance evolution was monitored at 37ºC and kinetic parameters were quantified as previously mentioned.

3.1.3.2.3 *Unreacted –NH_2 groups*

Hydrogels were prepared in 96-well plates and incubated with 100 µl of a 10.55 mM 2,4,6,-trinitrobenzenesulfonic acid (TNBS, Sigma) solution in 9:1 0.1 M $NaHCO_3$:0.1 M Na_2CO_3 (pH 8.93) in the dark at 4°C with gentle stirring for 30 hours. 200 µl of 6 M HCl were added to completely hydrolyze samples over a 75 hours period and resulting solutions were diluted 1/10 in ultrapure water. Absorbance was read at λ=342 nm and glycine was used to prepare standard curves to stoichiometrically quantify unreacted primary amines.

3.1.3.2.4 *Swelling*

Hydrogels were prepared on PDMS films and incubated consecutively in ultrapure water at 37°C, room temperature and 4°C for 24 hours. Following each incubation, excess water was carefully blotted and samples were weighted. Hydrogels were finally dried at 37ºC and weighted again. Swelling ratio, weight increase percentage due to water absorption, is defined by

$$\text{Swelling ratio (\%)} = \left(\frac{Ws - Wd}{Wd}\right) \cdot 100$$

where W_s and W_d correspond to weight in the swollen and dried states, respectively.

3.1.3.2.5 *Thermal stability*

Hydrogels were prepared on PDMS molds with 6 mm-diameter holes, dried at 37°C and analyzed by thermogravimetry with a TGA/DSC1-Star system thermobalance (Mettler-Toledo, Switzerland). Measurements were performed in a nitrogen atmosphere (50 cm^3/min) from 40°C to 800°C at a heating rate of 5°C/min.

3.1.3.2.6 *Resistance to enzymatic degradation*

A pilot study was performed to adjust the enzyme concentration to be used on degradation experiments. Briefly, E9C5 hydrogels were prepared in 96-well plates and incubated with $4.7 \cdot 10^{-1}$, $4.7 \cdot 10^{-2}$, $4.7 \cdot 10^{-3}$ and $4.7 \cdot 10^{-4}$ U/ml porcine pancreatic elastase (Worthington Biochemical Corporation), corresponding to 100 µg/ml, 10 µg/ml, 1 µg/ml and 0.1 µg/ml, respectively, in PBS for 1 h at 37ºC under agitation. This concentrations were selected as

consulted studies used the protein at concentrations in the 0.1 µg/ml – 300 µg/ml range [495–497]. Absorbance evolution at 750 nm was recorded as previously stated.

After optimizing enzyme concentration, E2C1, E9C1 and E9C5 setups were selected to simplify the degradation study. Hydrogels were prepared in 96-well plates and incubated with $2.82 \cdot 10^{-3}$ U/ml porcine pancreatic elastase in PBS at 37ºC for 1, 3 and 7 days. Hydrogels not exposed to elastase were used to set sample weight at day 0. At every time point, samples were washed with ultrapure water, dried at 37ºC and weighted.

3.1.3.2.7 *Structure*

Samples to be assessed by confocal microscopy were prepared on 16-well glass chamber slides and stained with 0.4% Trypan blue for 3 hours at room temperature. Several washing steps with PBS were performed until no apparent dye release was noticed. Hydrogels were fixed as previously mentioned, mounted with Mowiol 40-88 (Sigma-Aldrich) and sealed with nailpolish. Images were adquired at an emission wavelength range of 579-657 nm and a stepsize of 80 nm by using a TCS SP5 confocal microscope and LAS-AF software. The size of polymer aggregates was measured with Fiji [498].

Hydrogels to be observed by Field Emission Scanning Electron Microscopy (FESEM) were prepared in PDMS molds, washed with water several times to remove salts, lyophilized and sputtered with graphite. FESEM images were obtained by using a NOVA NANOSEM 230 microscope (FEI, United States) at a 3.00 kV voltage and 5.2 mm working distance.

3.1.3.2.8 *Percentage polymer-occupied volume*

Sections obtained by confocal microscopy were used to quantify PV/TV (Polymer volume fraction; i.e. polymer-occupied volume/total volume). PV/TV was quantified with Volume Fraction tool (BoneJ [499] plugin v.1.3.11 for Fiji) using the surface algorithm with a surface resampling value of 2 and a specific threshold for each set of images. 3D reconstructions of quantified volumes were analyzed to assess volume calculations were performed using proper thresholding.

3.1.3.2.9 *Surface stiffness*

All seven different hydrogels were prepared as previously stated to test the effect of molar ratios on surface stiffness. All samples were prepared in 6 mm-diameter PDMS molds and kept in PBS at 37°C until use. Molds were mounted on glass slides using double-sided tape and ten force curves per sample were acquired in Force Mode using IGOR Pro sofware (Wavemetrics, version 6.2.2.2A) and a MFP-3D stand alone unit (Asylum Research, United States). Measurements were made in PBS at 37°C using chromium and gold-coated, pyramidal silicon nitride cantilevers (NanoWorld) with a nominal spring constant of 0.08 N/nm and assuming Poisson's ratio to be 0.5. A custom-made script considering cone-shaped tip was used to calculate Young's modulus by means of Hertz model.

3.1.3.3 Effect of reaction conditions on hydrogels cytotoxicity and RGD integrity

3.1.3.3.1 *Cytotoxicity*

rMSCs were expanded as previously mentioned and 10^4 viable cells/well were seeded on 24-well plates and allowed to adhere for 4 hours. Non-adhered cells were washed out with PBS and attached cells were quantified with 10% Alamar blue (TREK Diagnostic Systems) in complete medium to verify homogenous adhesion in all wells. Cells were then washed with PBS and wells were subsequently replenished with complete medium.

Selected hydrogels were tested for cytotoxicity by indirect contact. Samples prepared in PDMS molds were sterilized with 70% ethanol under UV irradiation for 1 hour, washed thrice with PBS and kept in the buffer at 37°C until use. Polyethylene terephthalate (PET) Millicell Inserts (Millipore) with a 0.4 µm pore size were placed into wells and 300 µl of culture medium were added to each insert. Hydrogels were then washed twice with PBS to remove remaining ethanol and transferred to inserts. Negative controls (TCPS) consisted on inserts containing just complete medium; positive controls consisted on the use of complete medium supplemented with 1% phenol (Sigma-Aldrich) in both the wells and the inserts.

After a 42.5 hours incubation period at 37°C and 5% CO_2, cytotoxicity by indirect contact was assessed by cell quantification with Alamar blue and cell morphology examination. For cell shape visualization, cells were washed with DPBS (Gibco), stained in the dark

with 2 µM Calcein AM (Sigma-Aldrich) for 20 minutes at 37°C and washed with the buffer to remove excess dye. Images were acquired using an Eclipse TE200 inverted microscope and MetaMorph Microscopy Automation & Image Analysis Software.

3.1.3.3.2 *Cell adhesion*

Samples were prepared on 16-well Lab-Tek glass chamber slides, stained with Trypan blue and washed until no apparent dye release was noticed. rMSCs were expanded as previously stated, seeded at a final density of $2.5 \cdot 10^3$ viable cells/sample and kept in complete medium for 24 hours. Samples were fixed with paraformaldehyde, permeabilized with 0.1% Triton X-100 (Sigma-Aldrich) for 5 minutes, blocked with PBS-gly supplemented with 6% bovine serum albumin (BSA; Sigma) for 45 minutes and stained in the dark at room temperature for vinculin and nuclei observation. Briefly, cell staining consisted on: (i) incubation with mouse anti-vinculin primary antibody (Sigma) at a 1/400 dilution in PBS-gly supplemented with 3% BSA (PBS-gly-BSA 3%) for 1h, (ii) incubation with Alexa 488-conjugated goat anti-mouse secondary antibody (Molecular Probes) at a 1/300 dilution in PBS-gly-BSA 3% for 1h, and (iii) incubation with 4 µg/ml DAPI (Sigma) for 2 minutes. Hydrogels were then mounted, sealed and observed by confocal microscopy. Volocity 3D Image Analysis Software (Pelkin Elmer, version 6.2.1) was used to obtain 3D reconstructions.

3.1.3.4 Design and characterization of tailored hydrogels

3.1.3.4.1 *Surface stiffness*

An EDC:COOH 9.3:1, COOH:NH_2 1.06:1 combination of molar ratios was selected to test the influence of polymer concentration on stiffness. Samples were prepared at 40, 54, 80 and 160 mg/ml polymer concentrations and stiffness was quantified as previously stated.

3.1.3.4.2 *Structure of mechanically-tailored hydrogels*

Hydrogels were prepared at a polymer concentration of 54 mg/ml using the EDC:COOH 9.3:1, COOH:NH_2 1.06:1 combination of molar ratios (from now on, RGD-C samples), incubated with 0.1 M Na_2HPO_4 for 3h at RT and washed with PBS by performing swelling/shrinking cycles. Samples to be observed by confocal microscopy were stained with Trypan blue, and mounted and visualized as previously stated. Hydrogels to be

visualized by FESEM were subjected to serial dehydration in ethanol and critical point drying with CO_2. A voltage of 5 kV and a working distance of 6 mm were used to acquire images. The diameter of polymeric trabeculae was quantified using Fiji.

3.1.3.4.3 *In vitro mineralization*

To assess citrate-related calcium phosphate nucleation capacity, citric acid-crosslinked hydrogels with tailored stiffness (RGD-C) were compared to samples crosslinked with glutaraldehyde (RGD-G). RGD-C and RGD-G hydrogels were prepared as previously stated in 6 mm-diameter PDMS molds and thoroughly washed to remove remaining reagents, by-products and salts.

Simulated body fluids (SBF) were prepared as specified in the literature [500]. Samples were incubated with filtered, pre-warmed SBF at 37ºC for 1, 7, 14 and 28 days; SBF was replaced every 3 days. At endpoints, hydrogels were washed 3 times with ultrapure water and kept at 37ºC until the end of the experiment.

RGD-C samples were subjected to serial dehydration in ethanol and critical point drying with CO_2; RGD-G samples were frozen with liquid N_2 and lyophilized for two days. Hydrogels were then graphite-sputtered and analyzed using a Quanta 200 Scanning Electron Microscope (SEM; FEI) equipped with a Genesis Energy Dispersive X-Ray Spectroscope (EDS) system (EDAX, United States). A voltage of 20 kV and a working distance of 10 mm were used.

3.1.3.4.4 *Statistical analysis*

Data were analyzed by means of t-test or one-way ANOVA with Dunnett's post hoc test. All analyses were performed using Prism (GraphPad, version 6.01). Results were considered significant when $p \leq 0.05$ unless otherwise specified.

3.2 RESULTS

3.2.1 Glutaraldehyde-crosslinked hydrogels

3.2.1.1 Autofluorescence: selection of candidate chemical treatments

Collagen and elastin are known to possess autofluorescence [501,502], and this phenomenon is thought to stem from Schiff bases in the crosslinks present in these structural proteins [503–505]. Schiff bases are also considered to be behind the autofluorescence induced by glutaraldehyde upon reaction with primary amines [490,505]. Thus, in the case of glutaraldehyde-crosslinked ELRs hydrogels, treatments aiming to reduce Schiff bases, to block unreacted aldehyde groups to prevent them from leading to newly-formed Schiff bases or to unselectively quench fluorescence are potentially useful to reduce background signal.

Fluorescence microscopy revealed that aldehyde-blocking treatments (glycine and NH_4Cl) didn't substantially reduce autofluorescence (Figure 23d-f and j-l). $NaBH_4$ led to reduced signal in the green (ca. 495-570 nm) and red (ca. 620-750 nm) channels (Figure 23g-i), while $NaBH_4$ and Schiff's reagent led to globally reduced fluorescence (Figure 23m-o). Toluidine blue almost completely suppressed autofluorescence in all three channels (Figure 23p-r), while trypan blue suppressed signal in blue and green channels and reduced it in the red channel (Figure 23s-u).

Lambda scans showed that all treatments led to reduced intensity in the blue (ca. 450-495 nm) and green channels; emission in the red channel was at least slightly reduced by all treatments (Figure 24). Aldehyde-blocking reagents, glycine and NH_4Cl, led to preferentially reduced signal in the blue and green channels (Figure 24b and d), while the reduction of Schiff bases mainly led to reduced signal in the red channel (Figure 24c), although a decreased signal in blue and green was also noticed. Interestingly, combining aldehyde blockage and Schiff base reduction led to reduced signal in all three channels (Figure 24e). Fluorescence quenching suppressed the signal in blue and green channels and reduced fluorescence in the red channel (Figure 24f and g).

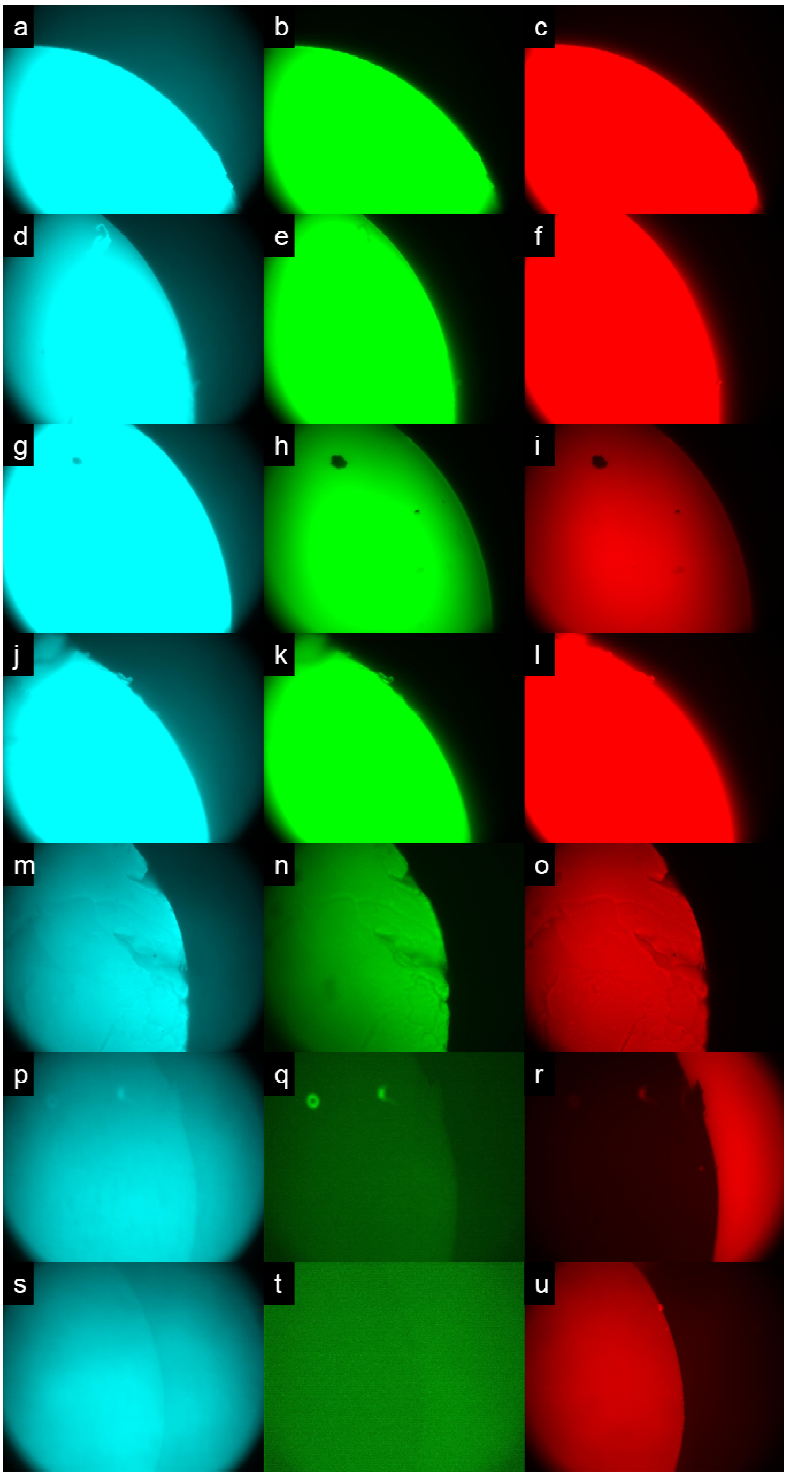

Figure 23. Gross autofluorescence of glutaraldehyde-crosslinked HRGD6 hydrogels. The signal in control hydrogels (a-c) was compared to that in samples treated with glycine (d-f), $NaBH_4$ (g-i), NH_4Cl (j-l), Schiff's reagent + NaBH4 (m-o), toluidine blue (p-r), trypan blue (s-u).

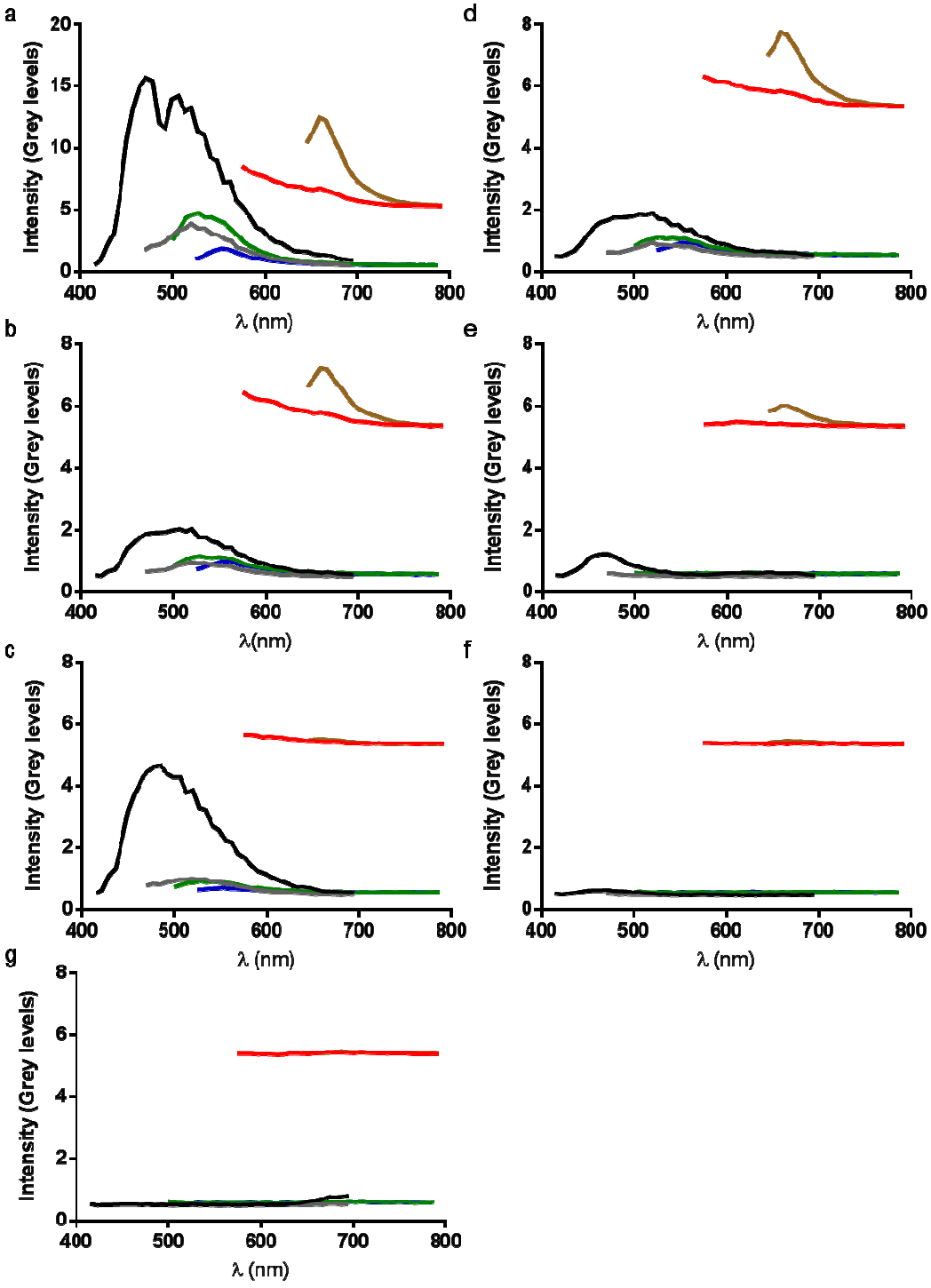

Figure 24. Emission spectra of glutaraldehyde-crosslinked hydrogels. Control hydrogels (a) and samples treated with glycine (b), $NaBH_4$ (c), NH_4Cl (d), Schiff's reagent + $NaBH_4$ (e), toluidine blue (f) and trypan blue (g) were excited at 405 nm (black), 458 nm (grey), 488 nm (green), 514 nm (blue), 561 nm (red) and 633 nm (brown) wavelengths.

3.2.1.2 Optimization of candidate chemical treatments to reduce autofluorescence

Toluidine blue and trypan blue were selected as candidate treatments to reduce nonspecific fluorescence. Given that both compounds are generic fluorescence quenchers and can potentially reduce specific fluorescence, the suitability of applying them prior to cell seeding and after cell staining with DAPI was studied. Toluidine blue didn't effectively reduced background fluorescence in any of the cases (Figure 25a and c). Although trypan blue in pre-treatment seeding improved the signal-to-noise ratio, the background signal remained quite high (Figure 25b). In contrast, when applied before cell seeding, trypan blue led to highly reduced background signal and allowed the proper visualization of cell nuclei (Figure 25d and e). Thus, trypan blue was selected to be used to reduce the autofluorescence of samples previous to cell seeding.

3.2.2 Citric acid-crosslinked hydrogels

3.2.2.1 Reaction setup

3.2.2.1.1 *Reaction optimization*

The solubility of the reagents of interest was assessed in several solvents. N-hexane and diethyl ether were discarded given that citric acid didn't dissolve in these solvents (Table 7); IK24 didn't dissolve in tetrahydrofuran nor in ethanol and partially dissolved in 8:2 ethanol:water, so these solvents were also discarded. All reagents dissolved in 0.109 M MES buffer, which was selected as the solvent for the crosslinking reaction.

Solvent	Citric acid	IK24	NHS	EDC	ε
N-hexane	No	-	-	-	1.88
Et_2O	No	-	-	-	4.3
THF	Yes	No	Yes	Yes	7.5
Ethanol	Yes	No	Yes	Yes	24.55
Ethanol:water 8:2	Yes	NC	Yes	Yes	?
0.109 M MES buffer	Yes	Yes	Yes	Yes	?

Table 7. Summary of reagent solubility in different solvents. Et_2O: diethyl ether; THF: tetrahydrofuran; NC: not completely.

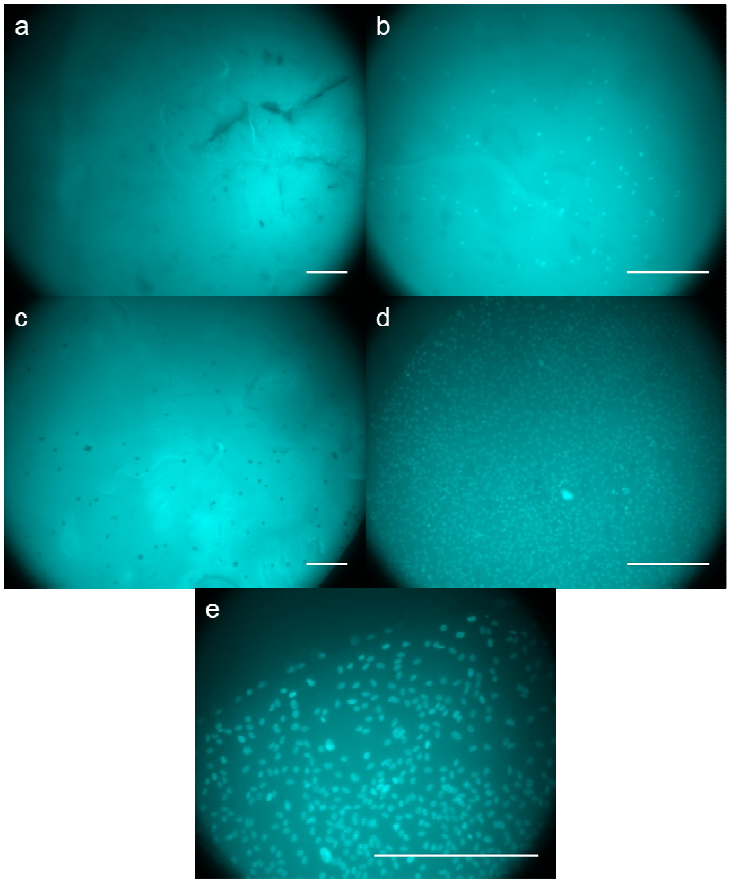

Figure 25. Assessment of candidate treatments for autofluorescence reduction. Toluidine blue (a and c) and trypan blue (b and d) were applied after cell nuclei staining (a and b) and before cell seeding (c and d). Cell nuclei were stained with DAPI. Scale bar: 100 µm.

When studying the effect of pH on crosslinking occurrence in the case of reaction mixes with non-adjusted pH, crosslinking was just achieved for 1:1 and 1:3 samples, which had pH 5.6 and pH 6.02, respectively (Figure 26a, i). 1:5 and 1:10 mixes just led to crosslinking after adjusting the initial pH down to ca. 5.8 (Figure 26a, ii). Interestingly, when the pH of 1:3 mixes was decreased to 5.7, obtained hydrogels displayed a decreased integrity. These results suggest that (i) a pH in the range of 5.6-6 is permissive for crosslinking of IK24 polymer with citric acid and that (ii) a pH of 6 would lead to hydrogels with improved consistency. When studying the effect of using EDC or EDC+NHS, both 1:1 reaction mixes prepared at 2:2:1 and 2:-:1 EDC:NHS:COOH molar ratios led to reticulation (Figure 26b), suggesting that EDC is sufficient to achieve crosslinking in herein used conditions (i.e. the reaction evolves through the route leading to amide bond formation).

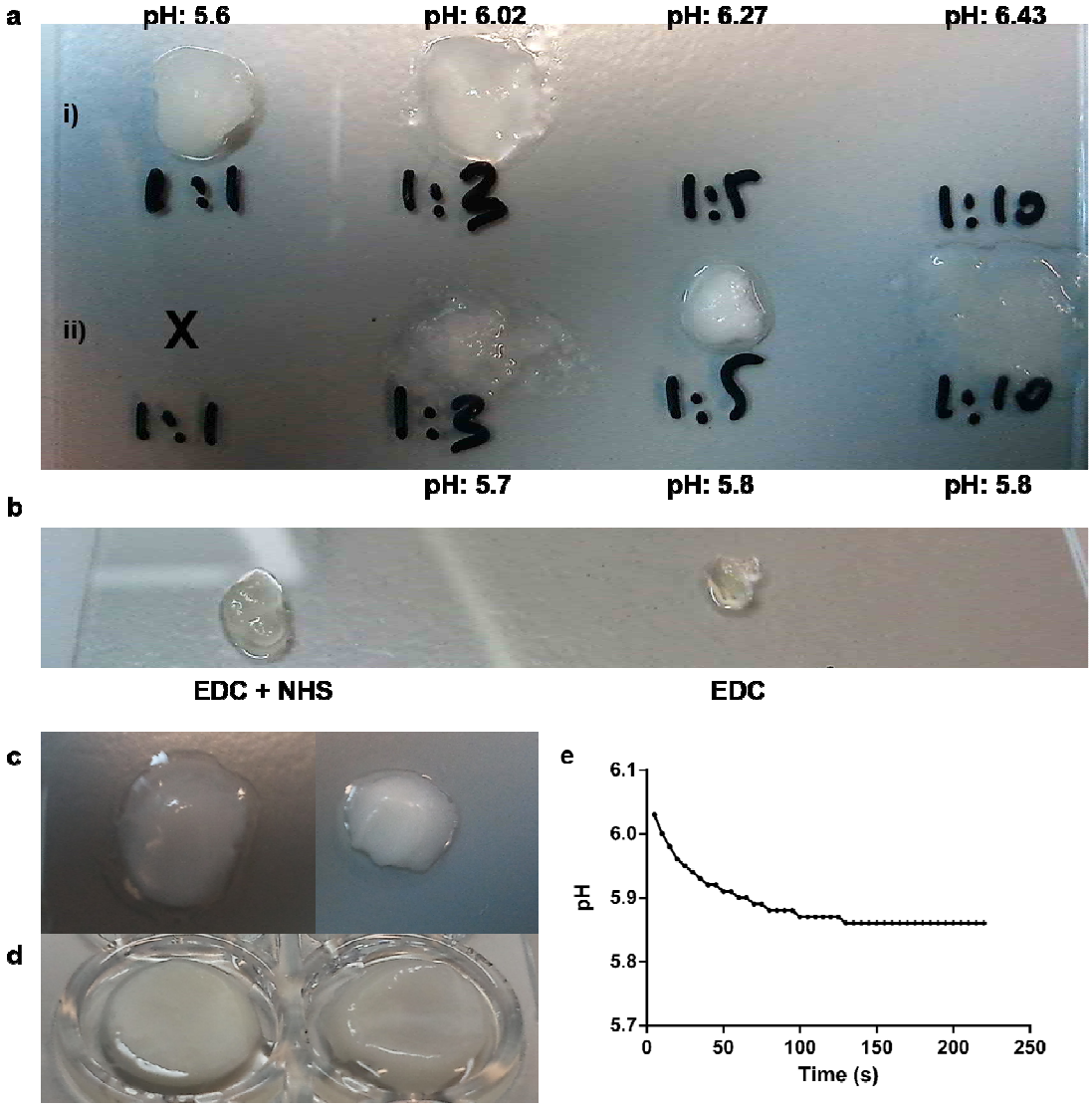

Figure 26. Summary of tests for crosslinking optimization. (a, i) Reaction mixes with non-adjusted pH; (a,ii) reaction mixes with adjusted pH. (b) Reaction mixes containing EDC+NHS or just EDC. (c) Hydrogels prepared at 26.7 mg/ml (left) and 40 mg/ml (right) IK24 concentrations. (d) IK24 (left) and HRD6 (right) hydrogels prepared at 40 mg/ml polymer concentration. (e) pH evolution during the gelation of 40 mg/ml HRGD6 hydrogels prepared at EDC:COOH 9.3:1 and COOH:NH_2 3.25:1 molar ratios.

The effect of increasing polymer concentration on hydrogel consistency was qualitatively assessed. A 40 mg/ml IK24 concentration led to hydrogels with increased consistency and easier to handle when compared to their 26.7 mg/ml counterparts (Figure 26c). The overall optimized conditions were proven useful to produce 40 mg/ml HRGD6 hydrogels (Figure 26d). In these conditions, the pH of the solution remained in a permissive range (pH 6.02-

5.85) during the crosslinking reaction (Figure 26e), which confirmed that MES buffer is a proper solvent to perform the herein optimized reaction.

Hydrogels were not achieved in the case of REDV polymer, which contains a high number of acidic residues and has a low ITT [306]. Even in the absence of citric acid and at low EDC:COOH molar ratios, the material rapidly precipitated upon mixing the reagents (the higher the EDC:COOH ratio, the faster the precipitation), so reaction mixes couldn't be properly homogenized nor dispensed into molds. In light of this phenomenon, REDV was discarded as a polymer to be crosslinked with citric acid and EDC.

3.2.2.1.2 *Effect of acid/base temperature*

The effect of the temperature of the acid/base used to adjust the pH of reaction mixes on the kinetic variability of crosslinking was studied. The pH of reaction mixes prepared at 4ºC was adjusted with HCl either at 4ºC or RT. When compared to mixes whose pH was adjusted with HCl at RT, those adjusted with the acid at 4ºC showed increased variability in the case of reaction length (Figure 27b). However, using HCl at 4ºC led to highly consistent latency time, Vmax and Amax values. In light of these results, solutions at 4ºC for pH adjustment were selected to be used ever since.

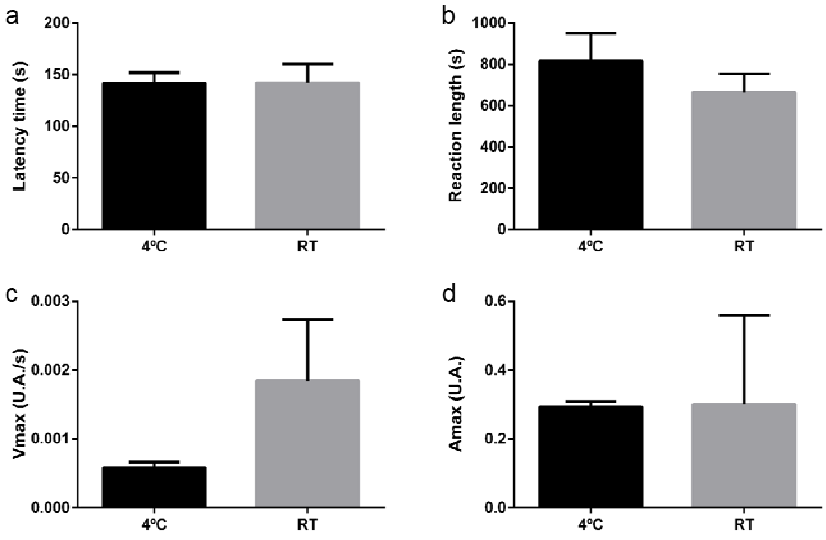

Figure 27. Effect of the temperature of acid/base on kinetic variability. (a) Latency time, (b) reaction length, (c) Vmax, and (d) Amax were studied.

3.2.2.1.3 *Effect of substrate temperature*

Reaction mixes prepared at 4ºC and poured into substrates at 4ºC, RT and 37ºC. Substrates at 37ºC led to considerable variability for all four kinetic parameters, while those at 4ºC and RT led to quite homogenous results (Figure 28). Substrates at RT were chosen for simplicity.

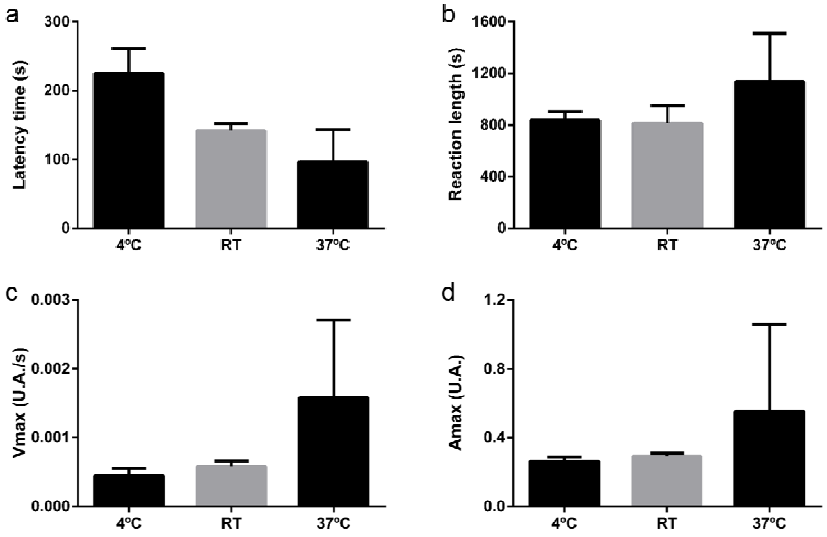

Figure 28. Effect of substrate temperature on kinetic variability. (a) Latency time, (b) reaction length, (c) Vmax, and (d) Amax were studied.

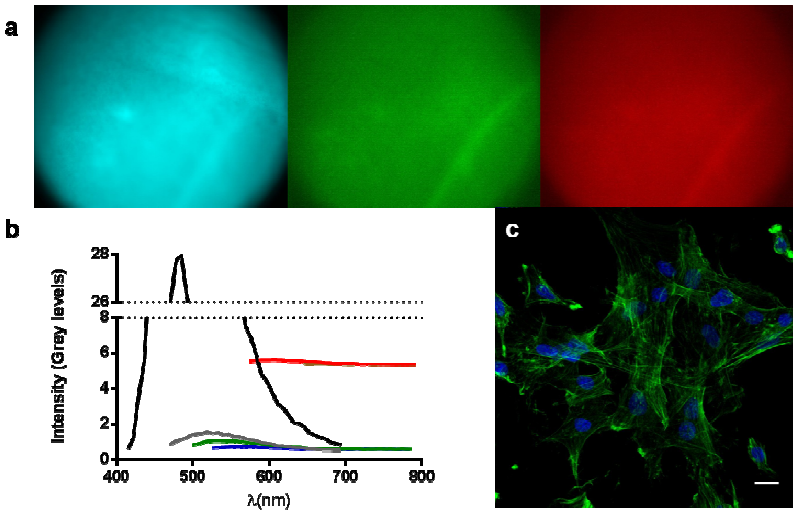

Figure 29. Autofluorescence of citric acid-crosslinked hydrogels (a) Autofluorescence in blue, green and red channels. (b) Emission spectrum, (c) rMSCs on hydrogels pre-treated with trypan blue; blue: nuclei; green: actin. Scale bar: 20 µm.

3.2.2.1.4 *Autofluorescence of citric acid-crosslinked hydrogels*

Citric acid-crosslinked hydrogels were prepared in optimized conditions and tested for the presence of autofluorescence. Tested samples fluoresced in all three channels (Figure 29a), as confirmed by emission spectra (Figure 29b), suggesting that ELRs are autofluorescent. Staining samples with trypan blue prior to cell seeding suppressed the autofluorescence in the blue and green channels, allowing the visualization of DAPI-stained cell nuclei and green phalloidin-stained actin filaments (Figure 29c).

3.2.2.2 Effect of molar ratios on hydrogels properties

3.2.2.2.1 *Gelification and kinetics*

Hydrogels became gradually opaque during reticulation (Figure 30a). This phenomenon made possible the monitoring of absorbance changes at a wavelength of 750 nm, at which none of the components showed remarkable light absorption. The increase in absorbance followed a sigmoidal curve that was mathematically derived to calculate latency time, reaction length, Vmax and Amax. These parameters were calculated to decipher how the relative abundance of reactive species (EDC and, -COOH and -NH_2 groups) involved in the reaction kinetically affect polymer aggregation. With this purpose, seven different hydrogels were prepared using particular combinations of EDC:COOH and COOH:NH_2 molar ratios. Reaction length, Vmax and Amax didn't show any trend as to the effect of molar ratios (Figure 38, Supplementary data). In contrast, latency time (Figure 30b) was found to be clearly influenced by the relative abundance of reactive species: increasing any of the two molar ratios led to a reduction in latency time (EDC:COOH, from 568.33±91.45 s to 371.11±6.97 s; COOH:NH_2, from 371.11±6.97s to 120.77±26.37 s).

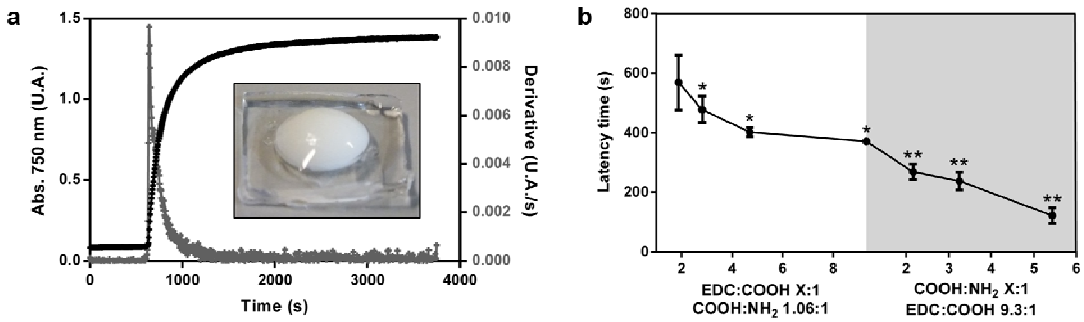

Figure 30. Study of citric acid-crosslinked hydrogels gelification. (a) Changes in absorbance ocurring during crosslinking reaction tracked at 750 nm (black) and mathematical derivative

(gray), from which kinetic parameters were extracted. Inset: citric acid-crosslinked hydrogel at reaction completion; U.A.: Units of absorbance. (b) Latency time calculated for all seven different samples. Plotting area was colored to clearly distinguish the separate contribution of the two molar ratios. *p *value*≤0.05 with respect to E2C1 samples; **p *value*≤0.05 with respect to E9C1 samples.

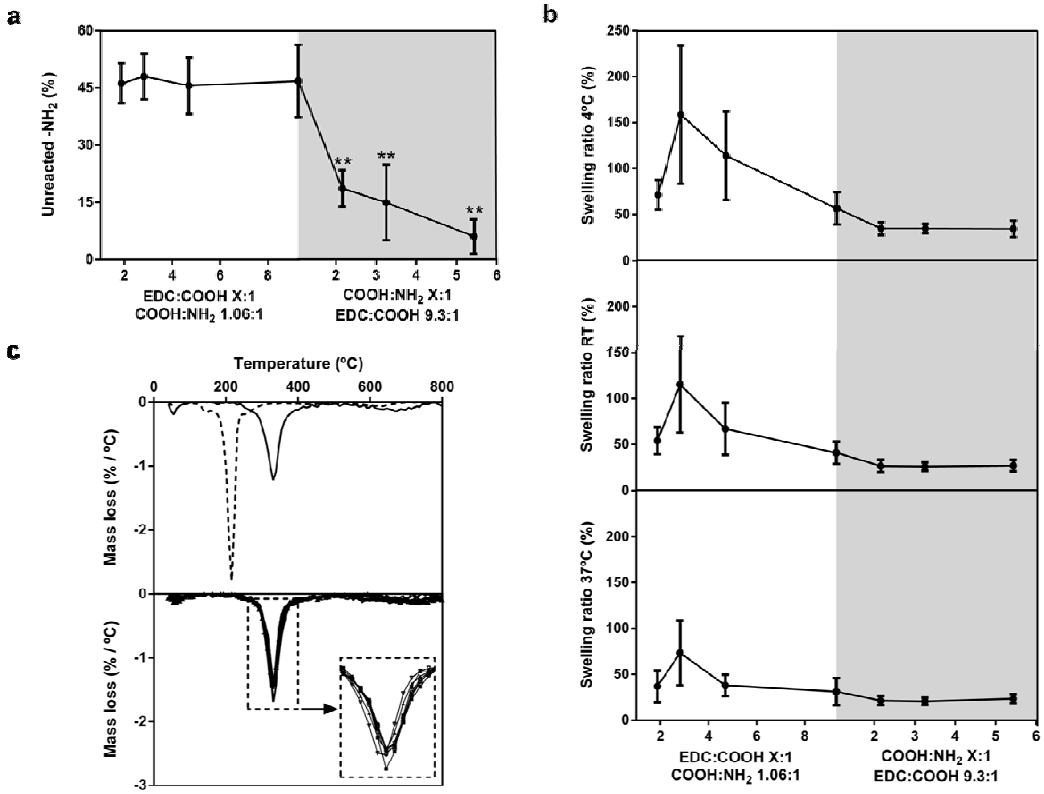

Figure 31. Effect of molar ratios on functional group consumption, and on the swelling and thermal stability of hydrogels. (a) Quantification of unreacted primary amines after crosslinking with citric acid and EDC; **p *value*≤0.05 with respect to E9C1 samples. (b) Equilibrium swelling ratio of hydrogels incubated at different temperatures. (c, top) Mass loss profile of pure citric acid (dotted line) and HRGD6 polymer (solid line) when subjected to temperatures up to 800ºC. (c, bottom) Mass loss profile of citric acid-crosslinked hydrogels.

3.2.2.2.2 *Unreacted –NH_2 groups*

The number of primary amines remaining unreacted after reticulation was quantified by using TNBS [506]. Although HRGD6 polymer was designed to display ε-amino groups from lysine residues to be used for crosslinking purposes, α-amino groups from the N-terminus of polymeric chains may also participate in the EDC-mediated reaction. Thus, results presented herein correspond to the sum of unreacted α- and ε-amino groups.

As shown in Figure 31a, increasing the EDC-to-COOH ratio did not have an effect on the percentage of primary amines involved in the reticulation reaction (all samples displayed ca. 46% free $–NH_2$), suggesting that EDC is efficient even at a 2-fold molar excess respect to carboxyl groups for a fixed $COOH:NH_2$ ratio. In contrast, increasing the $COOH:NH_2$ ratio led to a remarkable decrease in the amount of unreacted amines, leading to an almost total consumption of $–NH_2$ groups in samples E9C5 (6.01±4.48% free $–NH_2$).

3.2.2.2.3 *Swelling*

Swellability was studied by incubating samples at different temperatures and comparing their weight both in the swollen and dried states. Hydrogels crosslinked with citric acid seem to retain ELR's smart behavior [309], displaying characteristic swellability when incubated at different temperatures (Figure 31b). Generally, the lower the temperature the higher the mean swelling ratio, although just subtle differences were noticed in the case of E9C1, E9C2, E9C3 and E9C5 samples.

When it comes to molar ratios, it was found that the tendency was similar in the case of the three temperatures tested. Briefly, increasing EDC:COOH from 1.88:1 to 2.82:1 led to an initial increase in the amount of absorbed water while further increase in EDC:COOH entailed a marked reduction of water absorption. On the other hand, $COOH:NH_2$ caused a subtle decrease in swelling ratio when increasing from 1.06:1 to 2.16:1, at which an asymptotic value was reached. None of the molar ratios was found to seemingly affect swelling.

3.2.2.2.4 *Thermal stability*

The thermal stability of samples prepared in different conditions was studied by thermogravimetry, which has been shown to provide qualitative information about the nature [404,507] and density [397,508,509] of covalent bonds in a given polymeric network, besides allowing the semiquantification of those species present in analyzed samples. After subjecting hydrogels to temperatures up to 800ºC, the weight evolution was monitored and mathematically derived to obtain degradation temperature (temperature at which maximum mass loss/ºC is achieved) and citric acid content. Citric acid and HRGD6 polymer showed degradation temperatures of 216ºC and 331º, respectively (Figure 31c, top). In all cases, hydrogels showed one-step degradation with maximum mass loss/ºC at

331ºC (Figure 31c, bottom), rendering the estimation of the weight percentage of citric acid in hydrogels impossible. None of the molar ratios seemed to have an effect on the thermal stability of citric acid-crosslinked hydrogels.

3.2.2.2.5 *Resistance to enzymatic degradation*

To investigate differences between samples regarding resistance to enzymatic degradation, hydrogels were incubated with porcine pancreatic elastase. A pilot study was performed to find a proper setting allowing for a fast degradation, yet slow enough to detect differences between conditions. Elastase at $4.7 \cdot 10^{-1}$, $4.7 \cdot 10^{-2}$ and $4.7 \cdot 10^{-3}$ U/ml led to an excessively fast degradation, while $4.7 \cdot 10^{-4}$ U/ml led to a really slow mass loss (Figure 32a). Thus, $2.82 \cdot 10^{-3}$ U/ml was chosen to be used in degradation studies.

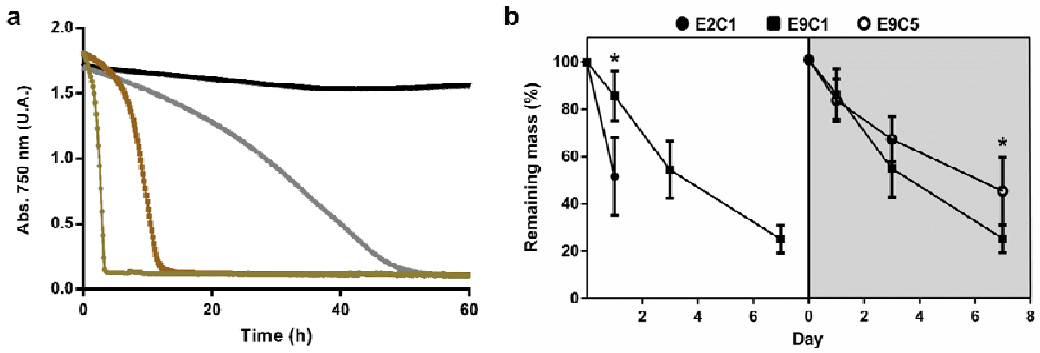

Figure 32. In vitro enzymatic degradation with porcine pancreatic elastase. (a) Pilot test performed to select a proper amount of elastase to be used in degradation experiments; $4.7 \cdot 10^{-1}$ (black), $4.7 \cdot 10^{-2}$ (grey), $4.7 \cdot 10^{-3}$ (brown) and $4.7 \cdot 10^{-4}$ (light brown) U/ml were tested. (b) Degradation profiles of selected hydrogels after in vitro exposure to porcine pancreatic elastase; (left) E2C1 and E9C1 samples; (right) E9C1 and E9C5 samples. **p* value≤0.01.

In order to simplify the experiments and to provide a proof of concept, 3 out of the 7 different hydrogels were chosen to be used in this part of the study: E2C1, E9C1 and E9C5. E2C1 samples were found to degrade quickly, losing ca. 50% of their mass within the first day and being completely dissolved by day 3 (Figure 32b, left). In contrast, E9C1 hydrogels showed reduced degradation at day 1 and sustained mass loss along the experiment, by the end of which ca. 75% of the material had been digested. E9C5 samples showed a significantly reduced mass loss rate from day 3 to day 7, at which ca. 55% of the material had been enzymatically processed (Figure 32b, right).

3.2.2.2.6 *Structure*

The effect of molar ratios on hydrogel architecture was studied both by confocal microscopy and FESEM. Observation of the structure by confocal microscopy was possible thanks to treating hydrogels with trypan blue, a fluorescence quenching compound [493] known to fluoresce in red [510–513]. This treatment allowed the visualization of three different architectures (globular, globulo-fibrillar and dense) and structural changes regarding polymer aggregation, aggregate size and matrix density.

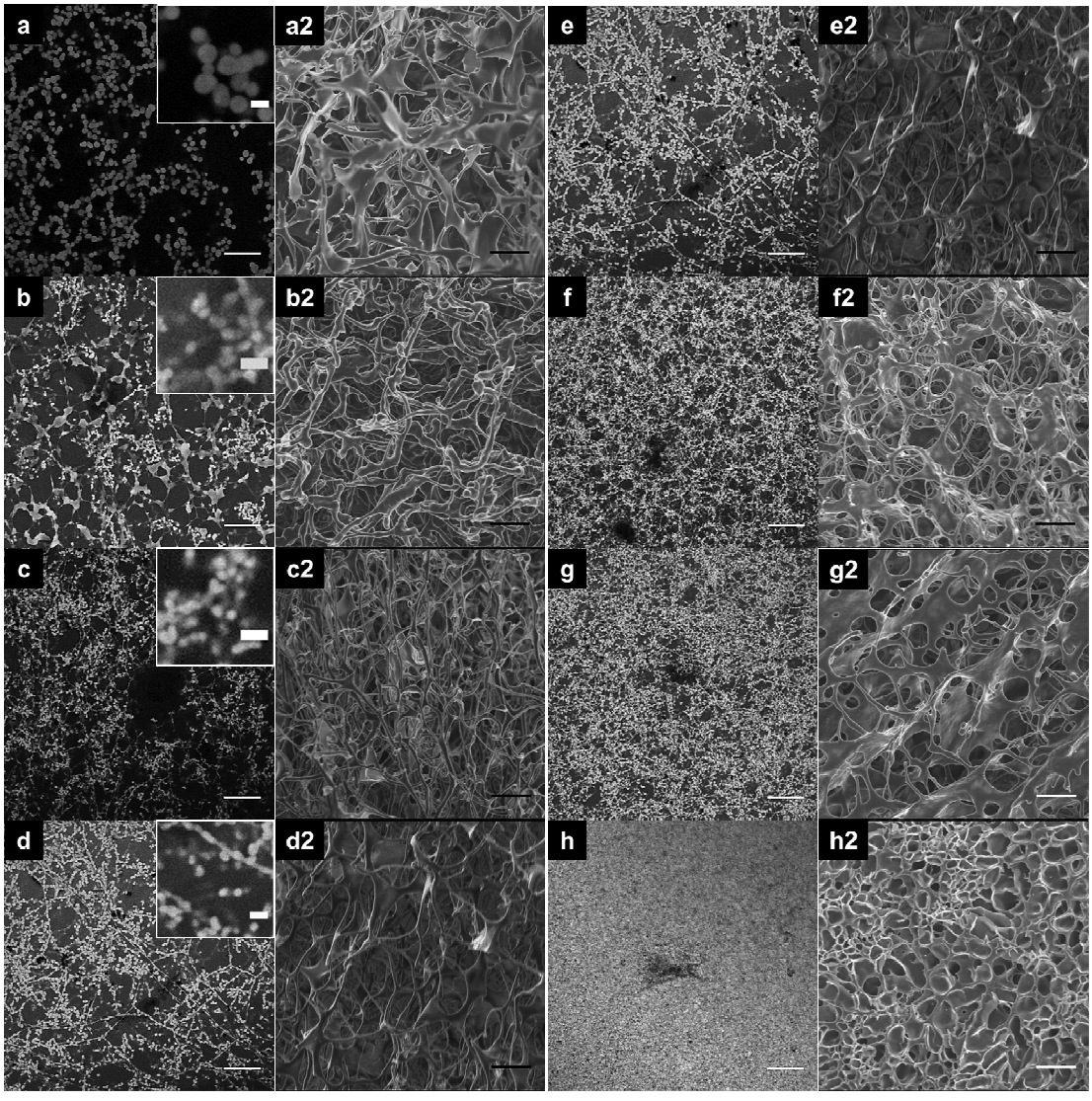

Figure 33. Structure of citric acid-crosslinked hydrogels prepared using different combinations of EDC:COOH and COOH:NH_2 molar ratios. The architecture of hydrogels prepared using specific combinations of molar ratios visualized under confocal microscopy (a-h) and FESEM (a2-h2). Images a-h are representative confocal microscopy slices displaying the

characteristic architecture of citric acid-crosslinked hydrogels prepared in different reaction conditions. a,a2: E2C1; b, b2: E3C1; c, c2: E5C1; d-e, d2-e2: E9C1; f, f2: E9C2; g, g2: E9C3; h, h2: E9C5. Insets in images a-d illustrate changes in the size of polymer aggregates induced by using increasing COOH:NH_2 molar ratios while keeping the EDC-to-COOH ratio constant. Confocal microscopy scale bar: 20 µm; inset scale bar: 3 µm. FESEM scale bar: 5 µm.

Polymer in E2C1 samples assembled in the form of globules with a diameter of ca. 3 µm (Figure 33a). Increasing EDC:COOH to obtain E3C1 samples led to a transitional structure in which large aggregates and nascent elongated entities (trabeculae) formed by smaller aggregates (diameter of ca. 1.5 µm) were observed (Figure 33b). E5C1 and E9C1 samples displayed architectures enriched with fiber-like structures where polymer aggregates had a diameter of ca. 1.3 µm and 1.2 µm, respectively (Figure 33c and d). Although it was not possible measuring the size of aggregates in E9C2, E9C3 and E9C5 samples, increasing COOH:NH_2 seemingly led to a reduction of the aggregate and trabeculae size down to the nanoscale (Figure 33f-h). This latter phenomenon was accompanied by an increase in hydrogels density.

FESEM was used to confirm what was observed by confocal microscopy. No globules were observed in any of the samples. However, changes in the density of the structure and in polymer aggregation were confirmed. Increasing EDC:COOH molar ratio led to mesh constituents transitioning from irregular-shaped (Figure 33a2) to thin connecting fiber-like entities or trabeculae (Figure 33b2-d2). Increasing the COOH-to-NH_2 ratio led to obtaining hydrogels with dense structures displaying sublimation-derived pores typical of lyophilized hydrogels [514] (Figure 33f2-h2).

3.2.2.2.7 *Percentage polymer-occupied volume*

In order to confirm the apparent effect of excess –COOH with respect to –NH_2 on scaffold density, sections obtained by confocal microscopy were processed to quantify the volume occupied by HRGD6 polymer. The EDC:COOH ratio was found not to affect PV/TV; in contrast, COOH:NH_2 had a strong effect on reducing the void volume (from 31.56±0.69% to 74.09±7.33% of polymer-occupied volume; Figure 34a) in such a way that the higher the COOH-to-NH2 ratio, the more dense the scaffold. 3D reconstructions of calculated volumes were compared to the original 3D sections to ensure proper calculations were performed; images can be seen in Figure 34b). After pairing PV/TV and swelling ratio mean values for all hydrogels, the way polymer is distributed along the sample was found

to strongly affect swellability. Briefly, an increase in the low-range PV/TV was associated to a decrease in the swelling ratio (i.e. the denser the hydrogel, the lower the equilibrium water content), reaching an asymptote at a PV/TV value of ca. 40%, beyond which swelling ratio remained unaffected (Figure 34c). These results suggest that the few tens of microns analyzed by confocal microscopy are likely to be representative of the bulk structure of herein described hydrogels.

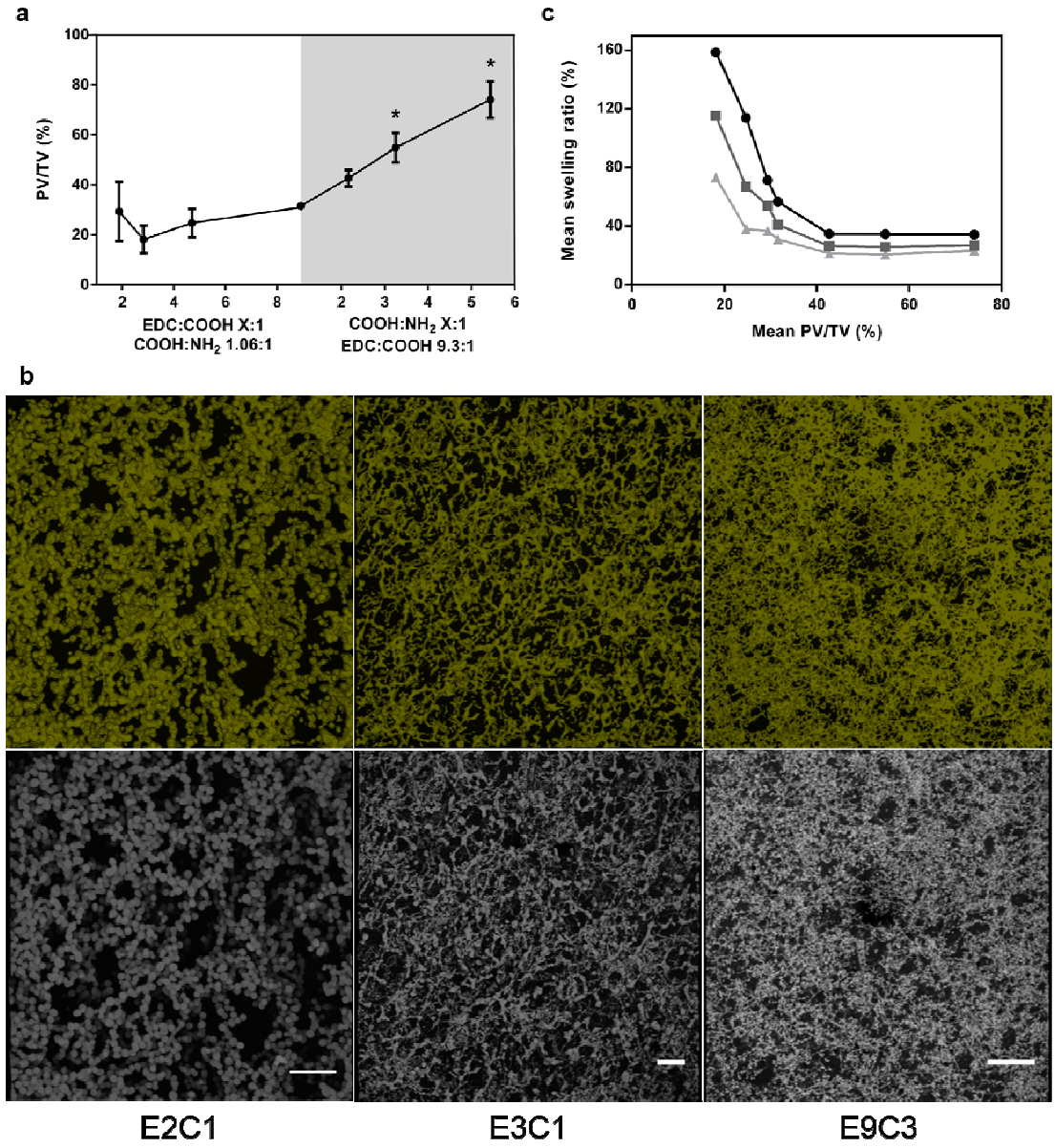

Figure 34. Study on the effect of EDC:COOH and COOH:NH_2 molar ratios on polymer volume fraction. (a) Quantification of the percentage polymer-occupied volume (PV/TV) in hydrogels prepared under different conditions. *p value≤0.01 with respect to E9C1 samples. (b) Comparison of 3D reconstructions of calculated polymer-occupied volume (top) to 3D

reconstructions of sections obtained by confocal microscopy (bottom). Scale bar: 20 µm. (c) Mean values for PV/TV paired to mean value for swelling ratio at 4ºC (black), RT (gray) and 37ºC (light gray).

3.2.2.2.8 *Surface stiffness*

An interesting question to answer was whether the apparent differences regarding crosslinking yield and structure between samples would influence their mechanical properties at a surface level. As it is shown in Table 8, stiffness was seemingly unaffected by molar ratios, none of which proved useful to mechanically tailor citric acid-crosslinked hydrogels. Additionally, none of the samples was shown to possess a Young's modulus value in the range of interest (25-40 kPa [242]).

Sample	Young's modulus (kPa)
E2C1	1.81 ± 1.56
E3C1	10.37 ± 6.53
E5C1	3.32 ± 1.87
E9C1	7.85 ± 5.51
E9C2	3.13 ± 1.75
E9C3	7.26 ± 3.26
E9C5	5.19 ± 4.46

Table 8. Young's modulus of citric acid-crosslinked hydrogels prepared at a 40 mg/ml polymer concentration.

3.2.2.3 Effect of reactions conditions on hydrogels properties and RGD integrity

3.2.2.3.1 *Cytotoxicity*

Cytotoxicity (by indirect contact) experiments were performed to test hydrogels for the release of excess EDC and its toxic by-product, N-acylurea. Again, E2C1, E9C1 and E9C5 samples were selected to simplify the experiment. Cells were seeded on tissue culture polystyrene (TCPS), let to adhere for 4 hours and quantified. Results were normalized to cell number in the negative control. No differences in cell number were observed (Figure 35a), assuring that all the wells used in the experiment had approximately the same initial cell density, thus avoiding artifacts due to uneven adhesion. Cells were exposed to different agents for 42.5 h and quantified again. After normalization, it was found that E2C1 and E9C1 samples led to an increased number of cells when compared to that in TCPS. In contrast, E9C5 hydrogels produced a decrease in

cell number of about 70%. No cell survival was observed in those wells treated with culture medium supplemented with 1% phenol. After staining with Calcein AM, cells exposed to culture medium and samples E2C1 and E9C1 were found to display normal morphology (Figure 35b); exposure to E9C5 induced morphological alterations. No cells were observed in those wells treated with 1% phenol.

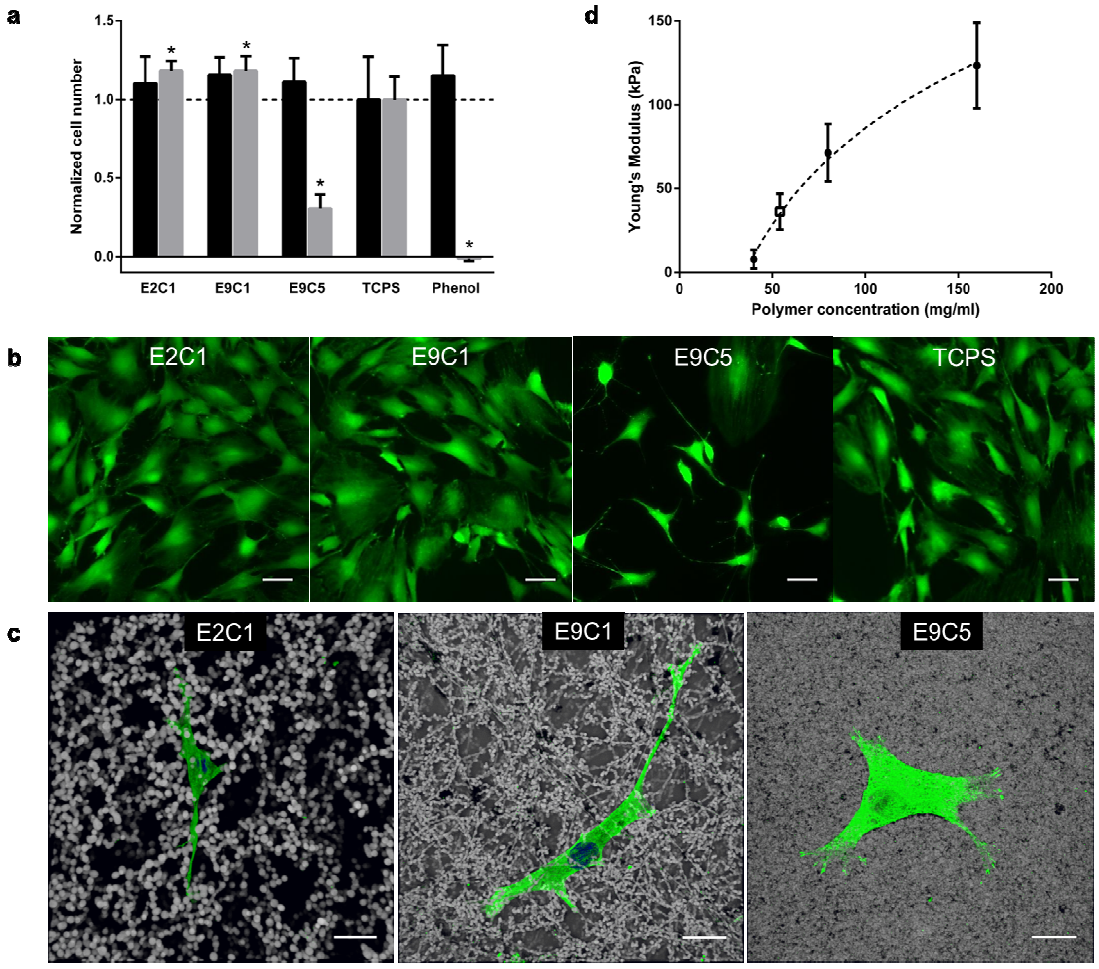

Figure 35. Effect of molar ratios on cytotoxicity and cell adhesion, and effect of polymer concentration on hydrogels stiffness. (a) Citotoxicity assessment of selected hydrogels by indirect contact. Cell numbers were quantified after adhesion (black bars) and after a 2-days exposure period (gray bars), and normalized to those in the control surface (TCPS) for each time point. (b) Morphology of rMSCs exposed to hydrogels and to control surface for 2 days; scale bar: 20 µm. (c) rMSCs on selected samples after preliminary 24-hour cultures. Green: vinculin; blue: nuclei. Scale bar: 20 µm. (d) Effect of polymer concentration on stiffness (filled dots) and Young's modulus of E9C1 samples prepared at a 54 mg/ml polymer concentration (empty square). *p value≤0.001 with respect to TCPS.

3.2.2.3.2 *Cell adhesion*

Cell adhesion experiments were performed to test hydrogels for RGD integrity. rMSCs were seeded on the surface of hydrogels and kept in culture for 24 hours. Immunocytochemical staining revealed that cells adhered to hydrogels regardless of their architecture (Figure 35c) and produced filopodia able to penetrate those matrices with an open structure (Figure 39, Supplementary data). Cells displayed normal morphology in all cases, although focal contacts were just observed in those samples with a dense matrix structure, in which nuclei were not visualized due to the strong autofluorescence of E9C5 samples in the $\lambda_{emission}$= 430-476 nm range (blue channel).

3.2.2.4 Design and characterization of tailored hydrogels

3.2.2.4.1 *Surface stiffness*

Given that molar ratios were found not useful to achieve target Young's modulus, the effect of a third variable, polymer concentration, was explored. The E9C1 setup was chosen to study how polymer concentration influences stiffness at a surface level. The use of different amounts of polymer led to obtaining a logarithmic function from which the polymer concentration needed to achieve hydrogels with target Young's modulus was extrapolated (Figure 35d). A Young's modulus in the 25-40 kPa range is considered to be osteogenic; a modulus of 34 kPa was specifically targeted given that it has been already shown to induce the expression of osteogenic markers [242]. E9C1 hydrogels with a polymer concentration of 54 mg/ml -corresponding to a theoretical stiffness of 34.83 kPa- exhibited an experimental value of 36.13±10.72 kPa.

3.2.2.4.2 *Structure of mechanically-tailored hydrogels*

Mechanically-tailored RGD-C hydrogels (i.e. E9C1 samples prepared at a polymer concentration of 54 mg/ml) were analyzed by confocal microscopy and FESEM. Sections obtained by confocal microscopy revealed that RGD-C samples retained the fiber-like architecture seen in their 40 mg/ml counterparts (Figure 36a, i). Polymer globules in RGD-C hydrogels organized in the form of fiber-like entities (trabeculae) with a diameter of 952.64 ± 210.57 nm (Figure 36a, ii). Under FESEM, RGD-C samples were found to possess a reduced number of globules and to be shaped by trabeculae with a diameter of 106.30 ± 30.75 nm that locally arranged with varying degrees of alignment (Figure 36b, i and ii).

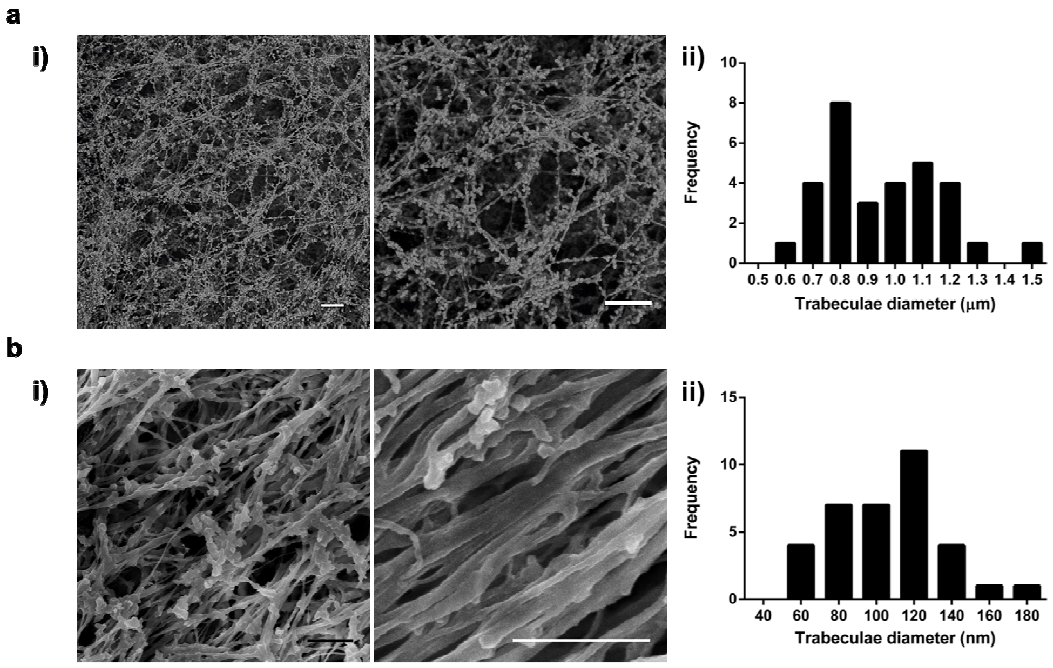

Figure 36. Structure of mechanically-tailored hydrogels. Study of the structure of 54 mg/ml hydrogels under (a) confocal microscopy and (b) FESEM. i) Detailed visualization and ii) size distribution of fiber-like entities in hydrogels with tailored stiffness. Confocal microscopy scale bar: 20 µm; FESEM scale bar: 1 µm.

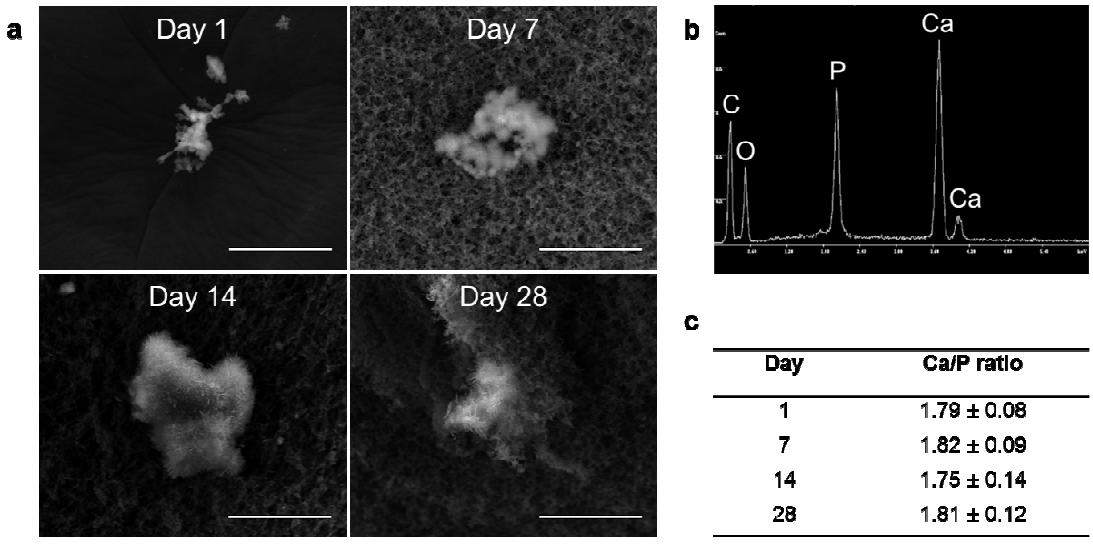

Day	Ca/P ratio
1	1.79 ± 0.08
7	1.82 ± 0.09
14	1.75 ± 0.14
28	1.81 ± 0.12

Figure 37. In vitro mineralization of RGD-C hydrogels by using SBF 1x. (a) Detail on the sparse mineral deposits found along the experiment. Scale bar: 20 µm. (b) Representative EDS profile showing the presence of calcium phosphates. (c) Calcium/phosphate ratio of mineral deposits found at different time points.

3.2.2.4.3 *In vitro mineralization*

RGD-C hydrogels were tested for citric acid-related mineralization capacity using SBF 1x. RGD-G samples were included in this experiment in order to account for HRGD6-derived nucleation capacity, if any. No calcium phosphates were found on glutaraldehyde-crosslinked hydrogels at any time point (Figure 40, Supplementary data). In contrast, sparse mineral deposits with a Ca/P ratio of ca. 1.8 were detected in RGD-C hydrogels at all time points (Figure 37).

3.3 DISCUSSION

The studies described in the present chapter were performed with the aim of designing biomimetic hydrogels for *in situ* bone tissue engineering. The chemistry of carbodiimides was selected to induce the crosslinking of ELRs by activated citric acid. Reaction optimization studies demonstrated that hydrogels with good integrity were achieved when prepared at a 40 mg/ml polymer concentration and at a pH≈6 in MES buffer, which properly buffered the system for crosslinking to occur (Figure 26). Additionally, it was demonstrated that EDC allowed the proper formation of amide bonds (without the need of displacing the reaction with NHS) and that crosslinking with citric acid can be achieved in a polymer-independent manner as long as polypeptides are rich in lysine residues and poor in acidic amino acids. Additionally, in order for the reaction to be kinetically consistent, cold acid/base needs to be used to adjust the pH of reaction mixes (Figure 27), which should be poured into substrates at RT (Figure 28).

HRGD6 elastin-like recombinamer was crosslinked with citric acid by means of EDC-mediated catalysis. EDC and citric acid have already been combined to produce hydrogels involving the multistep, time-consuming chemical synthesis of N-hydroxysuccinimide esters of citric acid that can be then used to crosslink polymers containing free primary amines [418]. In the present chapter, a one-step, organic solvent-free reaction to achieve citric acid-crosslinked hydrogels in mild conditions was designed.

As previously mentioned, the carbodiimide-mediated activation of –COOH groups to achieve the formation of peptide bonds is known to be affected by different parameters such as pH, reaction time, and EDC:COOH and COOH:NH_2 molar ratios. Once general reaction parameters were set, the effect of the relative abundance of reactive species on hydrogels properties was studied. With this purpose, seven setups characterized by particular combinations of EDC:COOH and COOH:NH_2 molar ratios were prepared (Table 6) at 4ºC and pH≈6, and let to react for 1 h at 37ºC. Under these conditions, the reticulation reaction was characterized by an increase in turbidity following a sigmoidal curve (Figure 30a), a phenomenon already described for decellularized extracellular matrix [515] and a variety of polysaccharides and proteins such as coagulin [516], fibrin

[517] and agarose [518]. A typical analysis of this phenomenon involves dividing the reticulation curve into three main stages: (i) lag phase or induction period (herein, latency time), (ii) network growth stage and (iii) pseudo-equilibrium stage [518].

HRGD6 polymer has the ability to self-aggregate in response to changes in temperature and pH, displaying an inverse transition temperature of 32ºC in PBS at pH=7.4, although ITT would be somewhat lower at the pH used herein [304]. During latency time, the temperature of the solution gradually rises along the incubation period. When the solution reaches the ITT, polymer molecules undergo conformational rearrangement leading to intermolecular hydrophobic aggregation [311], giving rise to supramolecular aggregates with size increasing up to few micrometers over time [366]. In the presence of a crosslinker, aggregates are linked to each other, thus conferring hydrogels their characteristic nano-microarchitecture (network growth and pseudo-equilibrium stages). On this basis, it was hypothesized that the length of latency time, found to be affected by both molar ratios (Figure 30b), would have a direct effect on the size of polymer aggregates building up citric acid-crosslinked hydrogels, in such a way that the shorter the latency time, the smaller the aggregates shaping the network.

The amount of $–NH_2$ groups remaining unreacted after crosslinking was quantified for all seven hydrogels and found to be remarkably affected by the COOH-to-NH_2 molar excess (Figure 31a). Specifically, the higher the COOH:NH_2 molar ratio, the higher the amount of $–NH_2$ groups involved in the reaction, boosting the number of crosslinking points and thus reducing polymer chain mobility and inter-chain void space [265]. This phenomenon didn’t directly affect thermal resistance nor swelling, although the latter was found to be influenced by PV/TV (Figure 34b) in such a way that (i) the higher the PV/TV, the lower the swelling and that (ii) PV/TV $\geq$ 40% leads to minimized swelling. As shown in Figure 31a, Figure 34a and Figure 34b, PV/TV (i.e. hydrogel density) increases as the number of unreacted groups diminishes, suggesting that the degree of crosslinking, along with latency time, define the architecture of citric acid-crosslinked hydrogels, whose PV/TV defines their swelling degree.

The structure of scaffolds prepared using different reaction conditions was studied (Figure 33). As revealed by confocal microscopy, the EDC:COOH molar ratio affects (i) polymer

aggregation, which ranged from purely globular to globulo-fibrillar (i.e. globules organized in the form of fibrous structures), and (ii) aggregate size, which is also seemingly affected by the COOH-to-NH_2 molar excess. Additionally, the COOH:NH_2 ratio influences hydrogel density (as confirmed by FESEM observations and PV/TV calculations), an increase in which is likely to be the consequence of reduced aggregate size and of increased globule interconnectivity. Together, these results support the hypotheses that latency time and crosslinking degree dictate the organization of HRGD6 polymer thus defining the architecture of herein described hydrogels. Furthermore, they point out that the architecture of citric-acid crosslinked hydrogels can be tuned by using specific combinations of EDC:COOH and COOH:NH_2 molar ratios.

FESEM failed to reveal the nano-microstructure (globules) seen by confocal microscopy, which was presumably lost during sample preparation for their visualization under electron microscopy (Figure 33 and Figure 36). This phenomenon proved the usefulness of red-shifting samples' autofluorescence with trypan blue to visualize hydrogels' intact structural features when no nanometric resolution is required. This is a cheap, fast and easy method to visualize hydrogel architecture, to perform structural calculations such as PV/TV or to visualize how cells interact with scaffolds (Figure 38, Supplementary data) in short duration cultures without the need of going through fluorophore grafting protocols.

The resistance to in vitro degradation of selected samples (E2C1, E9C1 and E9C5) was assessed. The amount of unreacted –NH_2 groups and PV/TV for E2C1 and E9C1 samples are not significantly different (Figure 31a and Figure 34a). However, E9C1 hydrogels showed improved resistance to enzymatic degradation (Figure 32b, left). Structurally, when increasing EDC:COOH, there was an apparent reduction in the occurrence of dangling polymeric ends accompanied by an increase of trabeculae interconnectivity (Figure 33a2-d2), which would be the reason for the increased stability of E9C1 hydrogels compared to that of E2C1 ones. E9C5 samples displayed improved resistance to degradation in comparison to E9C1 gels (Figure 32b, right), which would be due to (i) a higher polymer network connectivity [519] derived from a much higher consumption of –NH_2 groups [367] (Figure 31a), and (ii) a consequently increased PV/TV (Figure 34a) further limiting enzyme accessibility and ultimately slowing down degradation. Given that network and structural features are dependent on the reaction conditions used to prepare

structurally tailored scaffolds, it is noteworthy that the degradation of citric acid-crosslinked HRGD6 hydrogels can't be independently tuned.

Hydrogels were tested for cytocompatibility by indirect contact with rMSCs. E2C1, E9C1 and E9C5 samples were selected to simplify indirect cytotoxicity assays. After a 42.5 hour-exposure period, cell number in wells exposed to E2C1 and E9C1 samples was significantly higher than that in control wells (Figure 35a). This phenomenon could be due to the release of unbound or partially bound citric acid, which would be incorporated into the cell through the Na-coupled citrate transporter; once in the cytosol, citrate would be turned into lipids to meet the requirements for MSCs proliferation-related membranogenesis [520]. In contrast, E9C5 samples led to a highly reduced viability and altered cell morphology (Figure 35b), most likely due to the slow release of N-acylurea, the toxic and water-soluble by-product of EDC. This would be due to an incomplete removal of N-acylurea during the washing steps because of reduced diffusion in dense E9C5 hydrogels, leading to the slow release of the by-product during the experiment. This cytotoxic effect was not noticed when rMSCs were seeded on E9C5 hydrogels (Figure 35c), most likely due to the extra washes applied after pre-staining with trypan blue. Cell adhesion experiments revealed that rMSCs were able to adhere to all seven hydrogels, suggesting that –COOH groups from aspartic acid's side chain are not involved in the EDC-mediated reaction in the conditions used herein, so RGD tripeptides remain unaffected and functional for cells to attach to them.

The effect of the relative reactive species abundance on hydrogels mechanical properties was studied. Given molar ratios were found not useful to tune stiffness (Table 8), the influence of polymer concentration was explored. To do so, the E9C1 setup was chosen since it led to obtaining cytocompatible hydrogels possessing fiber-like microstructure and ca. 45% of free primary amines, a functional group shown to induce and maintain the osteogenic differentiation of MSCs [237,243]. After preparing E9C1 hydrogels at different polymer concentrations, 54 mg/ml was extrapolated (Figure 35d) as the concentration needed to achieve samples with a target Young's modulus value of 34.83 kPa. Experimentally, RGD-C hydrogels were shown to possess a Young's modulus of 36.13±10.72 kPa and to retain its 40mg/ml counterpart's fiber-like structure (Figure 36a). Interestingly, these results point out that the structure and surface stiffness of citric acid-

crosslinked hydrogels can be separately tuned by modifying the combination of molar ratios and the polymer concentration used to prepare them, respectively.

RGD-C hydrogels were shown to nucleate calcium phosphate when incubated with SBF 1x. Although sparse at all time points, mineral deposits were found even by day 1 and kept a quite stable Ca/P ratio along the experiment (Figure 37). The presence of mineral phase in RGD-C but not in RGD-G hydrogels points out that unreacted –COOH groups from citric acid provide HRGD6 polymer with apatite-nucleating capacity [383], suggesting that RGD-C hydrogels would be able to bond to damaged bone. Additionally, the early formation of apatite in vitro suggests that hydrogel-to-bone bonding would occur shortly upon implantation [500], helping the scaffold to stay in place and thus reducing the risk of incomplete defect closure due to scaffold misplacement.

The production of hydrogels for bone regeneration exhibiting calcium phosphate-nucleation capacity has gained momentum in the last years due to hydroxyapatite's osteogenic potential [521,522]. Mineralizing hydrogels can be achieved by means of strategies such as the post-gelation partial hydrolysis to expose –COOH groups [368], functionalization with carboxylate-terminated spacers [369], or the use of polymers, either recombinantly [307,523] or chemically-synthetized [486], containing hydroxyapatite-binding motifs. Post-gelation treatments and functionalization usually require the use of chemicals that can compromise the biocompatibility of the construct, while those hydrogels with internal nucleation motifs possess a polymer-dependent mineralization capacity. In contrast, our hydrogels are produced in mild conditions and display citric acid-dependent mineralization capacity. Citric acid, herein used both as a non-toxic crosslinker and a calcium phosphate-nucleating molecule, possesses carboxylates spaced by a distance matching that spacing calcium ions in hydroxyapatite and thus has been suggested to be both a natural HA-stabilizing and nucleating molecule [6]. Interestingly, it can be used in combination with EDC to produce hydrogels as long as the polymer to be crosslinked possesses a proper balance of –COOH and $–NH_2$ groups, making this method a versatile strategy to achieve mineralizing hydrogels for bone regeneration. Globally, we have shown that crosslinkers are a useful tool to tune hydrogel physical properties as well as to provide polymers with new functionalities such as calcium phosphate nucleation capacity.

CHAPTER 2

3.4 SUPPLEMENTARY DATA

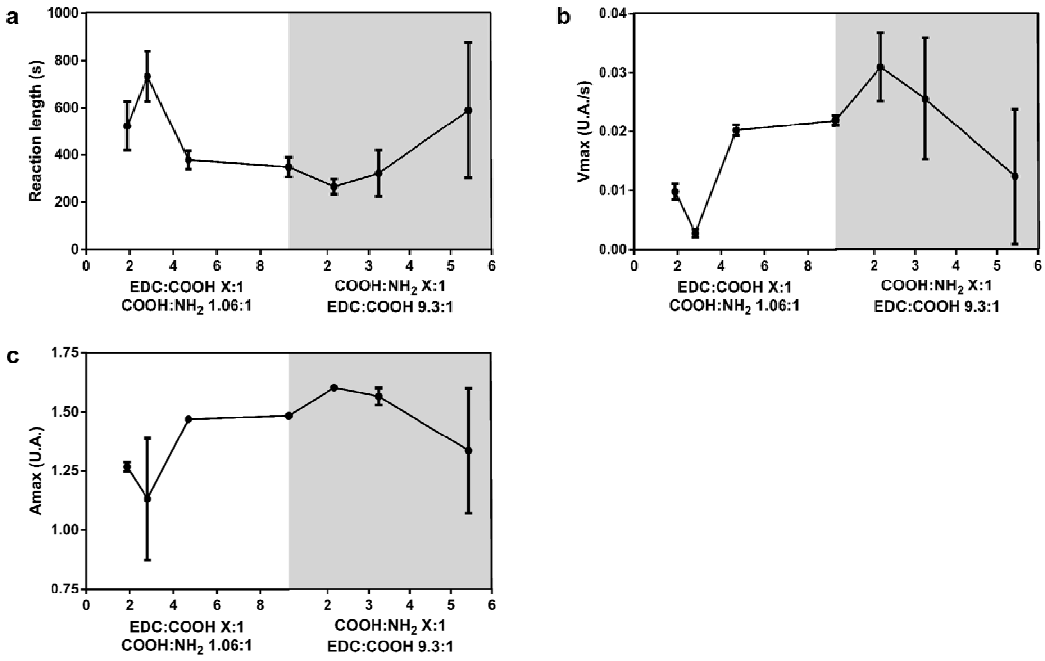

Figure 38. Additional kinetic parameters for the study of the effect of molar ratios on polymer aggregation. (a) Reaction length, (b) Vmax, and (c) Amax for all seven setups.

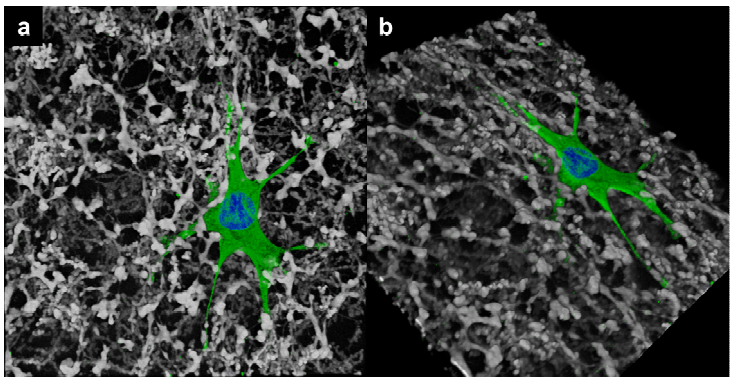

Figure 39. Cell-scaffold interactions visualized by staining scaffolds with trypan blue. (a) Front and (b) tilted view of a rMSC with filopodia entering a E3C1 hydrogel. Green: vinculin; blue: nuclei.

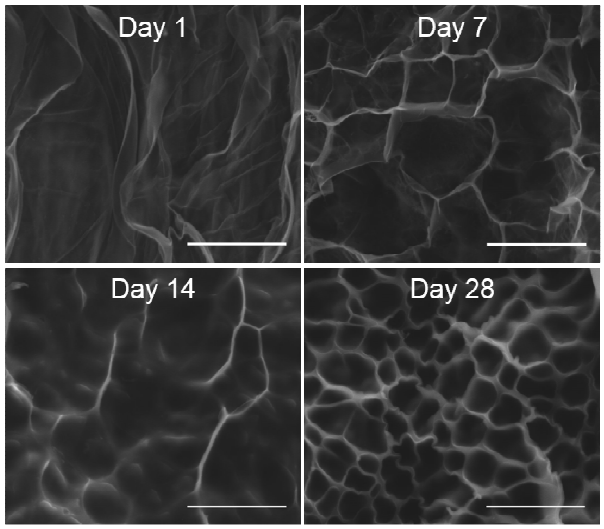

Figure 40. SEM pictures of RGD-G hydrogels incubated with SBF 1x. Scale bar: 20 µm.

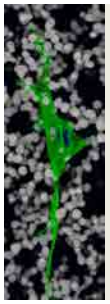

Chapter 3

3. BIOLOGICAL CHARACTERIZATION OF TAILORED CITRIC ACID-CROSSLINKED HYDROGELS

CHAPTER 3

PREFACE

The present chapter represents the study of the biological performance of mechanically-tailored citric acid-crosslinked hydrogels both in vitro and in vivo. First, the effect of citric acid, a degradation product of our matrices, on stem cell proliferation and differentiation was studied. Second, tailored hydrogels were subjected to in vitro and in vivo experiments to determine their osteogenic potential in comparison to their non-tailored counterparts.

4.1 MATERIALS AND METHODS

4.1.1 Citric acid as a soluble factor

4.1.1.1 Cytotoxicity

Human mesenchymal stem cells (hMSCs; Lonza) were expanded in complete medium (Advanced DMEM supplemented with 10% FBS, 2 mM L-glutamine, 100 U/ml Penicillin and 100 µg/ml Streptomycin), and detached at a confluence of about 80% with Tryp-LE Express. The number of viable cells was determined after staining with Trypan blue and 10^4 viable cells in complete medium were seeded in 24-well plates and kept in culture for 24 h. Non-adhered cells were washed out with PBS and wells were subsequently replenished with complete medium. PET Millicell Inserts with a 0.4 µm pore size were placed into wells and 300 µl of complete medium supplemented with 0.15, 0.75 or 1.25 mM citric acid were added to each insert. Negative controls consisted on inserts containing complete medium; positive controls consisted on the use of complete medium supplemented with 1% phenol in both the wells and the inserts. After a 42.5 hours incubation period at 37°C and 5% CO_2, cytotoxicity by indirect contact was assessed by cell quantification with Alamar blue and live/dead staining. For cell shape visualization, cells were washed with Dulbecco's buffered-saline (DPBS), stained in the dark with 2 µM Calcein AM (Sigma) and 4 µM propidium iodide (Fluka) for 20 minutes at 37°C and washed with the buffer to remove excess dye. Images were acquired using an Eclipse TE200 inverted microscope and MetaMorph Microscopy Automation & Image Analysis Software. For cell quantification, cells were incubated with complete medium supplemented with 10% Alamar blue; absorbance at 570 nm was read using an Infinite Pro200 microplate reader (Tecan, Switzerland).

4.1.1.2 Cell culture for proliferation and differentiation assays

hMSCs were expanded as abovementioned. 10^4 viable cells were seeded in 24-well plates in either complete (normal) medium or differentiation medium (complete medium supplemented 50 µg/ml ascorbic acid, 10 mM β-glycerolphosphate and 10 nM dexamethasone) with or without citric acid (Table 9). Cells were kept in culture for up to 21 days at 37ºC, 5% CO_2 and culture medium was replaced twice a week.

Medium	[Citric acid] (mM)
Complete	0
Complete	0.15
Complete	0.75
Complete	1.25
Osteogenic	0
Osteogenic	0.15
Osteogenic	0.75
Osteogenic	1.25

Table 9. Summary of conditions used to test the effect of citric acid on hMSCs proliferation and osteogenic differentiation.

4.1.1.3 Proliferation

Proliferation was quantified at days 1, 3, 7 and 14. At every time point, culture medium was discarded and cells were incubated for 24 h with the corresponding medium supplemented with 10% Alamar blue. Medium containing Alamar blue was transferred to 96-well plates and aborbance was read at 570 nm. Wells were then replenished with the corresponding medium and kept in culture.

4.1.1.4 In vitro osteogenic differentiation

4.1.1.4.1 *Alkaline phosphatase*

At every time point, cells were lysed by incubation with mammalian protein extraction reagent (M-PER; Life Technologies) and subjected to three freezing/thawing cycles at -80ºC/RT.

Samples were transferred to microtubes and centrifuged at 2,500 g for 10 minutes at 4ºC using an Eppendorf 5415 R centrifuge. Cell debris were discarded and cell number was quantified by using a Cytotoxicity detection plus kit (Roche) according to manufacturer's instructions. Briefly, cell lysates were incubated with reaction solution at a 1:1 volume ratio. Mixtures were incubated for 20 minutes at RT and absorbance was read at 490 nm using a reference wavelength of 600 nm.

For alkaline phosphatase (ALP) expression quantification, lysates were incubated with the p-Nytrophenyl phosphate (pNPP) substrate at a 1:1 volume ratio. Reagents were

homogenized for few seconds and incubated at 37ºC for 40 minutes; absorbance was read at 450 nm. ALP expression results were normalized to cell number.

4.1.1.4.2 *Osteopontin*

Osteopontin (OPN) expression was assessed at days 3, 14 and 21 both by immunofluorescence and Enzyme-linked immunosorbent assay (ELISA). For immunofluorescence, cells were treated with fixative solution (3% paraformaldehyde and 40 mM sucrose in PBS) for 10 minutes at 4°C and washed three times with cold 0.15% glycine in PBS (PBS-gly). Cells were then permeabilized with 0.1% Triton X-100 (Sigma-Aldrich) for 5 minutes, blocked with PBS-gly supplemented with 6% bovine serum albumin (BSA; Sigma) for 45 minutes and stained in the dark at room temperature for actin, nuclei and OPN visualization. Briefly, cell staining consisted on: (i) incubation with rabbit anti-OPN primary antibody (Abcam) at a 1/600 dilution in PBS-gly supplemented with 3% BSA (PBS-gly-BSA 3%) for 1h, (ii) incubation with Alexa 488-conjugated goat anti-rabbit secondary antibody (Molecular Probes) at a 1/300 dilution in PBS-gly-BSA 3% for 1h, (iii) incubation with rhodamine-phalloidin (Life technologies) for 30 minutes, and (iv) incubation with DAPI for 2 minutes. Cells were then mounted with Mowiol 40-88 (Sigma-Aldrich) and sandwiched with 15 mm diameter circular glass coverslips. Samples were visualized under a DM-IRBE inverted microscope (Leica) by using the MetaMorph Microscopy Automation & Image Analysis Software.

For the quantitative assessment of OPN expression, cell number was quantified using the Cytotoxicity detection plus kit as abovementioned. OPN was quantified from supernatants by means of the Human osteopontin platinum ELISA kit (eBioscience) according to manufacturer's instructions. Briefly, wells were washed twice using wash buffer and samples were loaded into wells and incubated for 2 h at RT to allow the binding of the protein. Wells were thoroughly washed by incubating six times with wash buffer and incubated with biotin-conjugated anti-human OPN antibody for 1 h at RT under mild agitation. Wells were washed to remove excess antibody and incubated with streptavidin-conjugated horseradish peroxidase (HRP) for 1 h at RT under mild agitation. Wells were washed again and incubated with tetramethyl-benzidine substrate solution for 30 minutes at RT and the reaction was stopped with 1 M phosphoric acid. Absorbance was read at 450 nm using a reference wavelength of 620 nm. Data were analyzed by means of

Readerfit.com online software (Hitachi) by using a 5 parameter logistic nonlinear regression model. Results were normalized to cell number.

4.1.1.4.3 *Osteocalcin*

For the quantitative assessment of osteocalcin (OCN) expression, cell number was quantified using the Cytotoxicity detection plus kit as previously stated. OCN was quantified in duplicates from supernatants by means of a MicroVue bone osteocalcin EIA kit (Quidel) according to manufacturer's instructions. Briefly, cell lysates were transferred into wells and incubated with anti-OCN antibody for 2 h at RT. Wells were washed twice and incubated with ALP-conjugated goat anti-mouse antibody for 60 minutes at RT. Excess antibody was removed by washing two times and wells were incubated with pNPP substrate for 35 minutes at RT. Stop solution was then added and the absorbance was read at 450 nm. Data were analyzed by means of Readerfit.com online software (Hitachi) by using a 4 parameter logistic nonlinear regression model. OCN expression was normalized to cell number.

4.1.1.4.4 *Mineralization*

Mineralization was assessed at days 3, 14 and 21 by Alizarin red staining. Cells were washed with PBS to remove cell debris and fixed with absolute ethanol (Panreac) for 2 h at -20ºC. Wells were washed with PBS to remove ethanol and incubated with 40 mM alizarin red (Sigma) in water (pH 4.2) for 10 minutes at RT under mild agitation. Excess alizarin red was removed by washing with ultrapure water and non-specifically bound calcium was removed by washing with PBS. Specifically-bound calcium was solubilized by incubation with solubilization buffer (0.1 mg/ml cetylpyridinium chloride in 10 mM sodium dihydrogen phosphate, pH 7) for 20 minutes at RT. Supernatants were transferred to 96-well plates and absorbance was read at 570 nm. Calculations were performed using a standard curve prepared using Alizarin red in solubilization buffer and considering that one alizarin red molecule binds two calcium ions.

4.1.2 Tailored hydrogels

4.1.2.1 Hydrogels preparation

HRGD6 citric acid-crosslinked hydrogels were prepared using EDC:COOH 9.3:1 and COOH:NH_2 1.06:1 molar ratios (code E9C1) at either 54 mg/ml (tailored hydrogels) or 40 mg/ml (non-tailored hydrogels) polymer concentrations. Briefly, HRGD6 polymer was dissolved at 4ºC overnight in MES buffer containing citric acid; EDC was also dissolved in MES buffer at 4ºC. Polymer-citrate and EDC solutions were mixed at a 1:1 volume ratio and pH was adjusted to ca. 6 by adding cold HCl. Mixes were homogenized and reaction mixes were poured into substrates (96-well plates or 16-well glass chamber slides) and let to react for 1 h at 37ºC. The reaction was stopped by incubation with 0.1 M Na_2HPO_4 at room temperature for 3 hours. Samples were then washed by performing 5 swelling/shrinking incubation cycles in ultrapure water at 4°C (swelling)/37°C (shrinking) to allow excess EDC and reaction by-products to be released.

4.1.2.2 In vitro biological characterization

4.1.2.2.1 *Cytotoxicity*

10^4 viable hMSCs were seeded in 24-well plates with complete medium and let to adhere for 24 h. Wells were washed with PBS to remove non-adhered cells and E9C1 hydrogels prepared at 54 mg/ml polymer concentration were assessed for cytotoxicity.

Briefly, hydrogels were prepared in 6 mm PDMS molds as abovementioned. Samples were sterilized with 70% ethanol under UV irradiation for 1 hour, washed thrice with PBS and kept in the buffer at 37°C until use. PET Millicell Inserts with a 0.4 µm pore size were placed into wells and 300 µl of complete medium were added to each insert. Hydrogels were then washed twice with PBS to remove remaining ethanol and transferred to inserts. TCPS and complete medium supplemented with 1% phenol were used as positive and negative controls, respectively. After a 42.5 h incubation period, cell were quantified with Alamar blue and subjected to live/dead staining as previously mentioned.

4.1.2.2.2 *Proliferation*

hMSCs proliferation on hydrogels was assessed both quantitatively and qualitatively. 40 mg/ml and 54 mg/ml HRGD6 hydrogels were prepared in 16-well glass chamber slides

and sterilized as abovementioned. Scaffolds were seeded with $2 \cdot 10^3$ viable cells and kept in culture for 1, 7, 14 and 21 days in either complete medium or osteogenic medium. For qualitatively assessing proliferation, samples were washed with PBS, fixed with paraformaldehyde as previously described, stained with 1% osmium tetroxide, and subjected to serial dehydration in ethanol and to critical point drying in CO_2. Hydrogels were then graphite-sputtered and visualized under a Quanta 200 Scanning Electron Microscope (SEM; FEI) at a 10 mm working distance and a 20 kV voltage.

For the quantitative assessment of cell proliferation in complete medium, hydrogels prepared in 96-well plates were degraded at days 1, 3, 7, 14 and 21 by using 2 mg/ml porcine pancreatic elastase in PBS for 3 h at 37ºC. After hydrogel degradation, M-PER was added to a 1:1 volume ratio and samples were subjected to three freezing/thawing cycles at -80ºC/RT. Cell lysates were used to quantify cell number by using the cytotoxicity detection plus kit as previously stated.

4.1.2.2.3 *In vitro osteogenic differentiation*

In vitro differentiation was assessed by quantifying (i) the expression of ALP from cell lysates, and (ii) the expression of OPN and OCN from cell supernatants. Quantification were performed as previously stated and results were normalized to cell number.

4.1.2.3 In vivo biological characterization

4.1.2.3.1 *Sample preparation*

E9C1 reaction mixes were prepared at 40 mg/ml and 54 mg/ml polymer concentrations and to a final volume of 17.5 µl. Mixtures were poured into circular PDMS molds with a diameter of 3.5 mm and let to react at 37ºC for 30 minutes to avoid sample drying. Samples were then incubated with 0.1 M Na_2HPO_4 to stop the crosslinking reaction and washed by performing 5 swelling/shrinking cycles. Sterilization consisted on incubating samples with 70% ethanol for 1 h under UV irradiation subsequently washing hydrogels several times with PBS. Samples were kept at 37ºC until use.

4.1.2.3.2 *Scaffold implantation*

7-week-old CB17/*lcr-Prkdc*^{scid}*/lcrlcoCrl* (Severe combined immunodeficiency; SCID) female mice (Charles River) were anesthetized with IsoVet® (Braun) and the surgical site

was cleaned with povidone-iodine (Braun). Calvariae were exposed by performing sagittal midline incisions and cutting periostea. Two 3.5-mm critical size defects were created on the parietal of each animal by using a sterile drill bit (Dremel), avoiding damaging the dura mater (Figure 41a). Surgical sites were cleaned with sterile phosphate-buffered saline and hydrogels were placed in the defects (Figure 41b). The incisions were closed by using absorbable sutures and animals were administered with subcutaneous analgesic (0.05 mg/ml buprenorphine; Schering-Plough). Mice with empty defects were used as negative controls. All animals were kept in a pathogen-free environment throughout the experiment and sacrificed by cervical dislocation. Skulls were then harvested, fixed with 10% formalin (Sigma) for 48 h and kept at 4ºC in 70% ethanol until use. A summary of the treatment groups can be seen in Table 10.

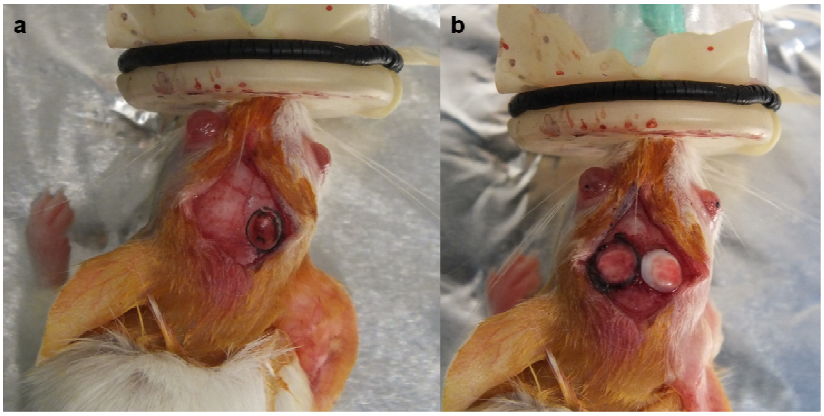

Figure 41. Implantation of 40 mg/ml and 54 mg/ml hydrogels in mouse calvaria. a) Defects with a diameter of 3.5 mm were created on parietal bone in mice. b) Hydrogels fitting the diameter of defects were implanted.

Time	Treatment	Number of defects
Day 0	Empty	6
6 weeks	Empty	6
	54 mg/ml	6
	40 mg/ml	6
12 weeks	Empty	6
	54 mg/ml	6
	40 mg/ml	6

Table 10. Summary of the treatment groups used in the in vivo experiment.

4.1.2.3.3 *Micro-computed tomography*

Micro-computed tomography (µCT) was performed using a Skyscan 1076 in-vivo µCT (Bruker, USA). Images were acquired using a 0.5 mm Al filter in high resolution mode (pixel size: 9 µm) at 50 kV, 199 µA and 10 W with a rotation step of 0.5º and with a total rotation of 180º. Reconstruction was performed in the conditions specified in Table 11; all parameters were set for all samples except post-alignment, which was set for each sample. Images of 0.25 g/cm^3 and 0.75 g/cm^3 bone mineral density (BMD) standards (Bruker) were acquired and reconstructed as abovementioned.

Parameter	Conditions
Beam hardening correction	45
Smoothing	Gaussian filter, 3
Ring artifact reduction	6
Contrast limits	0-0.1
Post-alignment	As required
Hounsfield units (HU) calibration	OFF
Format	JPEG

Table 11. Summary of the conditions used to perform reconstructions.

Reconstructed data sets were reoriented using Dataviewer software (Bruker). The diameter of defects in animals sacrificed after surgery was calculated using CTAn software (Bruker) and a cylinder-shaped volume of interest (VOI) with 3.51 mm diameter and 1.82 mm height was created. Whole-set histograms were adjusted to 48-218 grey levels and BMD calibration was carried out as recommended by the manufacturer. Calculations were performed using the 3D quantification tools included in CTAn; non-defected areas in calvaria frontal bone at 12 weeks post-implantation were used as a reference. Coronal and axial 3D images of the VOI were taken using a custom transfer function in CTVox software (Bruker).

4.1.2.3.4 *Histology*

Calvariae were partially decalcified by incubation with rapid decalcifier (Casa Álvarez) for 2.5 h at RT and washed three times in PBS for 20 minutes. Samples were then subjected to three different stainings.

Regressive hematoxylin and eosin staining. Samples were incubated with Harris hematoxylin (Sigma) for 2.5 minutes and thoroughly washed with tap water. Differentiation was carried out by incubation with 0.3% acid alcohol for 1 minute and stopped by washing samples with tap water. Samples were then incubated with ammonia water (bluing solution) for 1 minute, washed with tap water and incubated with eosin Y (Sigma) for 1 minute; eosin staining was differentiated by incubation with 95% ethanol for 15 seconds. Dehydration and clearing consisted on (i) incubation with 100% ethanol for 30 seconds, (ii) incubation with 100% ethanol for 1 minute, and (iii) and two 3-minutes incubation with xylene (Sigma). Samples were then mounted with Eukitt (Panreac) and sandwiched with coverslips.

Goldner's trichrome. Samples were incubated with Weigert's iron hematoxylin (Sigma), washed with tap water and differentiated in 1% acid alcohol for 5 seconds. After being washed with tap water and rinsed in distilled water, samples were incubated with solution A (1.56 mM Ponceau 2R, 0.43 mM acid fuchsin and 0.196 mM azophloxine in 0.2% acetic acid) for 5 minutes and rinsed in 1% acetic acid. Glass slides were then incubated with solution B (44.2 mM orange G and 21.08 mM phosphomolybdic acid in distilled water) for 3 minutes and rinsed in 1% acetic acid. Samples were then incubated with solution C (2.52 mM light green in 0.2% acetic acid) for 5 minutes and treated with 1% acetic acid for 5 minutes. Dehydration, clearing and mounting were performed as abovementioned.

Alcian blue. Glass slides were incubated with alcian blue solution (7.7 mM alcian blue 8GX in 3% acetic acid, pH 2.5) for 30 minutes, washed with tap water and rinsed in distilled water. Samples were counterstained with nuclear fast red (Sigma) for 5 minutes and washed with tap water. Dehydration, clearing and mounting were performed as previously stated.

4.1.2.3.5 *Statistical analysis*

Data were analyzed by means of t-test or one-way ANOVA with Tukey's post hoc test. All analyses were performed using Prism (GraphPad, version 6.01). Results were considered significant when $p \leq 0.05$ unless otherwise specified.

4.2 RESULTS

4.2.1 Citric acid as a soluble factor

4.2.1.1 Cytotoxicity

A cytotoxicity by indirect contact experiment was performed to assess whether the selected citric acid concentrations were toxic for hMSCs. After a 42.5-h exposure to complete medium supplemented with citric acid, cell number was quantified and normalized to that in control wells (i.e. complete medium without citric acid). Cell quantification revealed that none of the selected concentrations were toxic (Figure 42a). These results were confirmed by live/dead staining (Figure 42b), which showed that almost all cells exposed to citric acid were viable (green cells), with only few cells being dead (red cells). No cells were observed in wells exposed to medium containing phenol.

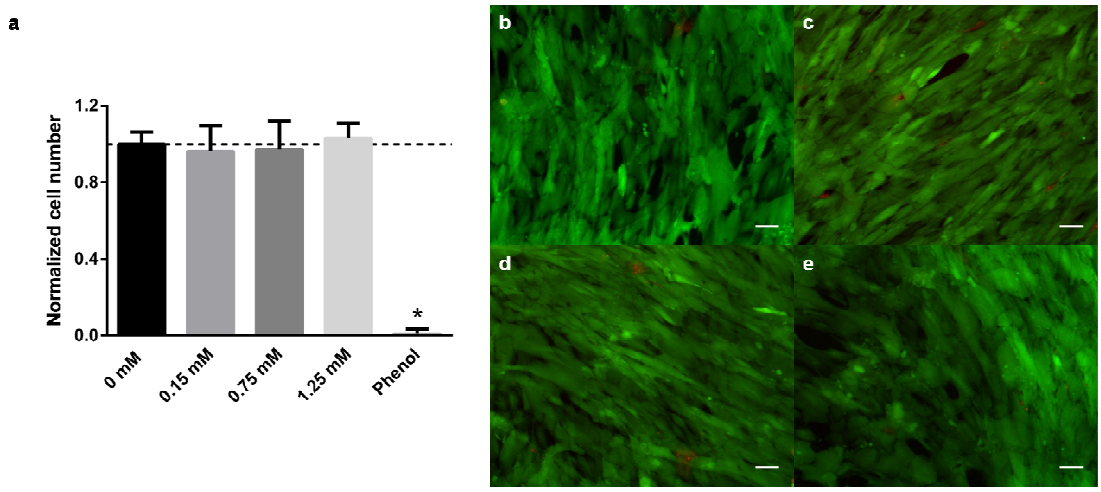

Figure 42. Cytotoxicity of complete medium supplemented with citric acid. a) Cell quantification after a 42.5-h exposure period. Live/dead staining of cells exposed b) 0 mM, c) 0.15 mM, d) 0.75 mM, and e) 1.25 mM citric acid. Scale bar: 10 µm. *p value≤0.0001.

4.2.1.2 Proliferation

Proliferation assays were performed to assess whether the presence of citric acid affects hMSCs proliferation. Cells were cultured for up to 14 days in complete medium and quantified with Alamar blue; cell number at a given time was normalized to that in control wells (i.e. 0 mM citric acid). Cell number at day 1 seemingly increased as higher citric

acid concentrations were used, although just wells exposed to 1.25 mM citric acid displayed significantly increased cell number (Figure 43). Despite the presence of citric acid seemingly led to increased adhesion efficiencies, the cell number in control wells equaled those exposed to citric acid throughout the experiment, at the end of which all conditions led to similar cell numbers.

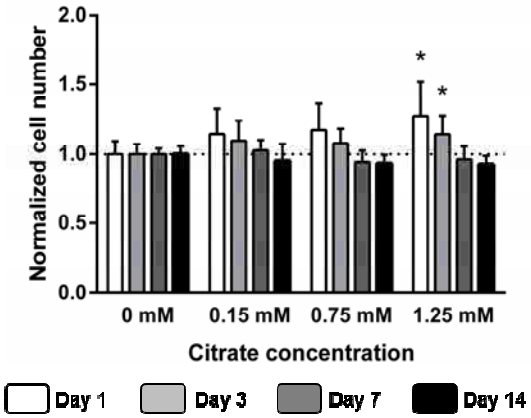

Figure 43. hMSCs proliferation in citric acid-supplemented complete media. **p* value≤0.05.

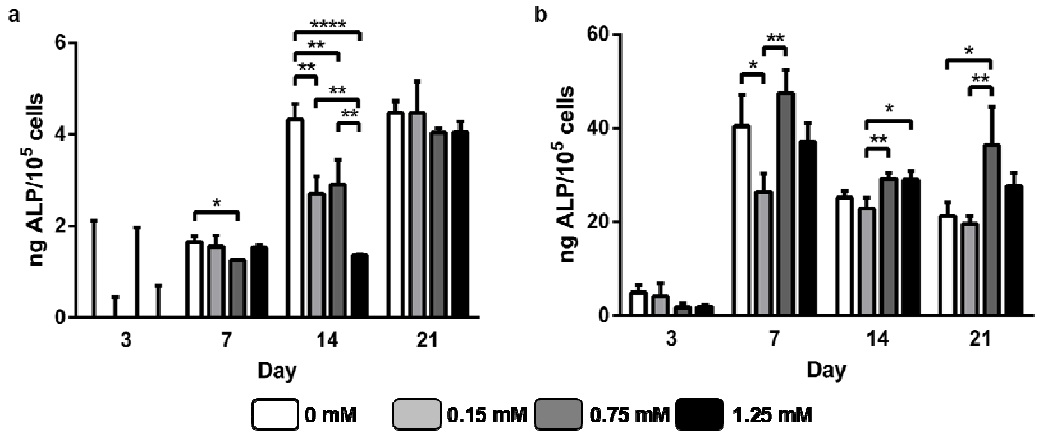

Figure 44. ALP expression in hMSCs cultured in culture media containing citric acid. hMSCs were cultured either in a) complete medium or b) osteogenic medium. **p* value≤0.05; ****p* value≤0.01; *****p* value≤0.0001.

4.2.1.3 ALP expression

hMSCs were cultured in either complete or osteogenic media to assess whether the presence of citric acid might either induce osteogenic differentiation or potentiate the effect of differentiation medium. As shown in Figure 44a, low ALP expression was found in all conditions and at all times when cells were cultured in complete medium; ALP

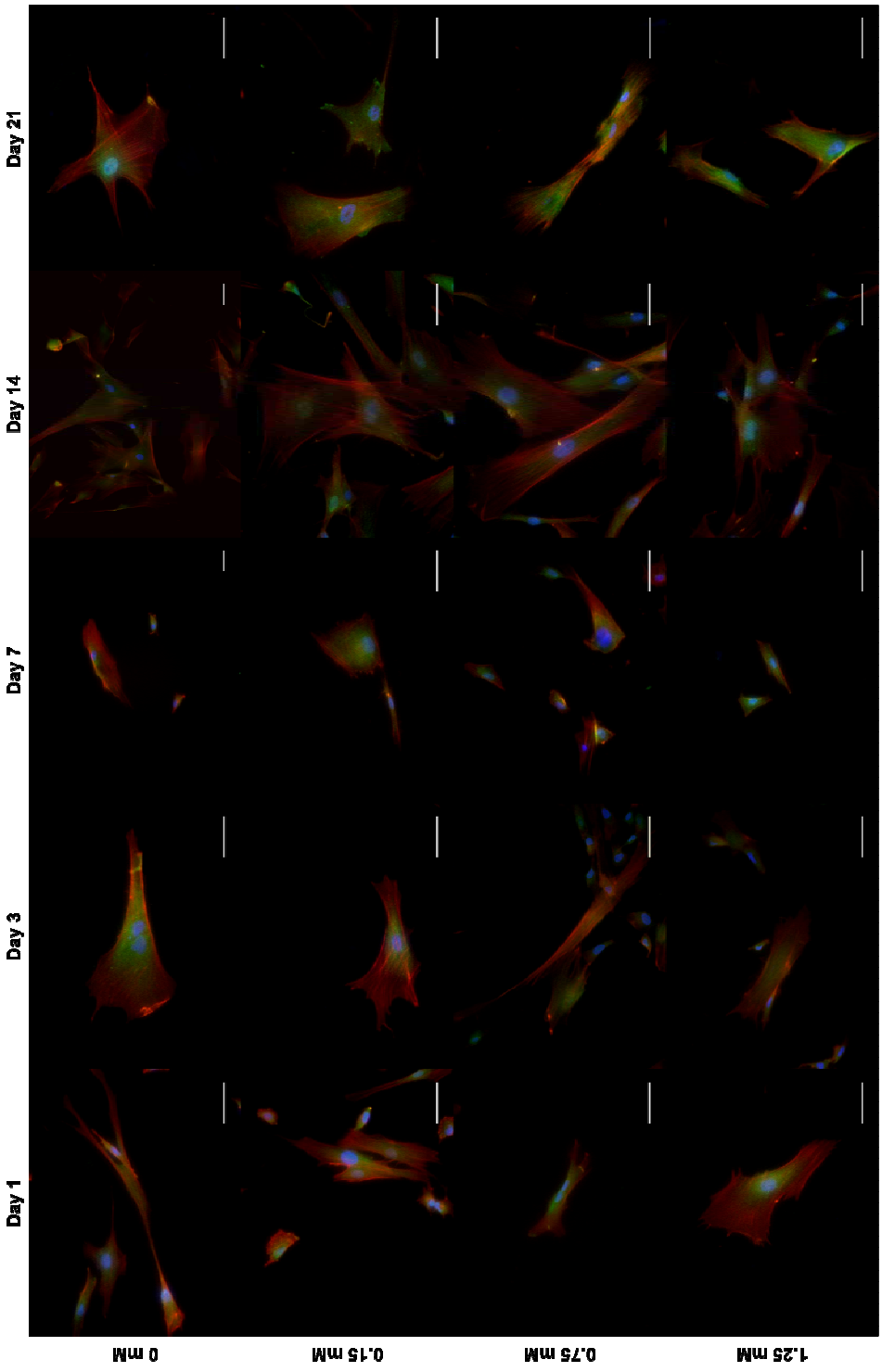

Figure 45. Immunostaining for OPN expression in hMSCs cultured in complete medium. Scale bar: 100 µm.

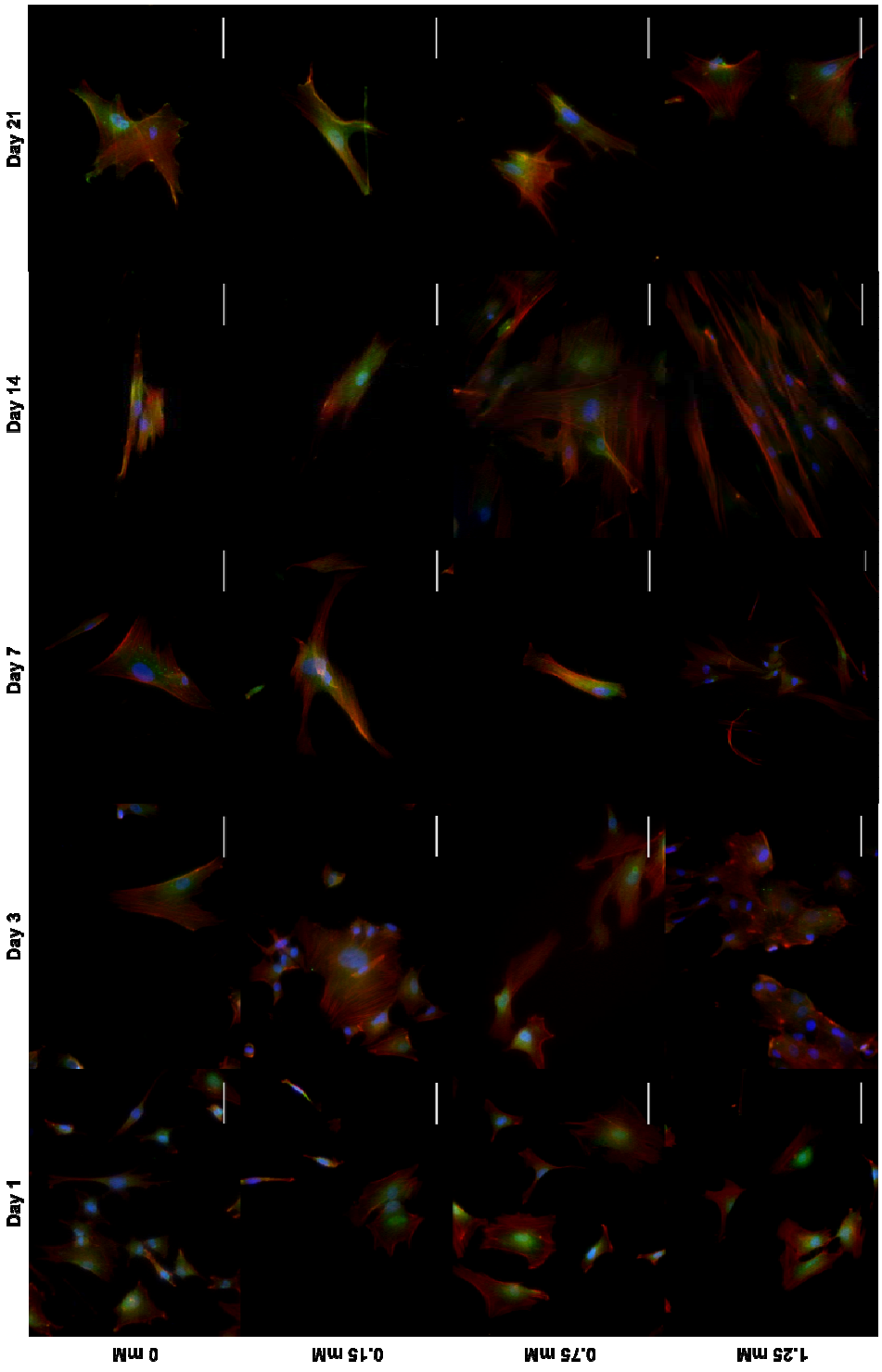

Figure 46. Immunostaining for OPN expression in hMSCs cultured in osteogenic medium. Scale bar: 100 µm.

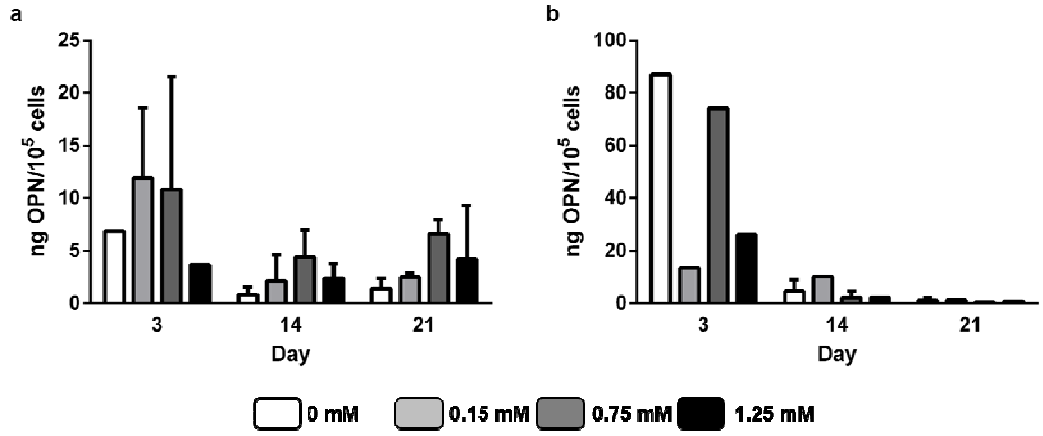

Figure 47. OPN expression in hMSCs cultured in culture medium containing citric acid. hMSCs were cultured either in a) complete medium or b) osteogenic medium.

levels in control medium (0 mM) were significantly higher than those in citric acid-containing media at day 14, but by day 21, ALP levels in cells cultured with citric acid equaled those in control cells. ALP expression was found to peak at day 7 in osteogenic media and to be increased in cells cultured with either 0 mM or 0.75 mM citric acid (Figure 44b). From day 7 on, ALP expression decreased and a second peak was found at day 21 in cells cultured with 0.75 mM citric acid.

4.2.1.4 OPN expression

OPN expression in hMSCs cultured in culture media with or without citric acid was assessed by immunofluorescence and ELISA. Despite immunofluorescence didn't reveal substantial changes throughout the experiment in OPN expression in cells in complete medium, cells cultured in the presence of citric acid seemingly expressed higher levels of the marker by day 21 (Figure 45). Quantification by ELISA showed that OPN expression decreased throughout the experiment and revealed higher expression at day 21 in cells cultured with citric acid when compared to that in control cells, although differences were not statistically significant (Figure 47a). Immunofluorescence of cells cultured with osteogenic medium showed that OPN levels didn't significantly change throughout the experiment in any of the conditions (Figure 46). Quantification by ELISA revealed OPN levels in cells cultured in osteogenic medium also decreasing along the experiment in all the conditions (Figure 47b). High expression levels at day 3 in cells cultured in osteogenic medium containing 0 mM and 0.75 mM were due to one of the replicates being discarded.

4.2.1.5 OCN expression

OCN expression was assessed by ELISA. Similar to the OPN case, OCN was found to decrease along the experiment in all the conditions either in complete (Figure 48a) or osteogenic media (Figure 48b). No statistically significant differences were found in any case.

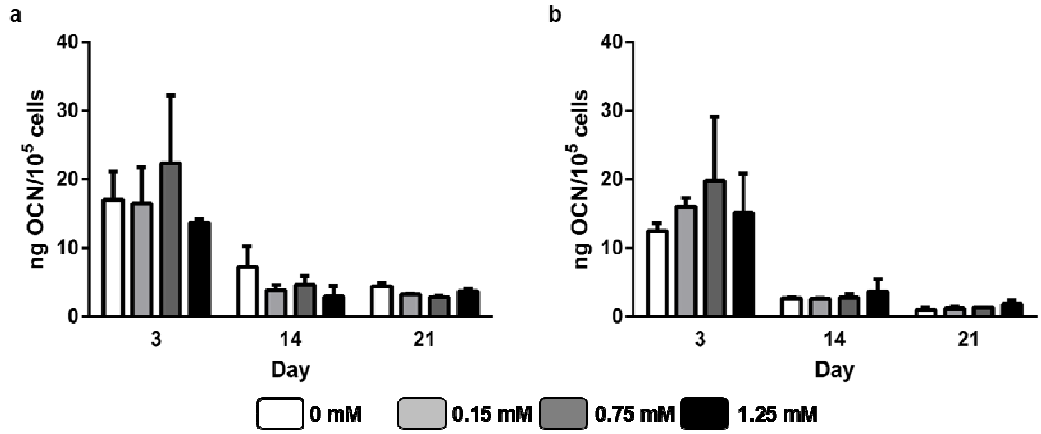

Figure 48. OCN expression in hMSCs cultured in culture medium containing citric acid. hMSCs were cultured either a) complete medium or b) osteogenic medium.

4.2.1.6 Mineralization

Mineralization was assessed by staining calcium deposits with Alizarin red, which was subsequently quantified. Alizarin red staining revealed that low calcium deposition occurred in all the conditions at all time points, either in complete or osteogenic media (Figure 49a-x); in the case of osteogenic medium, slightly darker staining was observed in cells cultured with 0.15 mM and 0.75 mM citric acid. These results were confirmed by quantification of bound alizarin red, which showed low calcium deposition in all the conditions at all time points and slightly increased calcium levels in cells cultured with osteogenic medium plus 0.15 mM and 0.75 mM citric acid, although differences were not significant (Figure 49y and z).

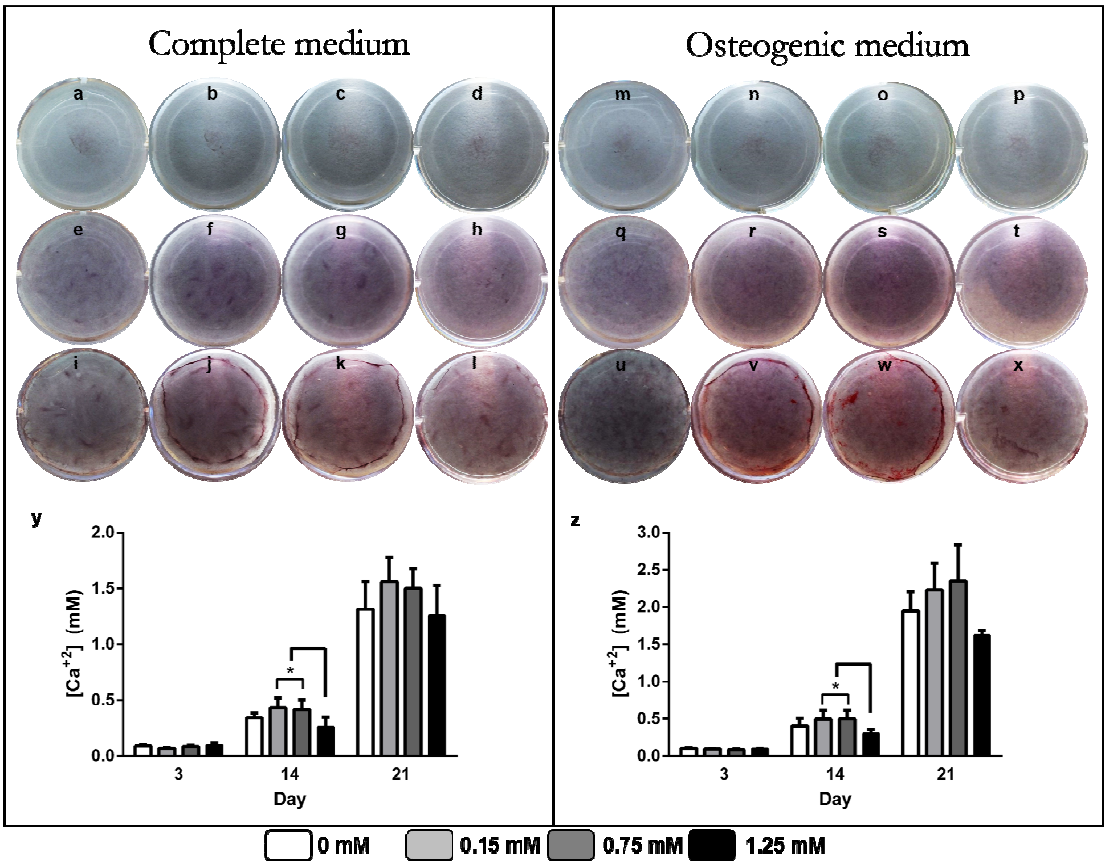

Figure 49. Mineralization expression in hMSCs cultured in culture medium containing citric acid. Alizarin red staining was performed on hMSCs cultured with 0 mM (a,e,i,m,q,u), 0.15 mM (b,f,j,n,r,v), 0.75 mM (c,g,k,o,s,w) or 1.25 mM (d,h,l,p,t,x) for 3 (upper row), 14 (mid row) or 21 days (lower row). Bound alizarin red in complete (y) or osteogenic media (z) was quantified. **p* value≤0.05.

4.2.2 Tailored hydrogels

4.2.2.1 In vitro biological characterization

4.2.2.1.1 *Cytotoxicity*

A cytotoxicity by indirect contact assay was performed to assess tailored hydrogels (E9C1 54 mg/ml) for the release of toxic molecules. After a 42.5-h exposure period, cells were quantified with Alamar blue and subjected to live/dead staining. Alamar blue quantification showed that exposure to hydrogels led to a cell number reduced by 20% compared to that in control wells (TCPS; Figure 50a). Live/dead staining revealed almost no dead cells in control wells (Figure 50b) nor in those exposed to hydrogels (Figure 50c); in the latter case, this phenomenon was probably due to dead cells being removed during the wash step previous to staining.

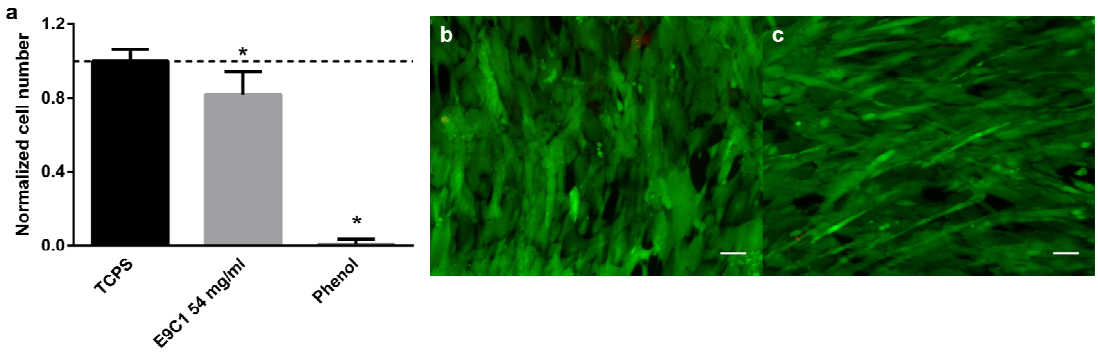

Figure 50. Cytotoxicity of 54 mg/ml E9C1 hydrogels. a) Cell quantification after a 42.5-h exposure period. Live/dead staining of b) controls cells and c) cells exposed to 54 mg/ml E9C1 hydrogels. Scale bar: 10 µm. *p value≤0.01.

4.2.2.1.2 *Proliferation*

The proliferation of hMSCs in 54 mg/ml and 40 mg/ml E9C1 hydrogels was quantified at days 3, 7, 14 and 21. As shown in Figure 51, cell numbers in hydrogels were significantly higher than those in TCPS at days 3 (4269.3 ± 697.8 in 54 mg/ml samples, 3610.7 ± 460 in 40 mg/ml samples, and 289.3 ± 267.3 in TCPS), 7 (10633.3 ± 1037.3 in 54 mg/ml matrices, 10062.7 ± 575.1 in 40 mg/ml samples, and 458.7 ± 148 in TCPS) and 14 (29636.7 ± 7706.3 in 54 mg/ml hydrogels, 34040 ± 9127.5 in 40 mg/ml hydrogels, and 11286.7 ± 993.2 in TCPS); by the end of the experiment, just RGD-C samples displayed cell numbers significantly higher than those in TCPS (71206.7 ± 25666.2 in 54 mg/ml hydrogels, 51953 ± 4437.7 in 40 mg/ml hydrogels, and 29120 ± 13286.96 in TCPS). No statistically significant differences between hydrogels were noticed at any time point.

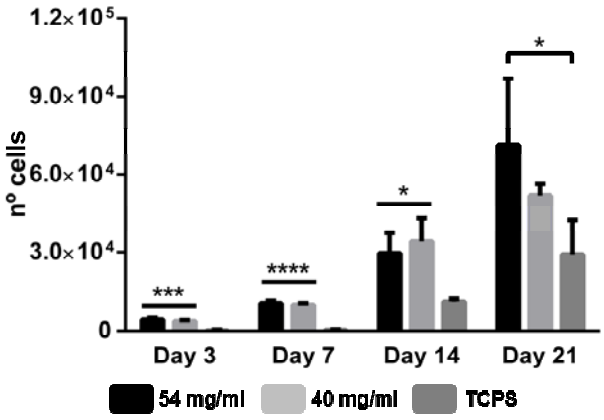

Figure 51. hMSCs proliferation on tailored and non-tailored hydrogels in complete medium. *p value≤0.05.

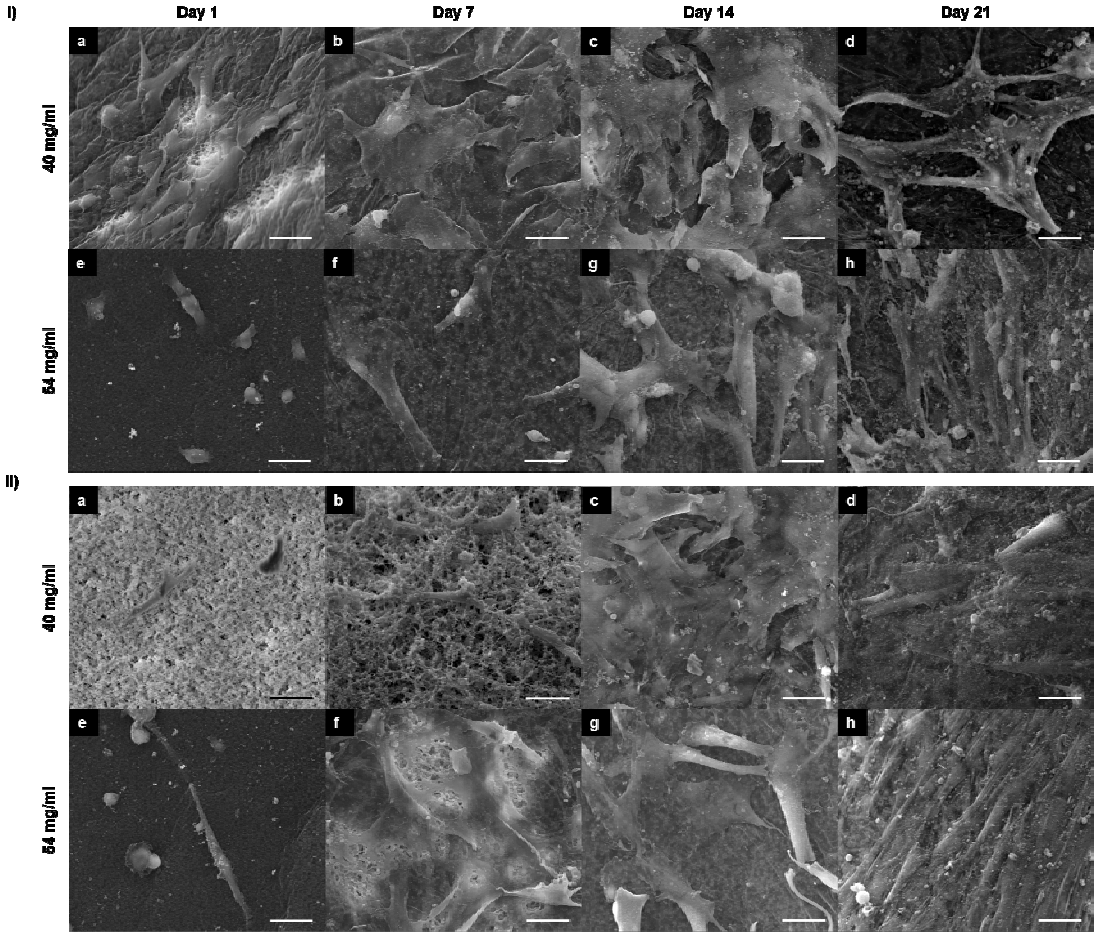

Figure 52. Qualitative assessment of hMSCs proliferation seeded on hydrogels in i) complete and ii) osteogenic media. Scale bar: 50 µm.

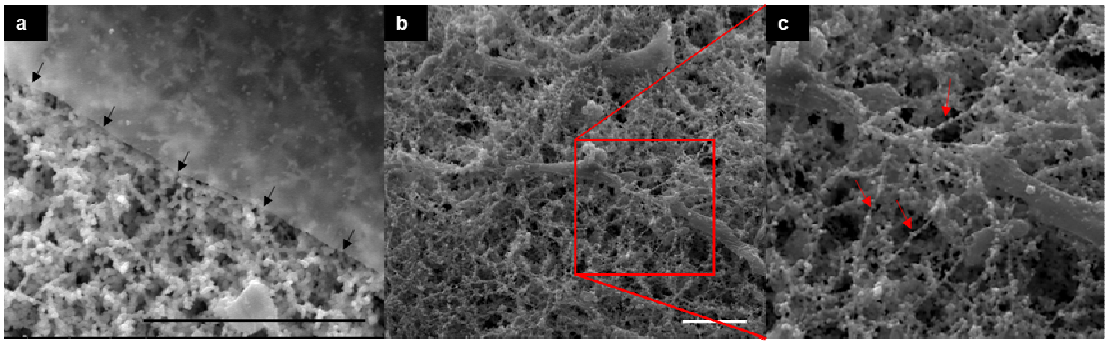

Figure 53. Detailed view of hydrogels surface by SEM. a) Surface of a 54 mg/ml E9C1 hydrogel containing a thin layer of polymer (black arrows). b-c) Surface of a 40 mg/ml E9C1 hydrogel exposing the polymeric fiber-like structures (red arrows) in E9C1 hydrogels. Scale bar: 50 µm.

Cell proliferation in complete medium was qualitatively assessed by SEM, which confirmed that hMSCs are able to proliferate both in tailored and non-tailored hydrogels to

a similar extent (Figure 52,i). Additionally, the proliferation in hydrogels in osteogenic medium was qualitatively assessed by SEM. This test showed that cells behaved normally in differentiation medium, displaying a normal morphology (Figure 52,ii). No cells were observed inside hydrogels in any condition and at any time point. Interestingly, SEM observations revealed that most of the hydrogels displayed a thin layer on their surface (Figure 52 i) and ii), and Figure 53) assumed to be "collapsed polymer" and that was seemingly shielding hydrogels microarchitecture and hindering 3D cell colonization.

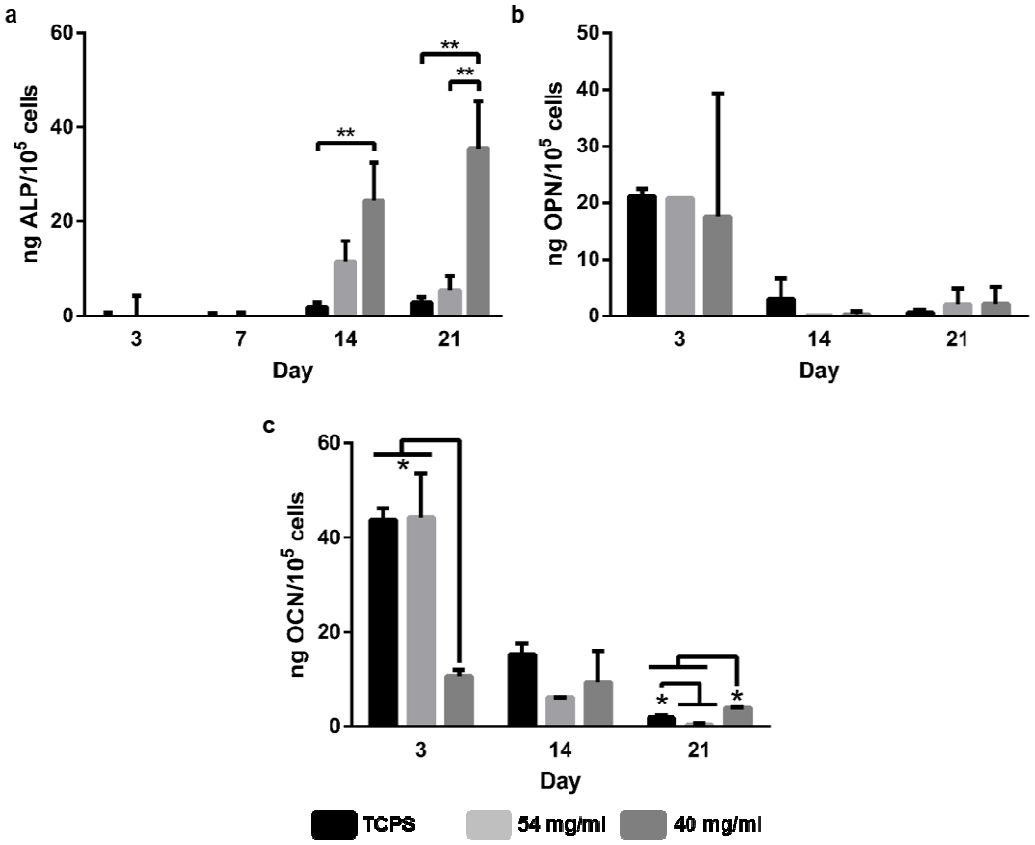

Figure 54. Expression of osteogenic markers in hMSCs seeded in tailored and non-tailored hydrogels. *p value≤0.05; **p value≤0.01.

4.2.2.1.3 *In vitro osteogenic differentiation*

The expression of ALP, OPN and OCN in cells cultured in hydrogels was quantified and compared to that in cells cultured in TCPS. As shown in Figure 54a, ALP seemingly peaked at day 21, with cells cultured in TCPS expressing the higher amount of the marker. Globally, although it seemingly increased over time, ALP expression in cells cultured in

both hydrogels (and specially those seeded on 54 mg/ml) was consistently low. No statistically significant differences were observed between hydrogels.

As for the expression of OPN (Figure 54b) and OCN (Figure 54c), levels of the markers were found to decrease along the experiment. No clear differences between hydrogels and TCPS were observed beyond OCN expression at day 3, when significantly increased levels were found in the case of cells seeded on hydrogels.

4.2.2.2 In vivo biological characterization

4.2.2.2.1 *µCT*

µCT was performed to quantify bone within defects. Defects with 3.5-mm diameter were created in SCID mice calvaria and implanted with 40 mg/ml and 54 mg/ml E9C1 hydrogels; control defects were left empty. Bone was quantified at 6 and 12 weeks after implantatation; empty defects at day 0 were used to determine the mean diameter of defects to create a VOI with a proper diameter, and to account for the initial amount of bone. A VOI with 3.51-mm diameter and 1.82-mm height was created; the VOI was allowed to possess a little excess in height to ensure that all the new tissue was enclosed within it. 3D reconstructions of all the defects at day 0, and 6 and 12 weeks after implantation used for quantification are shown in Figure 55; coronal and axial views of defects are presented to illustrate bone growth in diameter and thickness.

Different parameters were quantified using non-defected areas of frontal bones at 12 weeks post-implantation as a reference. First, bone volume was quantified. As shown in Figure 56a, bone wasn't completely removed during surgery; thin pieces of bone were found in empty defects at day 0 (Figure 55a). Bone volume was found to increase to a similar extent in the three groups during the first 6 weeks of treatment (2.06 ± 0.20 mm^3 in empty defects, and 2.42 ± 0.72 mm^3 and 2.56 ± 0.37 mm^3 in 54 mg/ml and 40 mg/ml hydrogel-treated defects). By the end of the experiment, defects treated with hydrogels displayed a bone volume (3.38 ± 0.48 mm^3 in 54 mg/ml group and 3.47 ± 0.82 mm^3 in 40 mg/ml group) significantly higher than that in empty defects (1.92 ± 0.40 mm^3), in which no differences between the two time points were observed. Interestingly, defects treated with 40 mg/m hydrogels displayed a bone volume significantly higher than that in frontal

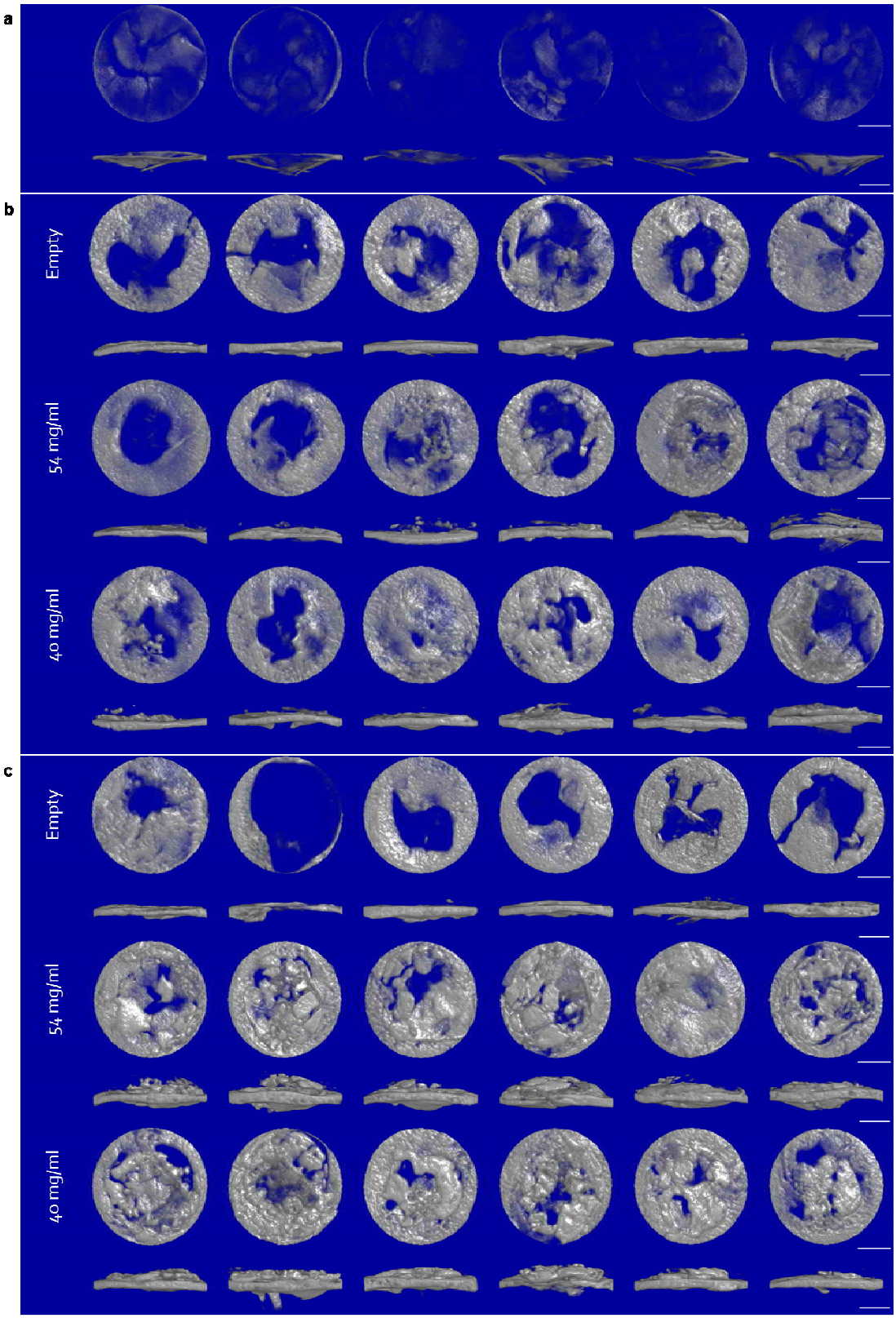
a
b
Empty
54 mg/ml
40 mg/ml
c
Empty
54 mg/ml
40 mg/ml

Figure 55. 3D reconstructions of defects in SCID mice. Coronal and axial views of defects (a) at day 0, and after (b) 6 and (c) 12 weeks of implantation were generated. Scale bar: 1 mm. Apparent density in the 3D reconstructions is representative of bone thickness.

bone (namely, calvaria; 2.71 ± 0.16 mm^3). No statistically significant differences between hydrogels were found at any time point.

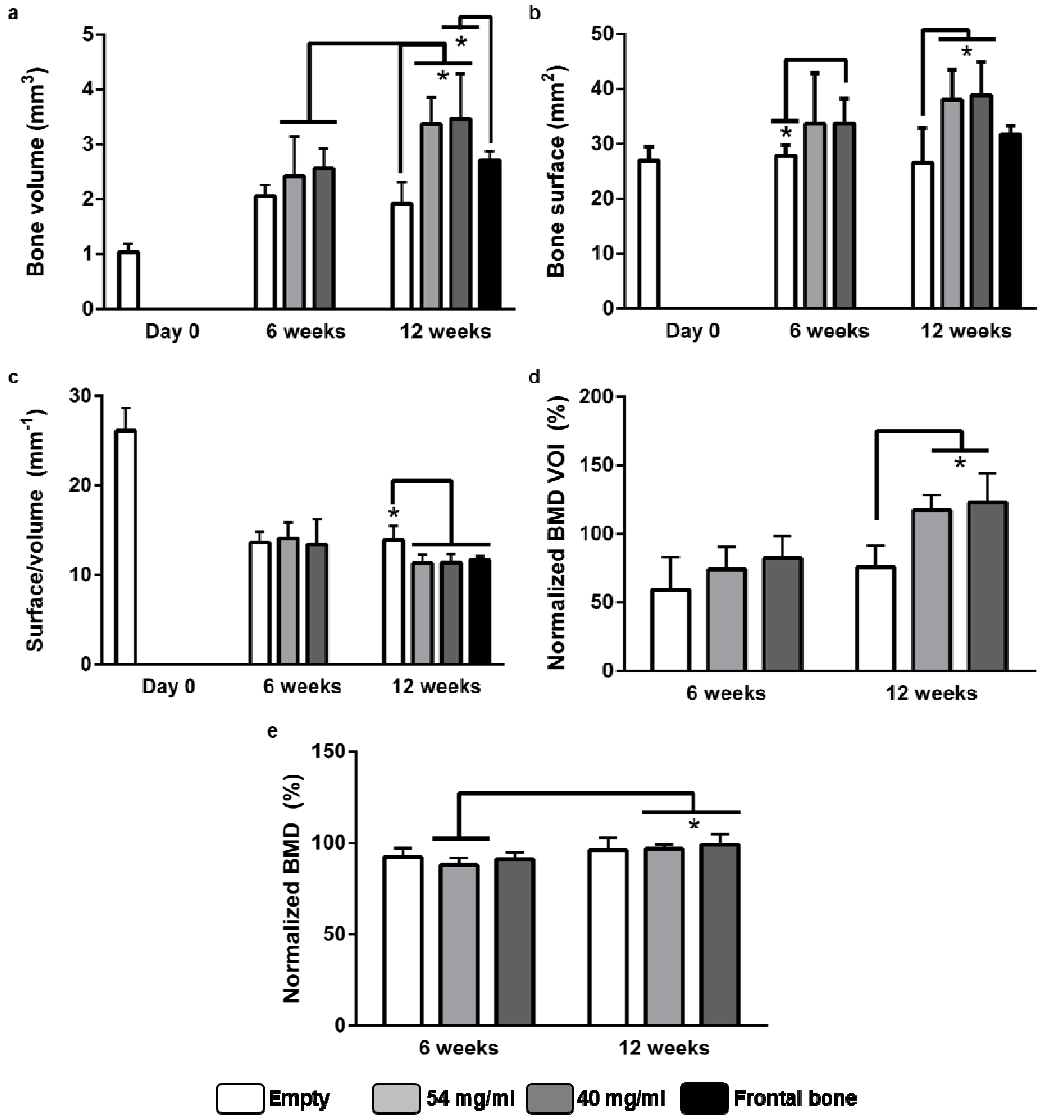

Figure 56. Summary of µCT quantitative results. a) Bone volume, b) bone surface, c) surface/volume, d) volumetric BMD, and e) BMD were quantified. **p* value≤0.05.

Bone surface was also quantified (Figure 56b). Bone surface in empty defects was found to not significantly change along the experiment (26.96 ± 2.51 mm^2 at day 0, 27.92 ± 1.89 mm^2 at 6 weeks, and 26.60 ± 6.29 mm^2 at 12 weeks). Animals in the 40 mg/ml group were found to display a bone surface (33.75 ± 4.47 mm^2) significantly higher than that in

control defects (27.92 ± 1.89 mm^2) at week 6 and, by the end of the experiments, both hydrogels led to significantly increased bone surface (38.02 ± 5.48 mm^2 in the 54 mg/ml group, and 38.76 ± 6.13 mm^2 in the 40 mg/ml group). No differences between hydrogels were observed during the experiment.

Bone in day 0 defects was found to possess a high surface/volume ratio (or surface density; 26.14 ± 2.51 mm^{-1}; Figure 56c). Surface density was found to have decreased to a similar extent in all three groups at week 6(13.63 ± 1.18 mm^{-1} in empty defects, 14.11 ± 1.78 mm^{-1} in the 54 mg/ml group, and 13.42 ± 2.82 mm^{-1} in the 40 mg/ml group). This trend was kept during the rest of the experiment, by the end of which surface density of hydrogel-treated defects (11.30 ± 1.02 mm^{-1} in the 54 mg/ml group, and 11.36 ± 1.03 mm^{-1} in the 40 mg/ml group) was significantly lower than that in empty defects (13.94 ± 1.60 mm^{-1}) and no significantly different from that in frontal bone (11.72 ± 0.41 mm^{-1}).

Two bone mineral density (BMD) calculations were performed. First, the volumetric BMD results are presented (Figure 56d). The volumetric BMD (namely, BMD VOI) results from calculating mean BMD in the whole VOI, considering both bone and void volume; results were normalized to that in un-defected frontal bone. This parameter was found to be similar for all three groups at week 6 (59.31 ± 23.61 % in empty defects, 74.18 ± 16.22 % in the 54 mg/ml group, and 82.56 ± 16.05 % in the 40 mg/ml group) and to be significantly higher in hydrogel-treated defects by 12 weeks (117.59 ± 11.05 % in the 54 mg/ml group, and 122.96 ± 21.15 % in the 40 mg/ml group) when compared to that in empty defects (75.70 ± 15.57 %). No differences between hydrogels were found.

Results of BMD calculations, corresponding just to the BMD of bone enclosed in the VOI normalized to that in frontal bone, are presented in Figure 56e. At a given time point and along the experiment, all groups were found to possess non-statistically different BMD values (6 weeks: 92.52 ± 4.65 % in empty defects, 87.95 ± 4.03 % in the 54 mg/ml group, and 91.14 ± 3.83 % in the 40 mg/ml group; 12 weeks: 96.18 ± 6.80 % in empty defects, 96.79 ± 2.38 % in the 54 mg/ml group, 99.09 ± 5.78 % in the 40 mg/ml group).

4.2.2.2.2 *Histology*

The tissue in treated and untreated defects was studied by histology. Hematoxylin and eosin (H&E), Goldner's trichrome and alcian blue stainings were performed to assess cell infiltration into the defects/hydrogels, the formation of osteoid and mineralized bone, and the mode of osteogenesis, respectively. A general view of the three stainings in all 7 study groups can be found in Figure 57.

As shown by µCT, thin pieces of bone remaining in the defects after surgery (namely, day 0) were observed after H&E staining (Figure 57). Histological stainings showed that little regeneration occurred in empty defects, in which low amount of tissue was observed reconnecting defects ends at either 6 or 12 weeks (Figure 57, and Figure 58a and b). This connecting tissue was shown to contain both osteoid and mineralized bone (Figure 58c and d), with defects at 6 weeks containing more osteoid and less mineralized tissue than their 12 weeks counterparts. Alcian blue staining, here used to detect the presence of cartilage, wasn't performed on empty defects as calvaria is naturally formed by intramembranous ossification [3].

40 mg/ml hydrogels were found to be partially degraded after 6 weeks of implantation (Figure 57). At this time point, cells had entered the scaffold (Figure 59d, e and f), which was found to be bound to native bone (Figure 59e). Additionally, cells entering the scaffold were seemingly undergoing osteogenic differentiation, as evidenced by the presence of osteoid (Figure 59f). Mineralized matrix, if present, couldn't be detected given that the hydrogel strongly stained in green. 40 mg/ml scaffolds displayed higher degradation and cellularity (Figure 57 and Figure 59j) at 12 weeks post-implantation, when new bone was found to have formed within the hydrogel (Figure 59k and n). Interestingly, this new bone was seemingly undergoing remodeling as suggested by the presence of resorption sites and osteoclasts (Figure 59k and n); bone remodeling was parallel to bone formation, as evidenced by the presence of osteoid inside the hydrogel (Figure 59l). Alcian blue staining was negative (Figure 57), pointing out that bone formation occurred by intramembranous ossification.

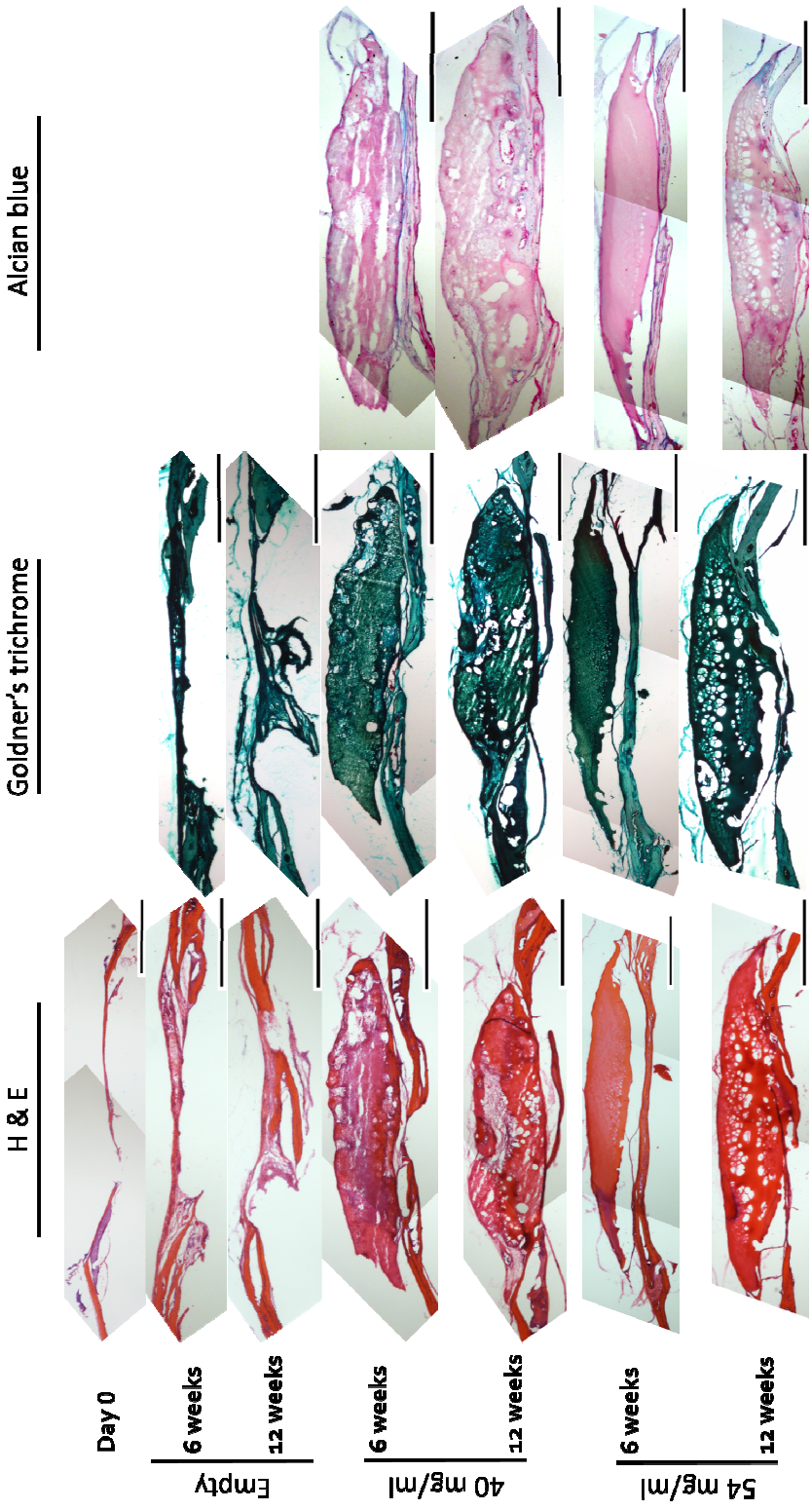

Figure 57. General view of hydrogel-treated and control defects subjected to hematoxylin & eosin (H&E), Goldner's trichrome, and alcian blue histological stainings. H&E) Purple: nuclei; pink: cytoplasm; orange: mineralized bone. Goldner's trichrome) Green: mineralized

bone; blue: cytoplasm, black: nuclei. Alcian blue) Blue: glycosaminoglycans; pink: cytoplasm; pink-red: nuclei. Scale bar: 0.5 mm.

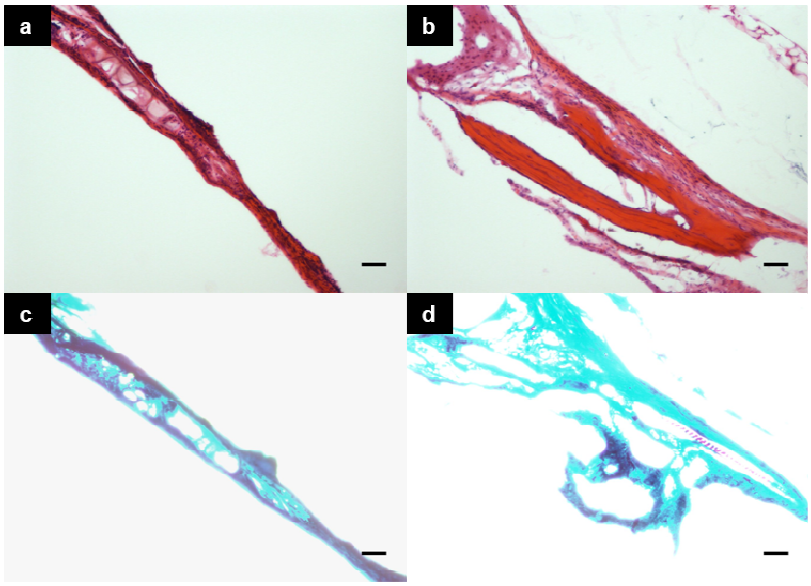

Figure 58. Detailed view of control defects. Empty defects at 6 (a,c) and 12 weeks (b,d) were subjected to hematoxylin & eosin (a-b), and Goldner's trichrome stainings (c-d). a-b) Purple: nuclei; pink: cytoplasm; orange: mineralized bone. c-d) Due to the strong greenish staining of mineralized collagen masking osteoid, overexposed pictures are shown. Light blue: mineralized bone; red-purple: osteoid. Scale bar: 50 µm.

54 mg/ml hydrogels were found to be barely degraded (Figure 57) and invaded by cells at 6 weeks (Figure 59a); cells were mainly found in the outer part of scaffolds, with cell invasion occurring at discrete places. Degradation and invasion were found to be increased at 12 weeks (Figure 57 and Figure 59g); although increased, cell invasion was also found to be discrete. Despite low cell invasion, osteoid was found at both time points (Figure 59c and i); mineralized matrix couldn't be detected at any time point due to hydrogels getting strongly stained in green. Hydrogels were found to be discretely bound to bone by week 6 (Figure 57 and Figure 59b) and to be integrated into the tissue at 12 weeks post-implantation (Figure 59g and h), time at which blood vessels were noticed in the bone-hydrogel interface (Figure 59h and m). As in the case of 40 mg/ml hydrogels, alcian blue staining was negative (Figure 57), suggesting that bone formation took place by intramembranous ossification.

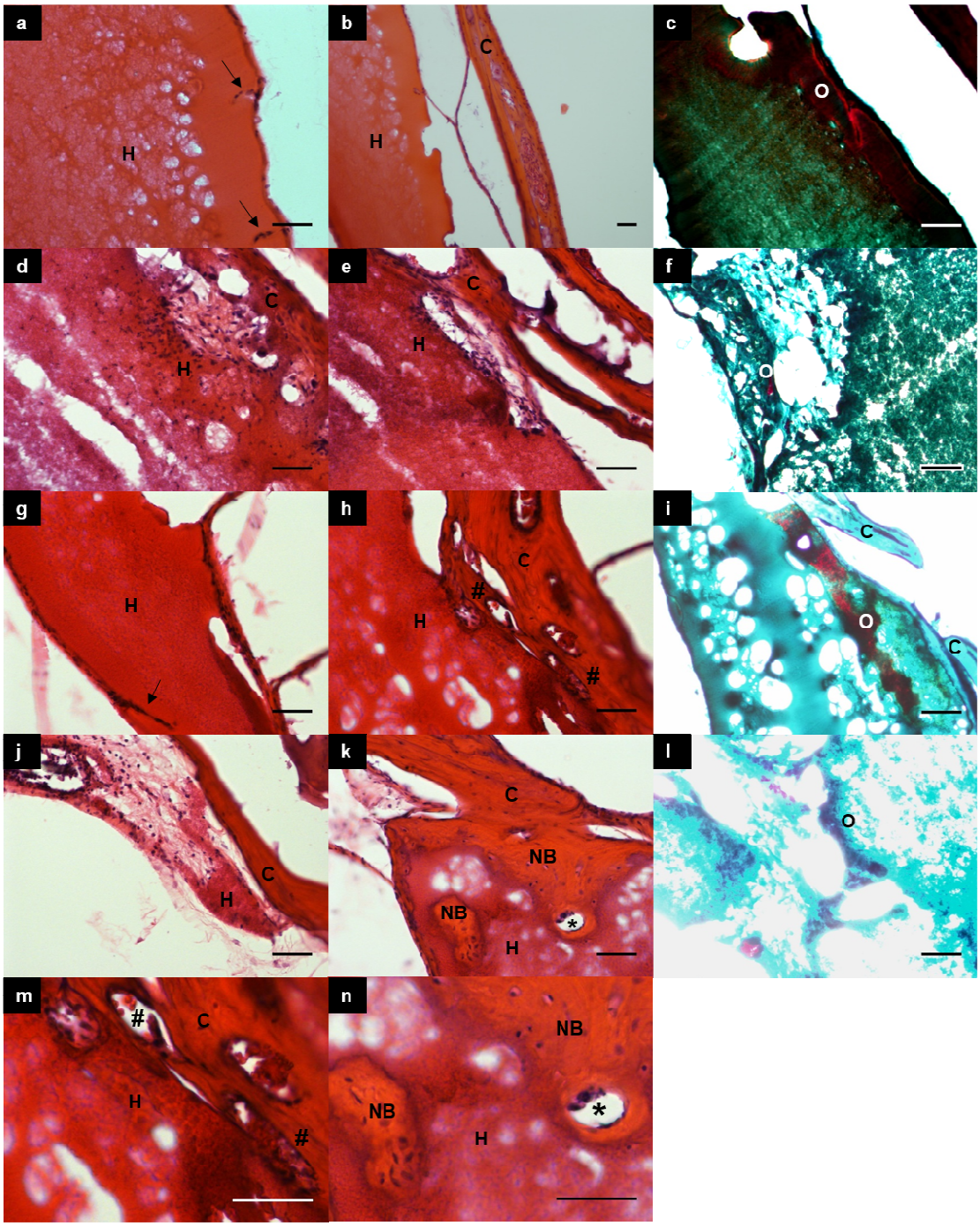

Figure 59. Detailed view of hydrogel-treated defects. Defects treated with 54 mg/ml (a-c, g-i, m) or 40 mg/ml (d-f, j-l,n) hydrogels at 6 (a-f) and 12 (g-n) weeks post-implantation were stained with H&E (a,b,d,e,g,h,j,k,m,n) and Goldner's trichrome (c,f,i,l). H&E) Purple: nuclei; pink: cytoplasm; orange: mineralized bone. Goldner's trichrome) Green: mineralized bone; blue: cytoplasm; black: nuclei; red: osteoid. Overexposed pictures of Goldner's trichrome) light blue: mineralized bone; red-purple: osteoid. H: hydrogels; C: calvaria; O: osteoid; NB: new bone. Arrows: cells invading 54 mg/ml hydrogels; hash: blood vessels in the hydrogel-bone interface; asterisk: osteoclast. Scale bar: 50 µm.

4.3 DISCUSSION

Citrate has been known to have bone as its main deposit since the early 40s [370,372]. Despite the fact that such a localized citrate accumulation was likely to be a reflection of its pivotal role in bone biology, important questions as to its origin and function have been left unattended for decades.

Citric acid in bone has been long assumed to be incorporated from blood through the sodium-citrate transporter, which is seemingly not expressed in osteoblasts [524]; instead, citric acid seems to be locally overexpressed and secreted by osteoblasts [32,524]. Once secreted, it has been hypothesized to bind to hydroxyapatite to control the size [6] and crystallinity [525] of the mineral phase in concert with NCPs [25] and, thus, to be essential for an optimum mechanical performance of the tissue.

Citric acid has been shown to be essential for the adipogenic differentiation of pre-adipocytes [526]. During adipogenic differentiation, mitochondria-to-cytosol transported citrate is seemingly used for the synthesis of fatty acids. Interestingly, when this transport is abrogated, not only fat accumulation is reduced but the expression of PPARγ (Peroxisome proliferation-activated receptor gamma), a master regulator of adipogenic differentiation [527], is abolished [526]. Lipogenesis is not just essential in the case of fat-accumulating phenotypes, but is also involved in general eukaryotic processes such as membranogenesis (i.e. synthesis of plasma membrane). Membranogenesis is especially active during cell proliferation and it's related to high bioenergetic and synthetic requirements. In this context, it has been hypothesized that extracellular citrate could be transported into the cytosol, where it would be used to produce acetyl-CoA and thus to synthetize fatty acids [520]. This transport would be carried out by the sodium-coupled citrate transporter (NaCT), as demonstrated in human colon carcinoma cells [528] and cells from rat liver [529]. Despite this seems not to be a common metabolic route, we asked ourselves whether citrate being released during the in vivo degradation of our citric-acid crosslinked hydrogels could have an effect on hMSCs metabolism and thus affect their proliferation and/or differentiation. To perform this study, three citrate concentrations were selected: 0.15 mM, 0.75 mM and 1.25 mM. 0.15 mM corresponds to the lower citric

acid levels in plasma, which are in the 0.15 mM-0.25 mM range (Dr. Costello, personal communication). 1.25 mM corresponds to the complete release of citric acid from 54 mg/ml HRGD6 hydrogels in a volume of 200 µl (volume of medium used to perform cell culture on our hydrogels) assuming that citric acid used to produce aforesaid hydrogels is completely incorporated into the network. 0.75 mM was selected as an intermediate concentration.

Prior to testing their effect on hMSCs proliferation and osteogenic differentiation, the three selected concentrations were assessed for cytotoxicity using supplemented complete medium. Cytotoxicity has been reported after exposing osteoblasts [530] and fibroblasts [531] to culture medium supplemented with citric acid at concentrations higher than 11.9 mM. In these studies, the pH of supplemented media was left unadjusted, rendering impossible to clearly attribute the cytotoxic effect to citric acid itself rather than to the acidic pH of supplemented media. As shown in Figure 42, our selected concentrations, well below the reported cytotoxic values, were 100% cytocompatible, leading to unaffected cell number and morphology. When hMSCs were cultured with supplemented medium, a concentration-dependent increase in cell adhesion was observed, with the 1.25 mM concentration leading to a significantly increased cell number at days 1 and 3 (Figure 43). However, cell numbers in citric acid-treated wells equaled those in control wells along the experiment, suggesting that herein used concentrations were safe for hMSCs and thus feasible to be used to test the effect of the tricarboxylic acid on hMSCs osteogenic differentiation.

The effect of citric acid on hMSCs differentiation was studied by quantifying calcium deposition and the expression of ALP, OCN and OPN, which are routinely used to assess osteogenic differentiation. Both complete and osteogenic culture media were supplemented with citric acid to investigate whether the tricarboxylic acid can either induce osteogenic differentiation or potentiate the effect of osteogenic supplements, respectively. Calcium deposition was found to increase over time in both cases; slightly higher values were obtained when osteogenic medium was used, with an apparent concentration-dependent increase in calcium deposition (although not statistically significant) for concentrations up to 0.75 mM by day 21 (Figure 49).

ALP expression in complete medium increased along the experiment, but overall values were low in all cases (Figure 44a), suggesting that none of the concentrations induced osteogenic differentiation. When osteogenic medium was used, ALP expression dramatically increased from day 3 to day 7, at which expression peaked in cells cultured with 0 mM and 0.75 mM citric acid (Figure 44b). From day 7 on, ALP expression slightly decreased in all conditions and a second peak at day 21 was observed in cells cultured with 0.75 mM citric acid for 21 days (although the peak was lower than that at day 7). ALP, an early marker of osteogenic differentiation, is involved in mineralization [532] and its expression precedes the formation of mineral deposits. Herein, despite ALP expression seemingly peaked at day 7 in cells cultured in osteogenic medium and reached values ca. 10 times higher than those reached when using complete medium, calcium deposition in osteogenic medium was barely higher than that in complete medium. In order to rule out abnormal cell behavior as a reason for reduced mineralization, calcium deposition should have been measured beyond day 21, given that herein used cells may take longer to mineralize.

The quantification of OPN (Figure 47) and OCN (Figure 48) expression revealed high expression of the late markers at day 3 and expression returning to basal levels throughout the experiment. Stem cells are well known to undergo spontaneous differentiation upon physical contact with neighboring cells, so culturing them to high confluence can lead to pre-commitment, an undesirable outcome if differentiation experiments are to be performed. Despite herein used hMSCs were cultured avoiding confluence, primary cells can undergo culture-induced alterations (reduced migration, proliferation, differentiation potential and trophic activity among others [61,143–149]) that, together with donor-related variability [533], can result in unforeseen behavior. Thus, it is hypothesized that hMSCs might have pre-committed during expansion culture and once exposed to osteogenic medium they would have had to readjust the machinery to undergo osteogenic differentiation, taking longer times to reach osteogenic phenotypes. Again, in order to rule out altered cell behavior as a reason for the apparent lack of differentiation, the expression of OCN and OPN should have been quantified beyond day 21. Globally, citric acid at herein used concentrations, which are much higher than those expected upon in vivo degradation, seems not to affect hMSCs behavior (i.e. it seems not to affect proliferation

nor to induce differentiation/potentiate the effect of osteogenic supplements), suggesting that the degradation products of our hydrogels (i.e. citric acid and amino acids) are biocompatible.

Having shown that citrate can be used as a non-toxic crosslinker, mechanically-tailored hydrogels were tested for biological performance. Cytotoxicity studies revealed cell number reduced by 20% but normal cell morphology (Figure 50) after indirect exposure to 54 mg/ml E9C1 hydrogels. According to ISO 10993-5:2009, these hydrogels would be slightly cytotoxic, which might be solved by subjecting samples to more extensive washing protocols to completely remove toxic by-products generated during crosslinking. hMSCs were able to proliferate both in 40 mg/ml and 54 mg/ml E9C1 hydrogels (Figure 51 and Figure 52), which points out that –COOH groups from aspartic acid's side chain is not involved in the crosslinking reaction, preserving the integrity of RGD sequences. Higher cell numbers were consistently obtained in hydrogels in comparison to TCPS, suggesting that hydrogels provide at least a 2.5D (since most hydrogels displayed a thin layer of polymer on the surface, which would explain why cells weren't found within hydrogels; Figure 52 and Figure 53) environment for cell (in)growth. Interestingly, no significant differences between hydrogels were observed at any time point; however, 54 mg/ml hydrogels led to significantly increased cell number by day 21 when compared to that in TCPS.

A delayed expression of ALP was observed in all conditions, with the expression in cells cultured in TCPS seemingly peaking and being significantly higher than that in hydrogels at day 21 (Figure 55a). No differences were observed between hydrogels, the expression in which was consistently low. This phenomenon, given the proliferation results (Figure 51) and the presence of the polymeric layer on surface, could be due to (i) most of the cells in hydrogels being in a proliferative state while some of them would have activated the differentiation machinery, or to (ii) hydrogels containing a high cell density, shown to lead to reduced ALP expression [532]. As shown in the study of citric acid as a soluble factor, the expression of both OCN and OPN was found to decrease along the experiment (Figure 54 b and c). Despite the high levels at day 3, the low expression levels of OPN and OCN by the end of the experiment could be due to delayed differentiation, as suggested by observed delayed ALP expression.

The in vivo performance of 54 mg/ml and 40 mg/ml hydrogels was tested using a critical size defect model in SCID mice calvariae. Two critical size defects [534] were generated in the parietal bone of female SCID mice and treated with hydrogels; control defects were left empty. Bone regeneration was assessed by μCT and histology at 6 and 12 weeks post-implantation. μCT revealed that higher bone formation had occurred at 12 weeks in hydrogel-treated defects in comparison to those left untreated, as evidenced by bone volume (Figure 56a) and surface (Figure 56b) calculations. Interestingly, bone fragments in hydrogel-treated defects were bigger (i.e. they possessed lower surface-to-volume values) than those in empty defects, as demonstrated by surface density calculations (Figure 56c). It is noteworthy to mention that the density of bone fragments in all conditions was essentially the same (Figure 56c), pointing out that differences between hydrogel-treated and non-treated defects regarding volumetric BMD (Figure 56e) are due to differences in bone volume rather than to differences in the density of bone fragments.

Histology was performed to study the tissue in both untreated and hydrogel-treated defects. Defects were found to not spontaneously heal (Figure 57), although some bone was formed, as revealed by the presence of osteoid and mineralized tissue at both 6 and 12 weeks post-implantation (Figure 58). Regarding hydrogels, higher cell invasion was observed in samples prepared at 40 mg/ml polymer concentration (Figure 57 and Figure 59) when compared to their 54 mg/ml counterparts at both time points and, subsequently, scaffold degradation was found to be also higher in those hydrogels prepared at a lower polymer concentration. Despite low cell invasion, osteoid within 54 mg/ml hydrogels, as well as in 40 mg/ml ones, was noticed at both time points (Figure 59); bone formation in both cases seems to proceed through intramembranous ossification, as suggested by negative Alcian blue staining. The presence of mineralized tissue within hydrogels could not be observed due to strong staining of the polymer when performing Goldner's trichrome staining (Figure 57 and Figure 59), but H&E staining revealed that bone formation occurred in the interface of the native tissue with either one of the hydrogels and inside 40 mg/ml samples at 12 weeks (Figure 59h,k,m and n). Interestingly, both hydrogels were found to be biodegradable, with 40 mg/ml being already partially degraded by week 6 (Figure 57); degradation of 54 mg/ml was initially noticed at week 12.

Despite 54 mg/ml hydrogels were designed to possess target mechanical properties to induce osteogenic differentiation [242], histology results suggest cell invasion and bone formation to be higher in non-tailored 40 mg/ml samples and µCT results show that no differences exist between hydrogels regarding the amount and properties of dense material. First, this phenomenon could be due to cell-independent mineralization of 54 mg/ml due to calcium and phosphate ions diffusing through hydrogels and binding to dangling –COOH groups from citric acid, which would act as nucleation sites for HA. Second, it could be due to 54 mg/ml hydrogels seemingly possessing a density hindering cell infiltration which would result in delayed bone formation and thus lower amount of bone in comparison to that in 40 mg/ml counterparts. This apparent high density would not only hinder cell infiltration, but also prevent the tailored mechanical properties on exerting their potential osteoinductive effect. A third possibility would be that the mechanical properties of 54 mg/ml hydrogels, found to be osteoinductive in polyacrylamide hydrogels [242], wouldn't be so in our ELRs hydrogels. Different authors have pointed out that cell behavior depends on the synergistic effect of matrix properties [246–248] in such a way that the Young's modulus required to induce osteogenic differentiation might depend on scaffold chemical properties [245]. In order to find out if that's the case, it would have been interesting to test hydrogels with several Young's modulus values in vivo to find the best one given the chemistry of our matrices. It may well be that 40 mg/ml samples are the ones possessing a combination of chemical and mechanical properties feasible to induce osteogenic differentiation. Despite bone in 40 mg/ml hydrogels-treated defects was mainly found in the tissue-material interface at herein analyzed time points (and thus, samples would be ostoconductive rather than osteoinductive) longer implantation times would be required to rule out osteoinduction. In any case, both hydrogels seem to be biodegradable and at least osteoconductive, as suggested by the presence of bone in the bone-scaffold interface, where the presence of blood vessels (Figure 59h and m) and resorption cavities and osteoclasts (Figure 59k and n) was noticed; once again, longer implantation times might help finding differences between hydrogels as to the amount and quality of new bone.

These results evidence that more data are required in order to achieve the design of hydrogels with multiple tailored properties able to recreate the complex in vivo cell

microenvironment. Additionally, they suggest that, although functional studies on 2D may serve as a proof of concept, the conclusions drawn may not be valid when moving to a 3D environment. Thus, combinatorial studies assessing the synergistic effect of 3D scaffolds properties are required to achieve osteoinductive hydrogels.

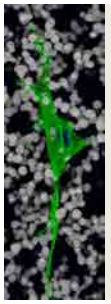

Chapter 4

4. LYSYL OXIDASE AS A TOOL TO PRODUCE BIOMIMETIC HYDROGELS

CHAPTER 4

PREFACE

The present chapter represents our efforts to obtain active lysyl oxidase for the production of biomimetic hydrogels for tissue engineering. Water-soluble and urea-soluble versions of LOX were overexpressed using transformed bacteria. Purified LOX was characterized and a systematic study was performed to optimize the overexpression/purification system in order to obtain LOX with improved copper content and activity.

5.1 MATERIALS AND METHODS

5.1.1 Production and purification of chimeric water-soluble LOX

5.1.1.1 Amplification of the LOX gene

The human aorta LOX gene was amplified from vector pLOX01 [535], which was provided by Dr. Karlo M. Lopez, from California State University Bakersfield. The polymerase chain reaction (PCR) was performed in 25 cycles by using LOXTAGF and MLOXR primers (Midland Certified Reagent Company, Inc.; Table 12) and Herculase Hotstart DNA polymerase (Agilent Technologies). The PCR program consisted on denaturing DNA at 94ºC for 1 minute, primer-DNA annealing at 62ºC for 1 minute and extension for 5 minutes at 72ºC. The proper amplification of the gene was confirmed by performing a 0.8% agarose gel electrophoresis at 100 V for 45 minutes by using a 1Kb DNA ladder (New England Biolabs).

Primer	Sequence
LOXTAGF	5'-AAGGGGCCCGGGACGACCCTTACAACCCC-3'
MLOXR	5'-AAGGGGCTCGAGATACGGTGAAATTGTGCAGCC-3'

Table 12. Primers for the amplification of the LOX gene from human aorta. LOXTAGF and MLOXR introduce a SmaI and XhoI restriction sites for DNA ligation.

5.1.1.2 Washing and concentration of the LOX gene

The amplified gene was purified by using a DNA Clean & Concentrator-5 kit (Zymo Research). Briefly, DNA binding buffer was added to the mix resulting from PCR at a 9:1 volume ratio, and the mixture was transferred to a Zymo-Spin column and centrifuged at 10,000 g for 30s. The flow-through was discarded and 200 µl Wash buffer were added to the column, which was centrifuged at 10,000 g for 30 s. 10 µl PCR grade water were added to the column, and DNA was eluted by centrifugation 10,000 g for 30 s after a 1 minute incubation at RT.

5.1.1.3 Generation of the pLOX09 construct

The LOX gene and pET-43.1a(+) (Novagen) vector were doubly digested with SmaI and XhoI (New England Biolabs) in NEB buffer 4 supplemented with BSA (New England

Biolabs) for 45 minutes at 37ºC. After digestion, DNA binding buffer was added to LOX and vector digestion mixes at 5:1 and 2:1 volume ratio, respectively. The LOX gene and the vector were then washed and concentrated as abovementioned. Ligation was carried out by incubating gene and vector with T4 DNA ligase (New England Biolabs) for 5 minutes at RT.

5.1.1.4 Transformation of competent NEB 10β *Escherichia coli* with the pLOX09 construct

3, 7 or 10 µl of the ligated plasmid (pLOX09; Figure 60) were added to competent 10β *Escherichia coli* (New England Biolabs) aliquots and the mixtures were incubated for 30 minutes on ice. Bacteria were heat-shocked at 37ºC for 1 minute and 250 µl S.O.C. medium (Super optimal broth with catabolite repression; New England Biolabs) were added. The mixture was incubated at 37ºC for 2 hours at 200 rpm. Transformed bacteria were plated on Luria Broth (LB; Melford) agar plates (one plate for each amount of ligated plasmid) containing 100 µg/ml ampicillin (Melford) and incubated overnight at 37ºC.

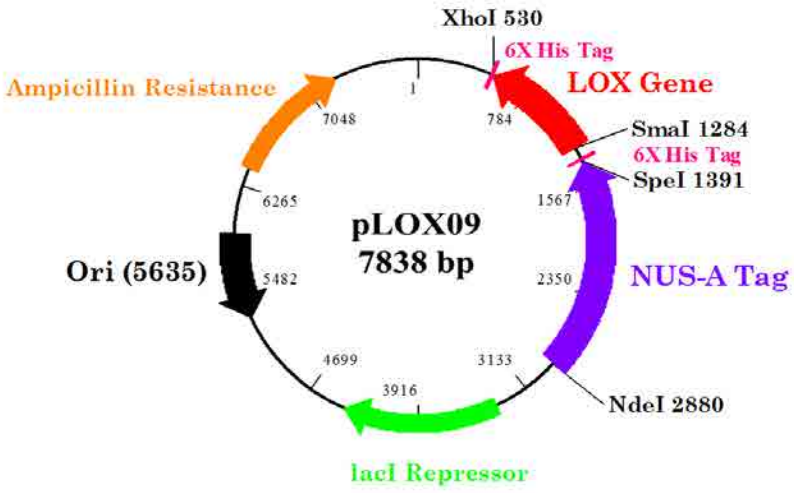

Figure 60. pLOX09 map. The plasmid contains ampicillin resistance (yellow) for the selection of transformed cells; a lacI repressor (green) for the selective expression of recombinant proteins upon induction; the LOX gene (red) and a Nus-A Tag (violet) to increase the solubility of chimeric proteins; and polyhistidine tags (His tags; pink) for protein purification.

5.1.1.5 Purification of the pLOX09 construct

One colony from each plate was transferred to 15-ml tubes containing 10 ml LB medium supplemented with 100 µg/ml ampicillin and incubated overnight at 37ºC and 200 rpm. The pLOX09 plasmid was independently purified from the three overnight cultures by using a QIAprep Spin Miniprep kit (QIAGEN). Briefly, bacteria were centrifuged at 8,000 g for 3 minutes, resuspended in 250 µl buffer P1 and transferred to 1.5-ml tubes. 250 µl buffer P2 were added and the mixtures were homogenized by inverting the tubes; cell lysis was allowed to proceed for 5 minutes. 350 µl buffer N3 were added, and the mixtures were homogenized and centrifuged at 13,000 rpm for 10 minutes. Supernatants were transferred to spin columns and centrifuged at 13,000 rpm for 60 s; flow-throughs were discarded. The columns were washed by adding 750 µl buffer PE and by centrifugation at 13,000 rpm for 60 s; a second centrifugation step was applied to completely remove PE buffer. The spin columns were placed in new 1.5-ml tubes and 50 µl ultrapure water were added; after a 2-minute incubation at RT, DNA was eluted by centrifugation at 13,000 rpm for 1 minute. Purified pLOX09 from the three different colonies was doubly digested with SmaI and XhoI in NEB buffer 4 for 2 h at 37ºC. A DNA electrophoresis in 0.8% agarose was performed to select the purified fraction containing the construct.

5.1.1.6 Transformation of competent SHuffle T7 *E.coli* with the pLOX09 construct

2 µl of properly ligated pLOX09 were added to a Shuffle T7 *E.coli* (New England Biolabs) aliquot and the mixture was incubated on ice for 30 minutes. Bacteria were heat-shocked at 37ºC for 1 minute and 250 µl S.O.C. medium were added. The mixture was incubated at 37ºC for 2 hours at 200 rpm and transformed bacteria were plated in LB agar with ampicillin and incubated overnight at 37º. After bacterial growth, plates were stored at 4ºC and used as a stock of transformed bacteria for protein overexpression. Plates were discarded 3 weeks after plating.

5.1.1.7 LOX09 overexpression

One colony of transformed SHuffle T7 *E.coli* was transferred to 15-ml tubes containing 10 ml LB medium containing 100 µg/ml ampicillin and incubated overnight at 37ºC and 200 rpm. Eight 1-ml aliquots of overnight culture were transferred to sterile 1.5-ml tubes and bacteria were centrifuged at 13,000 rpm for 2 minutes; supernatants were discarded to remove lactamases. Each pellet was resuspended in 1 ml of terrific broth (TB; Melford)

containing 100 µg/ml ampicillin. 500 ml TB supplemented with ampicillin were inoculated with 2 ml of resuspended bacteria and incubated at 37ºC and 200 rpm until the optical density (O.D.) was in the 0.6-0.8 range. At this point, the overexpression of recombinant LOX was induced by adding Isopropyl β-D-1-thiogalactopyranoside (IPTG; Melford) to a working concentration of 1 mM to induce protein overexpression. Additionally, $CuSO_4$ was added to a final concentration of 1 µM to provide the enzyme with Cu^{+2}. Bacteria were incubated overnight at RT and 200 rpm for LOX09 overexpression.

5.1.1.8 LOX09 purification

Bacteria were centrifuged at 4,000 g for 20 minutes and the supernatant was discarded. Pelleted bacteria were resuspended in non-urea lysis buffer (15 mM imidazole and 0.3 M NaCl in 50 mM Tris-HCl, pH 7.8) and sonicated. Sonication was performed on ice at a 30-35% amplitude in 15 s on – 45 s off (total time of effective sonication: 8 minutes) to avoid sample overheating. After sonication, cell debris were pelleted by centrifugation at 8500 rpm for 20 minutes and discarded. Supernatants were collected and incubated overnight at 4ºC with Ni-NTA (Nickel-nitriloacetic acid) agarose (QIAGEN) in an orbital shaker to allow the binding of the His-tagged enzyme to the resin.

The lysate-resin mixture was centrifuged for 20 minutes at 8,500 rpm at 4ºC. The supernatant was discarded and the resin pellet was resuspended with non-urea lysis buffer. The centrifugation-resuspension steps were repeated 11 times to completely remove cell debris. Non-urea elution buffer (250 mM imidazole and 0.3 M NaCl in 50 mM Tris-HCl,pH 7.8) was added to the resin, and the mixture was incubated in an orbital shaker for 1 h at 4ºC to maximize the release of LOX09 and centrifuged. Purified LOX09 was stored at 4ºC and protected from light until use.

The purity of LOX09 was assessed by Sodium dodecyl sulfate-polyacrylamide gel (SDS-PAGE) electrophoresis using a resolving gel prepared at a 12.5% polyacrylamide concentration. Samples were mixed 1:1 with loading buffer (0.23 M SDS, 4% glycerol, 16.7% β-mercaptoethanol and 0.083% bromophenol blue in water) and denaturalized by exposure to boiling water for 5 minutes. 20 µl of samples were loaded in the gel and electrophoresis was performed at 200 V for 45 minutes; a broad range (2-212 kDa) protein

marker (New England Biolabs) was used. At electrophoresis completion, the gel was incubated overnight with staining solution (0.125% Coomassie brilliant blue R-250, 50% methanol and 10% glacial acetic acid in water). Excess staining was removed by sequentially incubating the gel overnight in de-stain solutions I (50% methanol and 10% glacial acetic acid in water) and II (5% methanol and 7% glacial acetic acid in water) at 4ºC.

5.1.1.9 Protein quantification

The amount of purified protein was quantified by using the bicinchoninic acid (BCA) assay kit (Pierce). Briefly, reagents A and B were mixed at a 50:1 volume ratio and thoroughly homogenized. Samples were mixed with the working solution at a 1:20 volume ratio and incubated at RT for 2 hours. At the end of the incubation, absorbance was read at 562 nm; non-urea elution buffer was used as a blank to account for the contribution of the components in the buffer to absorbance.

5.1.2 Production and purification of native urea-soluble LOX

5.1.2.1 Generation of the pLOX02 construct

The LOX gene from human aorta was amplified from vector pLOX01 [535]. The PCR was performed in 25 cycles by using MLOXF and MLOXR primers (Table 13) and Herculase Hotstart DNA polymerase. The amplified gene was washed and concentrated as previously stated, and both LOX gene and pET-21b vector (Novagen) were doubly digested with NdeI (New England Biolabs) and XhoI restriction enzymes for 45 minutes at 37ºC. The washing and ligation of digested gene and vector were performed as previously mentioned, leading to obtaining the plasmid pLOX02 (Figure 61).

Primer	Sequence
MLOXF	5'-AAGGGGCATATGGACGACCCTTACAACCCC -3'
MLOXR	5'-AAGGGGCTCGAGATACGGTGAAATTGTGCAGCC-3'

Table 13. Primers for the amplification of the LOX gene from human aorta. MLOXF and MLOXR introduce a NdeI and XhoI restriction sites for DNA ligation.

To make sure that the generated plasmid contained the LOX gene, pLOX02 was transformed into competent 10β *E. coli* as abovementioned. Cells were plated into LB agar

plates containing 100 µg/ml ampicillin and incubated overnight at 37ºC. Three colonies were independently inoculated into 10-ml LB medium + ampicillin and cultured overnight at 37ºC and 200 rpm. pLOX02 was purified and digested with NdeI and XhoI as previously stated, and a DNA electrophoresis in 0.8% agarose was performed. Digested LOX gene and pET-21b vector were used as controls.

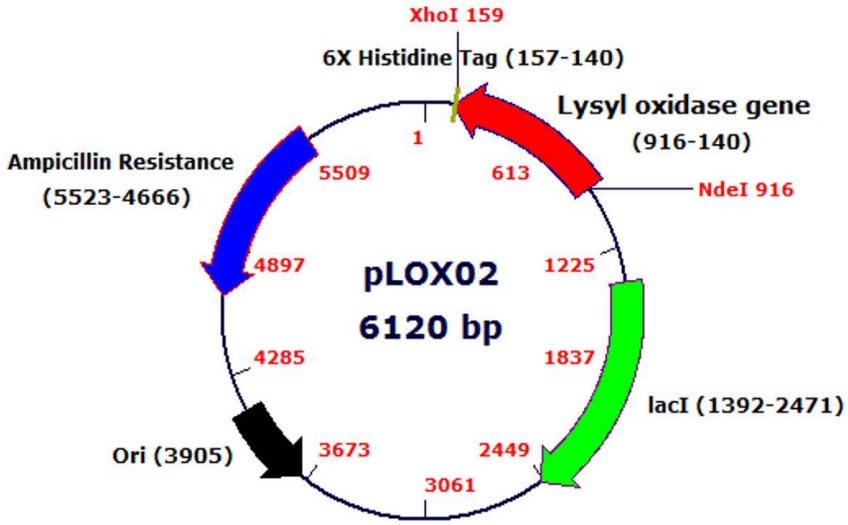

Figure 61. pLOX02 map. The plasmid contains ampicillin resistance (blue) for the selection of transformed cells; a lacI repressor (green) for the selective expression of recombinant proteins after induction; and the LOX gene (red) fused with a His-tag (yellow) for its purification.

Purified pLOX02 was transformed into SHuffle T7 *E.coli* as previously stated. Transformed bacteria were cultured overnight in LB media and plated in LB + ampicillin agar. LB agar plates were used as a source of transformed bacteria for protein overexpression and discarded three weeks after plating.

5.1.2.2 LOX02 overexpression

Several tests were performed to optimize the overexpression system for soluble LOX02; a summary of these tests can be found in Table 34, Supplementary data. Tests number 1, and 3 aimed the maximization of protein yield and purity; tests number 1, 6 and 7 aimed the maximization of the percentage of enzyme molecules containing the copper cofactor. Briefly, a colony of transformed Shuffle T7 *E. coli* was used to prepare an overnight culture in LB medium. Bacteria from the overnight were used to inoculate TB supplemented with 100 µg/ml ampicillin, and 500-ml cultures were performed at either

30ºC or 37ºC. When the O.D. reached values of 0.6-0.8, the overexpression was induced with 0.5 mM, 1 mM, 1.5 mM, 2 mM or 5 mM IPTG and $CuSO_4$ was added to 1 µM, 2 µM, 5 µM, 10 µM or 20 µM final concentrations. Overexpression was performed at 250 rpm and either 16ºC or 22ºC, and let to proceed overnight, for 24 h or for 48 h; in the latter case, extra ampicillin was added to the cultures at 24 h at a 100 µg/ml concentration to keep the selection pressure and prevent bacteria from getting rid of the pLOX02 plasmid.

The expression of LOX02 in inclusion bodies was also explored. Briefly, bacteria in 500-ml TB cultures were grown at 37ºC and overexpression was induced at an O.D. of 0.6-0.8 with IPTG at a final concentration of 1.5 mM; CuSO4 was added at a 1 µM concentration. Overexpression was performed at 250 rpm and 37ºC for 4 hours.

5.1.2.3 LOX02 purification

The purification system was also optimized for soluble LOX02. Tests number 1, 2 and 4 (Table 34, Supplementary data) were performed to maximixe protein yield and purity and/or the percentage of enzyme molecules containing the copper cofactor.

For the purification of soluble LOX02, bacteria were centrifuged at 8,500 rpm at 4ºC for 15 minutes and resuspended in urea lysis buffer (0.2 M NaCl, 6 M urea and 10 mM imidazole in 16 mM phosphate buffer, pH 7.8). Sonication was performed as previously mentioned and lysates were incubated with TALON cobalt resin (Clontech) or Copper chelating resin (G Biosciences) at 4ºC overnight or 15 min RT + 4ºC overnight, and subjected to four different purification methods (Table 14); in all cases, the purification was performed in urea lysis buffer at 4ºC, and LOX02 was recovered in urea elution buffer (0.2 M NaCl, 6 M urea and 250 mM imidazole in 16 mM phosphate buffer, pH 7.8). Eluted protein was stored in aluminium foil-wrapped tubes at 4ºC until use.

Method	Purification method	Steps	Speed	Time, T
1	Centrifugation in tube	11	3,000-4,500 rpm	15 min, 4ºC
2	Centrifugation in spin column	5	250 g	15 min, 4ºC
3	Centrifugation in tube	5	3,000-4,500 rpm	15 min, 4ºC
	Centrifugation in spin colum	5	250 g	15 min, 4ºC

4	Centrifugation in tube	5	3,000-4,500 rpm	15 min, 4ºC
	Gravity-flow in spin column	5	-	-

Table 14. Summary of methods used to purify soluble LOX02.

For the purification of LOX02 from inclusion bodies, bacteria were centrifuged at 8,500 rpm at 4ºC for 15 minutes and resuspended in lysis buffer (50 mM NaCl, 1 mM EDTA, 0.02% sodium azide and 1% Triton X-100 in 50 mM Tris-HCl, pH 8). Sonication was performed as abovementioned and lysates were centrifuged at 18,000 rpm at 4ºC for 10 minutes. Supernatants were discarded and pellets were resuspended in urea wash buffer (0.5 M NaCl and 2 M urea in 50 mM Tris-HCl, pH 8) and centrifuged at 15,000 rpm for 10 minutes at 4ºC. Supernatants were discarded and pellets were resuspended in solubilization buffer (8 M urea, 2 mM β-mercaptoethanol, 50 mM imidazole and NaCl 0.5 M in phosphate buffer 16 mM) and incubated overnight at 4ºC under magnetic stirring. Tubes were then centrifuged at 15,000 rpm at 4ºC for 10 minutes, and supernatants were recovered and transferred to disposable columns containing copper chelating resin. Five washing steps with urea lysis buffer were performed by gravity flow. For the elution of LOX02 from inclusion bodies, the resin was incubated with urea elution buffer at 4ºC for 15 minutes under agitation and the protein was eluted by gravity flow. A second elution was performed in the same conditions.

The purity of LOX02, either soluble or from inclusion bodies, was assessed by SDS-PAGE using a resolving gel prepared at 12.5% polyacrylamide and a ColorPlus prestained broad range (7-175 kDa) protein marker (New England Biolabs). The electrophoresis gels were stained and washed as previously stated.

5.1.2.4 Dialysis

The usefulness of dialysis to maximize the percentage of soluble LOX02 molecules containing the copper cofactor was investigated. The dialysis step was performed in 3 ml Slide-A-Lyzer G2 cassettes (Thermo Scientific) with a 10 kDa molecular weight cut-off (MWCO). The dialysis protocol was based on that in [536] and consisted on: (i) incubation in 0.15 M NaCl, 6 M urea and 10 mM 2,2′-dipyridine in 16 mM phosphate buffer, pH 7.8 for 48 h, (ii) incubation in 0.15 M NaCl, 6 M urea and 0.5 mM $CuSO_4$ in 16 mM phosphate buffer, pH 7.8 for 48 h, (iii) incubation in 0.15 M NaCl, 6 M urea, 10

mM EDTA in 16 mM phosphate buffer, pH 7.8 overnight, and (iv) two incubations in 0.15 M NaCl and 6 M urea in 16 mM phosphate buffer, pH 7.8 overday/overnight. All incubations were performed at 4ºC with gentle stirring and using a dialysis solution:sample volume ratio of 200:1. Dialyzed samples were concentrated using Amicon Ultra-4 devices with a 10 kDa MWCO (Millipore) by centrifugation at 3,000 rpm at 4ºC for 10 minutes. Dialyzed and concentrated protein was stored in aluminium foil-wrapped tubes at 4ºC until use.

In the case of LOX02 from inclusion bodies, dialysis was performed in order to refold the protein, which was diluted to ca. 100µg/ml. Briefly, the enzyme was dialyzed against (i) dialysis buffer (6 M urea and 0.15 M NaCl in 16 mM phosphate buffer, pH 8) overnight, (ii) refolding buffer (6 M urea, 0.15 M NaCl, 200 µM $CuSO_4$ and 2% N-lauroylsarcosinate (Sigma) in 16 mM phosphate buffer, pH 8) for 24 h, and (iii) dialysis buffer twice overday/overnight. Refolding was carried out in 3 ml Slide-A-Lyzer G2 cassettes using a buffer:sample volume ratio of 200:1. All steps were performed at 4ºC.

5.1.2.5 LOX02 quantification

LOX02 was quantified by the BCA assay. The working solution was prepared as previously stated and mixed with samples at a 8:1 volume ration in 96-well plates. Absorbance was read at 562 nm.

5.1.2.6 Cu^{+2} quantification

Solutions containing purified LOX were mixed with 1.84 M trichloroacetic acid (Sigma) in water at a 3:1 volume ratio. The resulting solution was mixed with 1.94 mM ascorbic acid (Sigma) in water and a 0.9375 M NaOH, 0.68 M HEPES and 2.67% BCA reagent A solution at a 1:0.2:0.8 volume ratio. The resulting solution was transferred to 96-well plates and absorbance was read at 360 nm. $CuSO_4$ was used to prepare a Cu^{+2} standard curve.

5.1.2.7 Detection of the LTQ cofactor

The presence of the LTQ cofactor in soluble LOX purified with the copper resin from test 1 (Table 34, Supplementary data) was assessed by spectrophotometry and Western Blot.

Spectrophotometry. A 0.13 M phenylhydrazine in 1 M Tris-HCl, pH 7 solution was prepared and mixed with purified LOXO2 at a 1:100 volume ratio. The mixture was incubated overnight at RT and the absorbance sprectrum (200-800 nm) was recorded. Urea elution buffer was used to substract background signal.

Western blot. Two SDS-PAGE gels with resolving gel prepared at a 12.5% polyacrylamide concentration were prepared. Samples were mixed with loading buffer at a 1:1 volume ratio and boiled for 5 minutes. SDS-PAGE was run at 200 V for 45 minutes using Precision plus protein dual color standards (Bio-rad). One of the gels was stained with Coomassie blue as previously stated and the other was used for Western blot. Briefly, the gel was sandwiched with fiber pads, filter paper and a nitrocellulose membrane and the sandwich was transferred to an electrophoresis cuvette filled with transfer buffer (25 mM Tris-HCl, 192 mM glycine and 10 % methanol in water). The transference was run at 100 V for 1 hour under mild stirring. The nitrocellulose membrane was removed from the sandwich and stained overnight in the dark at RT with 0.24 mM nitroblue tetrazolium (Sigma) and 2 M glycine in water solution (pH 10). The membrane was then washed with water and dried. In order to stain proteins, the membrane was incubated with 1.31 mM Ponceau S (Sigma) in 5% acetic acid for 1 h at RT and washed to remove excess staining.

5.1.2.8 Activity assays

The activity of LOX02 was assessed in 50 mM borate buffer pH 8.2 containing 1.2 M urea, 50 µM 10-Acetyl-3,7-dihydroxyphe-noxazine (Cayman Chemical), 10 mM cadaverine (Sigma) and 10 U/ml horseradish peroxidase (Sigma). The mixtures were prepared in 96-well plates and fluorescence evolution at 37ºC was recorded in a pre-warmed microplate reader. The activity was calculated from the slope of the fluorescence curve during the first five minutes; elution buffer instead of LOX02 was used to set background slope. 30% H_2O_2 was used to prepare a standard curve; activity is expressed as U/mg, where U = nmol H_2O_2/min.

5.2 RESULTS

5.2.1 Production and purification of chimeric water-soluble LOX

5.2.1.1 Amplification of the LOX gene

The human LOX gene was amplified from the pLOX01 plasmid. The use of LOXTAGF and MLOXR allowed the proper amplification of the gene, which had an expected length of 745 bp (Figure 62).

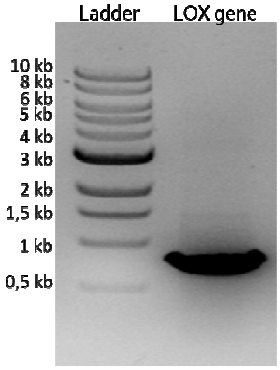

Figure 62. Amplification of the LOX gene from human aorta.

5.2.1.2 Generation of the pLOX09 construct

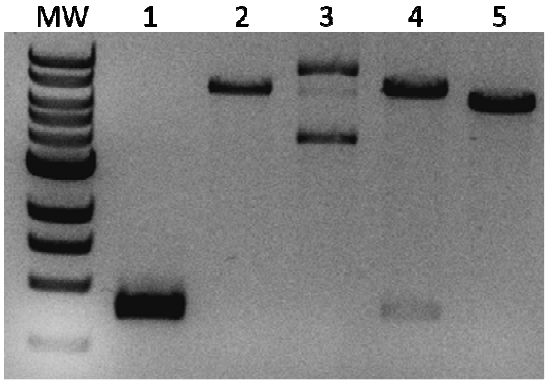

Figure 63. DNA electrophoresis of plasmids from cells transformed with 3 (lane 3), 7 (lane 4) or 10 µl (lane 5) ligation product. MW: 1 kb DNA ladder; lane 1: doubly digested LOX gene; lane 2: doubly digested pET-43.1a(+) vector.

10β *E. coli* cells were transformed with 3, 7 or 10 µl of the ligation product. After independently culturing cells transformed using the three ligation products, plasmids were

purified to select those cells containing the plasmid properly ligated. As shown in Figure 63, just those cells transformed with 7 µl ligation product contained the pLOX09 plasmid.

5.2.1.3 LOX09 purification

SHuffle T7 *E.coli* cells transformed with the properly ligated pLOX09 plasmid were used for LOX09 overexpression.LOX09 was expressed at an average yield of 1379.69 ± 379.63 µg/l of culture (Table 15) and was eluted to high purity (Figure 64).

[LOX09] (µg/ml)	Yield (µg/l of culture)
287,04 ± 65,11	1379,63 ± 379,63

Table 15. Average protein concentration in the eluted fraction and yield of the overexpression system in the production of LOX09.

Despite highly pure LOX09 was obtained, three main bands were consistently observed when running SDS-PAGE (Figure 64). These bands were assumed to correspond to the LOX09 fusion protein (upper band), Nus-A tag (58 kDa; mid band) and LOX (32 kDa; lower band), respectively, and to be the result of partial proteolysis.

5.2.2 Production and purification of native urea-soluble LOX

5.2.2.1 Generation of the pLOX02 construct

The human LOX gene was amplified from pLOX01 and ligated with the pET-21b vector. Three colonies of transformed *10β E.coli* were assessed for the presence of the properly ligated pLOX02 plasmid. As shown in Figure 65, all three selected colonies contained the pLOX02 plasmid, pointing out that any of them could be used to prepare cultures for the overexpression of LOX02.

5.2.2.2 LOX02 quantification

Several tests were performed in an effort to maximize the overexpression yield and the protein concentration in the eluted fraction. Affinity resins coordinated with either copper or cobalt were tested. In this study, cobalt-loaded resin led to a higher yield and to obtaining eluted solutions with higher protein concentration, although both yield and concentration were low in both cases (Table 16). Copper-loaded resin was used from then on.

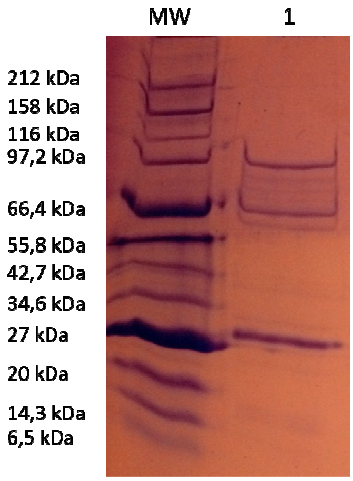

Figure 64. SDS-PAGE of purified LOX09. MW: protein ladder; lane 1: LOX09 elution fraction.

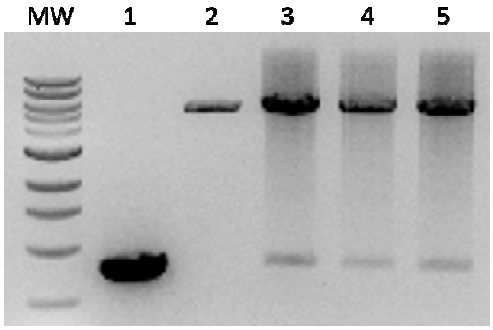

Figure 65. DNA electrophoresis of plasmids from three independent colonies of transformed 10β *E.coli* cells. MW: ladder; lane 1: doubly digested LOX gene; lane 2: doubly digested pET-21b vector; lanes 3-5: digested plasmids from colonies number 1, 2 and 3, respectively.

	Copper resin	Cobalt resin
[LOX02] (µg/ml)		
	250.33 ± 5.77	318.58 ± 11.79
Yield (µg/l of culture)		
	2503.33	3185.83

Table 16. Effect of metal-loaded resin on eluted protein concentration and yield.

Available protocols for protein purification recommend performing the protein-resin binding step at either RT or 4ºC. To test the influence of the binding temperature, cell lysates were incubated with copper-loaded resin at 4ºC overnight, with or without a pre-

incubation step at RT. As shown in Table 17, pre-incubating lysate and resin at RT led to reduced binding and thus to lower elution concentration and yield. An overnight incubation at 4ºC was used ever since.

4ºC	RT
[LOX02] (µg/ml)	
875.58 ± 7.14	581.92 ± 12.78
Yield (µg/l of culture)	
8755.33	5819.17

Table 17. Effect of resin binding temperature on eluted protein concentration and yield using copper-loaded resin.

A 1 mM IPTG concentration is routinely used to induce the expression of LOX in transformed *E.coli* [483,485]. A test was performed to assess whether the higher overexpression yields could be achieved by using higher [IPTG]. As shown in Table 18, the overexpression yield peaked at a 1.5 mM IPTG concentration, which was selected to be used from then on.

0.5 mM	1 mM	1.5 mM	2 mM	5 mM
[LOX02] (µg/ml)				
323.50 ± 5.77	250.33 ± 5.77	1007.17 ± 8.47	612.75 ± 19.18	904.42 ± 9.89
Yield (µg/l of culture)				
3235	2503.33	10071.67	6127.5	9044.167

Table 18. Effect of [IPTG] on overexpression yield and elution concentration.

A test was perfomed in order to assess whether extending the overexpression time leads to increased yield. Table 19 shows that good elution concentrations were obtained when performing overexpression either overnight or for 24 h, with the latter leading to increased yield.

Overnight	24 h	48 h
[LOX02] (µg/ml)		
2403.71 ± 1098.17	2502.917 ± 47.86	1474.67 ± 23.78

Total yield (µg/l of culture)		
7641.67 ± 1112.5	12514.58	7370.83

Table 19. Effect of overexpression time on yield and elution concentration.

In an effort to maximize the percentage of enzymes molecules incorporating a copper atom, $CuSO_4$ was added to induced cultures at 1, 2, 5, 10 and 20 µM final concentrations. As shown in Table 20, all $CuSO_4$ concentrations led to good elution concentrations and yield, with the latter peaking at a 20 µM $CuSO_4$ concentration.

1 µM	2 µM	5 µM	10 µM	20 µM
[LOX02] (µg/ml)				
1878.83 ± 68.59	1323 ± 123.18	1167.67 ± 45.67	1346.67 ± 42.74	1746 ± 17.36
Yield (µg/l of culture)				
9394.167	13230	11676.67	13466.67	17460

Table 20. Effect on [$CuSO_4$] on protein yield and elution concentration in overnight overex-pression cultures.

Four different purification protocols were used during the optimization of the overexpression and purification of LOX02. All four methods led to acceptable yields (Table 21), but method 4 allowed obtaining purified fractions at higher protein concentrations (up to 3.5 mg/ml). Thus, method 4 was established as the protocol for the purification of soluble LOX02.

Method 1	Method 2	Method 3	Method 4
[LOX02] (µg/ml)			
1007.17 ± 8.47	1800.92 ± 937.48	1938.29 ± 732.70	2403.75 ± 1098.17
Yield (µg/l of culture)			
10071.67	5595.93 ± 1268.51	6357.29 ± 311.04	7641.67 ± 1112.5

Table 21. Effect of the protein purification protocol on elution concentration and yield.

Although impurities were detected in the eluted fractions coming from all four methods (Figure 66), the intensity of unspecific bands is remarkably lower compared to that of the LOX02 band, suggesting that impurities would represent a low percentage of total protein.

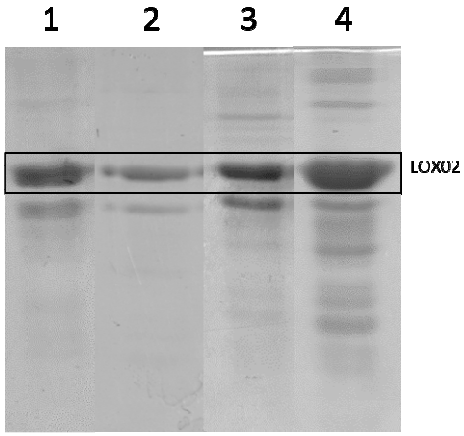

Figure 66. SDS-PAGE of eluted fractions obtained by means of four different purification methods. Lane 1: Centrifugation in tube; lane 2: centrifugation in spin column; lane 3: centrifugation in tube + centrifugation in spin column; lane 4: centrifugation in tube + gravity flow.

The purification of LOX02 from inclusion bodies was explored. Two eluted fractions were obtained for each purification to assess whether all the protein bound to the resin was effectively released during the one-step elution protocol used in the case of soluble LOX02. As shown in Table 22, most of the protein was recovered in the first elution step, while ca. 1/6 of the total amount of protein was released during the second elution step.

Elution 1	Elution 2
[LOX02] (µg/ml)	
1968.81 ± 1014.95	393.70 ± 165.05
Total yield (µg/l of culture)	
7087.537 ± 3366.63	

Table 22. Protein concentration and yield after the purification of LOX02 from inclusion bodies. Total yield represents the sum of LOX02 from both elutions.

5.2.2.3 Cu^{+2} quantification

Several tests were also performed in order to maximize the percentage of enzyme molecules incorporating the Cu^{+2} cofactor, essential for LOX activity. LOX02 purified with either copper or cobalt-loaded resins was subjected to copper quantification. Copper-loaded resin led to a remarkably higher copper content in eluted fractions (Table 23) and was thus selected to be used in further studies.

Copper resin	Cobalt resin
10.38 ± 2.95 %	1.75 ± 0.35 %

Table 23. Copper content of soluble LOX02 purified with copper or cobalt-loaded resins.

A test was performed to assess whether longer overexpression times would lead to higher copper incorporation into enzyme molecules. For this study, overexpression was let to proceed either overnight, for 24 h or for 48 h. As shown in Table 24, the percentage of enzyme molecules containing a copper atom decreased as overexpression time increased. Overnight overexpression was selected to be used in further experiments.

Overnight	24 h	48 h
29.07 ± 8.30 %	10.04 ± 4.11 %	4.50 ± 0.44 %

Table 24. Effect of overexpression time on soluble LOX02 copper content.

Given the low copper content of LOX02 purified from cultures with 1 µM $CuSO_4$, the effect of adding higher $CuSO_4$ concentrations after induction was studied. As shown in Table 25, $CuSO_4$ concentrations beyond 1 µM led to reduced copper content.

1 µM	2 µM	5 µM	10 µM	20 µM
29.07 ± 8.30 %	14.23 ± 1.98 %	12.81 ± 0.96 %	12.48 ± 2.85 %	8.02 ± 3.55 %

Table 25. Effect of $CuSO_4$ concentration on soluble LOX02 copper content.

Given that adding extra copper right after induction is not useful to increase copper incorporation into the enzyme, a dialysis step involving the removal of copper atoms from purified soluble LOX02 followed by adding $CuSO_4$ was performed. As shown in Table 26, dialysis was not effective and indeed it led to a decreased percentage of enzyme molecules with a copper atom.

Non-dialyzed	Dialyzed
%Cu^{+2}	
22.88 ± 7.04 %	11.07 ± 3.40 %
Average fold decrease	
2.26 ± 0.20	

Table 26. Effect of dialysis on soluble LOX02 copper content.

Two elution steps were performed when purifying LOX02 from inclusion bodies. Surprisingly, the enzyme in the second elution contained a considerably increased copper content when compared to that in LOX02 from the first elution (Table 27).

Elution 1	Elution 2
%Cu^{+2}	
10.05 ± 3.58 %	35.22 ± 5.46 %
Average fold increase	
4.11 ± 1.25	

Table 27. Copper content in LOX02 purified from inclusion bodies.

LOX02 from inclusion bodies in the second elution was subjected to refolding by dialysis at a protein concentration of 100 µg/ml. As shown in Table 28, refolding led to an increased copper content, with enzyme molecules containing ca. 2 copper atoms on average.

LOX02	Refolded LOX02
%Cu^{+2}	
36.84 ± 4.78 %	212.59 ± 18.50 %
Fold increase	
5.77	

Table 28. Copper content in LOX02 from inclusion bodies before and after refolding.

5.2.2.4 Detection of the LTQ cofactor

The presence of the LTQ cofactor was assessed by spectrophotometry and Western Blot. First, for its detection by spectrophotometry, soluble LOX02 was incubated with phenylhydrazine. Phenylhydrazine binds to LTQ, producing an adduct with an absorption maximum at λ= 454 nm [536]. As shown in Figure 67, the adduct peak was not observed upon incubation of soluble LOX02 purified by method 1 with phenylhydrazine.

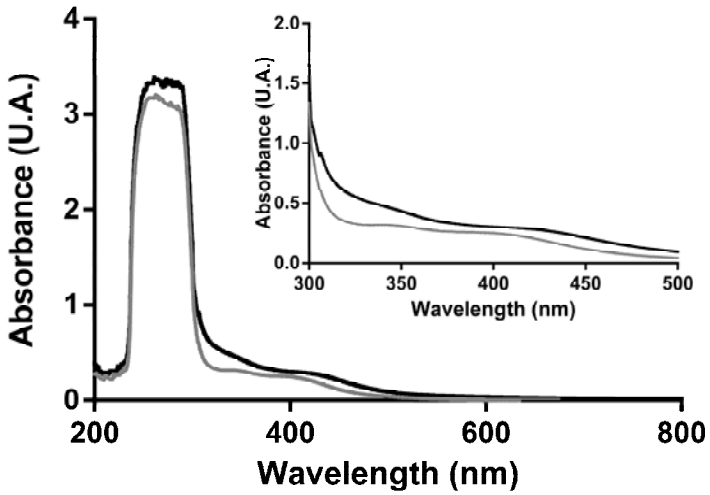

Figure 67. Detection of the LTQ cofactor by absorbance. Buffer (grey) and purified soluble LOX02 (black) were incubated with phenylhydrazine and the absorbance spectra were recorded in the 200 nm – 800 nm range. Inset: Detail on the 200 nm – 500 nm region.

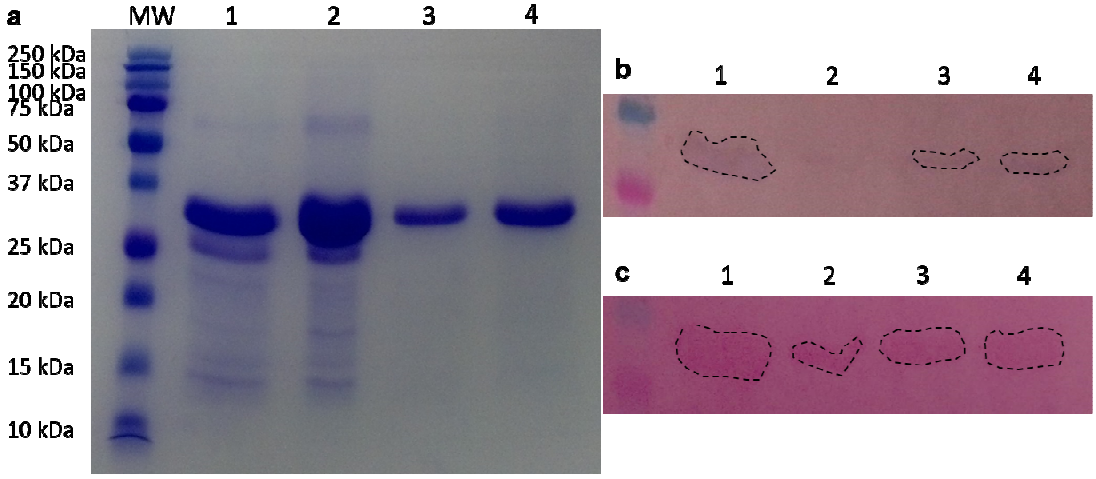

Figure 68. Detection of the LTQ cofactor by Western Blot. Four batches of LOX02 purified by means of method 1 were used. a) SDS-PAGE gel stained with Coomassie blue; b) nitrocellulose membrane stained with nitroblue tetrazolium; c) nitrocellulose membrane stained with Ponceau S. MW: ladder; lanes 1-4: LOX02 batches 1-4. Lightly stained bands in b) and c) have been contoured for clarity.

For the detection of LTQ by Western Blot, a double SDS-PAGE was performed. One of the gels was stained with Coomassie blue (Figure 68a) and the other one was used for Western Blot. Soluble LOX02 transferred to nitrocellulose membranes was stained with nitroblue tetrazolium (Figure 68b), which stains quinones with redox activity [537], and

Ponceau S for protein detection (Figure 68c). As shown in Figure 68b, slightly stained bands appeared after incubation with nitroblue tetrazolium in batches number 1, 3 and 4, and these bands corresponded to LOX02 in Coomassie blue-stained gels and Ponceau S-stained membranes. These results suggest that a low percentage of soluble LOX02 molecules contain the LTQ cofactor.

5.2.2.5 LOX02 activity

LOX02 purified from tests aiming to increase the percentage of enzyme molecules containing the copper cofactor was assessed for activity in order to assess whether increases in copper content result in boosted activity. First, the effect of overexpression time on soluble lysyl oxidase activity was tested in order to determine whether extending the time the enzyme has to incorporate copper and develop the LTQ cofactor results in increased activity. As shown in Table 29, the highest mean activity was achieved for overnight overexpression, while longer times led to reduced catalytic potential.

Overnight	24 h	48 h
Activity (U/mg)		
0.16 ± 0.10	0.047 ± 0.012	0.064 ± 0.013

Table 29. Effect of overexpression time on soluble LOX02 activity.

Adding extra $CuSO_4$ at the moment of induction didn't seem to be beneficial. While adding $CuSO_4$ at 2, 5 and 10 µM led to reduced activity compared to that when 1 µM was added, a 20 µM concentration didn't essentially affect activity (Table 30).

1 µM	2 µM	5 µM	10 µM	20 µM
Activity (U/mg)				
0.16 ± 0.10	0.05 ± 0.017	0.034 ± 0.025	0.035 ± 0.031	0.11 ± 0.012

Table 30. Effect of $CuSO_4$ concentration on soluble LOX02 activity.

Performing a dialysis involving the chelation of bound metallic atoms and subsequently adding copper led to reduced activity in dialyzed soluble LOX02 (Table 31).

Non-dialyzed	Dialyzed
Activity (U/mg)	
0.22 ± 0.11	0.106 ± 0.004
Fold decrease	
2.09	

Table 31. Effect of dialysis on soluble LOX02 activity.

The first two elutions performed to purify LOX02 from inclusion bodies were assayed for LOX activity. As shown in Table 32, second elutions were consistently more active (up to ca. 5.5 times) that first ones.

Elution 1	Elution 2
Activity (U/mg)	
0.13 ± 0.07	0.64 ± 0.15
Average fold increase	
4.95 ± 0.68	

Table 32. LOX02 activity in fractions purified from inclusion bodies.

Second elutions from the purification of LOX02 from inclusion bodies were subjected to a refolding protocol, which didn't seemingly have an effect on the catalytic potential of the enzyme (Table 33).

LOX02	Refolded LOX02
Activity (U/mg)	
0.58 ± 0.14	0.62 ± 0.17

Table 33. Activity of LOX02 from inclusion bodies before and after refolding.

5.3 DISCUSSION

Lysyl oxidase catalyzes the in vivo oxidative deamination of ε-NH_2 groups from lysine (or hydroxylysine) residues [424,425] to aldehyde groups that can condense with each other or react with primary amines to generate Schiff bases, being thus responsible for the crosslinking in collagen and elastin [24,454]. In vitro, LOX has proved able to oxidize both short [458,459] and long substrates [466]. Although the activity on the enzyme depends on substrate chemical parameters such as pI [458], and substrate sequence and length [459–461], a proper 3D conformation of the substrate is critical for the formation of LOX-catalyzed crosslinks [454] (i.e. for aldehyde groups and primary amines to be close enough to lead to aldol condensation products and Schiff bases). This has been demonstrated for collagen [425], tropoelastin [464] and for Urry's ELPs, whose oxidation seemingly depends on their ability to coacervate, being the oxidation of VPGXG-based ELPs higher as their coacervation is more favored [466].

LOX is commonly purified in buffers containing 4-6 M urea given its tendency to self-aggregate [474]. However, although urea seems not to affect LOX activity when short substrates are used [538], it strongly inhibits the enzyme when long substrates such as aortic elastin are to be crosslinked (a urea concentration "as low" as 0.2 M can inhibit LOX activity by 25%; [474]). Urea is a well-known chaotropic agent, being able to denaturate proteins [539,540] or, in other words, to prevent them from folding into their natural 3D conformation. On one hand, urea is required for LOX to be soluble; on the other hand, urea prevents LOX natural substrates from coacervating, thus hindering their crosslinking. In light of these conflicting facts, strategies aiming the production of biomimetic LOX-crosslinked hydrogels may rely on (i) modifying the enzyme to make it water-soluble or on (ii) optimizing the purification protocol to achieve highly concentrated LOX solutions to minimize the amount of urea the substrates are exposed to.

As previously mentioned, active LOX doesn't possess any post-translational modification other than proteolysis. This makes LOX a feasible protein to be produced in a recombinant form in *E. coli*. In this study, LOX from human aorta was fused with a Nus-A tag, commonly used to increase the solubility of recombinant proteins [541], by inserting the

LOX gene into a pET-43.1a(+) vector to generate the so-called pLOX09 plasmid (Figure 60). Properly ligated pLOX09 (Figure 63) was employed to transform SHuffle T7 *E.coli* cells, which were cultured and induced to overexpress the water-soluble version of LOX, LOX09. The fusion protein was expressed at low yield (Table 15) and recovered by affinity chromatography to high purity (Figure 64). However, SDS-PAGE revealed that LOX09 had undergone partial proteolysis resulting in the scission of the solubility tag, as evidenced by the presence of three bands (Figure 64). SHuffle T7 *E.coli* cells are deficient in proteases, so the proteolysis is likely to occur during purification. Given that all the batches of purified LOX09 showed signs of proteolysis, the use of the fusion protein was discarded.

As an alternative, native LOX (namely LOX02) from human aorta was produced. The LOX gene was properly inserted into a pET-21b vector to generate the pLOX02 plasmid (Figure 61 and Figure 65), which was used to transform SHuffle T7 *E. coli* cells for its overexpression either in soluble or insoluble forms. Several tests were performed to establish a protocol for the production soluble LOX02 at a high yield and to purify the enzyme in an active form and at a high concentration (Table 34, Supplementary data). Despite leading to a lower yield (Table 16), a copper-loaded resin was selected to purify the enzyme given that it allowed the retrieval of soluble LOX02 with higher copper content compared to that in LOX02 purified with cobalt-loaded resin (Table 23). Although manufacturers recommend performing the protein-binding step at RT, higher binding and thus higher yield and LOX02 concentration were achieved by performing binding at 4ºC (Table 17). Despite the expression of recombinant LOX is commonly achieved by induction with 1 mM IPTG [427,485], a 1.5 mM concentration was selected given that it led to a higher soluble LOX02 yield compared to 0.5, 1, 2 and 5 mM concentrations (Table 18). Following, an optimization of the purification protocol was performed and method 4 (Table 14) was selected on the basis of mean protein concentration on purified fractions (Table 21). Although fractions purified by means of the selected method contained impurities, purity was assumed to be high given the apparent relative abundance of soluble LOX02 and impurities (Figure 66).

The overexpression of soluble LOX02 was performed overnight, and for 24 and 48 h to assess whether longer overexpression times allowed the retrieval of higher amounts of

protein and a higher copper incorporation. Although extending the overexpression time to 24 h led to increased yield (Table 19), copper incorporation and activity were found to be lower as longer overexpressions were performed (Table 24 and Table 29), so overnight overexpression was selected. After inducing soluble LOX02 expression, $CuSO_4$ was added as a source of Cu^{+2} to be incorporated into the enzyme structure. Given that low copper incorporation was achieved when working at 1 µM $CuSO_4$ concentrations (Table 24), the use of higher amounts of $CuSO_4$ was explored. Despite copper is known to be toxic for bacteria [542–544], herein used concentrations were seemingly non- toxic and, indeed, higher yields were achieved when the highest $CuSO_4$ concentrations were used (Table 20). However, adding extra copper didn't improve copper incorporation and, in fact, led to lower percentage of enzyme molecules including the metallic cofactor (Table 25) and, subsequently to lower activity (Table 30). This could be due to the presence of impurities containing divalent cations in $CuSO_4$ preparations that could prevent copper atoms from binding to the protein. In case that was the case, a dialysis was performed involving the removal of metallic atoms with 2,2′-dipyridine and addition of $CuSO_4$ to reload the protein with copper. Unfortunately, dialysis was not effective, leading to a reduced percentage of enzyme molecules loaded with the metallic cofactor (Table 26) and to reduced lysyl oxidase activity (Table 31). This could be due to an improper folding of the protein during dialysis, thus hindering the incorporation of the metal.

Given that the activity of soluble LOX02 was low in all cases, the purification of the enzyme from inclusion bodies was explored. Overexpressed proteins are commonly accumulated in the form of inclusion bodies, insoluble aggregates of misfolded or partially-folded proteins [545,546]. Despite improper protein folding and the need to perform time-consuming refolding protocols, inclusion bodies are actually a tool for obtaining recombinant proteins at high purity [546]. LOX02 from inclusion bodies was purified in two elutions in order to maximize the amount of recovered protein (Table 22). Both fractions were independently characterized and the second elution was consistently found to contain more copper (Table 27) and to be more active (Table 32) than elution 1. Refolding of LOX02 in second elutions led to a striking increase in copper content (Table 28) but didn't lead to an improvement regarding protein activity (Table 33).

The presence of the LTQ cofactor in soluble LOX02 was assessed by spectrophotometry and Western Blot. Although LTQ couldn't be detected by spectrophotometry (Figure 67), Western Blot revealed weak staining for quinones (Figure 68a), suggesting that a low percentage of the enzyme molecules developed the LTQ cofactor, the active site of the enzyme [336,453]. LTQ is formed by autocatalysis upon a copper atom is properly incorporated into the enzyme [452,536]. A low copper content is then likely to result in low abundance of LTQ and thus low activity.

In vivo, LOX binds copper through specific histidine residues [451,536]. Free histidine has been shown to bind copper with high affinity, competing with proteins like albumin, which plays a role in copper transport [547], for the incorporation of the metallic atom [548], being histidine even able to remove copper bound to albumin [549]. It is feasible to think, then, that histidine residues in the His-tag would compete with those in LOX sequence for copper binding. Thus, it is hypothesized that the copper content quantified for LOX02 would correspond both to those copper ions bound to LOX02 specific residues and to those bound to the His-tag, with the latter not contributing to the development of LTQ . This would explain why soluble LOX02 produced with 1 µM $CuSO_4$ (Table 25 and Table 30) and LOX02 from inclusion bodies in second elutions (Table 27 and Table 32) contain similar amounts of copper but possess clearly differing levels of activity, or why refolding LOX02 results in a mean copper content above 200% (Table 28) and in an unmodified enzymatic activity (Table 33). A copper content-activity correlation couldn't be established. This might be due (i) to batch-to-batch differences, and (ii) to copper randomly binding to histidines either in the specific binding sites or in the His-tag, the presence of which may additionally lead to protein misfolding [550], which in turn may hinder specific copper incorporation. The removal of the polyhistidine tag by enzymatic proteolysis [551] seems an appealing approach to determine whether limited copper incorporation is related to the tag or to the expression/purification system itself.

This chapter illustrates our efforts to obtain active lysyl oxidase for the production of highly biomimetic hydrogels. Despite we achieved the production and purification of recombinant human LOX with a copper content and activity higher than those found in the literature [483,485], the insolubilization of ELRs was never achieved. Further work is required to yield a more efficient system (hundreds of mg/l of culture are commonly

achieved for recombinant proteins) allowing the production of highly active LOX feasible to be used to produce scaffolds for tissue engineering.

5.4 SUPPLEMENTARY DATA

Test	Parameter	C.T.	O.T.	O.t.	[IPTG]	[$CuSO_4$]	Resin	R.B.T.	Purification	Dialysis
1	Resin	30°C	O.N.	16°C	1 mM	1 µM	Cu^{+2}	4° C	1	No
							Co^{+2}	4°C	1	No
2	R.B.T.	30°C	O.N.	16°C	1 mM	2 µM	Cu^{+2}	4°C	1	No
								RT	1	No
3	[IPTG]	30°C	O.N.	16°C	0.5 mM	1 µM	Cu^{+2}	4°C	1	No
					1.5 mM	1 µM	Cu^{+2}	4°C	1	No
					2 mM	1 µM	Cu^{+2}	4°C	1	No
					5 mM	1 µM	Cu^{+2}	4°C	1	No
4	Purification	37 °C	O.N.	22°C	1.5 mM	1 µM	Cu^{+2}	4°C	1	No
									2	No
									3	No
									4	No
5	Dialysis	37°C	O.N.	22°C	1.5 mM	2 µM	Cu^{+2}	4°C	4	No
										Yes
6	O.t.	37°C	24 h	22°C	1.5 mM	1 µM	Cu^{+2}	4°C	4	No
			48 h		1.5 mM	1 µM	Cu^{+2}	4°C	4	No
7	[$CuSO_4$]	37°C	O.N.	22°C	1.5 mM	1 µM	Cu^{+2}	4°C	4	No
						2 µM	Cu^{+2}	4°C	4	No
						5 µM	Cu^{+2}	4°C	4	No
						10 µM	Cu^{+2}	4°C	4	No
						20 µM	Cu^{+2}	4°C	4	No

Table 34. Summary of the tests performed to adjust protein overexpression and purification conditions. C.T.: culture temperature; O.T.: overexpression temperature; O.N.:

overnight; O.t.: overexpression time; R.B.T.: resin binding temperature. Purification method 1: centrifugation in tube; 2: centrifugation in spin column; 3: centrifugation in tube + centrifugation in spin column; 4: centrifugation in tube + gravity-flow in spin column.

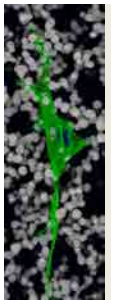

Conclusions

6.1 CONCLUSIONS

1. The production of hydrogels by EDC-mediated catalysis can be successfully achieved through a single-step reaction in mild conditions without the need of using NHS as a stabilizing agent.

2. Citric acid can be used both as a biocompatible crosslinker and a bioactive molecule providing hydrogels with calcium phosphate nucleation capacity.

3. Herein developed reaction can be used to produce hydrogels as long as polymers to be crosslinked possess $–NH_2$ groups and a low $–COOH/-NH_2$ ratio.

4. EDC-catalyzed crosslinking with citric acid can be used to control polymer aggregation and thus to tailor the architecture of so-produced hydrogels, while polymer concentration is useful to their mechanical properties.

5. EDC-catalyzed crosslinking with citric acid seems not to involve –COOH groups from aspartic acid in RGD tripeptides, thus preserving the integrity of cell adhesion motifs.

6. The degradation products of citric acid-crosslinked hydrogels are biocompatible, thus not altering MSCs behavior upon in vivo degradation.

7. Both mechanically-tailored and non-tailored hydrogels are biocompatible and able to integrate into native bone in vivo and to be at least osteoconductive, allowing bone formation by intramembranous ossification.

8. Mechanically-tailored hydrogels seem not to be superior to their non-tailored counterparts as to osteogenic potential in vivo, probably due to hindered cell invasion or to a non-osteogenic combination of chemical and physical signals.

9. The effect of single scaffold signals, either in 2D or 3D, on cell behavior needs to be considered a proof of concept given the complex and synergistic nature of ECM signals in vivo.

10. Despite having obtained recombinant human LOX with improved copper content and activity, it was not enough to achieve the insolubilization of ELRs. Thus, novel overexpression and purification systems are required to achieve highly active LOX to be used to produce scaffolds for in situ bone tissue engineering.

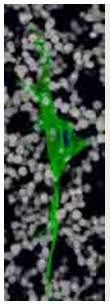

References

REFERENCES

[1] DiGirolamo DJ, Clemens TL, Kousteni S. The skeleton as an endocrine organ. Nat Rev Rheumatol 2012;8:674–83.

[2] Olsen B, Reginato A, Wang W. Bone development. Annu Rev Cell Dev Biol 2000;16:191–220.

[3] Ross MH, Pawlina W. Bone. In: Ross MH, Pawlina W, editors. Histol. a text atlas, with Correl. cell Mol. Biol. 6th ed., PA: Lippincott Williams & Wilkins; 2011, p. 218–53.

[4] Buckwalter JA, Glimcher MJ, Cooper RR, Recker R. Bone biology. Part I: structure, blood supply, cells, matrix, and mineralization. J Bone Jt Surg Am 1995;77:1256–75.

[5] Burr DB, Akkus O. Bone morphology and organization. In: Burr DB, Allen MR, editors. Basic Appl. bone Biol. 1st ed., London: Academic Press; 2014, p. 3–25.

[6] Hu Y-Y, Rawal A, Schmidt-Rohr K. Strongly bound citrate stabilizes the apatite nanocrystals in bone. Proc Natl Acad Sci U S A 2010;107:22425–9.

[7] Blausen.com staff. Blausen gallery. Wikiversity J Med 2014.

[8] Schlenker RA, VonSeggen WW. The distribution of cortical and trabecular bone mass along the lengths of the radius and ulna and the implications forin vivo bone mass measurements. Calcif Tissue Res 1976;20:41–52.

[9] Fuchs RK, Warden SJ, Turner CH. Bone anatomy, physiology and adaptation to mechanical loading. In: Planell JA, Best SM, Lacroix D, Merolli A, editors. Bone repair Biomater., Padstow, UK: Woodhead Publishing; 2009, p. 25–68.

[10] Donnelly E, Meredith DS, Nguyen JT, Boskey AL. Bone tissue composition varies across anatomic sites in the proximal femur and the iliac crest. J Orthop Res 2012;30:700–6.

[11] Nottestad SY, Baumel JJ, Kimmel DB, Recker RR, Heaney RP. The proportion of trabecular bone in human vertebrae. J Bone Miner Res 1987;2:221–9.

[12] Shapiro F. Variable conformation of GAP junctions linking bone cells: A transmission electron microscopic study of linear, stacked linear, curvilinear, oval, and annular junctions. Calcif Tissue Int 1997;61:285–93.

[13] Nudelman F, Lausch AJ, Sommerdijk NAJM, Sone ED. In vitro models of collagen biomineralization. J Struct Biol 2013;183:258–69.

[14] Hodge AJ, Petruska JA. Recent studies with the electron microscope on ordered aggregates of the tropocollagen molecule. In: Ramachandran GN, editor. Asp. protein Struct., New York: Academic Press; 1963, p. 289–300.

[15] Weiner S, Traub W. Bone structure: from angstroms to microns. FASEB J 1992;6:879–85.

[16] Hulmes DJS, Miller A. Quasi-hexagonal packing in collagen fibrils. Nature 1979;282:878–80.

[17] Orgel JPRO, Irving TC, Miller A, Wess TJ. Microfibrillar structure of type I collagen in situ. Proc Natl Acad Sci U S A 2006;103:9001–5.

[18] Landis WJ, Song MJ, Leith A, McEwen L, McEwen BF. Mineral and organic matrix interaction in normally calcifying tendon visualized in three dimensions by high-voltage electron microscopic tomography and graphic image reconstruction. J Struct Biol 1993;110:39–54.

[19] Alexander B, Daulton TL, Genin GM, Lipner J, Pasteris JD, Wopenka B, et al. The nanometre-scale physiology of bone: steric modelling and scanning transmission electron microscopy of collagen–mineral structure. J R Soc Interface 2012;9:1774–86.

[20] Nair AK, Gautieri A, Chang S-W, Buehler MJ. Molecular mechanics of mineralized collagen fibrils in bone. Nat Commun 2013;4:1724.

[21] McNally EA, Schwarcz HP, Botton GA, Arsenault AL. A model for the ultrastructure of bone based on electron microscopy of ion-milled sections. PLoS One 2012;7:e29258.

[22] Silver FH, Landis WJ. Deposition of apatite in mineralizing vertebrate extracellular matrices: A model of possible nucleation sites on type I collagen. Connect Tissue Res 2011;52:242–54.

[23] Gautieri A, Uzel S, Vesentini S, Redaelli A, Buehler MJ. Molecular and mesoscale mechanisms of osteogenesis imperfecta disease in collagen fibrils. Biophys J 2009;97:857–65.

[24] Knott L, Bailey AJ. Collagen cross-links in mineralizing tissues: a review of their chemistry, function, and clinical relevance. Bone 1998;22:181–7.

[25] Xie B, Nancollas GH. How to control the size and morphology of apatite nanocrystals in bone . Proc Natl Acad Sci U S A 2010;107:22369–70.

[26] Gao HJ, Ji BH, Jager IL, Arzt E, Fratzl P. Materials become insensitive to flaws at nanoscale: Lessons from nature. Proc Natl Acad Sci U S A 2003;100:5597–600.

[27] Neve A, Corrado A, Cantatore FP. Osteoblast physiology in normal and pathological conditions. Cell Tissue Res 2011;343:289–302.

[28] Doherty MJ, Ashton BA, Walsh S, Beresford JN, Grant ME, Canfield AE. Vascular pericytes express osteogenic potential in vitro and in vivo. J Bone Miner Res 1998;13:828–38.

[29] Boonrungsiman S, Gentleman E, Carzaniga R, Evans ND, McComb DW, Porter AE, et al. The role of intracellular calcium phosphate in osteoblast-mediated bone apatite formation. Proc Natl Acad Sci U S A 2012;109:14170–5.

[30] Narayanan K, Srinivas R, Peterson MC, Ramachandran A, Hao J, Thimmapaya B, et al. Transcriptional regulation of dentin matrix protein 1 by JunB and p300 during osteoblast differentiation. J Biol Chem 2004;279:44294–302.

[31] Gordon JAR, Tye CE, Sampaio A V, Underhill TM, Hunter GK, Goldberg HA. Bone sialoprotein expression enhances osteoblast differentiation and matrix mineralization in vitro. Bone 2007;41:462–73.

[32] Costello LC, Franklin RB, Reynolds MA, Chellaiah M. The important role of osteoblasts and citrate production in bone formation : " osteoblast citration " as a new concept for an old relationship. Open Bone J 2012:27–34.

[33] Franz-Odendaal T a, Hall BK, Witten PE. Buried alive: how osteoblasts become osteocytes. Dev Dyn 2006;235:176–90.

[34] Manolagas S. Birth and death of bone cells: basic regulatory mechanisms and implications for the pathogenesis and treatment of osteoporosis. Endocr Rev 2000;21:115–37.

[35] Hauge EM, Qvesel D, Eriksen EF, Mosekilde L, Melsen F. Cancellous bone remodeling occurs in specialized compartments lined by cells expressing osteoblastic markers. J Bone Miner Res 2001;16:1575–82.

[36] Dobnig H, Turner RT. Evidence that intermittent treatment with parathyroid hormone increases bone formation in adult rats by activation of bone lining cells. Endocrinology 1995;136:3632–8.

[37] Burger EH, Klein-Nulend J. Mechanotransduction in bone—role of the lacuno-canalicular network. FASEB J 1999;13:101–12.

[38] Tatsumi S, Ishii K, Amizuka N, Li M, Kobayashi T, Kohno K, et al. Targeted ablation of osteocytes induces osteoporosis with defective mechanotransduction. Cell Metab 2007;5:464–75.

[39] Wysolmerski JJ. Osteocytic osteolysis: time for a second look? Bonekey Rep 2012;1:229.

[40] Bellido T, Plotkin LI, Bruzzaniti A. Bone cells. In: Burr DB, Allen MR, editors. Basic Appl. bone Biol. 1st ed., London: Academic Press; 2014, p. 27–45.

[41] Charles JF, Aliprantis AO. Osteoclasts: more than "bone eaters". Trends Mol Med 2014;20:449–59.

[42] Blum B, Benvenisty N. The tumorigenicity of human embryonic stem cells. Adv Cancer Res 2008;100:133–58.

[43] Liu Z, Tang Y, Lü S, Zhou J, Du Z, Duan C, et al. The tumourigenicity of iPS cells and their differentiated derivates. J Cell Mol Med 2013;17:782–91.

[44] Strioga M, Viswanathan S, Darinskas A, Slaby O, Michalek J. Same or not the same? Comparison of adipose tissue-derived versus bone marrow-derived mesenchymal stem and stromal cells. Stem Cells Dev 2012;21:2724–52.

[45] Friedenstein AJ, Chailakhjan RK, Lalykina KS. The development of fibroblast colonies in monolayer cultures of guinea-pig bone marrow and spleen cells. Cell Tissue Kinet 1970;3:393–403.

[46] Pittenger MF, Mackay AM, Beck SC, Jaiswal RK. Multilineage potential of adult human mesenchymal stem cells. Science 1999;284:143–7.

[47] Dominici M, Le Blanc K, Mueller I, Slaper-Cortenbach I, Marini FC, Krause DS, et al. Minimal criteria for defining multipotent mesenchymal stromal cells. The International Society for Cellular Therapy position statement. Cytotherapy 2006;8:315–7.

[48] Caplan AI. Mesenchymal stem cells. J Orthop Res 1991;9:641–50.

[49] Kopen GC, Darwin JP, Phinney DG. Marrow stromal cells migrate throughout forebrain and cerebellum, and they differentiate into astrocytes after injection into neonatal mouse brains. Proc Natl Acad Sci U S A 1999;96:10711–6.

[50] Taran R, Mamidi MK, Singh G, Dutta S, Parhar IS, John JP, et al. In vitro and in vivo neurogenic potential of mesenchymal stem cells isolated from different sources. J Biosci 2014;39:157–69.

[51] Sato Y, Araki H, Kato J, Nakamura K, Kawano Y, Kobune M, et al. Human mesenchymal stem cells xenografted directly to rat liver are differentiated into human hepatocytes without fusion. Blood 2015;106:756–63.

[52] Lin ZB, Qian B, Yang YZ, Zhou K, Sun J, Mo XM, et al. Isolation, characterization and cardiac differentiation of human thymus tissue derived mesenchymal stromal cells. J Cell Biochem 2014.

[53] Czubak P, Bojarska-Junak A, Tabarkiewicz J, Putowski L. A modified method of insulin producing cells' generation from bone marrow-derived mesenchymal stem cells. J Diabetes Res 2014;2014:628591.

[54] Catacchio I, Berardi S, Reale A, De Luisi A, Racanelli V, Vacca A, et al. Evidence for bone marrow adult stem cell plasticity: properties, molecular mechanisms, negative aspects, and clinical applications of hematopoietic and mesenchymal stem cells transdifferentiation. Stem Cells Int 2013;2013:589139.

[55] Murray IR, West CC, Hardy WR, James AW, Park TS, Nguyen A, et al. Natural history of mesenchymal stem cells, from vessel walls to culture vessels. Cell Mol Life Sci 2014;71:1353–74.

[56] Zuk PA, Zhu M, Mizuno H, Huang J, Futrell JW, Katz AJ, et al. Multilineage cells from human adipose tissue: implications for cell-based therapies. Tissue Eng 2001;7:211–28.

[57] Campagnoli C, Roberts IAG, Kumar S, Bennett PR, Bellantuono I, Fisk NM. Identification of mesenchymal stem / progenitor cells in human first-trimester fetal blood, liver, and bone marrow. Blood 2001;98:2396–402.

[58] Da Silva Meirelles L, Chagastelles PC, Nardi NB. Mesenchymal stem cells reside in virtually all post-natal organs and tissues. J Cell Sci 2006;119:2204–13.

[59] Crisan M, Yap S, Casteilla L, Chen C-W, Corselli M, Park TS, et al. A perivascular origin for mesenchymal stem cells in multiple human organs. Cell Stem Cell 2008;3:301–13.

[60] Pachón-Peña G, Yu G, Tucker A, Wu X, Vendrell J, Bunnell BA, et al. Stromal stem cells from adipose tissue and bone marrow of age-matched female donors display distinct immunophenotypic profiles. J Cell Physiol 2011;226:843–51.

[61] Mohamad-Fauzi N, Ross PJ, Maga EA, Murray JD. Impact of source tissue and ex vivo expansion on the characterization of goat mesenchymal stem cells. J Anim Sci Biotechnol 2015.

[62] Ho AD, Wagner W, Franke W. Heterogeneity of mesenchymal stromal cell preparations. Cytotherapy 2008;10:320–30.

[63] Tormin A, Brune JC, Olsson E, Valcich J, Neuman U, Olofsson T, et al. Characterization of bone marrow-derived mesenchymal stromal cells (MSC) based on gene expression profiling of functionally defined MSC subsets. Cytotherapy 2009;11:114–28.

[64] Rada T, Reis RL, Gomes ME. Distinct stem cells subpopulations isolated from human adipose tissue exhibit different chondrogenic and osteogenic differentiation potential. Stem Cell Rev 2011;7:64–76.

[65] Jiang Y, Jahagirdar BN, Reinhardt RL, Schwartz RE, Keene CK, Ortiz-Gonzalez XR, et al. Pluripotency of mesenchymal stem cells derived from adult marrow. Nature 2002;418:41–9.

[66] Jiang Y, Jahagirdar BN, Reinhardt RL, Schwartz RE, Keene CD, Ortiz-Gonzalez XR, et al. Pluripotency of mesenchymal stem cells derived from adult marrow. Corrigendum. Nature 2007;447:880–1.

[67] D'Ippolito G, Diabira S, Howard GA, Menei P, Roos BA, Schiller PC. Marrow-isolated adult multilineage inducible (MIAMI) cells, a unique population of postnatal young and old human cells with extensive expansion and differentiation potential. J Cell Sci 2004;117:2971–81.

[68] Kögler G, Sensken S, Airey JA, Trapp T, Müschen M, Feldhahn N, et al. A new human somatic stem cell from placental cord blood with intrinsic pluripotent differentiation potential. J Exp Med 2004;200:123–35.

[69] Beltrami AP, Cesselli D, Bergamin N, Marcon P, Rigo S, Puppato E, et al. Multipotent cells can be generated in vitro from several adult human organs (heart, liver, and bone marrow). Blood 2007;110:3438–46.

[70] Holden C. Controversial marrow cells coming Into their own? Science 2007;315:760–1.

[71] Corselli M, Chen C-W, Sun B, Yap S, Rubin JP, Péault B. The tunica adventitia of human arteries and veins as a source of mesenchymal stem cells. Stem Cells Dev 2012;21:1299–308.

[72] Muguruma Y, Yahata T, Miyatake H, Sato T, Uno T, Itoh J, et al. Reconstitution of the functional human hematopoietic microenvironment derived from human mesenchymal stem cells in the murine bone marrow compartment. Blood 2006;107:1878–87.

[73] Chapel A, Bertho JM, Bensidhoum M, Fouillard L, Young RG, Frick J, et al. Mesenchymal stem cells home to injured tissues when co-infused with hematopoietic cells to treat a radiation-induced multi-organ failure syndrome. J Gene Med 2003;5:1028–38.

[74] Sasaki M, Abe R, Fujita Y, Ando S, Inokuma D, Shimizu H. Mesenchymal stem cells are recruited into wounded skin and contribute to wound repair by transdifferentiation into multiple skin cell type. J Immunol 2008;180:2581–7.

[75] Kinnaird T, Stabile E, Burnett MS, Lee CW, Barr S, Fuchs S, et al. Marrow-derived stromal cells express genes encoding a broad spectrum of arteriogenic cytokines and promote in vitro and in vivo arteriogenesis through paracrine mechanisms. Circ Res 2004;94:678–85.

[76] Kinnaird T, Stabile E, Burnett MS, Shou M, Lee CW, Barr S, et al. Local delivery of marrow-derived stromal cells augments collateral perfusion through paracrine mechanisms. Circulation 2004;109:1543–9.

[77] Caplan AI, Dennis JE. Mesenchymal stem cells as trophic mediators. J Cell Biochem 2006;98:1076–84.

[78] Uccelli A, Moretta L, Pistoia V. Mesenchymal stem cells in health and disease. Nat Rev Immunol 2008;8:726–36.

[79] Jones S, Horwood N, Cope A, Dazzi F. The antiproliferative effect of mesenchymal stem cells is a fundamental property shared by all stromal cells. J Immunol 2007;179:2824–31.

[80] Caplan A. Why are MSCs therapeutic? New data: new insight. J Pathol 2009;217:318–24.

[81] Munoz JR, Stoutenger BR, Robinson AP, Spees JL, Prockop DJ. Human stem/progenitor cells from bone marrow promote neurogenesis of endogenous neural stem cells in the hippocampus of mice. Proc Natl Acad Sci U S A 2005;102:18171–6.

[82] Lalu MM, McIntyre L, Pugliese C, Fergusson D, Winston BW, Marshall JC, et al. Safety of cell therapy with mesenchymal stromal cells (SafeCell): a systematic review and meta-analysis of clinical trials. PLoS One 2012;7:e47559.

[83] Salem HK, Thiemermann C. Mesenchymal stromal cells: current understanding and clinical status. Stem Cells 2010;28:585–96.

[84] U.S. National Institutes of Health. Clinicaltrials.gov 2015.

[85] Percival CJ, Richtsmeier JT. Angiogenesis and intramembranous osteogenesis. Dev Dyn 2013;242:909–22.

[86] Kronenberg HM. The role of the perichondrium in fetal bone development. Ann N Y Acad Sci 2007;1116:59–64.

[87] Schenk RK, Hofstetter W, Felix R. Morphology and chemical composition of connective tissue: bone. In: Royce PM, Steinmann B, editors. Connect. tissue its heritable Disord. Mol. Genet. Med. Asp. 2nd ed., New York: John Wiley & Sons, Ltd.; 2002, p. 67–120.

[88] Openstax college. Bone tissue and the skeletal system. Anat. Physiol., 2014, p. 207–42.

[89] Currey JD. The many adaptations of bone. J Biomech 2003;36:1487–95.

[90] Smit TH, Burger EH. Is BMU-coupling a strain-regulated phenomenon? A finite element analysis. J Bone Miner Res 2000;15:301–7.

[91] Allen MR, Burr DB. Bone modeling and remodeling. In: Allen MR, Burr DB, editors. Basic Appl. bone Biol. 1st ed., London: Academic Press; 2014, p. 75–90.

[92] Burr DB. Targeted and nontargeted remodeling. Bone 2002;30:2–4.

[93] Weinbaum S, Cowin S, Zeng Y. A model for the excitation of osteocytes by mechan. J Biomech 1994;27:339–60.

[94] Heino TJ, Hentunen TA, Kalervo Väänänen H. Osteocytes inhibit osteoclastic bone resorption through transforming growth factor-beta: enhancement by estrogen. J Cell Biochem 2002;85:185–97.

[95] Heino TJ, Hentunen T a., Väänänen HK. Conditioned medium from osteocytes stimulates the proliferation of bone marrow mesenchymal stem cells and their differentiation into osteoblasts. Exp Cell Res 2004;294:458–68.

[96] You L, Temiyasathit S, Lee P, Kim CH, Tummala P, Yao W, et al. Osteocytes as mechanosensors in the inhibition of bone resorption due to mechanical loading. Bone 2008;42:172–9.

[97] Verborgt O, Gibson GJ, Schaffler MB. Loss of osteocyte integrity in association with microdamage and bone remodeling after fatigue in vivo. J Bone Miner Res 2000;15:60–7.

[98] Van Oers RFM, Ruimerman R, Tanck E, Hilbers PAJ, Huiskes R. A unified theory for osteonal and hemi-osteonal remodeling. Bone 2008;42:250–9.

[99] Chambers TJ, Fuller K. Bone cells predispose bone surfaces to resorption by exposure of mineral to osteoclastic contact. J Cell Sci 1985;76:155–65.

[100] Canalis E, Giustina A, Bilezikian JP. Mechanisms of anabolic therapies for osteoporosis. N Engl J Med 2007;357:905–16.

[101] Parfitt AM. The bone remodeling compartment: a circulatory function for bone lining cells. J Bone Miner Res 2001;16:1583–5.

[102] Cappariello A, Maurizi A, Veeriah V, Teti A. The great beauty of the osteoclast. Arch Biochem Biophys 2014;558:70–8.

[103] Hadjidakis DJ, Androulakis II. Bone remodeling. Ann N Y Acad Sci 2006;1092:385–96.

[104] Parfitt AM. Osteonal and hemi-osteonal remodeling: the spatial and temporal framework for signal traffic in adult human bone. J Cell Biochem 1994;55:273–86.

[105] Jäger I, Fratzl P. Mineralized collagen fibrils: a mechanical model with a staggered arrangement of mineral particles. Biophys J 2000;79:1737–46.

[106] Currey JD. The mechanical consequences of variation in the mineral content of bone. J Biomech 1969;2:1–11.

[107] Ascenzi A, Bonucci E. The tensile properties of single osteons. Anat Rec 1967;158:375–86.

[108] Ascenzi A, Bonucci E. The compressive properties of single osteons. Anat Rec 1968;161:377–91.

[109] Ascenzi A, Baschieri P, Benvenuti A. The bending properties of single osteons. J Biomech 1990;23:763–71.

[110] Ascenzi A, Baschieri P, Benvenuti A. The torsional properties of single selected osteons. J Biomech 1994;27:875–84.

[111] Goldstein S, Goulet R, McCubbrey D. Measurement and significance of three-dimensional architecture to the mechanical integrity of trabecular bone. Calcif Tissue Int 1993;53:S127–33.

[112] Bouxsein ML. Determinants of skeletal fragility. Best Pract Res Clin Rheumatol 2005;19:897–911.

[113] Kanis JA, Johnell O, De Laet C, Johansson H, Oden A, Delmas P, et al. A meta-analysis of previous fracture and subsequent fracture risk. Bone 2004;35:375–82.

[114] Marsell R, Einhorn TA. The biology of fracture healing. Injury 2011;42:551–5.

[115] Gerstenfeld LC, Cho TJ, Kon T, Aizawa T, Cruceta J, Graves BD, et al. Impaired intramembranous bone formation during bone repair in the absence of tumor necrosis factor-alpha signaling. Cells Tissues Organs 2001;169:285–94.

[116] Timlin M, Toomey D, Condron C, Power C, Street J, Murray P, et al. Fracture hematoma is a potent proinflammatory mediator of neutrophil function. J Trauma Acute Care Surg 2005;58.

[117] Yang X, Ricciardi BF, Hernandez-Soria A, Shi Y, Pleshko Camacho N, Bostrom MPG. Callus mineralization and maturation are delayed during fracture healing in interleukin-6 knockout mice. Bone 2007;41:928–36.

[118] Cohen T, Nahari D, Cerem LW, Neufeld G, Levi BZ. Interleukin 6 induces the expression of vascular endothelial growth factor. J Biol Chem 1996;271:736–41.

[119] Schindeler A, McDonald MM, Bokko P, Little DG. Bone remodeling during fracture repair: the cellular picture. Semin Cell Dev Biol 2008;19:459–66.

[120] Einhorn TA, Gerstenfeld LC. Fracture healing: mechanisms and interventions. Nat Rev Rheumatol 2014;11:45–54.

[121] Malizos KN, Papatheodorou LK. The healing potential of the periosteum molecular aspects. Injury 2005;36 Suppl 3:S13–9.

[122] O'Driscoll SW, Fitzsimmons JS. The role of periosteum in artilage repair. Clin Orthop Relat Res 2001;391.

[123] Phillips AM. Overview of the fracture healing cascade. Injury 2005;36 Suppl 3:S5–7.

[124] Poynton AR, Lane JM. Bone healing and failure. In: Petite H, Quarto R, editors. Eng. bone, Georgetown: Landes Bioscience; 2005, p. 45–59.

[125] Claes LE, Heigele CA, Neidlinger-Wilke C, Kaspar D, Seidl W, Margevicius KJ, et al. Effects of mechanical factors on the fracture healing process. Clin Orthop Relat Res 1998:S132–47.

[126] Augat P, Margevicius K, Simon J, Wolf S, Suger G, Claes L. Local tissue properties in bone healing: influence of size and stability of the osteotomy gap. J Orthop Res 1998;16:475–81.

[127] Goodship AE, Kenwright J. The influence of induced micromovement upon the healing of experimental tibial fractures. J Bone Joint Surg Br 1985;67:650–5.

[128] Praemer A, Furner S, Rice P. Musculoskeletal conditions in the United States. Park Ridge, Illinois: 1992.

[129] Bauer TW, Muschler GF. Bone graft materials: an overview of the basic science. Clin Orthop Relat Res 2000;371.

[130] Nandi SK, Roy S, Mukherjee P, Kundu B, De DK, Basu D. Orthopaedic applications of bone graft & graft substitutes: a review. Indian J Med Res 2010;132:15–30.

[131] United Nations. World Population Prospects: The 2012 Revision, Volume II, Demographic profiles. vol. II. 2013.

[132] Hernlund E, Svedbom A, Ivergård M, Compston J, Cooper C, Stenmark J, et al. Osteoporosis in the European Union: medical management, epidemiology and economic burden. A report prepared in collaboration with the International Osteoporosis Foundation (IOF) and the European Federation of Pharmaceutical Industry Associations (EFPIA). Arch Osteoporos 2013;8:136.

[133] Apple DJ, Sims J. Harold Ridley and the invention of the intraocular lens. Surv Ophthalmol 1996;40:279–92.

[134] Voorhees ABJR, Jaretzki AIII, Blakemore AH. The use of tubes constructed from Vinyon "N" cloth in bridging arterial defects. A preliminary report. Ann Surg 1952;135.

[135] Hench L. Biomaterials. Science 1980;208:826–31.

[136] Hench LL, Wilson J. Surface-active biomaterials. Science 1984;226:630–6.

[137] Jackanicz TM, Nash HA, Wise DL, Gregory JB. Polylactic acid as a biodegradable carrier for contraceptive steroids. Contraception 2015;8:227–34.

[138] Hench LL, Polak JM. Third-generation biomedical materials. Science 2002;295:1014–7.

[139] Williams DF. Definitions in biomaterials. In: Williams DF, editor. Prog. Biomed. Eng. 4th ed., Amsterdam: Elsevier; 1987.

[140] Williams DF. On the nature of biomaterials. Biomaterials 2009;30:5897–909.

[141] Albrektsson T, Johansson C. Osteoinduction, osteoconduction and osseointegration. Eur Spine J 2001;10:S96–101.

[142] Langer R, Vacanti JP. Tissue Engineering. Science 1993;260:920–6.

[143] Rombouts WJC, Ploemacher RE. Primary murine MSC show highly efficient homing to the bone marrow but lose homing ability following culture. Leukemia 2003;17:160–70.

[144] Banfi A, Muraglia A, Dozin B, Mastrogiacomo M, Cancedda R, Quarto R. Proliferation kinetics and differentiation potential of ex vivo expanded human bone marrow stromal cells: Implications for their use in cell therapy. Exp Hematol 2000;28:707–15.

[145] Lee RH, Seo MJ, Pulin AA, Gregory CA, Ylostalo J, Prockop DJ. The CD34-like protein PODXL and α6-integrin (CD49f) identify early progenitor MSCs with increased clonogenicity and migration to infarcted heart in mice. Blood 2008;113:816–26.

[146] Bonab MM, Alimoghaddam K, Talebian F, Ghaffari SH, Ghavamzadeh A, Nikbin B. Aging of mesenchymal stem cell in vitro. BMC Cell Biol 2006;7:14.

[147] Briquet A, Dubois S, Bekaert S, Dolhet M, Beguin Y, Gothot A. Prolonged ex vivo culture of human bone marrow mesenchymal stem cells influences their

supportive activity toward NOD/SCID-repopulating cells and committed progenitor cells of B lymphoid and myeloid lineages. Haematologica 2010;95:47–56.

[148] Kang SK, Shin IS, Ko MS, Jo JY, Ra JC. Journey of mesenchymal stem cells for homing: strategies to enhance efficacy and safety of stem cell therapy. Stem Cells Int 2012;2012:342968.

[149] François S, Bensidhoum M, Mouiseddine M, Mazurier C, Allenet B, Semont A, et al. Local irradiation not only induces homing of human mesenchymal stem cells at exposed sites but promotes their widespread engraftment to multiple organs: A study of their uantitative distribution after irradiation damage. Stem Cells 2006;24:1020–9.

[150] Garvican ER, Cree S, Bull L, Smith RK, Dudhia J. Viability of equine mesenchymal stem cells during transport and implantation. Stem Cell Res Ther 2014;5:94.

[151] Yukawa H, Watanabe M, Kaji N, Okamoto Y, Tokeshi M, Miyamoto Y, et al. Monitoring transplanted adipose tissue-derived stem cells combined with heparin in the liver by fluorescence imaging using quantum dots. Biomaterials 2012;33:2177–86.

[152] Gao J, Dennis JE, Muzic RF, Lundberg M, Caplan AI. The dynamic in vivo distribution of bone marrow-derived mesenchymal stem cells after Infusion. Cells Tissues Organs 2001;169:12–20.

[153] Lienemann PS, Lutolf MP, Ehrbar M. Biomimetic hydrogels for controlled biomolecule delivery to augment bone regeneration. Adv Drug Deliv Rev 2012;64:1078–89.

[154] Karageorgiou V, Tomkins M, Fajardo R, Meinel L, Snyder B, Wade K, et al. Porous silk fibroin 3-D scaffolds for delivery of bone morphogenetic protein-2 in vitro and in vivo. J Biomed Mater Res Part A 2006;78A:324–34.

[155] Jansen JA, Vehof JWM, Ruhé PQ, Kroeze-Deutman H, Kuboki Y, Takita H, et al. Growth factor-loaded scaffolds for bone engineering. J Control Release 2005;101:127–36.

[156] Simmons CA, Alsberg E, Hsiong S, Kim WJ, Mooney DJ. Dual growth factor delivery and controlled scaffold degradation enhance in vivo bone formation by transplanted bone marrow stromal cells. Bone 2004;35:562–9.

[157] Schmoekel HG, Weber FE, Schense JC, Grätz KW, Schawalder P, Hubbell JA. Bone repair with a form of BMP-2 engineered for incorporation into fibrin cell ingrowth matrices. Biotechnol Bioeng 2005;89:253–62.

[158] Beck LS, Amento EP, Xu Y, Deguzman L, Lee WP, Nguyen T, et al. TGF-β1 induces bone closure of skull defects: Temporal dynamics of bone formation in defects exposed to rhTGF-β1. J Bone Miner Res 1993;8:753–61.

[159] Meinel L, Zoidis E, Zapf J, Hassa P, Hottiger MO, Auer JA, et al. Localized insulin-like growth factor I delivery to enhance new bone formation. Bone 2003;33:660–72.

[160] Kawaguchi H, Oka H, Jingushi S, Izumi T, Fukunaga M, Sato K, et al. A local application of recombinant human fibroblast growth factor 2 for tibial shaft fractures: A randomized, placebo-controlled trial. J Bone Miner Res 2010;25:2735–43.

[161] Axelrad TW, Steen B, Lowenberg DW, Creevy WR, Einhorn TA. Heterotopic ossification after the use of commercially available recombinant human bone morphogenetic proteins in four patients. J Bone Joint Surg Br 2008;90:1617–22.

[162] Boraiah S, Paul O, Hawkes D, Wickham M, Lorich DG. Complications of recombinant human BMP-2 for treating complex tibial plateau fractures: a preliminary report. Clin Orthop Relat Res 2009;467:3257–62.

[163] Carragee EJ, Hurwitz EL, Weiner BK. A critical review of recombinant human bone morphogenetic protein-2 trials in spinal surgery: emerging safety concerns and lessons learned. Spine J 2011;11:471–91.

[164] Bohner M, Gbureck U, Barralet JE. Technological issues for the development of more efficient calcium phosphate bone cements: A critical assessment. Biomaterials 2005;26:6423–9.

[165] Zhang J, Liu W, Schnitzler V, Tancret F, Bouler J. Calcium phosphate cements for bone substitution : Chemistry, handling and mechanical properties. Acta Biomater 2014;10:1035–49.

[166] Larsson S, Hannink G. Injectable bone-graft substitutes: current products, their characteristics and indications, and new developments. Injury 2011;42 Suppl 2:S30–4.

[167] Mastrogiacomo M, Scaglione S, Martinetti R, Dolcini L, Beltrame F, Cancedda R, et al. Role of scaffold internal structure on in vivo bone formation in macroporous calcium phosphate bioceramics. Biomaterials 2006;27:3230–7.

[168] Ginebra MP, Espanol M, Montufar EB, Perez RA, Mestres G. New processing approaches in calcium phosphate cements and their applications in regenerative medicine. Acta Biomater 2010;6:2863–73.

[169] Barrère F, Blitterswijk CA Van, de Groot K. Bone regeneration : molecular and cellular interactions with calcium phosphate ceramics. Int J Nanomedicine 2006;1:317–32.

[170] Samavedi S, Whittington AR, Goldstein AS. Calcium phosphate ceramics in bone tissue engineering : A review of properties and their influence on cell behavior. Acta Biomater 2013;9:8037–45.

[171] Bohner M, Galea L, Doebelin N. Calcium phosphate bone graft substitutes: Failures and hopes. J Eur Ceram Soc 2012;32:2663–71.

[172] Zhang G. Biomimicry in biomedical research. Organogenesis 2012;8:101–2.

[173] Holzapfel BM, Reichert JC, Schantz JT, Gbureck U, Rackwitz L, Nöth U, et al. How smart do biomaterials need to be? A translational science and clinical point of view. Adv Drug Deliv Rev 2013;65:581–603.

[174] Gullberg D, Ekblom P. Extracellular matrix and its receptors during development. Int J Dev Biol 1995;39:845–54.

[175] Von der Mark K, Park J, Bauer S, Schmuki P. Nanoscale engineering of biomimetic surfaces: cues from the extracellular matrix. Cell Tissue Res 2010;339:131–53.

[176] Bonnans C, Chou J, Werb Z. Remodelling the extracellular matrix in development and disease. Nat Rev Mol Cell Biol 2014;15:786–801.

[177] O'Callaghan CJ, Williams B. Mechanical strain−induced extracellular matrix production by human vascular smooth muscle cells: role of TGF- β1. Hypertension 2000;36:319–24.

[178] Chiquet M, Sarasa A, Fluck M. How do fibroblasts translate mechanical signals into changes in extracellular matrix production? Matrix Biol 2003;22:73–80.

[179] Ragan PM, Chin VI, Hung HK, Masuda K, Thonar EJA, Arner EC, et al. Chondrocyte extracellular matrix synthesis and turnover are influenced by static compression in a new alginate disk culture system. Arch Biochem Biophys 2000;383:256–64.

[180] Lu P, Takai K, Weaver VM, Werb Z. Extracellular matrix degradation and remodeling in development and disease. Cold Spring Harb Perspect Biol 2011;3:a005058.

[181] Radhakrishnan P, Lewis NT, Mao JJ. Zone-specific micromechanical properties of the extracellular matrices of growth plate cartilage. Ann Biomed Eng 2004;32:284–91.

[182] Behonick DJ, Werb Z. A bit of give and take: the relationship between the extracellular matrix and the developing chondrocyte. Mech Dev 2009;120:1327–36.

[183] Alini M, Matsui Y, Dodge GR, Poole AR. The extracellular matrix of cartilage in the growth plate before and during calcification : changes in composition and degradation of type II collagen. Calcif Tissue Int 1992;50:327–35.

[184] Daley WP, Peters SB, Larsen M. Extracellular matrix dynamics in development and regenerative medicine. J Cell Sci 2008;121:255–64.

[185] Rozario T, DeSimone DW. The extracellular matrix in development and morphogenesis: a dynamic view. Dev Biol 2011;341:126–40.

[186] Schiller J, Huster D. New methods to study the composition and structure of the extracellular matrix in natural and bioengineered tissues. Biomatter 2012;2:115–31.

[187] Yamada KM. Adhesive recognition sequences. J Biol Chem 1991;266:12809–12.

[188] Pierschbacher MD, Ruoslahti E. Cell attachment activity of fibronectin can be duplicated by small synthetic fragments of the molecule. Nature 1984;309:30–3.

[189] Schvartz I, Seger D, Shaltiel S. Vitronectin. Int J Biochem Cell Biol 1999;31:539–44.

[190] Dedhar S, Ruoslahti E, Pierschbacher MD. A cell surface receptor complex for collagen type I recognizes the Arg- Gly-Asp sequence. J Cell Biol 1987;104:585–93.

[191] Hubbell JA, Massia SP, Desai NP, Drumheller PD. Endothelial cell-selective materials for tissue engineering in the vascular graft via a new receptor. Nat Biotech 1991;9:568–72.

[192] Tashiro K, Sephel GC, Weeks B, Sasaki M, Martin GR, Kleinman HK, et al. A synthetic peptide containing the IKVAV sequence from the A chain of laminin mediates cell attachment, migration, and neurite outgrowth. J Biol Chem 1989;264 :16174–82.

[193] Engel J. EGF-like domains in extracellular matrix proteins: Localized signals for growth and differentiation? FEBS Lett 1989;251:1–7.

[194] Schenk S, Hintermann E, Bilban M, Koshikawa N, Hojilla C, Khokha R, et al. Binding to EGF receptor of a laminin-5 EGF-like fragment liberated during MMP-dependent mammary gland involution. J Cell Biol 2003;161 :197–209.

[195] Köhidai L, Kun L, Éva P, Csaba G, Mihala N, Majer Z, et al. Cell-physiological effects of elastin derived (VGVAPG)n oligomers in a unicellular model system. J Pept Sci 2004;10:427–38.

[196] Senior RM, Griffin GL, Mecham RP, Wrenn DS, Prasad KU, Urry DW. Val-Gly-Val-Ala-Pro-Gly, a repeating peptide in elastin, is chemotactic for fibroblasts and monocytes. J Cell Biol 1984;99:870–4.

[197] Adams JC, Watt FM. Regulation of development and differentiation by the extracellular matrix. Development 1993;117:1183–98.

[198] Mohammadi M, Olsen SK, Goetz R. A protein canyon in the FGF-FGF receptor dimer selects from an à la carte menu of heparan sulfate motifs. Curr Opin Struct Biol 2005;15:506–16.

[199] Wipff P-J, Hinz B. Integrins and the activation of latent transforming growth factor beta1 - an intimate relationship. Eur J Cell Biol 2008;87:601–15.

[200] Hynes RO. The extracellular matrix: not just pretty fibrils. Science 2009;1326:126–1219.

[201] Lu Y, Parker KH, Wang W. Effects of osmotic pressure in the extracellular matrix on tissue deformation. Philos Trans A Math Phys Eng Sci 2006;364:1407–22.

[202] Comper WD, Laurent TC. Physiological function of connective tissue polysaccharides. Physiol Rev 1978;58:255–315.

[203] McLaughlin PJ, Chen Q, Horiguchi M, Starcher BC, Stanton JB, Broekelmann TJ, et al. Targeted disruption of fibulin-4 abolishes elastogenesis and causes perinatal lethality in mice. Mol Cell Biol 2006;26:1700–9.

[204] Gupta V, Grande-Allen KJ. Effects of static and cyclic loading in regulating extracellular matrix synthesis by cardiovascular cells. Cardiovasc Res 2006;72:375–83.

[205] Hynes R. Integrins: versatility, modulation, and signaling in cell adhesion. Cell 1992;69:11–25.

[206] Giancotti FG, Ruoslahti E. Integrin signaling. Science 1999;285:1028–33.

[207] Ciobanasu C, Faivre B, Le Clainche C. Integrating actin dynamics , mechanotransduction and integrin activation : The multiple functions of actin binding proteins in focal adhesions. Eur J Cell Biol 2013;92:339–48.

[208] Burridge K, Chrzanowska-Wodnicka M. Focal adhesions, contractility, and signaling. Annu Rev Cell Dev Biol 1996;12:463–519.

[209] Kim S-H, Turnbull J, Guimond S. Extracellular matrix and cell signalling: the dynamic cooperation of integrin, proteoglycan and growth factor receptor. J Endocrinol 2011;209:139–59.

[210] Streuli CH, Edwards GM, Delcommenne M, Whitelaw CBA, Burdon TG, Schindler C, et al. Stat5 as a target for regulation by extracellular matrix. J Biol Chem 1995;270:21639–44.

[211] Vuori K, Ruoslahti E. Association of insulin receptor substrate-1 with integrins. Science 1994;266:1576–8.

[212] Jones PL, Crack J, Rabinovitch M. Regulation of tenascin-C, a vascular smooth muscle cell survival factor that interacts with the αvβ3 integrin to promote epidermal growth factor receptor phosphorylation and growth. J Cell Biol 1997;139:279–93.

[213] Van Oers RFM, Rens EG, LaValley DJ, Reinhart-King CA, Merks RMH. Mechanical cell-matrix feedback explains pairwise and collective endothelial cell behavior in vitro. PLoS Comput Biol 2014;10:e1003774.

[214] Zhang Z, Vuori K, Reed JC, Ruoslahti E. The alpha5beta1 integrin supports survival of cells on fibronectin and up-regulates Bcl-2 expression. Proc Natl Acad Sci U S A 1995;92:6161–5.

[215] Frith JE, Mills RJ, Hudson JE, Cooper-White JJ. Tailored integrin-extracellular matrix interactions to direct human mesenchymal stem cell differentiation. Stem Cells Dev 2012;21:2442–56.

[216] Tate MC, García AJ, Keselowsky BG, Schumm MA, Archer DR, LaPlaca MC. Specific beta1 integrins mediate adhesion, migration, and differentiation of neural progenitors derived from the embryonic striatum. Mol Cell Neurosci 2004;27:22–31.

[217] Woodard AS, Garcia-Cardena G, Leong M, Madri JA, Sessa WC, Languino LR. The synergistic activity of alphavbeta3 integrin and PDGF receptor increases cell migration. J Cell Sci 1998;111 :469–78.

[218] Lin CQ, Bissell MJ. Multi-faceted regulation of cell differentiation by extracellular matrix. FASEB J 1993;7 :737–43.

[219] Reyes CD, García AJ. Alpha2beta1 integrin-specific collagen-mimetic surfaces supporting osteoblastic differentiation. J Biomed Mater Res A 2004;69:591–600.

[220] Mizuno M, Fujisawa R, Kuboki Y. Type I collagen-induced osteoblastic differentiation of bone-marrow cells mediated by collagen- alpha2beta1 integrin interaction. J Cell Physiol 2000;184:207–13.

[221] Scatena M, Almeida M, Chaisson ML, Fausto N, Nicosia RF, Giachelli CM. NF-kappaB mediates alphavbeta3 integrin-induced endothelial cell survival. J Cell Biol 1998;141:1083–93.

[222] Strömblad S, Becker JC, Yebra M, Brooks PC, Cheresh DA. Suppression of p53 activity and p21 WAF1/CIP1 expression by vascular cell integrin alphavbeta3 during angiogenesis. J Clin Invest 1996;98:426–33.

[223] Meredith JE, Fazeli B, Schwartz MA. The extracellular matrix as a cell survival factor. Mol Biol Cell 1993;4 :953–61.

[224] Frisch SM, Francis H. Disruption of epithelial cell-matrix interactions induces apoptosis. J Cell Biol 1994;124 :619–26.

[225] Paoli P, Giannoni E, Chiarugi P. Anoikis molecular pathways and its role in cancer progression. Biochim Biophys Acta 2013;1833:3481–98.

[226] Yul J, Dreiss AD, Zhou Z, Hansen JC, Siedlecki CA, Hengstebeck RW, et al. The regulation of integrin-mediated osteoblast focal adhesion and focal adhesion kinase expression by nanoscale topography. Biomaterials 2007;28:1787–97.

[227] Pelham RJ, Wang Y-L. Cell locomotion and focal adhesions are regulated by substrate flexibility. Proc Natl Acad Sci U S A 1997;94:13661–5.

[228] Solon J, Levental I, Sengupta K, Georges PC, Janmey PA. Fibroblast adaptation and stiffness matching to soft elastic substrates. Biophys J 2007;93:4453–61.

[229] Klein EA, Yin L, Kothapalli D, Castagnino P, Byfield FJ, Xu T, et al. Cell-cycle control by physiological matrix elasticity and in vivo tissue stiffening. Curr Biol 2009;19:1511–8.

[230] Taubenberger A V, Woodruff MA, Bai H, Muller DJ, Hutmacher DW. The effect of unlocking RGD-motifs in collagen I on pre-osteoblast adhesion and differentiation. Biomaterials 2010;31:2827–35.

[231] Cavalcanti-Adam EA, Volberg T, Micoulet A, Kessler H, Geiger B, Spatz JP. Cell spreading and focal adhesion dynamics are regulated by spacing of integrin ligands. Biophys J 2007;92:2964–74.

[232] Kato M, Mrksich M. Using model substrates to study the dependence of focal adhesion formation on the affinity of integrin-ligand complexes. Biochemistry 2004;43:2699–707.

[233] Arnold M, Cavalcanti-Adam EA, Glass R, Blümmel J, Eck W, Kantlehner M, et al. Activation of integrin function by nanopatterned adhesive interfaces. Chemphyschem 2004;5:383–8.

[234] Paszek MJ, Boettiger D, Weaver VM, Hammer DA. Integrin clustering is driven by mechanical resistance from the glycocalyx and the substrate. PLoS Comput Biol 2009;5:e1000604.

[235] Keselowsky BG, Collard DM, García AJ. Surface chemistry modulates fibronectin conformation and directs integrin binding and specificity to control cell adhesion. J Biomed Mater Res A 2003;66:247–59.

[236] Keselowsky BG, Collard DM, García AJ. Surface chemistry modulates focal adhesion composition and signaling through changes in integrin binding. Biomaterials 2004;25:5947–54.

[237] Keselowsky BG, Collard DM, García AJ. Integrin binding specificity regulates biomaterial surface chemistry effects on cell differentiation. Proc Natl Acad Sci U S A 2005;102:5953–7.

[238] Miao H, Li S, Hu Y-L, Yuan S, Zhao Y, Chen BPC, et al. Differential regulation of Rho GTPases by beta1 and beta3 integrins: the role of an extracellular domain of integrin in intracellular signaling. J Cell Sci 2002;115:2199–206.

[239] Oh S, Brammer KS, Li YSJ, Teng D, Engler AJ, Chien S, et al. Stem cell fate dictated solely by altered nanotube dimension. Proc Natl Acad Sci U S A 2009;106:2130–5.

[240] Dalby MJ, Gadegaard N, Tare R, Andar A, Riehle MO, Herzyk P, et al. The control of human mesenchymal cell differentiation using nanoscale symmetry and disorder. Nat Mater 2007;6:997–1003.

[241] Kilian KA, Bugarija B, Lahn BT, Mrksich M. Geometric cues for directing the differentiation of mesenchymal stem cells. Proc Natl Acad Sci U S A 2010;107:4872–7.

[242] Engler AJ, Sen S, Sweeney HL, Discher DE. Matrix elasticity directs stem cell lineage specification. Cell 2006;126:677–89.

[243] Curran JM, Chen R, Hunt JA. The guidance of human mesenchymal stem cell differentiation in vitro by controlled modifications to the cell substrate. Biomaterials 2006;27:4783–93.

[244] Harbers GM, Healy KE. The effect of ligand type and density on osteoblast adhesion, proliferation, and matrix mineralization. J Biomed Mater Res A 2005;75:855–69.

[245] Higuchi A, Ling Q-D, Chang Y, Hsu S-T, Umezawa A. Physical cues of biomaterials guide stem cell differentiation fate. Chem Rev 2013;113:3297–328.

[246] Rowlands AS, George PA, Cooper-White JJ. Directing osteogenic and myogenic differentiation of MSCs: interplay of stiffness and adhesive ligand presentation. Am J Physiol Cell Physiol 2008;295:C1037–44.

[247] Zouani OF, Kalisky J, Ibarboure E, Durrieu M-C. Effect of BMP-2 from matrices of different stiffnesses for the modulation of stem cell fate. Biomaterials 2013;34:2157–66.

[248] Lee J, Abdeen AA, Zhang D, Kilian KA. Directing stem cell fate on hydrogel substrates by controlling cell geometry, matrix mechanics and adhesion ligand composition. Biomaterials 2013;34:8140–8.

[249] Sachot N, Castaño O, Mateos-Timoneda MA, Engel E, Planell JA. Hierarchically engineered fibrous scaffolds for bone regeneration. J R Soc Interface 2013;10:20130684.

[250] Lee J, Lee Y, Cho H, Kim D, Shin H. The incorporation of bFGF mediated by heparin into PCL/gelatin composite fiber meshes for guided bone regeneration. Drug Deliv Transl Res 2015;5:146–59.

[251] Koosha M, Mirzadeh H. Electrospinning, mechanical properties, and cell behavior study of chitosan/PVA nanofibers. J Biomed Mater Res Part A 2015;Epub.

[252] Hajiali H, Heredia-Guerrero JA, Liakos I, Athanassiou A, Mele E. Alginate nanofibrous mats with adjustable degradation rate for regenerative medicine. Biomacromolecules 2015;16:936–43.

[253] Kai D, Prabhakaran MP, Jin G, Tian L, Ramakrishna S. Potential of VEGF-encapsulated electrospun nanofibers for in vitro cardiomyogenic differentiation of human mesenchymal stem cells. J Tissue Eng Regen Med 2015;Epub.

[254] Gandhimathi C, Venugopal JR, Allister TY, Ramakrishna S, Kumar SD. Biomimetic hybrid nanofibrous substrates for mesenchymal stem cells differentiation into osteogenic cells. Mater Sci Eng C 2015;49:776–85.

[255] Gomes SR, Rodrigues G, Martins GG, Roberto MA, Mafra M, Henriques CMR, et al. In vitro and in vivo evaluation of electrospun nanofibers of PCL, chitosan and gelatin: A comparative study. Mater Sci Eng C 2015;46:348–58.

[256] Pezeshki-Modaress M, Mirzadeh H, Zandi M. Gelatin-GAG electrospun nanofibrous scaffold for skin tissue engineering: fabrication and modeling of process parameters. Mater Sci Eng C Mater Biol Appl 2015;48:704–12.

[257] Ladd MR, Hill TK, Yoo JJ, Lee SJ. Electrospun nanofibers in tissue engineering. In: Lin T, editor. Nanofibers - Prod. Prop. Funct. Appl., InTech; 2013, p. 347–72.

[258] Zeltinger J, Sherwood JK, Graham DA, Müeller R, Griffith LG. Effect of pore size and void fraction on cellular adhesion, proliferation, and matrix deposition. Tissue Eng 2001;7:557–72.

[259] Brauker JH, Carr-Brendel VE, Martinson LA, Crudele J, Johnston WD, Johnson RC. Neovascularization of synthetic membranes directed by membrane microarchitecture. J Biomed Mater Res 1995;29:1517–24.

[260] Mehdizadeh H, Sumo S, Bayrak ES, Brey EM, Cinar A. Three-dimensional modeling of angiogenesis in porous biomaterial scaffolds. Biomaterials 2013;34:2875–87.

[261] Somo SI, Akar B, Bayrak ES, Larson JC, Appel AA, Mehdizadeh H, et al. Pore Interconnectivity Influences Growth Factor-Mediated Vascularization in Sphere-Templated Hydrogels. Tissue Eng Part C Methods 2015;Epub.

[262] Geckil H, Xu F, Zhang X, Moon S, Demirci U. Engineering hydrogels as extracellular matrix mimics. Nanomedicine 2010;5:469–84.

[263] Peppas NA, Meadows DL. Macromolecular structure and solute diffusion in membranes: An overview of recent theories. J Memb Sci 1983;16:361–77.

[264] Peppas NA, Merrill EW. Crosslinked poly(vinyl alcohol) hydrogels as swollen elastic networks. J Appl Polym Sci 1977;21:1763–70.

[265] Omidian H, Hasherni S, Askari F, Nafisi S. Swelling and crosslink density measurements for hydrogels. Iran J Polym Sci Technol 1994;3:115–9.

[266] Lee F, Chung JE, Kurisawa M. An injectable enzymatically crosslinked hyaluronic acid–tyramine hydrogel system with independent tuning of mechanical strength and gelation rate. Soft Matter 2008;4:880.

[267] Pilipchuk SP, Vaicik MK, Larson JC, Gazyakan E, Cheng M-H, Brey EM. Influence of crosslinking on the stiffness and degradation of dermis-derived hydrogels. J Biomed Mater Res A 2013;101A:2883–95.

[268] Xing Q, Yates K, Vogt C, Qian Z, Frost MC, Zhao F. Increasing mechanical strength of gelatin hydrogels by divalent metal ion removal. Sci Rep 2014;4:4076.

[269] Duflo S, Thibeault SL, Li W, Shu XZ, Prestwich GD. Vocal fold tissue repair in vivo using a synthetic extracellular matrix. Tissue Eng 2006;12:2171–80.

[270] Ferreira LS, Gerecht S, Fuller J, Shieh HF, Vunjak-Novakovic G, Langer R. Bioactive hydrogel scaffolds for controllable vascular differentiation of human embryonic stem cells. Biomaterials 2007;28:2706–17.

[271] Park S-H, Park SR, Chung S Il, Pai KS, Min B-H. Tissue-engineered cartilage using fibrin/hyaluronan composite gel and its in vivo implantation. Artif Organs 2005;29:838–45.

[272] Stevens MM, Marini RP, Schaefer D, Aronson J, Langer R, Shastri VP. In vivo engineering of organs: The bone bioreactor. Proc Natl Acad Sci United States Am 2005;102 :11450–5.

[273] Willers C, Chen J, Wood D, Xu J, Zheng MH. Autologous chondrocyte implantation with collagen bioscaffold for the treatment of osteochondral defects in rabbits. Tissue Eng 2005;11:1065–76.

[274] Li Q, Williams CG, Sun DDN, Wang J, Leong K, Elisseeff JH. Photocrosslinkable polysaccharides based on chondroitin sulfate. J Biomed Mater Res Part A 2004;68A:28–33.

[275] Kim HJ, Kim U-J, Kim HS, Li C, Wada M, Leisk GG, et al. Bone tissue engineering with premineralized silk scaffolds. Bone 2015;42:1226–34.

[276] Lutolf MP, Lauer-Fields JL, Schmoekel HG, Metters AT, Weber FE, Fields GB, et al. Synthetic matrix metalloproteinase-sensitive hydrogels for the conduction of tissue regeneration: engineering cell-invasion characteristics. Proc Natl Acad Sci U S A 2003;100:5413–8.

[277] An Y, Hubbell JA. Intraarterial protein delivery via intimally-adherent bilayer hydrogels. J Control Release 2000;64:205–15.

[278] Bryant SJ, Nuttelman CR, Anseth KS. Cytocompatibility of UV and visible light photoinitiating systems on cultured NIH/3T3 fibroblasts in vitro. J Biomater Sci Polym Ed 2000;11:439–57.

[279] Suggs LJ, Mikos AG. Development of poly(propylene fumarate-co-ethylene glycol) as an injectable carrier for endothelial cells. Cell Transplant 1999;8:345–50.

[280] Vijayasekaran S, V.Chirila T, Robertson TA, Lou X, Fitton JH, Hicks CR, et al. Calcification of poly(2-hydroxyethyl methacrylate) hydrogel sponges implanted in the rabbit cornea: A 3-month study. J Biomater Sci Polym Ed 2000;11:599–615.

[281] Belkas JS, Munro CA, Shoichet MS, Johnston M, Midha R. Long-term in vivo biomechanical properties and biocompatibility of poly(2-hydroxyethyl methacrylate-co-methyl methacrylate) nerve conduits. Biomaterials 2005;26:1741–9.

[282] Burdick JA, Anseth KS. Photoencapsulation of osteoblasts in injectable RGD-modified PEG hydrogels for bone tissue engineering. Biomaterials 2002;23:4315–23.

[283] Kharkar PM, Kiick KL, Kloxin AM. Designing degradable hydrogels for orthogonal control of cell microenvironments. Chem Soc Rev 2013;42:7335–72.

[284] Gomes M, Azevedo H, Malafaya P, Silva S, Oliveira J, Silva G, et al. Natural Polymers in tissue engineering applications. In: Blitterswijk CA Van, Thomsen P, Lindahl A, Hubbell J, Williams DF, Cancedda R, et al., editors. Tissue Eng. First, Oxford, UK: Elsevier; 2008, p. 145–92.

[285] Langer R, Tirrell DA. Designing materials for biology and medicine. Nature 2004;428:487–92.

[286] Urry DW, Okamoto K, Harris RD, Hendrix CF, Long MM. Synthetic, crosslinked polypentapeptide of tropoelastin: an anisotropic, fibrillar elastomer. Biochemistry 1976;15:4083–9.

[287] Rodriguez-Cabello JC, Prieto S, Reguera J, Arias FJ, Ribeiro A. Biofunctional design of elastin-like polymers for advanced applications in nanobiotechnology . J Biomater Sci Ed 2007;18:269–86.

[288] Rodríguez-Cabello JC, Reguera J, Girotti A, Alonso M, Testera AM. Developing functionality in elastin-like polymers by increasing their molecular complexity: The power of the genetic engineering approach. Prog Polym Sci 2005;30:1119–45.

[289] Lee J, Macosko CW, Urry DW. Phase transition and elasticity of protein-based hydrogels. J Biomater Sci Ed 2001;12:229–42.

[290] Van Hest JCM, Tirrell DA. Protein-based materials, toward a new level of structural control. Chem Commun 2001:1897–904.

[291] Su RSC, Kim Y, Liu JC. Resilin: Protein-based elastomeric biomaterials. Acta Biomater 2014;10:1601–11.

[292] Martino M, Tamburro AM. Chemical synthesis of cross-linked poly(KGGVG), an elastin-like biopolymer. Biopolymers 2001;59:29–37.

[293] Bellingham CM, Lillie MA, Gosline JM, Wright GM, Starcher BC, Bailey AJ, et al. Recombinant human elastin polypeptides self-assemble into biomaterials with elastin-like properties. Biopolymers 2003;70:445–55.

[294] Winkler S, Wilson D, Kaplan DL. Controlling β-sheet assembly in genetically engineered silk by enzymatic phosphorylation/dephosphorylation. Biochemistry 2000;39:12739–46.

[295] Bini E, Foo CWP, Huang J, Karageorgiou V, Kitchel B, Kaplan DL. RGD-functionalized bioengineered spider dragline silk biomaterial. Biomacromolecules 2006;7:3139–45.

[296] Urry DW, Nico A, Gowda DC, Hoban LD, McKee A, Williams T, et al. Medical applications of bioelastic materials. In: Gebelein CG, editor. Biotechnol. Polym. medical, Pharm. Ind. Appl., Atlanta: Technomic Publishing Co. Inc.; 1993, p. 82–103.

[297] Keeley FW, Bellingham CM, Woodhouse KA. Elastin as a self-organizing biomaterial: use of recombinantly expressed human elastin polypeptides as a model for investigations of structure and self-assembly of elastin. Philos Trans R Soc Lond B Biol Sci 2002;357:185–9.

[298] Rosenbloom J, Abrams WR, Mecham R. Extracellular matrix 4: the elastic fiber. FASEB J 1993;7:1208–18.

[299] Bellingham CM, Keeley FW. Elastin as a self-assembling material. In: Shewry PR, Tatham AS, Bailey A, editors. Elastomeric Proteins Struct. Biomech. Prop. Biol. Roles. First, Cambridge, UK: Cambridge University Press; 2003, p. 39–53.

[300] Martino M, Perri T, Tamburro AM. Elastin-based biopolymers: Chemical synthesis and structural characterization of linear and cross-linked poly(OrnGlyGlyOrnGly). Biomacromolecules 2002;3:297–304.

[301] Castiglione Morelli MA, Bisaccia F, Spisani S, De Biasi M, Traniello S, Tamburro AM. Structure-activity relationships for some elastin-derived peptide chemoattractants. J Pept Res 1997;49:492–9.

[302] Urry D. Molecular machines: how motion and other functions of living organisms can result from reversible chemical changes. Angew Chemie Int Ed English 1993;32:819–41.

[303] Urry DW, Parker TM, Reid MC, Gowda DC. Biocompatibility of the bioelastic materials, poly(GVGVP) and its gamma-irradiation cross-linked matrix: summary of generic biological test results. J Bioact Compat Polym 1991;6:263–82.

[304] Costa RR, Custódio CA, Testera AM, Arias FJ, Rodríguez-Cabello JC, Alves NM, et al. Stimuli-responsive thin coatings using elastin-like polymers for biomedical applications. Adv Funct Mater 2009;19:3210–8.

[305] Welsh ER, Tirrell DA. Engineering the extracellular matrix: A novel approach to polymeric biomaterials. I. Control of the physical properties of artificial protein matrices designed to support adhesion of vascular endothelial cells. Biomacromolecules 2000;1:23–30.

[306] Girotti A, Reguera J, Rodriguez-Cabello JC, Arias FJ, Alonso M, Testera AM. Design and bioproduction of a recombinant multi(bio)functional elastin-like protein polymer containing cell adhesion sequences for tissue engineering purposes. J Mater Sci Med 2004;15:479–84.

[307] Prieto S, Shkilnyy A, Rumplasch C, Ribeiro A, Arias FJ, Rodríguez-Cabello JC, et al. Biomimetic calcium phosphate mineralization with multifunctional elastin-like recombinamers. Biomacromolecules 2011;12:1480–6.

[308] Volpin D, Urry DW, Cox BA, Gotte L. Optical diffraction of tropoelastin and alpha-elastin derivatives. Biochim Biophys Acta 1976;439:253–8.

[309] Urry DW. Physical chemistry of biological free energy transduction as demonstrated by elastic protein-based polymers. J Phys Chem B 1997;101:11007–28.

[310] Arias FJ, Reboto V, Martin S, Lopez I, Rodriguez-Cabello JC. Tailored recombinant elastin-like polymers for advanced biomedical and nano(bio)technological applications. Biotechnol Lett 2006;28:687–95.

[311] Yamaoka T, Tamura T, Seto Y, Tada T, Kunugi S, Tirrell DA. Mechanism for the phase transition of a genetically engineered elastin model peptide (VPGIG)(40) in aqueous solution. Biomacromolecules 2003;4:1680–5.

[312] Ribeiro A, Arias FJ, Reguera J, Alonso M, Rodriguez-Cabello JC. Influence of the amino-acid sequence on the inverse temperature transition of elastin-like polymers. Biophys J 2009;97:312–20.

[313] Chilkoti A, Dreher MR, Meyer DE. Design of thermally responsive, recombinant polypeptide carriers for targeted drug delivery. Adv Drug Deliv Rev 2002;54:1093–111.

[314] Reguera J, Lagaron JM, Alonso M, Reboto V, Calvo B, Rodriguez-Cabello JC. Thermal behavior and kinetic analysis of the chain unfolding and refolding and of the concomitant nonpolar solvation and desolvation of two elastin-like polymers. Macromolecules 2003;36:8470–6.

[315] Liu W, Dreher MR, Furgeson DY, Peixoto K V, Yuan H, Zalutsky MR, et al. Tumor accumulation, degradation and pharmacokinetics of elastin-like polypeptides in nude mice. J Control Release 2006;116:170–8.

[316] Meyer DE, Kong GA, Dewhirst MW, Zalutsky MR, Chilkoti A. Targeting a genetically engineered elastin-like polypeptide to solid tumors by local hyperthermia. Cancer Res 2001;61:1548–54.

[317] Dreher MR, Raucher D, Balu N, Colvin OM, Ludeman SM, Chilkoti A. Evaluation of an elastin-like polypeptide-doxorubicin conjugate for cancer therapy. J Control Release 2003;91:31–43.

[318] Urry DW, Gowda DC, Harris C, Harris RD, Cox BA. Development of bioelastic materials as biocompatible, transducible and degradable drug delivery matrices. Polym Prepr Div Polym Chem - Am Chem Soc 1992;204:209–85.

[319] Amruthwar SS, Janorkar A V. Preparation and characterization of elastin-like polypeptide scaffolds for local delivery of antibiotics and proteins. J Mater Sci Mater Med 2012;23:2903–12.

[320] Asai D, Xu D, Liu W, Garcia Quiroz F, Callahan DJ, Zalutsky MR, et al. Protein polymer hydrogels by in situ, rapid and reversible self-gelation. Biomaterials 2012;33:5451–8.

[321] Pierna M, Santos M, Arias FJ, Alonso M, Rodríguez-Cabello JC. Efficient cell and cell-sheet harvesting based on smart surfaces coated with a multifunctional and self-organizing elastin-like recombinamer. Biomacromolecules 2013;14:1893–903.

[322] Floss DM, Schallau K, Rose-John S, Conrad U, Scheller J. Elastin-like polypeptides revolutionize recombinant protein expression and their biomedical application. Trends Biotechnol 2010;28:37–45.

[323] Elsas FJ, Gowda DC, Urry DW. Synthetic polypeptide sleeve for strabismus surgery. J Pediatr Ophthalmol Strabismus 1992;29:284–6.

[324] Hoban LD, Pierce M, Quance J, Hayward I, Mckee A, Gowda DC, et al. Use of polypentapeptides of elastin to prevent postoperative adhesions - Efficacy in a contaminated peritoneal model. J Surg Res 1994;56:179–83.

[325] Urry DW, Pattanaik A, Xu J, Woods TC, McPherson DT, Parker TM. Elastic protein-based polymers in soft tissue augmentation and generation. J Biomater Sci Ed 1998;9:1015–48.

[326] Hrabchak C, Rouleau J, Moss I, Woodhouse K, Akens M, Bellingham C, et al. Assessment of biocompatibility and initial evaluation of genipin cross-linked elastin-like polypeptides in the treatment of an osteochondral knee defect in rabbits. Acta Biomater 2010;6:2108–15.

[327] Ozturk N, Girotti A, Kose GT, Rodriguez-Cabello JC, Hasirci V. Dynamic cell culturing and its application to micropatterned, elastin-like protein-modified poly(N-isopropylacrylamide) scaffolds. Biomaterials 2009;30:5417–26.

[328] Tejeda-Montes E, Klymov A, Nejadnik MR, Alonso M, Rodriguez-Cabello JC, Walboomers XF, et al. Mineralization and bone regeneration using a bioactive elastin-like recombinamer membrane. Biomaterials 2014;35:8339–47.

[329] McHale MK, Setton LA, Chilkoti A. Synthesis and in vitro evaluation of enzymatically cross-linked elastin-like polypeptide gels for cartilaginous tissue repair. Tissue Eng 2005;11:1768–79.

[330] Betre H, Ong SR, Guilak F, Chilkoti A, Fermor B, Setton LA. Chondrocytic differentiation of human adipose-derived adult stem cells in elastin-like polypeptide. Biomaterials 2006;27:91–9.

[331] Nettles DL, Kitaoka K, Hanson NA, Flahiff CM, Mata BA, Hsu EW, et al. In situ crosslinking elastin-like polypeptide gels for application to articular cartilage repair in a goat osteochondral defect model. Tissue Eng Part a 2008;14:1133–40.

[332] Panitch A, Yamaoka T, Fournier MJ, Mason TL, Tirrell DA. Design and biosynthesis of elastin-like artificial extracellular matrix proteins containing periodically spaced fibronectin CS5 domains. Macromolecules 1999;32:1701–3.

[333] Bozzini S, Giuliano L, Altomare L, Petrini P, Bandiera A, Conconi MT, et al. Enzymatic cross-linking of human recombinant elastin (HELP) as biomimetic approach in vascular tissue engineering. J Mater Sci Med 2011;22:2641–50.

[334] Lampe KJ, Antaris AL, Heilshorn SC. Design of three-dimensional engineered protein hydrogels for tailored control of neurite growth. Acta Biomater 2013;9:5590–9.

[335] Martínez-Osorio H, Juárez-Campo M, Diebold Y, Girotti A, Alonso M, Arias FJ, et al. Genetically engineered elastin-like polymer as a substratum to culture cells from the ocular surface. Curr Eye Res 2009;34:48–56.

[336] Williamson PR, Kagan HM. Reaction pathway of bovine aortic lysyl oxidase. J Biol Chem 1986;261:9477–82.

[337] Migneault I, Dartiguenave C, Bertrand MJ, Waldron KC. Glutaraldehyde: behavior in aqueous solution, reaction with proteins, and application to enzyme crosslinking. Biotechniques 2004;37:790–6.

[338] Burugapalli K, Thapasimuttu A, Chan JCY, Yao L, Brody S, Kelly JL, et al. Scaffold with a natural mesh-like architecture: isolation, structural, and in vitro characterization. Biomacromolecules 2007;8:928–36.

[339] Gough JE, Scotchford CA, Downes S. Cytotoxicity of glutaraldehyde crosslinked collagen/poly(vinyl alcohol) films is by the mechanism of apoptosis. J Biomed Mater Res 2002;61:121–30.

[340] Wang C, Lau TT, Loh WL, Su K, Wang DA. Cytocompatibility study of a natural biomaterial crosslinker-Genipin with therapeutic model cells. J Biomed Mater Res - Part B Appl Biomater 2011;97 B:58–65.

[341] Kolb HC, Finn MG, Sharpless KB. Click chemistry: diverse chemical function from a few good reactions. Angew Chemie Int Ed English 2001;40:2004–21.

[342] González de Torre I, Santos M, Quintanilla L, Testera A, Alonso M, Rodríguez Cabello JC. Elastin-like recombinamer catalyst-free click gels: Characterization of poroelastic and intrinsic viscoelastic properties. Acta Biomater 2014;10:2495–505.

[343] Lee J, Macosko CW, Urry DW. Mechanical properties of cross-linked synthetic elastomeric polypentapeptides. Macromolecules 2001;34:5968–74.

[344] Lee J, Macosko CW, Urry DW. Elastomeric polypentapeptides cross-linked into matrixes and fibers. Biomacromolecules 2001;2:170–9.

[345] Sallach RE, Cui W, Wen J, Martinez A, Conticello VP, Chaikof EL. Elastin-mimetic protein polymers capable of physical and chemical crosslinking. Biomaterials 2009;30:409–22.

[346] Lim DW, Nettles DL, Setton LA, Chilkoti A. Rapid cross-linking of elastin-like polypeptides with (hydroxymethyl)phosphines in aqueous solution. Biomacromolecules 2007;8:1463–70.

[347] Lim DW, Nettles DL, Setton LA, Chilkoti A. In situ cross-linkinig of elastin-like polypeptide block copolymers for tissue repair. Biomacromolecules 2008;9:222–30.

[348] Martin L, Alonso M, Girotti A, Arias FJ, Rodriguez-Cabello CJ. Synthesis and characterization of macroporous thermosensitive hydrogels from recombinant elastin-like polymers. Biomacromolecules 2009;10:3015–22.

[349] Nowatzki PJ, Tirrell DA. Physical properties of artificial extracellular matrix protein films prepared by isocyanate crosslinking. Biomaterials 2004;25:1261–7.

[350] Urry DW, Long MM, Hendrix CF, Okamoto K. Crosslinked polypentapeptide of tropoelastin: an insoluble, serum calcifiable matrix 1976;15:4089–94.

[351] Di Zio K, Tirrell DA. Mechanical properties of artificial protein matrices engineered for control of cell and tissue behavior. Macromolecules 2003;36:1553–8.

[352] McMillan RA, Conticello VP. Synthesis and characterization of elastin-mimetic protein gels derived from a well-defined polypeptide precursor. Macromolecules 2000;33:4809–21.

[353] Mithieux SM, Rasko JEJ, Weiss AS. Synthetic elastin hydrogels derived from massive elastic assemblies of self-organized human protein monomers. Biomaterials 2004;25:4921–7.

[354] Trabbic-Carlson K, Setton LA, Chilkoti A. Swelling and mechanical behaviors of chemically cross-linked hydrogels of elastin-like polypeptides. Biomacromolecules 2003;4:572–80.

[355] Vieth S, Bellingham CM, Keeley FW, Hodge SM, Rousseau D. Microstructural and tensile properties of elastin-based polypeptides crosslinked with genipin and pyrroloquinoline quinone. Biopolymers 2007;85:199–206.

[356] Chung C, Lampe KJ, Heilshorn SC. Tetrakis (hydroxylmethyl) phosphonium chloride as a covalent crosslinking agent for cell encapsulation within protein-based hydrogels. Biomacromolecules 2012;13:3912–6.

[357] Garcia Y, Hemantkumar N, Collighan R, Griffin M, Rodriguez-Cabello JC, Pandit A. In vitro characterization of a collagen scaffold enzymatically cross-Linked with a tailored elastin-like polymer. Tissue Eng Part a 2009;15:887–99.

[358] Nakajima N, Ikada Y. Mechanism of amide formation by carbodiimide for bioconjugation in aqueous-media. Bioconjug Chem 1995;6:123–30.

[359] Taylor JW, Bassett DR. The application of carbodiimide chemistry to coatings. In: Glass JE, editor. Technol. Waterborne Coatings, vol. 663, Washington, DC: American Chemical Society; 1997, p. 137–63.

[360] Sam S, Touahir L, Andresa JS, Allongue P, Chazalviel J-N, Gouget-Laemmel AC, et al. Semiquantitative study of the EDC/NHS activation of acid terminal groups at modified porous silicon surfaces. Langmuir 2010;26:809–14.

[361] Monagle JJ. Carbodiimides. III. Conversion of isocyanates to carbodiimides. Catalyst studies. J Org Chem 1962;27:3851–5.

[362] Olde Damink LHH, Dijkstra PJJ, van Luyn MJA, van Wachem PB, Nieuwenhuis P, Feijen J, et al. Cross-linking of dermal sheep collagen using a water-soluble carbodiimide. Biomaterials 1996;17:765–73.

[363] Tillet G, Boutevin B, Ameduri B. Chemical reactions of polymer crosslinking and post-crosslinking at room and medium temperature. Prog Polym Sci 2011;36:191–217.

[364] Maleki A, Kjoniksen A-L, Nystrom B. Characterization of the chemical degradation of hyaluronic acid during chemical gelation in the presence of different cross-linker agents . Carbohydr Res 2007;342:2776–92.

[365] Pieper JS, Hafmans T, Veerkamp JH, van Kuppevelt TH. Development of tailor-made collagen-glycosaminoglycan matrices: EDC/NHS crosslinking, and ultrastructural aspects. Biomaterials 2000;21:581–93.

[366] Kinikoglu B, Rodríguez-Cabello JC, Damour O, Hasirci V. A smart bilayer scaffold of elastin-like recombinamer and collagen for soft tissue engineering. J Mater Sci Mater Med 2011;22:1541–54.

[367] Liang H-C, Chang Y, Hsu C-K, Lee M-H, Sung H-W. Effects of crosslinking degree of an acellular biological tissue on its tissue regeneration pattern. Biomaterials 2004;25:3541–52.

[368] Song J, Saiz E, Bertozzi CR. A new approach to mineralization of biocompatible hydrogel scaffolds: an efficient process toward 3-dimensional bonelike composites. J Am Chem Soc 2003;125:1236–43.

[369] Phadke A, Zhang C, Hwang Y, Vecchio K, Varghese S. Templated mineralization of synthetic hydrogels for bone-like composite materials: Role of matrix hydrophobicity. Biomacromolecules 2010;11:2060–8.

[370] Dickens F. The citric acid content of animal tissues, with reference to its occurrence in bone and tumor. Biochem J 1941;35:1011–23.

[371] Lees H, Kuyper AC. The organic acids of bone. J Biol Chem 1957;225:641–9.

[372] Hartles RL. Citrate in mineralized tissues. In: Staple PH, editor. Adv. Oral Biol., New York: Academic Press; 1964, p. 225–53.

[373] Dixon TF, Perkins HR. Citric acid and bone metabolism. Biochem J 1952;52:260–5.

[374] Seifter E, Lavine LS. Aspects of citric acid chemistry related to bone. Bull N Y Acad Med 1961;37:156–66.

[375] Kandori K, Fudo A, Ishikawa T. Study on the particle texture dependence of protein adsorption by using synthetic micrometer-sized calcium hydroxyapatite particles. Colloids and Surfaces B-Biointerfaces 2002;24:145–53.

[376] Gonzalez-McQuire R, Chane-Ching JY, Vignaud E, Lebugle A, Mann S. Synthesis and characterization of amino acid-functionalized hydroxyapatite nanorods. J Mater Chem 2004;14:2277–81.

[377] Kandori K, Oda S, Fukusumi M, Morisada Y. Synthesis of positively charged calcium hydroxyapatite nano-crystals and their adsorption behavior of proteins. Colloids and Surfaces B-Biointerfaces 2009;73:140–5.

[378] Martins MA, Santos C, Almeida MM, Costa ME V. Hydroxyapatite micro- and nanoparticles: Nucleation and growth mechanisms in the presence of citrate species. J Colloid Interface Sci 2008;318:210–6.

[379] Qiu SR, Wierzbicki A, Orme CA, Cody AM, Hoyer JR, Nancollas GH, et al. Molecular modulation of calcium oxalate crystallization by osteopontin and citrate. Proc Natl Acad Sci U S A 2004;101:1811–5.

[380] Grohe B, O'Young J, Langdon A, Karttunen M, Goldberg HA, Hunter GK. Citrate modulates calcium oxalate crystal growth by face-specific interactions. Cells Tissues Organs 2011;194:176–81.

[381] Kuyper AC. The quantitative precipitation of citric acid. J Biol Chem 1938;123:405–7.

[382] Kuyper AC. The chemistry of bone formation. I, the composition of precipitates formed from salt solutions. J Biol Chem 1945;159:411–6.

[383] Tanahashi M, Matsuda T. Surface functional group dependence on apatite formation on self-assembled monolayers in a simulated body fluid. J Biomed Mater Res 1997;34:305–15.

[384] Rhee SH, Tanaka J. Hydroxyapatite coating on a collagen membrane by a biomimetic method. J Am Ceram Soc 1998;81:3029–31.

[385] Rhee SH, Tanaka J. Effect of citric acid on the nucleation of hydroxyapatite in a simulated body fluid. Biomaterials 1999;20:2155–60.

[386] Achelhi K, Masse S, Laurent G, Saoiabi A, Laghzizil A, Coradin T. Role of carboxylate chelating agents on the chemical, structural and textural properties of hydroxyapatite. Dalt Trans 2010;39:10644–51.

[387] Puvvada N, Panigrahi PK, Pathak A. Room temperature synthesis of highly hemocompatible hydroxyapatite, study of their physical properties and spectroscopic correlation of particle size. Nanoscale 2010;2:2631–8.

[388] Kumar GS, Girija EK, Thamizhayel A, Yokogawa Y, Kalkura SN. Synthesis and characterization of bioactive hydroxyapatite-calcite nanocomposite for biomedical applications. J Colloid Interface Sci 2010;349:56–62.

[389] Lopez-Macipe A, Gomez-Morales J, Rodriguez-Clemente R. Nanosized hydroxyapatite precipitation from homogeneous calcium/citrate/phosphate solutions using microwave and conventional heating. Adv Mater 1998;10:49–53.

[390] Hempel U, Reinstorf A, Poppe M, Fischer U, Gelinsky M, Pompe W, et al. Proliferation and differentiation of osteoblasts on biocement D modified with collagen type I and citric acid. J Biomed Mater Res Part B-Applied Biomater 2004;71B:130–43.

[391] Schneiders W, Reinstorf A, Pompe W, Grass R, Biewener A, Holch M, et al. Effect of modification of hydroxyapatite/collagen composites with sodium citrate, phosphoserine, phosphoserine/RGD-peptide and calcium carbonate on bone remodelling. Bone 2007;40:1048–59.

[392] Mitsionis AI, Vaimakis TC, Trapalis CC. The effect of citric acid on the sintering of calcium phosphate bioceramics. Ceram Int 2010;36:623–34.

[393] Yang J, Webb AR, Ameer GA. Novel citric acid-based biodegradable elastomers for tissue engineering . Adv Mater 2004;16:511–6.

[394] Kibbe MR, Martinez J, Popowich DA, Kapadia MR, Ahanchi SS, Aalami OO, et al. Citric acid-based elastomers provide a biocompatible interface for vascular grafts . J Biomed Mater Res Part a 2009;93A:314–24.

[395] Yang J, Motlagh D, Allen JB, Webb AR, Kibbe MR, Aalami O, et al. Modulating expanded polytetrafluoroethylene vascular graft host response via citric acid-based biodegradable elastomers. Adv Mater 2006;18:1493–8.

[396] Motlagh D, Allen J, Hoshi R, Yang J, Lui K, Ameer G. Hemocompatibility evaluation of poly(diol citrate) in vitro for vascular tissue engineering. J Biomed Mater Res Part a 2007;82A:907–16.

[397] Yang J, Webb AR, Pickerill SJ, Hageman G, Ameer GA. Synthesis and evaluation of poly(diol citrate) biodegradable elastomers. Biomaterials 2006;27:1889–98.

[398] Yang J, Motlagh D, Webb AR, Ameer GA. Novel biphasic elastomeric scaffold for small-diameter blood vessel tissue engineering . Tissue Eng 2005;11:1876–86.

[399] Qiu H, Yang J, Kodali P, Koh J, Ameer GA. A citric acid-based hydroxyapatite composite for orthopedic implants . Biomaterials 2006;27:5845–54.

[400] Zeimaran E, Pourshahrestani S, Pingguan-Murphy B, Kadri NA, Rothan HA, Yusof R, et al. Fabrication and characterization of poly(octanediol citrate)/gallium-containing bioglass microcomposite scaffolds. J Mater Sci 2014;50:2189–201.

[401] Chung EJ, Kodali P, Laskin W, Koh JL, Ameer GA. Long-term in vivo response to citric acid-based nanocomposites for orthopaedic tissue engineering. J Mater Sci Mater Med 2011;22:2131–8.

[402] Sun D, Chen Y, Tran RT, Xu S, Xie D, Jia C, et al. Citric acid-based hydroxyapatite composite scaffolds enhance calvarial regeneration. Sci Rep 2014;4:6912.

[403] Zhang X-Q, Tang H, Hoshi R, De Laporte L, Qiu H, Xu X, et al. Sustained transgene expression via citric acid-based polyester elastomers . Biomaterials 2009;30:2632–41.

[404] Dey J, Xu H, Shen J, Thevenot P, Gondi SR, Nguyen KT, et al. Development of biodegradable crosslinked urethane-doped polyester elastomers. Biomaterials 2008;29:4637–49.

[405] Yang J, Zhang Y, Gautam S, Liu L, Dey J, Chen W, et al. Development of aliphatic biodegradable photoluminescent polymers. Proc Natl Acad Sci U S A 2009;106:10086–91.

[406] Tran RT, Thevenot P, Gyawali D, Chiao J-C, Tang L, Yang J. Synthesis and characterization of a biodegradable elastomer featuring a dual crosslinking mechanism. Soft Matter 2010;6:2449–61.

[407] Djordjevic I, Szili EJ, Choudhury NR, Dutta N, Steele DA, Kumar S. Osteoblast biocompatibility on poly(octanediol citrate)/sebacate elastomers with controlled wettability. J Biomater Sci Ed 2010;21:1039–50.

[408] Halpern JM, Urbanski R, Weinstock AK, Iwig DF, Mathers RT, Von Recum HA. A biodegradable thermoset polymer made by esterification of citric acid and glycerol. J Biomed Mater Res - Part A 2014;102:1467–77.

[409] Ju YM, Park K, Son JS, Kim J-J, Rhie J-W, Han DK. Beneficial effect of hydrophilized porous polymer scaffolds in tissue-engineered cartilage formation. J Biomed Mater Res Part B-Applied Biomater 2008;85B:252–60.

[410] Yoon JJ, Park TG. Degradation behaviors of biodegradable macroporous scaffolds prepared by gas foaming of effervescent salts. J Biomed Mater Res 2001;55:401–8.

[411] Lewandrowski KU, Hile DD, Thompson BMJ, Wise DL, Tomford WW, Trantolo DJ. Quantitative measures of osteoinductivity of a porous poly(propylene fumarate) bone graft extender. Tissue Eng 2003;9:85–93.

[412] Hesaraki S, Moztarzadeh F, Sharifi D. Formation of interconnected macropores in apatitic calcium phosphate bone cement with the use of an effervescent additive. J Biomed Mater Res Part a 2007;83A:80–7.

[413] Sarda S, Fernandez E, Nilsson M, Balcells M, Planell JA. Kinetic study of citric acid influence on calcium phosphate bone cements as water-reducing agent. J Biomed Mater Res 2002;61:653–9.

[414] Gbureck U, Barralet JE, Spatz K, Grover LM, Thull R. Ionic modification of calcium phosphate cement viscosity. Part I: hypodermic injection and strength improvement of apatite cement . Biomaterials 2004;25:2187–95.

[415] Xu W, Karst D, Yang W, Yang Y. Novel zein-based electrospun fibers with the water stability and strength necessary for various applications. Polym Int 2008;57:1110–7.

[416] Jiang Q, Reddy N, Yang Y. Cytocompatible cross-linking of electrospun zein fibers for the development of water-stable tissue engineering scaffolds. Acta Biomater 2010;6:4042–51.

[417] Jiang Q, Reddy N, Zhang S, Roscioli N, Yang Y. Water-stable electrospun collagen fibers from a non-toxic solvent and crosslinking system. J Biomed Mater Res - Part A 2013;101 A:1237–47.

[418] Saito H, Taguchi T, Kobayashi H, Kataoka K, Tanaka J, Murabayashi S, et al. Physicochemical properties of gelatin gels prepared using citric acid derivative. Mater Sci Eng C-Biomimetic Supramol Syst 2004;24:781–5.

[419] Saito H, Taguchi T, Aoki H, Murabayashi S, Mitamura Y, Tanaka J, et al. pH-responsive swelling behavior of collagen gels prepared by novel crosslinkers based on naturally derived di- or tricarboxylic acids. Acta Biomater 2007;3:89–94.

[420] Taguchi T, Saito H, Uchida Y, Sakane M, Kobayashi H, Kataoka K, et al. Bonding of soft tissues using a novel acid derivative tissue adhesive consisting of a citric and collagen. Mater Sci Eng C-Biomimetic Supramol Syst 2004;24:775–80.

[421] Saito H, Murabayashi S, Mitamura Y, Taguchi T. Unusual cell adhesion and antithrombogenic behavior of citric acid-cross-linked collagen matrices. Biomacromolecules 2007;8:1992–8.

[422] Inoue M, Sasaki M, Katada Y, Fujiu K, Manabe I, Nagai R, et al. Poly-(L-lactic acid) and citric acid-crosslinked gelatin composite matrices as a drug-eluting stent coating material with endothelialization, antithrombogenic, and drug release properties. J Biomed Mater Res - Part A 2013;101 A:2049–57.

[423] Takayama T, Taguchi T, Koyama H, Sakari M, Kamimura W, Takato T, et al. The growth of a vascular network inside a collagen-citric acid derivative hydrogel in rats. Biomaterials 2009;30:3580–7.

[424] Pinell SR, Martin GR. The cross-linking of collagen and elastin: enzymatic conversion of lysine in peptide linkage to alpha-aminoadipic-delta-semialdehyde (allysine) by an extract from bone. Proc Natl Acad Sci U S A 1968;61:708–16.

[425] Siegel RC. Biosynthesis of collagen crosslinks - increased activity of purified lysyl oxidase with reconstituted collagen fibrils. Proc Natl Acad Sci U S A 1974;71:4826–30.

[426] Csiszar K. Lysyl oxidases: a novel multifunctional amine oxidase family. Prog Nucleic Acid Res Mol Biol 2001;70:1–32.

[427] Kim MS, Kim SS, Jung ST, Park JY, Yoo HW, Ko J, et al. Expression and purification of enzymatically active forms of the human lysyl oxidase-like protein 4. J Biol Chem 2003;278:52071–4.

[428] Thomassin L, Werneck CC, Broekelmann TJ, Gleyzal C, Hornstra IK, Mecham RP, et al. The pro-regions of lysyl oxidase and lysyl oxidase-like 1 are required for deposition onto elastic fibers. J Biol Chem 2005;280:42848–55.

[429] Jourdan-Le Saux C, Le Saux O, Gleyzal C, Sommer P, Csiszar K. The mouse lysyl oxidase-like 2 gene (mLOXL2) maps to chromosome 14 and is highly expressed in skin, lung and thymus. Matrix Biol 2000;19:179–83.

[430] Jourdan-Le Saux C, Tomsche A, Ujfalusi A, Jia L, Csiszar K. Central nervous system, uterus, heart, and leukocyte expression of the LOXL3 gene, encoding a novel lysyl oxidase-like protein. Genomics 2001;74:211–8.

[431] Mäki JM, Tikkanen H, Kivirikko KI. Cloning and characterization of a fifth human lysyl oxidase isoenzyme: The third member of the lysyl oxidase-related subfamily with four scavenger receptor cysteine-rich domains. Matrix Biol 2001;20:493–6.

[432] Asuncion L, Fogelgren B, Fong KSK, Fong SFT, Kim Y, Csiszar K. A novel human lysyl oxidase-like gene (LOXL4) on chromosome 10q24 has an altered scavenger receptor cysteine rich domain. Matrix Biol 2001;20:487–91.

[433] Kim YH, Boyd CD, Csiszar K. A new gene with sequence and structural similarity to the gene encoding human lysyl oxidase. J Biol Chem 1995;270:7176–82.

[434] Perryman L, Erler JT. Lysyl oxidase in cancer research. Futur Oncol 2014;10:1709–17.

[435] Barker HE, Cox TR, Erler JT. The rationale for targeting the LOX family in cancer. Nat Rev Cancer 2012;12:540–52.

[436] Kim Y, Peyrol S, So CK, Boyd CD, Csiszar K. Coexpression of the lysyl oxidase-like gene (LOXL) and the gene encoding type III procollagen in induced liver fibrosis. J Cell Biochem 1999;72:181–8.

[437] Trackman PC, Bedell-Hogan D, Tang J, Kagan HM. Posttranslational glycosylation and proteolytic processing of a lysyl oxidase precursor. J Biol Chem 1992;267:8666–71.

[438] Panchenko M V, Stetler-Stevenson WG, Trubetskoy O V, Gacheru SN, Kagan HM. Metalloproteinase activity secreted by fibrogenic cells in the processing of prolysyl oxidase. Potential role of procollagen C-proteinase. J Biol Chem 1996;271:7113–9.

[439] Uzel MI, Shih SD, Gross H, Kessler E, Gerstenfeld LC, Trackman PC. Molecular events that contribute to lysyl oxidase enzyme activity and insoluble collagen accumulation in osteosarcoma cell clones. J Bone Miner Res 2000;15:1189–97.

[440] Uzel MI, Scott IC, Babakhaniou-Chase H, Palamakumbura AH, Pappano WN, Hong HH, et al. Multiple bone morphogenetic protein 1-related mammalian metalloproteinases process pro-lysyl oxidase at the correct physiological site and control lysyl oxidase activation in mouse embryo fibroblast cultures. J Biol Chem 2001;276:22537–43.

[441] Cronshaw AD, Fothergill-Gilmore LA, Hulmes DJS. The proteolytic processing site of the precursor of lysyl oxidase. Biochem J 1995;306:279–84.

[442] Palamakumbura AH, Jeay S, Guo Y, Pischon N, Sommer P, Sonenshein GE, et al. The propeptide domain of lysyl oxidase induces phenotypic reversion of ras-transformed cells. J Biol Chem 2004;279:40593–600.

[443] Vora SR, Palamakumbura AH, Mitsi M, Guo Y, Pischon N, Nugent M a., et al. Lysyl oxidase propeptide inhibits FGF-2-induced signaling and proliferation of osteoblasts. J Biol Chem 2010;285:7384–93.

[444] Zhao Y, Min C, Vora SR, Trackman PC, Sonenshein GE, Kirsch KH. The lysyl oxidase pro-peptide attenuates fibronectin-mediated activation of focal adhesion kinase and p130 in breast cancer cells. J Biol Chem 2009;284:1385–93.

[445] Palamakumbura AH, Vora SR, Nugent MA, Kirsch KH, Sonenshein GE, Trackman PC. Lysyl oxidase pro-peptide inhibits prostate cancer cell growth by mechanisms that target FGF-2 cell binding and signaling. Oncogene 2010;28:3390–400.

[446] Jeay S, Pianetti S, Kagan HM, Sonenshein GE. Lysyl oxidase inhibits ras-mediated transformation by preventing activation of NF-kappa B. Mol Cell Biol 2003;23:2251–63.

[447] Kenyon K, Contente S, Trackman PC, Tang J, Kagan HM, Friedman RM. Lysyl oxidase and rrg messenger RNA. Science 1991;253:802.

[448] Kosonen T, Uriu-Hare JY, Clegg MS, Keen CL, Rucker RB. Incorporation of copper into lysyl oxidase. Biochem J 1997;327:283–9.

[449] Krebs CJ, Krawetz SA. Lysyl oxidase copper-talon complex: a model. Biochim Biophys Acta 1993;1202:7–12.

[450] Ryvkin F, Greenaway FT. A peptide model of the copper-binding region of lysyl oxidase. J Inorg Biochem 2004;98:1427–35.

[451] Lopez KM, Greenaway FT. Identification of the copper-binding ligands of lysyl oxidase. J Neural Transm 2011;118:1101–9.

[452] Dove JE, Klinman JP. Trihydroxyphenylalanine quinone (TPQ) from copper amine oxidases and lysyl tyrosylquinone (LTQ) from lysyl oxidase. Adv Protein Chem 2001;58:141–74.

[453] Williamson PR, Kagan HM. Alpha-proton abstraction and carbanion formation in the mechanism of action of lysyl oxidase. J Biol Chem 1987;262:8196–201.

[454] Brown-Augsburger P, Tisdale C, Broekelmann T, Sloan C, Mecham RP. Identification of an elastin cross-linking domain that joins 3 peptide chains. Possible role in nucleated assembly. J Biol Chem 1995;270:17778–83.

[455] Eyre DR, Weis MA, Wu JJ. Advances in collagen cross-link analysis. Methods 2008;45:65–74.

[456] Starcher BC, Partridge SM, Elsden DF. Isolation and partial characterization of a new amino acid from reduced elastin. Biochemistry 1967;6:2425–32.

[457] Davis NR, Anwar RA. On the mechanism of formation of desmosine and isodesmosine crss-links of elastin. J Am Chem Soc 1970;92:3778–82.

[458] Kagan HM, Williams MA, Williamson PR, Anderson JM. Influence of sequence and charge on the specificity of lysyl oxidase toward protein and synthetic peptide-substrates. J Biol Chem 1984;259:1203–7.

[459] Trackman PC, Kagan HM. Non-peptidyl amine inhibitors are substrates of lysyl oxidase. J Biol Chem 1979;254:7831–6.

[460] Gacheru SN, Trackman PC, Calaman SD, Greenaway FT, Kagan HM. Vicinal diamines as pyrroloquinoline quinone-directed irreversible inhibitors of lysyl oxidase. J Biol Chem 1989;264:12963–9.

[461] Ohkawa K, Fujii K, Nishida A, Yamauchi T, Ishibashi H, Yamamoto H. Lysyl oxidase-catalyzed cross-linking and insolubilization reactions of Lys-containing polypeptides and synthetic adhesive proteins. Biomacromolecules 2001;2:773–9.

[462] Kagan HM, Lerch RM. Amidated carboxyl groups in elastin. Biochim Biophys Acta 1976;434:223–32.

[463] Raju K, Anwar RA. Primary structures of bovine elastin a, b, and c deduced from the sequences of cDNA clones. J Biol Chem 1987;262:5755–62.

[464] Narayanan AS, Page RC, Martin GR. On the preparation of tropoelastin from embryonic chick aorta. Biochim Biophys Acta - Protein Struct 1974;351:126–32.

[465] Urry DW, Long MM. On the conformation, coacervation and function of polymeric models of elastin. Adv Exp Med Biol 1977;79:685–714.

[466] Kagan HM, Tseng L, Trackman PC, Okamoto K, Rapaka RS, Urry DW. Repeat polypeptide models of elastin as substrates for lysyl oxidase. J Biol Chem 1980;255:3656–9.

[467] Aeschlimann D, Wetterwald A, Fleisch H, Paulsson M. Expression of tissue transglutaminase in skeletal tissues correlates with events of terminal differentiation of chondrocytes. J Cell Biol 1993;120:1461–70.

[468] Aeschlimann D, Kaupp O, Paulsson M. Transglutaminase-catalyzed matrix cross-Linking in differentiating cartilage - Identification of osteonectin as a major glutaminyl substrate. J Cell Biol 1995;129:881–92.

[469] Bowness JM, Folk JE, Timpl R. Identification of a substrate site for liver transglutaminase on the aminopropeptide of type-III collagen. J Biol Chem 1987;262:1022–4.

[470] Kleman JP, Aeschlimann D, Paulsson M, van der Rest M. Transglutaminase-catalyzed cross-linking of fibrils of collagen V/XI in A204 rhabdomyosarcoma cells. Biochemistry 1995;34:13768–75.

[471] Kothapalli CR, Ramamurthi A. Biomimetic regeneration of elastin matrices using hyaluronan and copper ion cues. Tissue Eng Part a 2009;15:103–13.

[472] Kothapalli CR, Ramamurthi A. Copper nanoparticle cues for biomimetic cellular assembly of crosslinked elastin fibers. Acta Biomater 2009;5:541–53.

[473] Kothapalli CR, Ramamurthi A. Lysyl oxidase enhances elastin synthesis and matrix formation by vascular smooth muscle cells. J Tissue Eng Regen Med 2009;3:655–61.

[474] Kagan HM, Sullivan KA, Olsson TAIII, Cronlund AL. Purification and properties of four species of lysyl oxidase from bovine aorta. Biochem J 1979;177:203–14.

[475] Sullivan KA, Kagan HM. Evidence for structural similarities in the multiple forms of aortic and cartilage lysyl oxidase and a catalytically quiescentaortic protein. J Biol Chem 1982;257:13520–6.

[476] Tang SS, Simpson DE, Kagan HM. Beta-substituted ethylamine derivatives as suicide inhibitors of lysyl oxidase. J Biol Chem 1984;259:975–9.

[477] Shah MA, Bergethon PR, Boak AM, Gallop PM, Kagan HM. Oxidation of peptidyl lysine by copper complexes of pyrroloquinoline quinone and other quinones. A model for oxidative pathochemistry. Biochim Biophys Acta - Protein Struct Mol Enzymol 1992;1159:311–8.

[478] Bedell-Hogan D, Trackman P, Abrams W, Rosenbloom J, Kagan H. Oxidation, cross-linking, and insolubilization of recombinant tropoelastin by purified lysyl oxidase. J Biol Chem 1993;268:10345–50.

[479] Fogelgren B, Polgar N, Szauter KM, Ujfaludi Z, Laczko R, Fong KSK, et al. Cellular fibronectin binds to lysyl oxidase with high affinity and is critical for its proteolytic activation. J Biol Chem 2005;280:24690–7.

[480] Kuivaniemi H, Savolainen ER, Kivirikko KI. Human placental lysyl oxidase - Purification, partial characterization, and preparation of 2 specific antisera to the enzyme. J Biol Chem 1984;259:6996–7002.

[481] Narayanan AS, Page RC, Kuzan F, Cooper CG. Elastin cross-linking in vitro. Studies on factors influencing the formation of desmosines by lysyl oxidase action on tropoelastin. Biochem J 1978;173:857–62.

[482] Shackleton DR, Hulmes DJS. Purification of lysyl oxidase from piglet skin by selective interaction with Sephacryl S-200. Biochem J 1990;266:917–9.

[483] Jung ST, Kim MS, Seo JY, Kim HC, Kim Y. Purification of enzymatically active human lysyl oxidase and lysyl oxidase-like protein from Escherichia coli inclusion bodies. Protein Expr Purif 2003;31:240–6.

[484] Ouzzine M, Boyd A, Hulmes DJS. Expression of active, human lysyl oxidase in Escherichia coli. FEBS Lett 1996;399:215–9.

[485] Herwald SE, Greenaway FT, Lopez KM. Purification of high yields of catalytically active lysyl oxidase directly from Escherichia coli cell culture. Protein Expr Purif 2010;74:116–21.

[486] Gungormus M, Branco M, Fong H, Schneider JP, Tamerler C, Sarikaya M. Self assembled bi-functional peptide hydrogels with biomineralization-directing peptides. Biomaterials 2010;31:7266–74.

[487] Engelmayr GC, Cheng M, Bettinger CJ, Borenstein JT, Langer R, Freed LE. Accordion-like honeycombs for tissue engineering of cardiac anisotropy. Nat Mater 2008;7:1003–10.

[488] García-Arévalo C, Pierna M, Girotti A, Arias FJ, Rodríguez-Cabello JC. A comparative study of cell behavior on different energetic and bioactive polymeric surfaces made from elastin-like recombinamers. Soft Matter 2012;8:3239–49.

[489] Willingham MC. An alternative fixation-processing method for preembedding ultrastructural immunocytochemistry of cytoplasmic antigens: the GBS (glutaraldehyde-borohydride-saponin) procedure. J Histochem Cytochem 1983;31:91–8.

[490] Clancy B, Cauller LJ. Reduction of background autofluorescence in brain sections following immersion in sodium borohydride. J Neurosci Methods 1998;83:97–102.

[491] Ngwenya LB, Peters A, Rosene DL. Light and electron microscopic immunohistochemical detection of bromodeoxyuridine-labeled cells in the brain: different fixation and processing protocols. J Histochem Cytochem 2005;53:821–32.

[492] Tagliaferro P, Tandler CJ, Ramos AJ, Pecci Saavedra J, Brusco A. Immunofluorescence and glutaraldehyde fixation. A new procedure based on the Schiff-quenching method. J Neurosci Methods 1997;77:191–7.

[493] Srivastava GK, Reinoso R, Singh AK, Fernandez-Bueno I, Hileeto D, Martino M, et al. Trypan Blue staining method for quenching the autofluorescence of RPE cells for improving protein expression analysis. Exp Eye Res 2011;93:956–62.

[494] Chelvanayagam DK, Beazley LD. Toluidine blue-O is a Nissl bright-field counterstain for lipophilic fluorescent tracers Di-ASP, DiI and DiO. J Neurosci Methods 1997;72:49–55.

[495] Guan J, Fujimoto KL, Wagner WR. Elastase-sensitive elastomeric scaffolds with variable anisotropy for sof tissue engineering. Pharm Res 2008;25:2400–12.

[496] Hwang D, Moolchandani V, Dandu R, Haider M, Cappello J, Ghandehari H. Influence of polymer structure and biodegradation on DNA release from silk-elastinlike protein polymer hydrogels. Int J Pharm 2009;368:215–9.

[497] Guan J, Wagner WR. Synthesis, characterization and cytocompatibility of polyurethaneurea elastomers with designed elastase sensitivity. Biomacromolecules 2005;6:2833–42.

[498] Schindelin J, Arganda-Carreras I, Frise E, Kaynig V, Longair M, Pietzsch T, et al. Fiji: an open-source platform for biological-image analysis. Nat Methods 2012;9:676–82.

[499] Doube M, Kłosowski MM, Arganda-Carreras I, Cordelières FP, Dougherty RP, Jackson JS, et al. BoneJ: free and extensible bone image analysis in ImageJ. Bone 2010;47:1076–9.

[500] Kokubo T, Takadama H. How useful is SBF in predicting in vivo bone bioactivity? Biomaterials 2006;27:2907–15.

[501] Drezek R, Brookner C, Pavlova I, Boiko I, Malpica a, Lotan R, et al. Autofluorescence microscopy of fresh cervical-tissue sections reveals alterations in tissue biochemistry with dysplasia. Photochem Photobiol 2001;73:636–41.

[502] Thornhill DP. Elastin: locus and characteristics of chromophore and fluorophore. Connect Tissue Res 1972;1:21–30.

[503] Richards-Kortum R, Sevick-Muraca E. Quantitative optical spectroscopy for tissue diagnosis. Annu Rev Phys Chem 1996;47:555–606.

[504] Acharya AS, Manning JM. Reaction of glycolaldehyde with proteins: latent crosslinking potential of alpha-hydroxyaldehydes. Proc Natl Acad Sci U S A 1983;80:3590–4.

[505] Collins JS, Goldsmith TH. Spectral properties of fluorescence induced by glutaraldehyde fixation. J Histochem Cytochem 1981;29:411–4.

[506] Bubnis WA, Ofner CM. The determination of epsilon-amino groups in soluble and poorly soluble proteinaceous materials by a spectrophotometric method using trinitrobenzenesulfonic acid. Anal Biochem 1992;207:129–33.

[507] Yu Y-Q, Li Z-Z, Tian H-J, Zhang S-S, Ouyang P-K. Synthesis and characterization of thermoresponsive hydrogels cross-linked with acryloyloxyethylaminopolysuccinimide. Colloid Polym Sci 2007;285:1553–60.

[508] Levchik GF, Si K, Levchik S V, Camino G, Wilkie CA. The correlation between cross-linking and thermal stability: Cross-linked polystyrenes and polymethacrylates. Polym Degrad Stab 1999;65:395–403.

[509] Lim Y-M, Gwon H-J, Park J-S, Nho Y-C, Shim J-W, Kwon IK, et al. Synthesis and properties of hyaluronic acid containing copolymers crosslinked by gamma-ray irradiation. Macromol Res 2011;19:436–41.

[510] Harrisson F, Callebaut M, Vakaet L. Microspectrographic analysis of trypan blue-induced fluorescence in oocytes of the Japanese quail. Histochemistry 1981;72:563–78.

[511] Loike JD, Silverstein SC. A fluorescence quenching technique using trypan blue to differentiate between attached and ingested glutaraldehyde-fixed red blood cells in phagocytosing murine macrophages. J Immunol Methods 1983;57:373–9.

[512] Liesche J, Marek M, Günther-Pomorski T. Cell wall staining with Trypan blue enables quantitative analysis of morphological changes in yeast cells. Front Microbiol 2015;6.

[513] Busetto S, Trevisan E, Patriarca P, Menegazzi R. A single-step, sensitive flow cytofluorometric assay for the simultaneous assessment of membrane-bound and ingested Candida albicans in phagocytosing neutrophils. Cytom Part A 2004;58A:201–6.

[514] Kang HW, Tabata Y, Ikada Y. Fabrication of porous gelatin scaffolds for tissue engineering. Biomaterials 1999;20:1339–44.

[515] Wolf MT, Daly KA, Brennan-Pierce EP, Johnson SA, Carruthers CA, D'Amore A, et al. A hydrogel derived from decellularized dermal extracellular matrix. Biomaterials 2012;33:7028–38.

[516] Moody TP, Donovan MA, Laue TM. Turbidimetric studies of Limulus coagulin gel formation. Biophys J 1996;71:2012–21.

[517] Chernysh IN, Weisel JW. Dynamic imaging of fibrin network formation correlated with other measures of polymerization. Blood 2008;111:4854–61.

[518] Xiong JY, Narayanan J, Liu XY, Chong TK, Chen SB, Chung TS. Topology evolution and gelation mechanism of agarose gel . J Phys Chem B 2005;109:5638–43.

[519] Tibbitt MW, Kloxin AM, Sawicki LA, Anseth KS. Mechanical properties and degradation of chain and step- polymerized photodegradable hydrogels. Macromolecules 2013;46:2785–92.

[520] Costello LC, Franklin RB. A review of the important central role of altered citrate metabolism during the process of stem cell differentiation. J Regen Med Tissue Eng 2013;2:1.

[521] Kim SE, Choi HW, Lee HJ, Chang JH, Choi J, Kim KJ, et al. Designing a highly bioactive 3D bone-regenerative scaffold by surface immobilization of nano-hydroxyapatite. J Mater Chem 2008;18:4994.

[522] Phadke A, Shih Y-R V, Varghese S. Mineralized synthetic matrices as an instructive microenvironment for osteogenic differentiation of human mesenchymal stem cells. Macromol Biosci 2012;12:1022–32.

[523] Gomes S, Leonor IB, Mano JF, Reis RL, Kaplan DL. Spider silk-bone sialoprotein fusion proteins for bone tissue engineering. Soft Matter 2011;7:4964.

[524] Franklin RB, Chellaiah M, Zou J, Reynolds MA, Costello LC. Evidence that osteoblasts are specialized citrate-producing cells that provide the citrate for incorporation into the structure of bone. Open Bone J 2014;6:1–7.

[525] Davies E, Müller KH, Wong WC, Pickard CJ, Reid DG, Skepper JN, et al. Citrate bridges between mineral platelets in bone. Proc Natl Acad Sci U S A 2014;111:E1354–63.

[526] Kajimoto K, Terada H, Baba Y, Shinohara Y. Essential role of citrate export from mitochondria at early differentiation stage of 3T3-L1 cells for their effective differentiation into fat cells, as revealed by studies using specific inhibitors of mitochondrial di- and tricarboxylate carriers. Mol Genet Metab 2005;85:46–53.

[527] Farmer SR. Transcriptional control of adipocyte formation. Cell Metab 2006;4:263–73.

[528] Weerachayaphorn J, Pajor AM. Identification of transport pathways for citric acid cycle intermediates in the human colon carcinoma cell line, Caco-2. Biochim Biophys Acta 2008;1778:1051–9.

[529] Gopal E, Miyauchi S, Martin PM, Ananth S, Srinivas SR, Smith SB, et al. Expression and functional features of NaCT, a sodium-coupled citrate transporter, in human and rat livers and cell lines. Am J Physiol Gastrointest Liver Physiol 2007;292:G402–8.

[530] Guimarães LF, Fidalgo TKDS, Menezes GC, Primo LG, Costa e Silva-Filho F. Effects of citric acid on cultured human osteoblastic cells. Oral Surg Oral Med Oral Pathol Oral Radiol Endod 2010;110:665–9.

[531] Lan WC, Lan WH, Chan CP, Hsieh CC, Chang MC, Jeng JH. The effects of extracellular citric acid acidosis on the viability, cellular adhesion capacity and

protein synthesis of cultured human gingival fibroblasts. Aust Dent J 1999;44:123–30.

[532] Marom R, Shur I, Solomon R, Benayahu D. Characterization of adhesion and differentiation markers of osteogenic marrow stromal cells. J Cell Physiol 2005;202:41–8.

[533] Siegel G, Kluba T, Hermanutz-Klein U, Bieback K, Northoff H, Schäfer R. Phenotype, donor age and gender affect function of human bone marrow-derived mesenchymal stromal cells. BMC Med 2013;11:146.

[534] Vila OF, Martino MM, Nebuloni L, Kuhn G, Pérez-Amodio S, Müller R, et al. Bioluminescent and micro-computed tomography imaging of bone repair induced by fibrin-binding growth factors. Acta Biomater 2014;10:4377–89.

[535] Machado R, Azevedo-Silva J, Correia C, Collins T, Arias FJ, Rodríguez-Cabello JC, et al. High level expression and facile purification of recombinant silk-elastin-like polymers in auto induction shake flask cultures. AMB Express 2013;3:11.

[536] Bollinger JA, Brown DE, Dooley DM. The formation of lysine tyrosylquinone (LTQ) is a self-processing reaction. Expression and characterization of a Drosophila lysyl oxidase. Biochemistry 2005;44:11708–14.

[537] Paz MA, Flückiger R, Boak A, Kagan HM, Gallop PM. Specific detection of quinoproteins by redox-cycling staining. J Biol 1991;266:689–92.

[538] Palamakumbura AH, Trackman PC. A fluorometric assay for detection of lysyl oxidase enzyme activity in biological samples. Anal Biochem 2002;300:245–51.

[539] Zou Q, Habermann-Rottinghaus SM, Murphy KP. Urea effects on protein stability: hydrogen bonding and the hydrophobic effect. Proteins 1998;31:107–15.

[540] Lim WK, Rösgen J, Englander SW. Urea, but not guanidinium, destabilizes proteins by forming hydrogen bonds to the peptide group. Proc Natl Acad Sci U S A 2009;106:2595–600.

[541] Harrison RG. Expression of soluble heterologous proteins via fusion with NusA protein. Innovations 2000;11:4–7.

[542] Domek MJ, Robbins JE, Anderson ME, McFeters GA. Metabolism of Escherichia coli injured by copper. Can J Microbiol 1987;33:57–62.

[543] Singh A, Yeager R, McFeters GA. Assessment of in vivo revival, growth, and pathogenicity of Escherichia coli strains after copper- and chlorine-induced injury. Appl Environ Microbiol 1986;52:832–7.

[544] Steck TR, Steck TR. Concentrations of copper thought to be toxic to Escherichia coli can induce the viable but nonculture able condition. Appl Environ Microbiol 2001;67:5325–7.

[545] Singh SM, Panda AK. Solubilization and refolding of bacterial inclusion body proteins. J Biosci Bioeng 2005;99:303–10.

[546] Krueger JK, Kulke MH, Schutt C, Stock J. Protein inclusion body formation and purification. BioPharm 1989;3:40–5.

[547] Gordon DT, Leinart AS, Cousins RJ. Portal copper transport in rats by albumin. Am J Physiol - Endocrinol Metab 1987;252:E327–33.

[548] Masuoka J, Saltman P. Zinc(II) and copper(II) binding to serum albumin. J Biol Chem 1994;269:25557–61.

[549] Venelinov TI, Davies IM, Beattie JH. Dialysis-Chelex method for determination of exchangeable copper in human plasma. Anal Bioanal Chem 2004;379:777–80.

[550] Halliwell CM, Morgan G, Ou CP, Cass AE. Introduction of a (poly)histidine tag in L-lactate dehydrogenase produces a mixture of active and inactive molecules. Anal Biochem 2001;295:257–61.

[551] Waugh DS. An overview of enzymatic reagents for the removal of affinity tags. Protein Expr Purif 2011;80:283–93.

[552] Tortora GJ, Nielsen MT. Bone tissue. In: Tortora GJ, Nielsen MT, editors. Princ. Hum. Anat. 11th ed., Danvers: John Wiley & Sons, Ltd.; 2008, p. 140–63.

[553] Marieb EN. Bones and skeletal tissues. In: Marieb EN, editor. Hum. Anat. Physiol. 6th ed., San Francisco: Pearson Benjamin Cummings; 2004, p. 175–201.

REFERENCES

Appendix

8.1 SCIENTIFIC COMMUNICATIONS

8.1.1 Posters

Aitor Sánchez-Ferrero, Miguel Ángel Mateos Timoneda, Óscar Castaño, Matilde Alonso, Josep Anton Planell, Elisabeth Engel. Elastin-like polymers electrospun fibers for bone tissue engineering. 3rd IBEC symposium on Bioengineering and Nanomedicine, 1-2 June 2010, Barcelona, Spain.

Aitor Sánchez-Ferrero, Álvaro Mata, Matilde Alonso, José Carlos Rodríguez-Cabello, Josep Planell, Elisabeth Engel. Preparation and characterization of glutaraldehyde-cross-linked RGD-containing elastin-like polymer matrices. 24th European Conference on Biomaterials of the European Society for Biomaterials (ESB), 4-9 September 2011, Dublin, Ireland.

Aitor Sánchez-Ferrero, Álvaro Mata, Matilde Alonso, José Carlos Rodríguez-Cabello, Josep Planell, Elisabeth Engel. Setup of citric acid-cross-linked elastin-like polymers hydrogels for bone tissue engineering. 4th IBEC symposium on Bioengineering and Nanomedicine, 18-19 October 2011, Barcelona, Spain.

Aitor Sánchez-Ferrero, Álvaro Mata, Matilde Alonso, José Carlos Rodríguez-Cabello, Josep Planell, Elisabeth Engel. Matrices made of nature-inspired RGD-containing elastin-like polymers for bone tissue engineering. Cross-linking and biological characterization. Advanced summer school: Interrogations at the interface, 20-24 June 2011, Porto, Portugal.

Aitor Sánchez-Ferrero, Álvaro Mata, Adam Engler, José Carlos Rodríguez-Cabello, Josep Planell, Matilde Alonso, Elisabeth Engel. Elastin-like recombinamers/citric acid hydrogels for bone tissue engineering. 6th IBEC symposium on Bioengineering and Nanomedicine, 9 May 2013, Barcelona, Spain.

8.1.2 Oral presentations

Aitor Sánchez-Ferrero, Álvaro Mata, Matilde Alonso, José Carlos Rodríguez-Cabello, Josep Planell, Elisabeth Engel. Carbodiimide and citric acid-mediated generation of elastin-like polymers hydrogels for bone tissue engineering. Characterization of cross-linking reaction. 9th World Biomaterials Congress, 1-5 June 2012, Chengdu, China.

Aitor Sánchez-Ferrero, Álvaro Mata, Adam Engler, José Carlos Rodríguez-Cabello, Josep Planell, Matilde Alonso, Elisabeth Engel. Elastin-like recombinamers/citric acid hydrogels for bone tissue engineering. 6th IBEC symposium on Bioengineering and Nanomedicine, 9 May 2013, Barcelona, Spain. FLASH PRESENTATION.

Aitor Sánchez-Ferrero, Álvaro Mata, José Carlos Rodríguez-Cabello, Adam Engler, Josep Planell, Matilde Alonso, Elisabeth Engel. Citric acid-cross-linked hydrogels: characterization of potentially self-mineralizing scaffolds. 25th European Conference on Biomaterials of the European Society for Biomaterials (ESB), 8-12 September 2013, Madrid, Spain.

8.1.3 Publications

Sánchez-Ferrero A, Mata A, Mateos-Timoneda MA, Rodríguez-Cabello JC, Alonso M, Planell J, Engel E. Development of tailored and self-mineralizing citric acid-crosslinked hydrogels for *in situ* bone regeneration. Biomaterials 2015;68:42-53.

Pages 225 to 237 of the thesis, which contains the article cited below, are available in the editor

Sánchez-Ferrero, A.; Mata, A.; Mateos-Timoneda, M.A.; Rodríguez-Cabello, J.C.; Alonso, M.; Planell, J.; Engel, E. *Development of tailored and self-mineralizing citric acid-crosslinked hydrogels for in situ bone regeneration*. Biomaterials, Vol.68, Nov. 2015, pp. 42–53.

doi:10.1016/j.biomaterials.2015.07.062

http://www.sciencedirect.com/science/article/pii/S014296121500650X